5-1-2012

Heat, Mass and Force Flows in Supersonic Shockwave Interactions

John Michael Dixon
University of Nevada, Las Vegas, dixonj19@unlv.nevada.edu

HEAT, MASS AND FORCE FLOWS IN SUPERSONIC SHOCKWAVE INTERACTION

by

John Michael Dixon

Bachelor of Science
Purdue University
2009

A thesis submitted in partial fulfillment of the
requirements for the degree of

Master of Science in Aerospace Engineering

Department of Mechanical Engineering
Howard R. Hughes College of Engineering
Graduate College

University of Nevada, Las Vegas
December 2011

THE GRADUATE COLLEGE

We recommend the thesis prepared under our supervision by

John Michael Dixon

entitled

Heat, Mass and Force Flows in Supersonic Shockwave Interaction

be accepted in partial fulfillment of the requirements for the degree of

Master of Science in Aerospace Engineering
Department of Mechanical Engineering

Darrell Pepper, Committee Chair

Hui Zhao, Committee Member

William Culbreth, Committee Member

Evangelos Yfantis, Graduate College Representative

Ronald Smith, Ph. D., Vice President for Research and Graduate Studies
and Dean of the Graduate College

May 2012

ABSTRACT

Heat, Mass, and Force Flows in Supersonic Shockwave Interaction

By

John Michael Dixon

Dr. Darrell Pepper, Examination Committee Chair

Professor of Engineering

University of Nevada, Las Vegas

There is no cost effective way to deliver a payload to space and, with rising fuel prices, currently the price to travel commercially is also becoming more prohibitive to the public. During supersonic flight, compressive shock waves form around the craft which could be harnessed to deliver an additional lift on the craft. Using a series of hanging plates below a lifting wing design, the total lift generated can be increased above conventional values, while still maintaining a similar lift-to-drag ratio. Here, we study some of the flows involved in supersonic shockwave interaction. This analysis uses ANSYS Fluent Computational Fluid Dynamics package as the modeler. Our findings conclude an increase of up to 30% lift on the modeled craft while maintaining the lift-to-drag profile of the unmodified lifting wing. The increase in lift when utilizing the shockwave interaction could increase transport weight and reduce fuel cost for space and commercial flight, as well as mitigating negative effects associated with supersonic travel.

ACKNOWLEDGMENTS

I would like to thank my Professor, Dr. Darrell Pepper, for his continued support and encouragement throughout my Graduate career, my parents for their continued emotional, mental, and monetary support in pursuit of my education, and my wife, Shayna, without whom I would not have had the motivation to come this far.

TABLE OF CONTENTS

LIST OF TABLES

Number *Page*

LIST OF FIGURES

Number *Page*

CHAPTER 1 : INTRODUCTION

Determining if lift is possible using nothing more than supersonic aerodynamic properties is a step towards creating a reusable launch vehicle whose launch mass would not primarily be made up of fuel. The idea of intersecting shockwaves is to manipulate properties of a rarefied gas in the atmosphere in order to harness energy which doesn't have to be brought on board the craft. By using energy which already exists in the atmosphere, the mass of fuel can be decreased, the fuel expense of the craft is decreased, and the amount the craft is able to carry can be increased. With current technology, the cost to launch an entirely new craft into orbit every time something needs to be done in space is staggering. Additionally, with larger payloads, the craft needs to be larger and the fuel cost then increases.

At the present time, there is no cost effective way to achieve orbit. Using shockwave interactions to generate lift also reduces the excess structural mass which has to be carried to hold large amounts of extra fuel. Eliminating removable, single-use parts means more of the craft is reusable, and will reduce the cost for subsequent launches, while maximizing payload space.

Creating a cost effective reusable launch vehicle unlocks an entirely new avenue for access to space. If the craft can trade fuel and structural mass for payload mass, more opportunities for moving into space become available. One opportunity currently being explored is space tourism. Space tourism not only provides a monetary income for multiple new space companies, it also reignites interest in space travel in the general population. However, the cost of one time launch vehicles is prohibitive to the majority of

the population, as well as for companies with long term interest. In response to this, multiple forms of "Waverider" lifting wing hypersonic planes have been created to slowly reach the desired Mach 25 escape velocity. The RAM/SCRAM jet engines use high stagnation pressure to compress the air through the inlet, combusting and expelling the air to generate a momentum transfer translating to lift. While such planes are able to breach hypersonic speeds, they experience failure due to complex flowfields of viscous interactions. Viscous interactions produce boundary layer separation, regions of high pressure, and heat transfer, which can result in flow degradation or separation in an inlet. The shockwave interaction removes the combustion instability through the inlet and engine, and instead relies on creating areas of high pressure to create a lifting force between the top and bottom surface of the craft. In essence it is a RAM/SCRAM jet engine without the engine, and instead of relying on the momentum transfer to generate lift, it is generated directly by manipulating the forces above and below the craft.

STATEMENT OF PROBLEM

The primary known method of generating lift is using momentum transfer generated by the engines to create a lifting force on the body of the craft as it passes through a fluid. Besides requiring large amounts of fuel and bulky equipment necessary to achieve flight, the achieved lift is not able to be directly affected, merely a derivative of the momentum transfer occurring at the engines. Generating shockwaves along the bottom surface of the craft and reflecting them back using a positioned plate, a lifting force can be generated by

creating differential pressures between the top and bottom surface of the craft. The available heating gradient can also be channeled as a useful energy source for the craft. Using a proper configuration for the reflecting surface below the craft is required to generate the proper shockwave interactions, as well as reduce the outlet mach number to sonic or subsonic speeds.

The interacting shockwaves will create a pressure multiplier which will cause a gradient between the top and bottom of the craft. While the pressure below the craft continually increases, the pressure above the craft remains constant after the initial shock. The drag and negative lift effects on the top surface of the craft can be minimized by modifying the angle of the top surface. As the shockwaves intersect each other, the velocity will decrease, and the pressure will increase by a multiplier based on the strength and angle of the two shockwaves. The pressure calculations are done using various computational programs, including ANSYS Fluent, as well as created programming specific to the application. The created programs attempt to follow the flow using constructed meshes to generate a computational domain that shows angles of shockwaves, Prandtl-Meyer Expansion fan formation, and areas of maximum and minimum pressure. From the mesh, the total pressure along the bottom of the craft and the hanging plate are analyzed to determine maximum lifting force on the craft, as well as determine the ideal configuration of the hanging plate. By determining the look and layout of the pressure points, it can be shown that once supersonic speeds are reached, lift – and then self-sustaining lift – can be generated with reduced fuel or energy expense.

The pressure gradients create large heating gradients along the base of the craft. The heating pattern on the base of the craft can be detrimental if left unchecked. However, with proper channeling the heat can be transported and harnessed as an additional energy source for the craft. As the flow speed increases, the temperature increases as well, with the largest temperature gradients occurring at the surface of the craft where the flows stagnate. The heating which requires close examination stems from the convective currents from the craft to the air, with conductive transfer into the craft. The heating from the craft into the air must be considered because in the enclosed area it has the potential to change the properties of the rarefied gas. The heat transferred to the gas becomes rarefied with an approximate value for the convective transfer coefficient. The extreme heating moving into the craft can lead to potential structural damage. Initial calculations were done assuming the craft to be a lump-sum body, and then with variable properties to approximate the presence of heat sinks and heat channeling equipment on the craft. Temperature gradients were calculated and analyzed using a Gas Dynamics FEM Tool, ANSYS Fluent, as well as created programming specific to the application.

The reflecting shockwaves only benefit the craft if they can be properly configured to generate the desired amounts of lift at various mach speeds. When shockwaves are free to interact without control, they have the potential to create unwanted pressure, heating, and stress gradients which can cripple a craft. Aligning the plate on the underside of the craft to properly reflect the shockwaves in order to create the desired aerodynamic properties is dependent on the speed of the inlet flow. The variation in configuration factor means multiple simulations must be run to determine both the two dimensional and the three

dimensional impact of shockwaves on the underside of the craft. A second consideration is whether to use a solid plate as the reflecting surface or a series of segmented plates. There are benefits and consequences to both configurations, with specific arrangements that will give a lifting force or a dragging force.

When shockwaves interact with each other, in order to create a useful lifting or dragging force, a specific configuration is needed with, the resulting physical effects being pressure and heating gradients. The goal of determining the configuration of the craft and hanging plate is to show that after supersonic speed is achieved, the aerodynamic properties of the rarefied gas can be manipulated to generate enough lift to keep the craft aloft, and in other applications generate the escape velocity necessary to reach orbit with the minimum expense of fuel. Examining the aerodynamic properties contributing to the pressure gradients also allow a greater understanding of shockwave interactions and their usefulness in air travel. The examination of the heating gradients can give insight into turning waste – and potentially damaging – heating issues into useable energy sources for extended flights.

PURPOSE OF STUDY

Current research regarding shockwave interactions indicates their effects as detrimental forces of uncontrolled pressure and heating gradients. Further research obtained from two and three dimensional simulations show an increasingly comprehensive analysis of shockwaves along plates. Manipulating the properties of air within a controlled environment has the potential to enhance the constructive effects of supersonic flow.

Discovering ways to dampen the destructive effects of shockwaves and increase the positive effects is the biggest step towards creating cheap, reusable launch vehicles, as well creating more fuel efficient and faster travel.

The primary focus for current technological advancement is to create feasible, cost effective, and innovative approach. Historically, shockwave interactions were viewed as a negative inevitability in supersonic flow. The intent of this research is to explore alternative shock-shock geometries that would lead to positive enhancements. From various experiments examining shock configurations, as well as the fundamental fluid dynamic equations characterizing supersonic flow, the outcome of intersecting shockwaves can produce multiplication of the pressures. Minimizing the amount of fuel a craft will need to carry reduces the total fuel cost as well as the structural mass cost for fuel tanks. By reducing the total number of engines required, the structural mass can also be greatly reduced, thus significantly lowering the total cost of the craft. By creating a reusable launch vehicle, there is no longer a need to purchase an entirely new system for each launch, creating a process where merely performing maintenance on the craft after each mission is required. Designing a craft which uses shockwave interaction to generate lift does not rely on reaching a new level of technology, as it is merely a combination of current technologies to manipulate a known phenomenon. The research performed in this study relies primarily on computer simulations and theoretical concepts. A successful proof-of-concept resulting from this modeling can be used to design physical prototypes for further studies.

CHAPTER 2 : PHYSICS REVIEW

The following section is divided into three parts. 1) physical modeling constraints for supersonic and hypersonic flow; 2) supersonic flow past an airfoil in terms of the aerodynamic properties, and 3) aerothermodynamics and viscous boundary layer interaction of the flow. By reviewing the subject matter in this order, specific effects of air flow and heat transfer can be examined, while still focusing on the major influences as it relates to the craft configuration.

Physical models are difficult for computer simulations to approximate due to large changes in flow properties over short distances (steps) caused by the shock and expansion waves. As flow approaches M=5, predictions of accurate real gas formulations are required due to several consequences of air chemistry. The first issue is due to the large density variations during separation, which causes errors in the continuum regime. This issue is typically fixed by combining the Navier-Stokes equations in high density areas with a Direct Simulation Monte Carlo Method for low density regions. The second and third problems stem from the kinetic reactions of some non-equilibrium reactions not being known or fully understood. The gas transfer properties and descriptions of physical and chemical gas properties need to be known to predict skin friction coefficient and flow thermodynamics. The fourth issue deals with the catalyst effects at the high temperatures which occur in supersonic flows. For non-equilibrium flows, the heat transfer due to catalytic effects for an adiabatic case is minimized or amplified for a fully catalytic wall. The catalytic effect changes the size of the separated region and heating on the surface of

the craft. A fifth problem is the laminar-turbulent flows occurring in shockwave boundary layer interaction. While the gross characteristics of laminar and turbulent flows are fairly well known, the transition from one to the next can be subtle in supersonic flows. The final issue is the modeling of turbulence in supersonic flows. Current transport methods can predict interacting flows only if the Mach number is small and the separation region is small. For M>6, density fluctuations become significant and can no longer be neglected. The biggest difference between real and theoretical flows lies in the maximum temperature at reattachment, a discrepancy which cannot be attributed to the compressibility terms. Due to the bulk of problems existing in non-equilibrium, hypersonic simulations the current investigation is limited to perfect gas approximations, equilibrium flows, and Mach = 2,3,4.

Flow before shocks is modeled using Euler's 1-D gas dynamics equations. Using Euler's equations assumes that the flow is a calorically perfect, adiabatic, polytropic process. Assuming inviscid flow to negate viscous effects in the gas allows the flow to be modeled using equations 2.1, 2.2, 2.3 (NASA, 2010),

$$\frac{\partial \rho}{\partial t} = -\frac{\partial}{\partial x}(\rho u) \tag{2.1}$$

$$\frac{\partial \rho u}{\partial t} = -\frac{\partial}{\partial x}(\rho u^2 + p) \tag{2.2}$$

$$\frac{\partial \rho E}{\partial t} = -\frac{\partial}{\partial x}[\rho u\left(e + \frac{1}{2}u^2 + \frac{p}{\rho}\right)] \tag{2.3}$$

Where ρ is the fluid density, u is the fluid velocity, e is the internal energy of the fluid, p is the fluid pressure, t is the time in seconds, x is the distance along the streamwise axis, and

E is the fluid specific total energy. When the fluid reaches the front of a shock, discontinuity in the flow requires a piecewise jump condition. The jump condition follows the Rankine-Hugoniot conditions for 1-D gas dynamics. For the hyperbolic conservation law (Freytag, 2010)

$$\frac{\partial w}{\partial t} + \frac{\partial}{\partial x} f(w) = 0 \tag{2.4}$$

The jump condition is*

$$s(w_1 - w_2) = f(w_1) - f(w_2) \tag{2.5}$$

a function which satisfies the flow's entropy condition. Equation 2.5 is a characteristic equation relating the entropy of the flow to the characteristic speeds ($f(w_{1,2})$) of upstream and downstream flow (1,2, respectively). Rearranging the characteristic variable, *w*, with the vector state $[\rho,\rho u,\rho E]^T$, the jump conditions become (Freytag, 2010)

$$s(\rho_2 - \rho_1) = \rho_2 u_2 - \rho_1 u_1 \tag{2.6}$$

$$s(\rho_2 u_2 - \rho_1 u_1) = (\rho_2 u_2^2 + p_2) - (\rho_1 u_1^2 + p_1) \tag{2.7}$$

$$s(\rho_2 E_2 - \rho_1 E_1) = \left[\rho_2 u_2 \left(e_2 + \frac{1}{2}u_2^2 + p_2/\rho_2\right)\right] - \left[\rho_1 u_1 \left(e_1 + \frac{1}{2}u_1^2 + p_1/\rho_1\right)\right] \tag{2.8}$$

Equations (2.6), (2.7), and (2.8) are the Rankine-Hugoniot conditions for Euler equations, and are the basis for calculations to determine shock strength and speed and characteristic values for flows at Mach 2, 3, and 4.

AERODYNAMIC PROPERTIES

In order to show the feasibility of lift on the craft, the properties of physics governing super- and hypersonic flow must be examined as it travels past an airfoil. This is separated into four sections. The first section to be examined is the initial attached bow shock of the main body. The bow shock is based on the same formulation for the main body as well as the thin hanging plate, with minor adjustments for angle of attack and angle of inclination. The aerodynamics of the top surface of the craft is also examined briefly to show methods of using the bow shock to minimize the pressure and drag. The second section analyzes the intersecting shockwaves in a parallel plated system. Utilizing parallel plates creates the desired pressure gradients along the bottom surface of the craft, but they also decrease the speed of the flow as a result of the flow intersection. The third point of interest examines boundary layer effects and section four looks at the potential for Prandtl-Meyer expansion flows along the top and bottom surfaces of the parallel plates. Boundary layer interaction creates potential flow instabilities as well as areas of high pressure and stress gradients, while Prandtl-Meyer expansion regions have the potential to increase the velocity of the flow while posing a hazard of reducing the pressure.

The first interaction between the air and the craft is the bow shock interaction. For flows above Mach one but below hypersonic Mach speeds, the properties of the bow shock can be determined according to the isentropic equations for oblique shocks (NASA, 2010),

$$\frac{p_1}{p_0} = \frac{2\gamma M^2 sin^2\theta - (\gamma - 1)}{(\gamma + 1)} \tag{2.9}$$

$$\frac{T_1}{T_0} = \frac{[2\gamma M^2 sin^2\theta - (\gamma - 1)][(\gamma - 1)M^2 sin^2\theta + 2]}{(\gamma + 1)^2 M^2 sin^2\theta} \tag{2.10}$$

The reflection angle and the Mach number of the inlet flow dictates the wave angle coming off the bow according to the equation (2.11). Also, for design purposes, the ideal wave angle can be determined using the θ-β-M chart shown in Figure (2.1) (NASA, 2010).

$$tan\theta = 2cot\beta \frac{M_1^2 sin^2\beta - 1}{M_1^2(\gamma + cos2\beta) + 2} \tag{2.11}$$

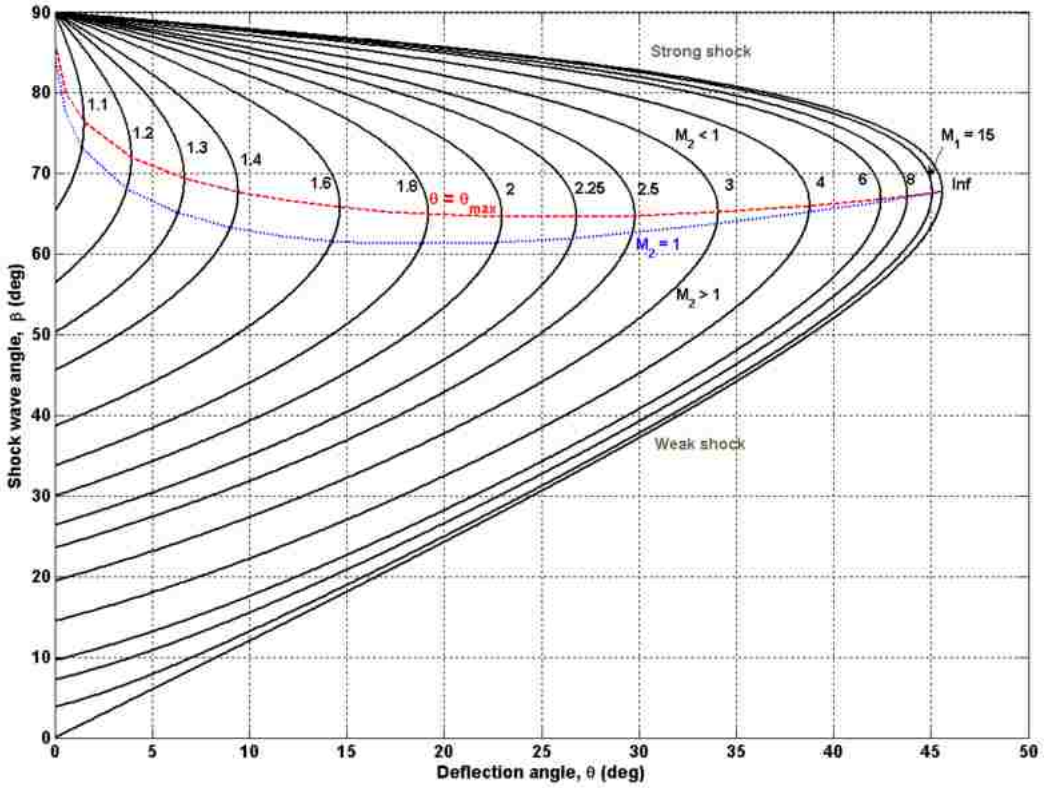

Figure 2.2.1 Theta-Beta-Mach Chart

For M > 5, the properties after the shock reach a mathematical limit. Using perfect gas approximation with the specific heat ratio equal to 1.4, the limit for the density ratio is 6. The equations for the pressure, density, and temperature are adjusted to the following relations (NASA, 2010)

$$\frac{p_2}{p_1} \approx \frac{2\gamma}{\gamma+1} M_1^2 sin^2\beta \tag{2.12}$$

$$\frac{\rho_2}{\rho_1} \approx \frac{\gamma+1}{\gamma+1} \tag{2.13}$$

$$\frac{T_2}{T_1} \approx \frac{2\gamma(\gamma-1)}{(\gamma+1)^2} M_1^2 sin^2\beta \tag{2.14}$$

For non-equilibrium flows, there is a hypersonic post shock dissociation of Oxygen (O_2) and Nitrogen (N_2) into elemental Oxygen (O) and Nitrogen (N) allowing for higher values to occur in nature. However, the simulations and computations can be done with the assumption of equilibrium flows. On the top surface of the craft, the deflection angle is minimized to reduce drag and shock angle in order to create the highest pressure differential between the top and bottom surface.

The bottom surface of the craft relies on multiple shockwave interactions to maximize the pressure differential between the top and bottom surfaces. Using the shock created by the hanging plate and the bow shock from the main craft, the shockwaves intersect and reflect off of the top surface and hanging plate multiple times. Each reflection changes the velocity of the freestream after the shock, as well as the direction of flow. This requires the hanging plates to be separate attachments so each can modify their respective position to maximize lift at various Mach numbers. The direction of the flow after each intersection

changes according the angle of interaction between the two shock waves, balancing around a slip line, as shown in Figure 2.2.

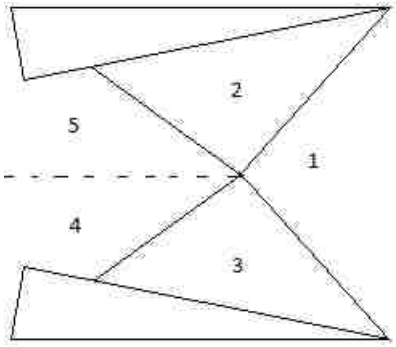

Figure 2.2.2 Shockwave Interaction Regions with Slip-Line

After each shock wave interaction, the pressure balances around the slip line according to the equation (2.14). The pressure equilibrium implies flow similarities on either side of the slip; however what is occurring is instead a contact discontinuity, or a region of space separating two areas of equal pressure and velocity but varying density and temperature (National Aeronautics and Space Administration, 2008)

$$\frac{P_5}{P_1} = \frac{P_4}{P_1} \qquad (2.14)$$

$\rho_5 \neq \rho_4$

The pressures in the final region balances according to a supersonic flow area pressure ratio and a subsonic flow area pressure ratio. It should also be noted that due to conduction between gasses across the slip line, it cannot feasibly be maintained for an infinite length, but will eventually fade out. In the present work, the distance of each slip line is assumed much less than the distance to fade, and therefore must be considered in the analysis. Free stream velocity in the area surrounding the affected area is maintained at the original Mach

speed, creating a buffer area between the degraded Mach region and the ambient conditions.

The shock wave interaction passing through the boundary layers can create areas of extreme pressure, stress, and temperature. The boundary layer types present in the current investigation are ramp flow and incident-reflecting shock. The ramp flow comes from an abrupt change in the wall inclination, causing the origin of a shock related to the wedge angle. The second flow is an impingement on the wall as the flow undergoes a deflection through the incident shock, making the flow parallel to the wall. For the compression ramp flow, as Mach number increases, the upstream ramp influence increases in length, causing an increase in distance between the separation point and the theoretical incident shock impact point. The first shock associated with separation forms upstream of the ramp, and a second shock originates in the reattachment region intersecting the separation shock a short distance from the wall. The arrangement of the shock and boundary lines can be seen in Figure 2.3, (Amaha, Singh, & Martis, 2011).

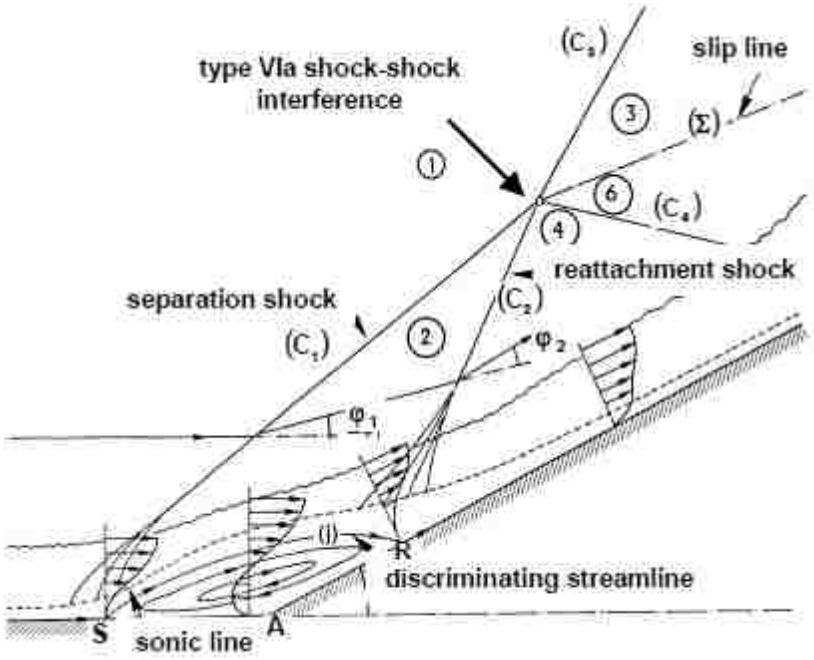

Figure 2.2.3 Structure of a ramp flow with boundary layer separation

The resulting separation of the flow from the wall, and associated reattachment, causes low speed flow accelerated by the viscous forces until the momentum increase is enough to overcome the secondary pressure rise at reattachment. The increase in overall pressure rise depends only on the upstream flow conditions and therefor causes a higher pressure rise at reattachment. The second boundary layer interaction is the impinging-reflecting oblique shock, and occurs at each reflection off the bottom surface of the craft. Similar to ramp flow, a subsonic inner layer allows for upstream propagation of the shock's influence. At separation, the separation shock intersects with the incident shock away from the wall, creating a type I shock-shock interference pattern. The pattern configuration is shown in the Figure 2.4, below (Arnal & Delery, 2004).

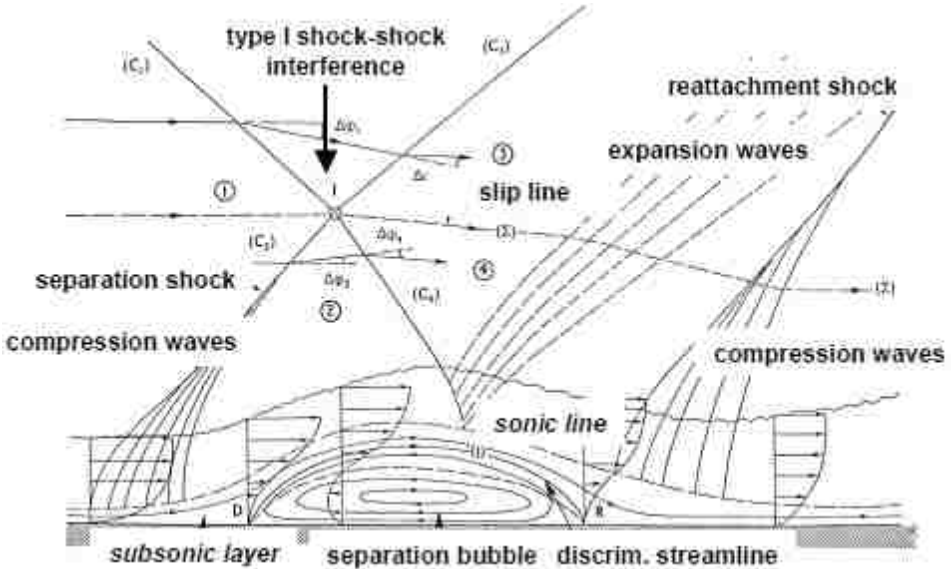

Figure 2.2.4 Impinging-reflecting shock with extended separation

As they relate to the current investigation, both ramp flow and impinging-reflecting shock will increase the pressure distribution along the surface of the main body, contributing to the total pressure increase. However, when the shock becomes strong enough to separate the boundary layer, the inviscid outer stream depends heavily on the boundary layer development in the interaction region. The change in the shock pattern results in refracted and transmitted shocks leading to difficulties in accurate modeling of the waves and discontinuities.

Prandtl-Meyer Expansion fans can be used to increase the flow velocity however they can also reduce the pressure between shocks. Expansion fans can form from the hanging plates in the 2-D approximation, as well as from the struts supporting the plates in the 3-D modeling. The expansion fans which can occur at concave corners of the hanging plates will affect the flow field according to the following equations (NASA, 2010)

$$\frac{T_2}{T_1} = \left(\frac{1 + \frac{\gamma - 1}{2} M_1^2}{1 + \frac{\gamma - 1}{2} M_2^2} \right) \tag{2.15}$$

$$\frac{p_2}{p_1} = \left(\frac{1 + \frac{\gamma - 1}{2} M_1^2}{1 + \frac{\gamma - 1}{2} M_2^2} \right)^{\gamma/(\gamma-1)} \tag{2.16}$$

$$\frac{\rho_2}{\rho_1} = \left(\frac{1 + \frac{\gamma - 1}{2} M_1^2}{1 + \frac{\gamma - 1}{2} M_2^2} \right)^{1/(\gamma-1)} \tag{2.17}$$

$$v(M) = \int \frac{\sqrt{M^2 - 1}}{1 + \frac{\gamma - 1}{2} M^2} \frac{dM}{M} \tag{2.18}$$

Where v(M) is the Prandtl-Meyer function determined by the Mach number. For some of the hanging plates and struts, the turn will be greater than the maximum turning angle, causing the flow to become unparallel to the new wall. In order to determine these values and their associated effects, equations (2.19) and (2.20) are used (NASA, 2010)

$$v_{max} = \frac{\pi}{2} \left(\sqrt{\frac{\gamma + 1}{\gamma - 1}} - 1 \right) \tag{2.19}$$

$$\theta_{max} = v_{max} - v(M_1) \tag{2.20}$$

Even though the pressure will decrease during the turn, the areas of high pressure being sought will occur after bow shocks from the hanging plates. The benefit of placing expansions in the flow causes stronger bow shocks to form giving the system more pressure differentials each time shock interactions occur.

AEROTHERMODYNAMICS

The aerothermodynamics is divided into three sections. The first section focuses on the thermal boundary layer and wall conditions present during the flow. The separation length and thermal effects from the thermal boundary layer gives insight into the expected heat flux and temperature into the body of the craft inside the thermal boundary. At each reflected shock, viscous and frictional forces at the wall cause a heating gradient into the surface of the craft. The location of the reflected shockwaves along the bottom surface of the craft with respect to the thermal boundary layer will greatly influence the amount of energy absorbed into the system, and can give insight as to potential failure points along the surface of the craft at increasing speeds. The second section examines some known and theorized real gas effects in supersonic and hypersonic flow. The structure of the inviscid flow region deviates from the constant specific heat ratio case, and transport properties are affected by dissociation. The second point occurs more during hypersonic flow; and as this work assumes equilibrium chemical properties, the discussion for dissociation is done more as a consideration for real world effects. The final section discusses the problems that exist using physical modeling in the computer simulation programs. Real gas dissociation effects, gas transfer properties, and turbulence modeling are only three of the difficulties with creating an accurate real gas/real world approximation of the physical model.

In the thermal boundary layer for supersonic and hypersonic interactions, there are three major outcomes from the shockwave-boundary layer interactions: 1) If the wall temperature is well below the outer stream stagnation temperature, a cold wall scenario

exists which may alter interaction properties; 2) the heat transfer process has a large effect in separated flows where the shear layer emanating from the separation region impacts the reattachment surface; 3) real gas effects modify the thermodynamic and transport properties of the gas (Kienappel, Koppenwallner, & Legge, 1974). Of the three effects, the first two have been experimentally verified, while the third case is more theoretical. The wall temperature effects are characterized by the ratio of the wall temperature and the recovery temperature, with most situations closely resembling the cold wall situation as the outer stream temperature is typically higher than the vehicle temperature. A lower wall temperature also affects the separation length of the stream during the turbulent flows over the craft. The lowered temperature creates an increase in skin friction coefficient and an increase in density, reducing the boundary layer displacement thickness. Assuming a cold wall condition on the base of the craft, as well as on the hanging plates, the larger separation area can aid in convective heat transfer to the heat sink areas of the craft, avoiding detrimental heat buildup on the vehicle and plates (Berry & Vas, 1972).

The passage of air through the bow shock and hanging plate shocks undergoes transition due to ionization, dissociation, and vibration. The changes which occur can be compared to a calorically perfect case, which highlights the two main issues of change: inviscid structure and transport properties. The modified inviscid structure has an impact on both the inviscid region shock angle, and the viscous boundary layer thickness. While the perfect gas case has been modeled and results from experiments achieved, the real gas effects on shockwave boundary layer interaction are difficult to accurately model. Some results determined during an experiment while at Mach numbers ranging from 7.5 to 9.1,

making the assumption of laminar flow to avoid turbulence modeling, found smaller separation areas formed during ramp flow from weaker shock waves due to dissociation. During trials examining impinging-reflecting shock cases, the interaction is only weakly affected by real gas effects at low Reynolds number. This implies the ability to accurately calculate the flow using constant local values for the specific heat. However, at higher Reynolds numbers, dissociation and other chemical effects created noticeable differences in the wall pressure and heat transfer. An overall conclusion from multiple studies is that the chemical length scale for non-equilibrium flows will be much greater than the boundary layer thickness scale, meaning the flow can be considered frozen with no influence of relaxation on the interaction (Koppenwallner, 1987).

CHAPTER 3 : METHODOLOGY

Using the values from Table 3.1 as the control model, the test models have hanging plates in addition to the geometry of the base model. The Finite Element Method and Computational Fluid Dynamics packages used are the ANSYS Workbench v13, and ANSYS Fluent v13. The algorithm uses a patch independent method, in order to increase accuracy around the named edges and boundaries. The patch conforming method creates a mesh of the edges, then the faces, and then the volume. This method does not have a problem capturing edges but creates lower quality meshes. Using the patch independent method, the algorithm first meshes the entire volume then cut out areas around the faces and edges, achieving a higher density mesh around the areas of shockwave and shock boundary layer interaction. The mesh is created using a minimum element size of 0.05 m, which allows a greater amount of accuracy of the elements and nodes in the mesh. The source of the sizing is based on the face curvature for the 3D model and local element sizing of selected faces, specifically regarding the faces of the hanging plates and lower surface of the main body. The advantage of the small element size combined with the independent patching method means the default minimum element length of the mesh can more accurately represent the areas (reduced discretization error) in between the plates and the craft. However, small element size has disadvantages such as an increase in computation time, an increase in residual error, and an increase in computational power (Pepper & Heinrich, 2006).

The element size is variable in the mesh, enabling refinement around areas of interest. Mesh shape sizes are inflated around boundary areas to reduce accuracy of the mesh around the entrance, the exit, and the sides of the flow, and is deflated around the unnamed boundaries of the craft body and hanging plates to increase accuracy. To improve the speed of regenerating the mesh as new models are created and various areas examined, a post-processed algorithm solver was used during the patch independent method. The post processing algorithm leaves the majority of the tetrahedral mesh intact, so only areas of interest are refined during updates to the system. Elements around sharp corners, such as the bow of the hanging plates and main craft, are pinched to create nodal points along the edging to capture shock locations (Zienkiewicz, Taylor, & Nithiarasu, 2005).

CONTROL CASE

The purpose of the research design is to develop a high lift vehicle utilizing an unmodified lifting wing arrangement as a starting point. The vehicle employs the same lifting wing model and dimensions, except it also has a set of hanging plates to reflect the shockwaves back into the craft. The overall vehicle layout is shown in Figure (3.1), followed by Table (3.1) showing the dimensions and important angles of the model.

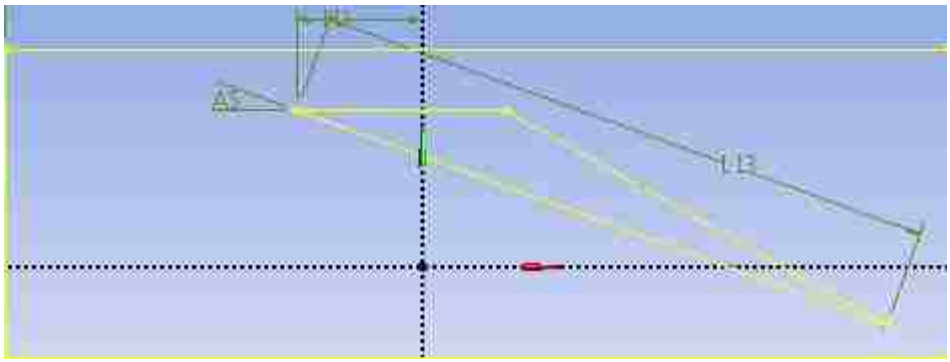

Figure 3.1 Control Vehicle Model

Table 3.1 Control Vehicle Dimensions

Dimension	Value
H1	0.4 m
L13	1.6718 m
A5	20°

The same control dimensions and set up is used for the Mach 3 and Mach 4 cases.

MACH CASES

The Mach 2 case is shown below in Figure (3.2) Table 3.2 lists the dimensions and angles for the hanging plates with respect to the world axis. The length triangle legs comprising the hanging plate sections are all equal. The hypotenuse legs are 0.25 m and the long leg is 0.2 m.

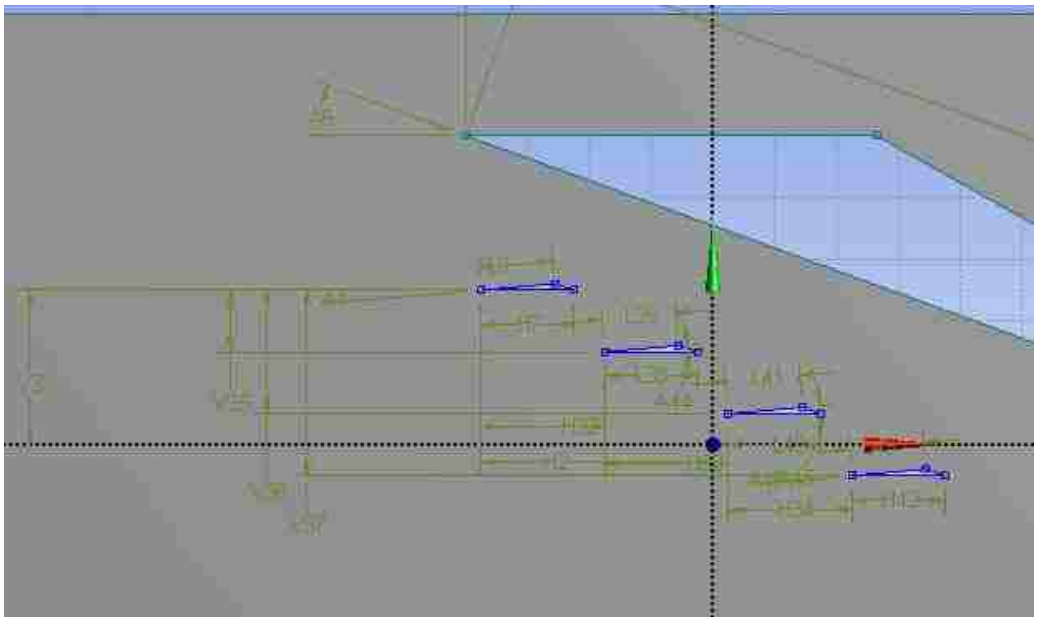

Figure 3.2 Mach 2 Hanging Plate Locations

Table 3.2 Mach 2 Hanging Place Location

Dimension	Value
A4	5deg
A44	5deg
A45	5deg
A46	5deg
H2	0.375m
H32	0.2m
H33	0.2m
H34	0.2m
H42	0.15m
H7	0.15m
L38	0.15m
L39	0.12m
L40	0.15m
L41	0.12m
L43	0.12m
L6	0.12m
V3	0.4m
V35	0.1m
V36	0.2m
V37	0.3m

In order to negate edge effects and accurately compute pressure distribution for a unit thickness craft, the meshing is applied to a 3D model with a 1 m thickness. To remove edge boundary effects, the sample line for results is taken at 0.5 m into the model. The mesh created for the Mach 2 case is shown in Figure (3.3),

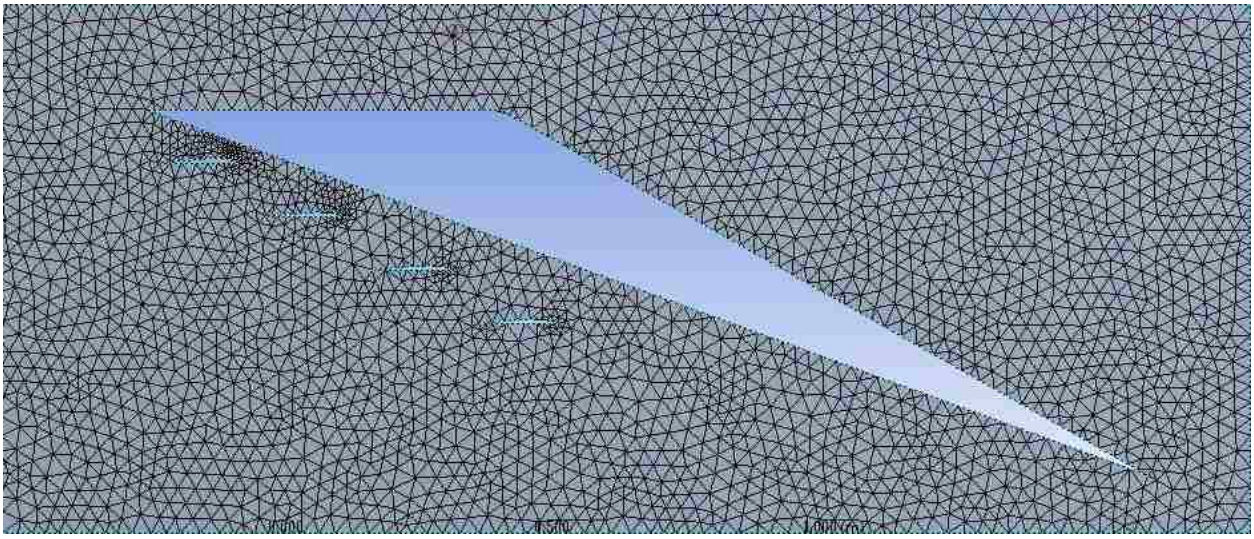

Figure 3.3 Mach 2 Mesh Setup

For the Mach 2 case, there are 479562 elements and 715882 nodes. The Mach 2 case is the basis for the hanging plate setup for the faster velocity cases. In order to design a craft capable of travel during higher velocities, the hanging plates will adapt by rotating up into the craft as the bow shock angle decreases. The deflection angle of the main craft body is set at 20^{o}, which sets the Mach 2 wave angle at approximately 53^{o}. The other Mach wave angles are displayed in Table 3.3.

Table 3.3 Wave Angles for Experimental Mach Speeds

Mach Speed	Wave Angle (at θ = 20°)
2	53^o
3	38^o
4	33^o
5	30^o

In order to successfully mesh and map the Mach 2 case, the main body of the craft has minimal top surface features. This also helps to keep the mesh relatively simple on the top surface and reduce computation time. Over complicating sections of the system which are not in use can result in flow errors due to unnecessary coupled analysis between pressure and temperature, which can create residual and divergence errors in the system.

The Mach 2 cases for the other tiers and angles have the same craft formation, except the hanging plates are translated in 5 steps using 2.5 cm increments away from the y-axis for each trial. The trials were done in 6 tiers in order to generate a trend in the data, with the beginning tier at 40 cm above the x-axis, and translating in 5 cm increments towards the x-axis. Using this approach, plots were generated for 30 different locations for each of the angles tested, or 120 locations and angle combinations overall. The consistent dimensions during the simulations are the main body size, dimensions, and location relative to the world axis; the distance between the hanging plates is maintained at 5 cm horizontal and 10 cm vertical displacement.

The simulation was also run at Mach 3 and Mach 4. The hanging plates were located at the fifth tier, at horizontal displacements of 2.5 cm in front of the bow of the main craft,

even with the main craft, and 2.5 cm aft of the bow of the main craft. The neutral displacement at tier five is shown in Figure (3.4),

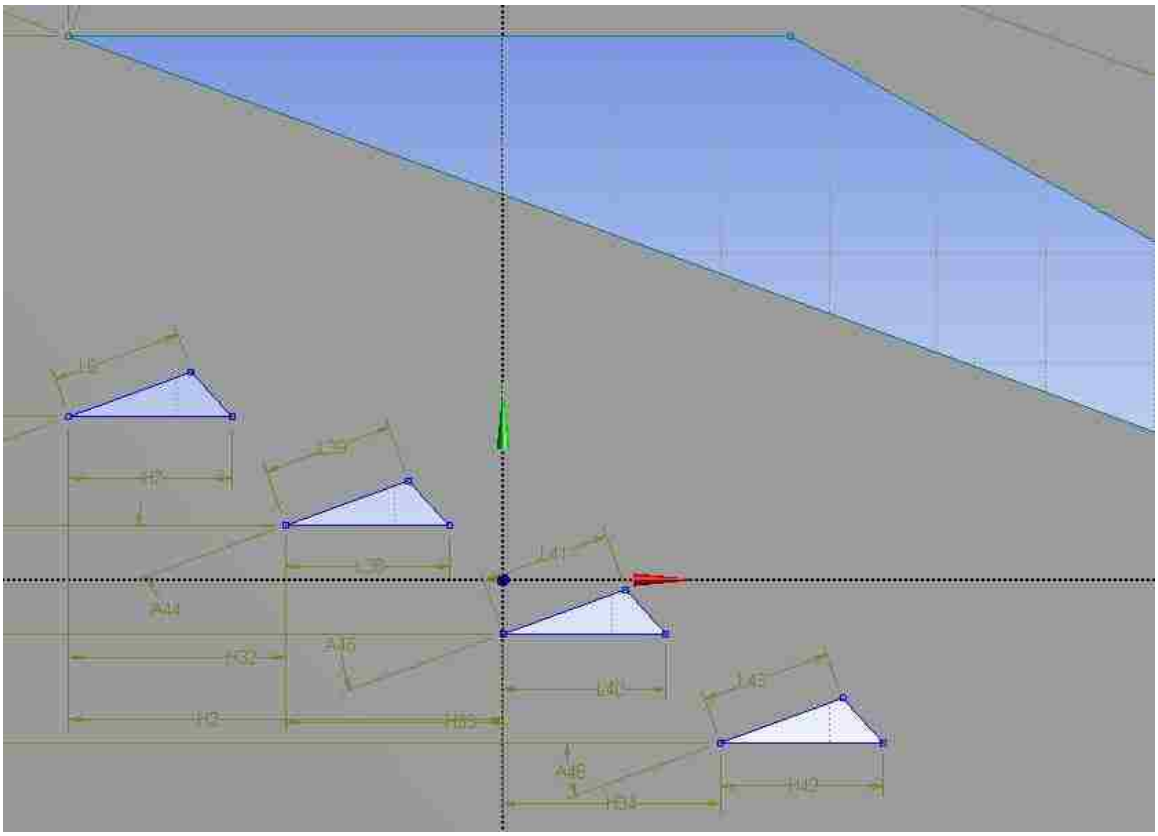

Figure 3.4 Mach 3/Mach 4 Neutral Position

RESULTS

The present analysis examines the advantages of using hanging plates to reflect shock waves into the surface of a lifting wing design vehicle versus the conventional design. The pressure, density, temperature, and velocity streamlines for the unmodified vehicle were examined, and then compared to the charts for the Mach 2 case with hanging plates at various locations. The Mach 3 and Mach 4 control cases were tested against the peak

geometry found from the Mach 2 case. The desired results are to see a greater pressure gradient between the upward force and the downward force, while maintaining a similar lift to drag ratio.

The control vehicle for the Mach 2 case is the currently used arrangement for a lifting wing vehicle. Arranging the setup shown in Figure (3.1) under Mach 2 airflow, with an inlet pressure of 101.325 kPa, Figure (3.5) through (3.7) show the graphs of the pressure, temperature, and density versus movement in the x direction.

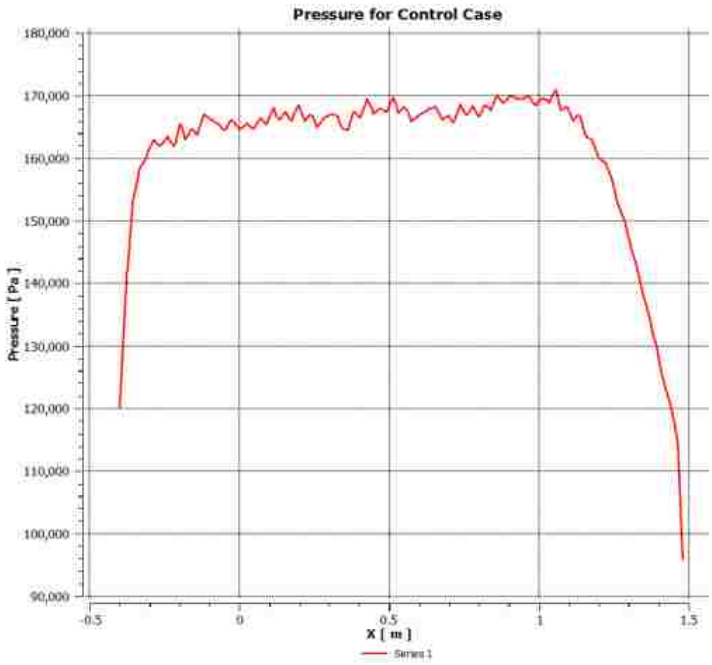

Figure 3.5 Pressure for Control Case

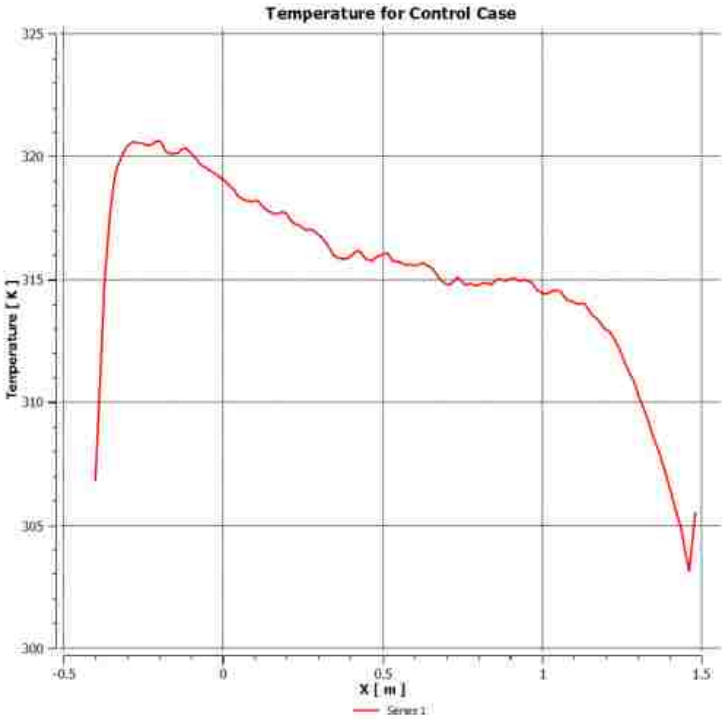

Figure 3.6 Temperature for Control Case

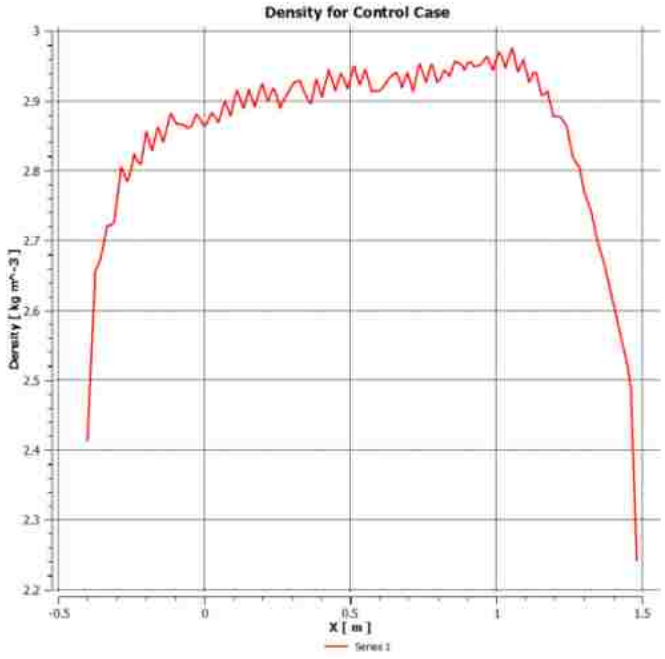

Figure 3.7 Density for Control Case

From the pressure plot we see that the bottom surface of the craft is maintained at an average Pressure of 161100 Pa over the full length. The temperature plot gives an increase as the shock forms on the bow reaching a peak temperature of 321 K, and settles after the boundary layer flow develops after about 0.3 m. The density plot varies from the 2.53 kgm^{-3}ideal gas density of air as the shockwave increases the pressure on the working fluid. The density peaks at 2.98 kg/m^3 towards the trailing edge of the craft, showing locations of boundary layer shocks formed. Following the contour lines in the density plot, the shockwaves created by the hanging plate and main body can be traced by their impact on the freestream density. This helps to verify that shockwaves are created and intersected accurately from the CFD process. A contour plot of the density for an arbitrary plane placed along the center line of the craft is shown in figure.

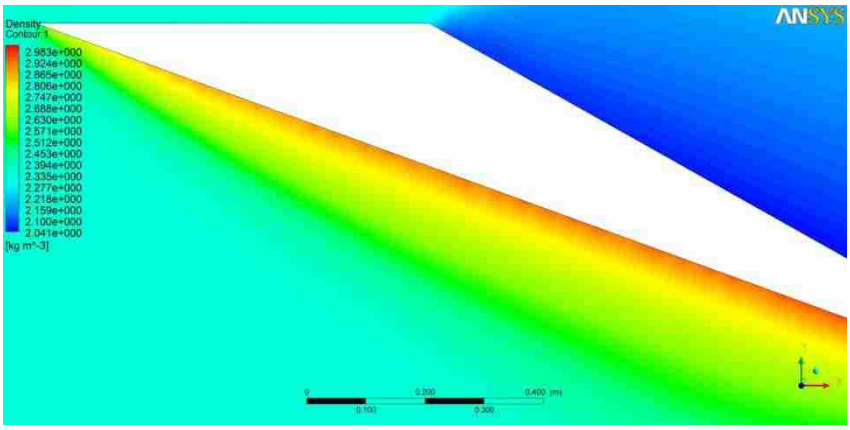

Figure 3.8 Density Contour Plot

The contour plot allows for a quick visual inspection to areas of interest in the control case when compared to the Mach 2 hanging plate arrangement. As can be seen, the pressure distribution along the bottom surface is even for the entire surface. This implies that for

reflecting shockwaves into the bottom surface in the hanging plate design, specific optimization will be required in order to mimic the uniform distribution generated by the conventional case. The temperature distribution plot provides the normal temperature range for a lifting wing craft with the design found in the control case. The density shows the effect of the freestream Mach values along the base of the craft.

The pressure, density, and temperature plots for the Mach 3 control case are shown in Figures (4.9) through (4.11),

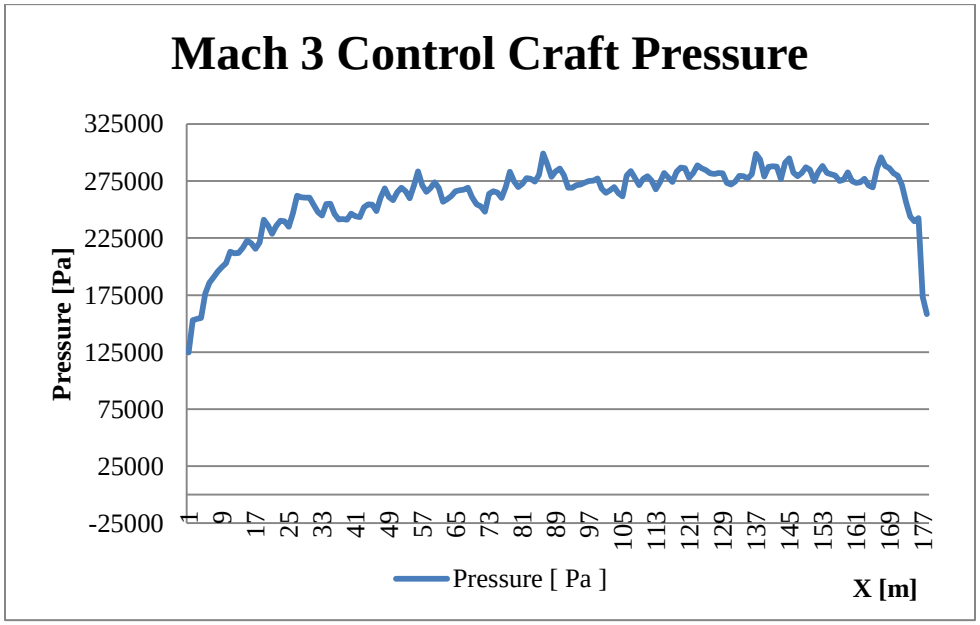

Figure 3.9 Mach 3 Control Case Pressure

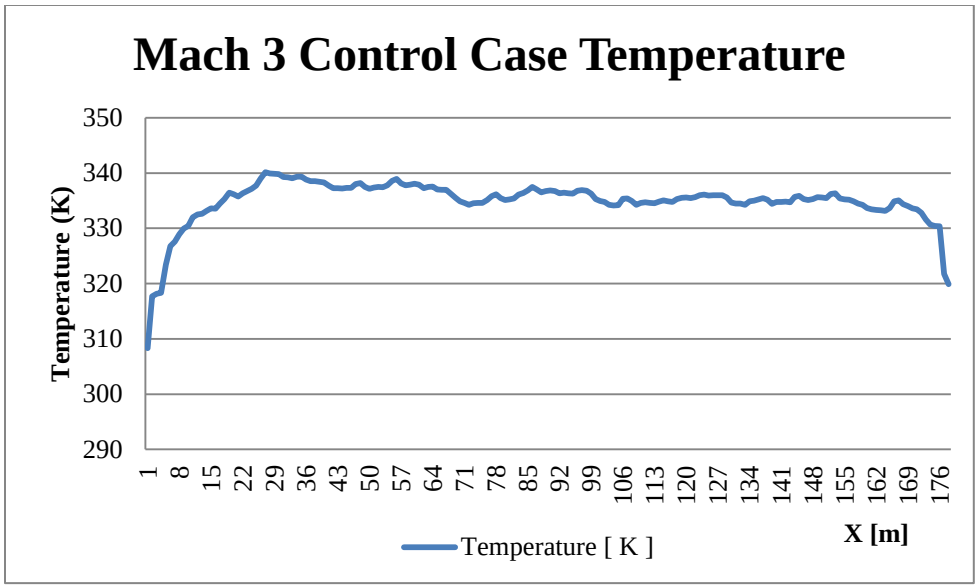

Figure 3.10 Mach 3 Control Case Temperature

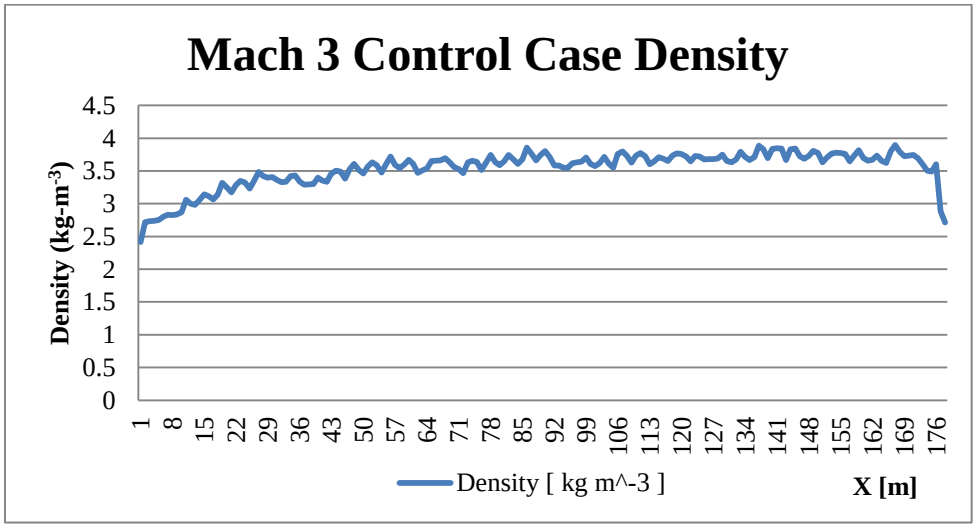

Figure 3.11 Mach 3 Control Case Density

The Mach 3 control case reaches a maximum pressure of 299 kPa, and maintains a mean pressure of 261 kPa. The temperature reaches a maximum of approximately 340 K, and the density has an average of 3.5 kg/m^3, and a maximum of 3.9 kg/m^3. The oscillations in

the plots of the pressure and density are evidence of shockwave boundary layer interaction. Table 3.5 summarizes the notable results for the Mach 3 control case.

The Mach 4 control case pressure, temperature and density plots are shown in Figures (3.12) through (3.14),

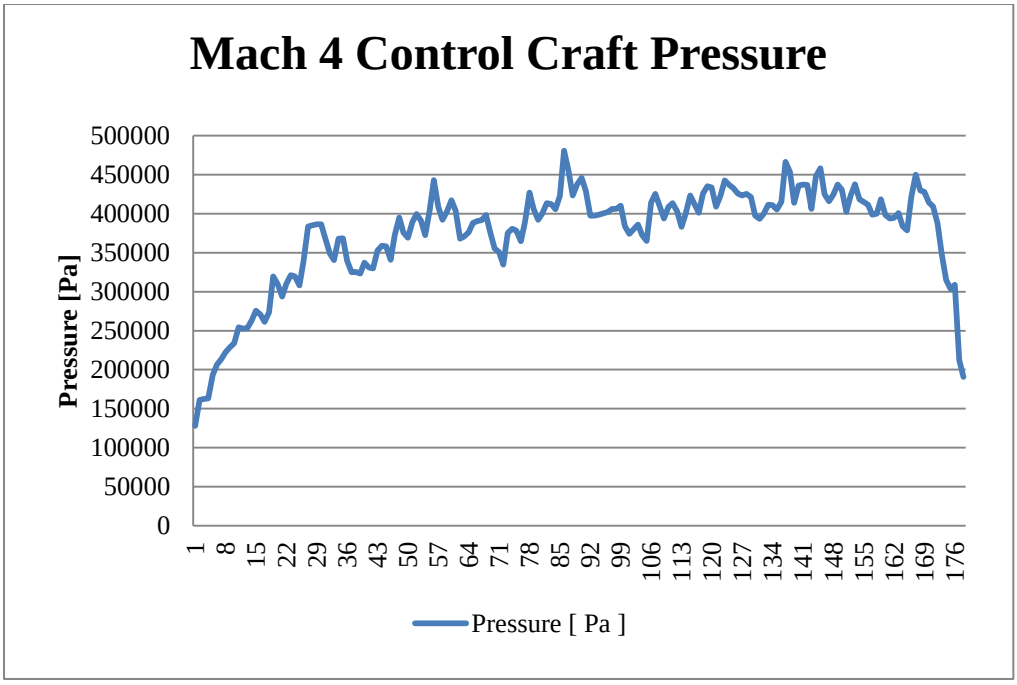

Figure 3.12 Mach 4 Control Pressure

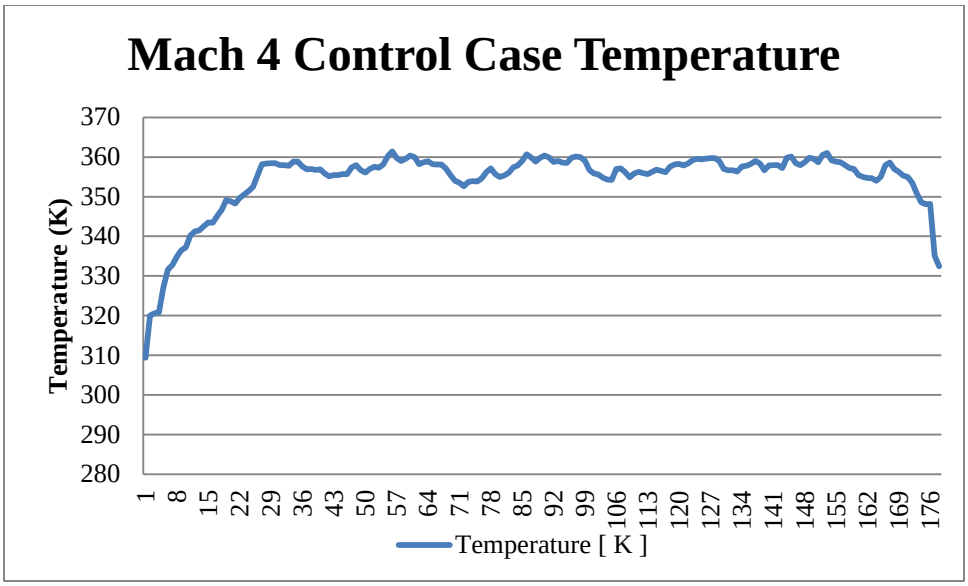

Figure 3.13 Mach 4 Control Case Temperature

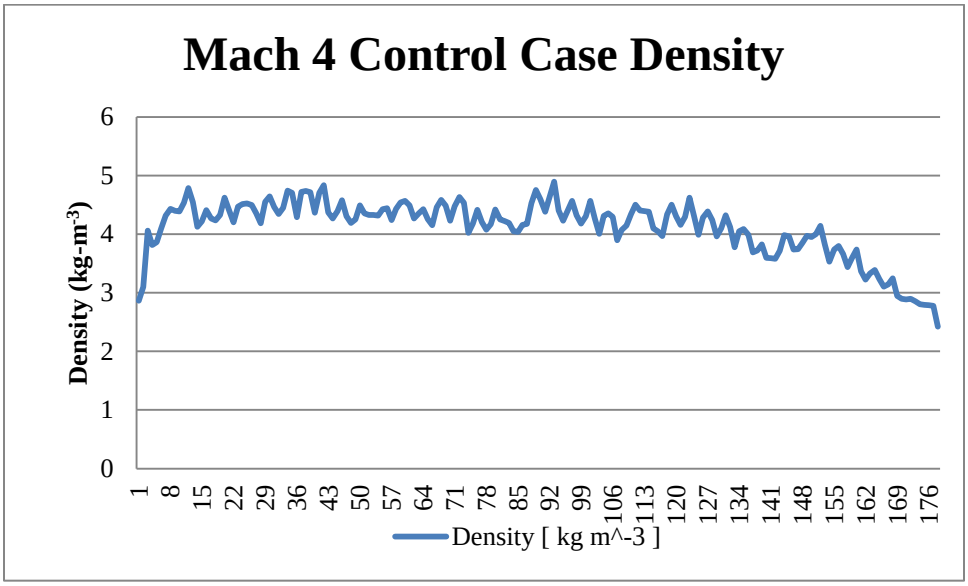

Figure 3.14 Mach 4 Control Case Density

The Mach 4 control case reaches a maximum pressure of 480 kPa, and maintains a mean pressure of 374 kPa. The temperature reaches a maximum of approximately 362 K, and the density has an average of 4.4 kg/m^3, and a maximum of 4.9 kg/m^3. The oscillations in

the plots of the pressure and density are evidence of shockwave boundary layer interaction. Table 3.6 summarizes the notable results for the Mach 4 control case.

The case using hanging plates is placed in a Mach 2, Mach 3, and Mach 4 flow, with an operating pressure of 101325 Pa. The regions examined in the hanging plate design case are the solid bottom surface of the craft and the pressure along the top and bottom surfaces of the hanging plates. Mach 2 is first simulated at various locations with the hanging plates having an angle of 5^{o}. Mach 3 plots are simulated at optimal locations found from the Mach 2 case, and then checked at another location. Plots showing the pressure, temperature, and density versus movement along the x-axis on the bottom surface of the craft for neutral location of a 0.0 cm offset from the front of the craft and a 40 cm offset from the x-axis are shown in the figure.

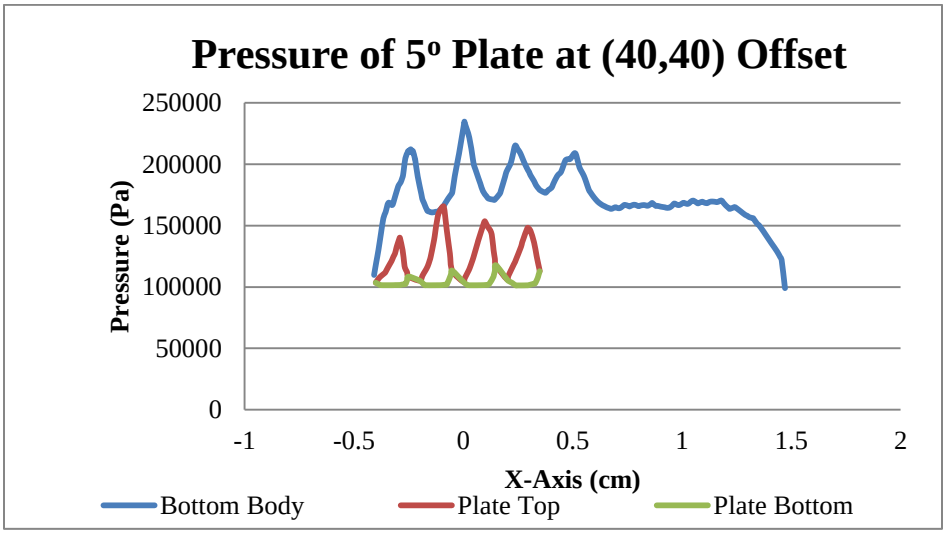

Figure 3.15 Pressure of 5^{o} Plate at (40,40) Offset

The oscillations in Figure (3.15) are a result of the hanging plates creating shocks that intersect with the bow shock created by the main craft. The peaks on the "Bottom Body"

line are regions where the shocks from the hanging plates intersect off of the main craft. Along the "Plate Top", the peaks in oscillations are the weak shocks forming inside the boundary layer after the flow separates along the surface. The bottom of the plate is parallel to the flow, therefor has minimal oscillations, gaining pressure as the flow turns around the stern of the plate and rejoins with the flow from the top surface of the plate.

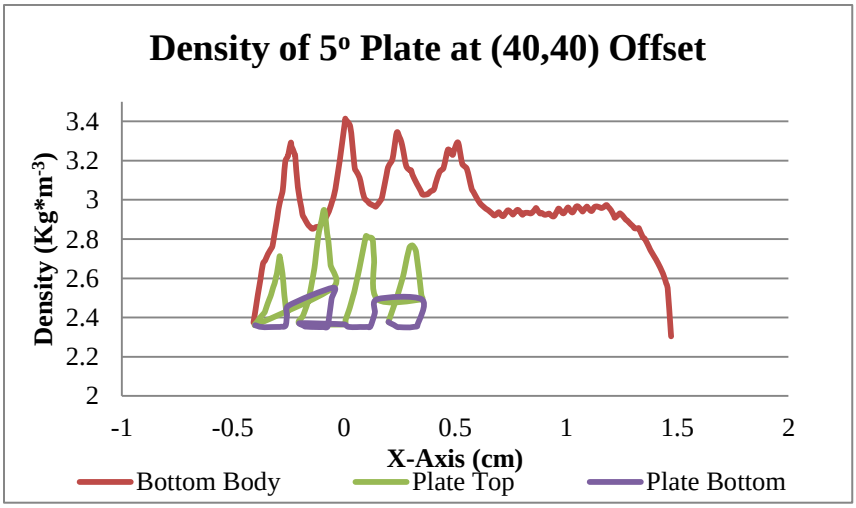

Figure 3.16 Density of 5° Plate at (40,40) Offset

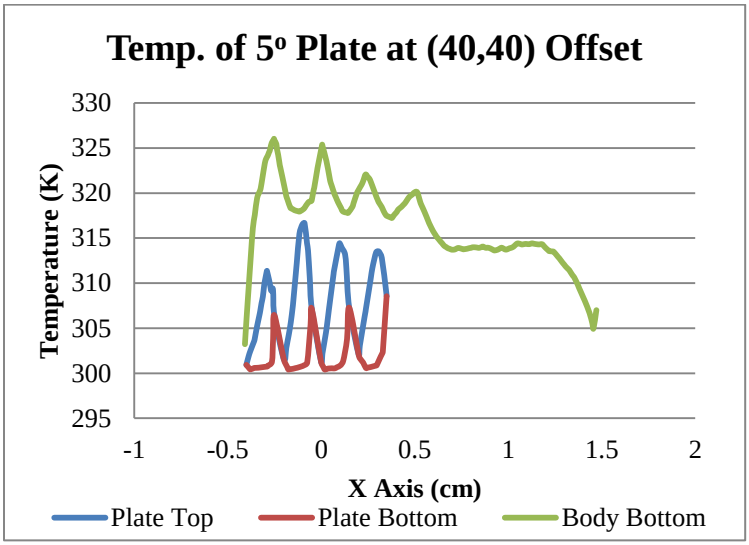

Figure 3.17 Temperature of 5° Plate at (40,40) Offset

The pressure distribution created on the underside of the craft in the Mach 2 case, with hanging plate angle of 5^o, peaks at 235 kPa. This compares to the 161 kPa generated by the conventional case. The hanging plate top surface has a maximum pressure of 165 kPa and an average pressure over all the plates of 126 kPa. The bottom surfaces of the hanging plates have a maximum pressure of 117 kPa, and a mean pressure of 103 kPa. Temperature distribution rises to a maximum of 326 K on the craft body and 316 K for the top and bottom surfaces of the hanging plates. The density fluctuations mimic the pressure plots in shape, but not in magnitude, highlighting regions of compression along the surfaces. The density at the craft bottom reaches 3.4 kgm^{-3} and maintains an average of 3.13 kgm^{-3}. The hanging plate's maximum density is 2.95 kgm^{-3} and the mean is 2.55 kgm^{-3} with fluctuations signaling shock-shock and shock-boundary layer interactions.

The preceding values are summarized in the following table for the Control Case and the Hanging Plate Case at a 40 cm height, 40 cm length offset from the X,Y axis of the model, and a 5^o shock angle.

Table 3.4 Control Case and Mach 2 Hanging Plate Case Values

	Value	Unit
Pressure, Mean, CC	161	kPA
Temperature, Mean, CC	315	K
Density, Mean, CC	2.81	$Kg\text{-}m^{-3}$
Pressure, Max, CC	170	kPA
Temperature, Max, CC	321	K
Density, Max, CC	2.98	$Kg\text{-}m^{-3}$
Pressure, Mean, HP, BB	175	kPA
Density, Mean, HP, BB	3.1	$Kg\text{-}m^{-3}$
Temperature, Mean, HP, BB	320	K
Pressure, Max, HP, BB	235	kPA
Density, Max, HP, BB	3.4	$Kg\text{-}m^{-3}$
Temperature, Max, HP, BB	326	K

Pressure, Mean, HP, PT	126	kPA
Density, Mean, HP, PT	2.55	$Kg\text{-}m^{-3}$
Temperature, Mean, HP, PT	308	K
Pressure, Max, HP, PT	165	kPA
Density, Max, HP, PT	2.98	$Kg\text{-}m^{-3}$
Temperature, Max, HP, PT	316	K
Pressure, Mean, HP, PB	104	kPA
Density, Mean, HP, PB	2.42	$Kg\text{-}m^{-3}$
Temperature, Mean, HP, PB	304	K
Pressure, Max, HP, PB	118	kPA
Density, Max, HP, PB	2.54	$Kg\text{-}m^{-3}$
Temperature, Max, HP, PB	309	K
CC=Control Case HP=Hanging Plate Case BB=Bottom Body PT=Plate Top PB=Plate Bottom		

The test was also run for plate angles of 10^o, 15^o, 20^o. The tests are run at offsets from the x-axis measured at 42.5 cm, 40 cm, and 37.5 cm. Each case is run at a vertical offset from the y-axis from 40.0 cm, 35 cm, 30 cm, 25 cm, 20 cm, and 15 cm. Associated figures and tables can be found in Appendix A, while the analysis uses information from all trial runs.

The contour plot of the density for the case results being examined here allows for an examination of shock wave formation, shock-shock interaction, and shock boundary layer interaction by its manipulation along the wall surfaces. The contour plot in Figure (3.18) is from the 5^o case at a displacement of (40,40).

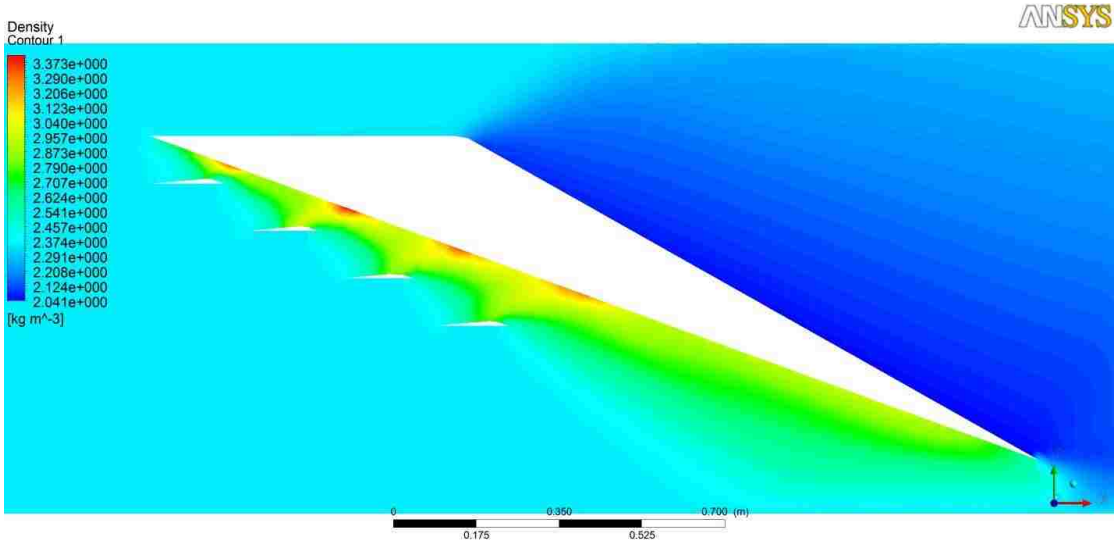

Figure 3.18 Density Contour Plot for 5° Hanging Plate at Mach 2

The density fluctuations along the bottom body of the main craft show where boundary layer-shockwave interaction occurs and temporarily compresses the flow, while regions around the hanging plates show the formation of shockwaves slightly downstream of the bow shock point which follows theory.

Results in pressure, temperature, and density plots for the Mach 3 case are for tier 5 at a neutral x-position relative to the bow of the main craft with hanging plate shock angles of 20^{o}, and figures are shown in Figures (3.19) to (3.21)

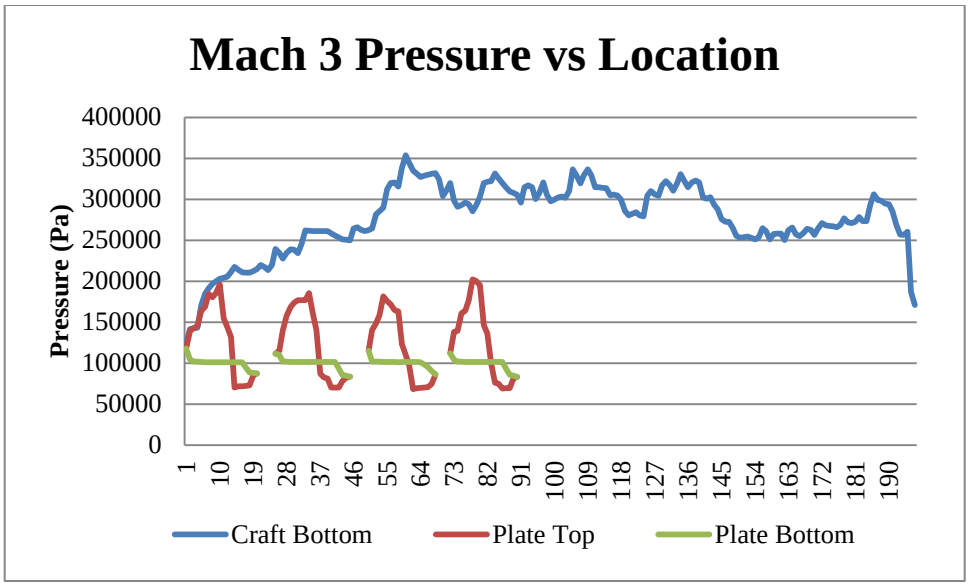

Figure 3.19 Mach 3 Pressure vs Location

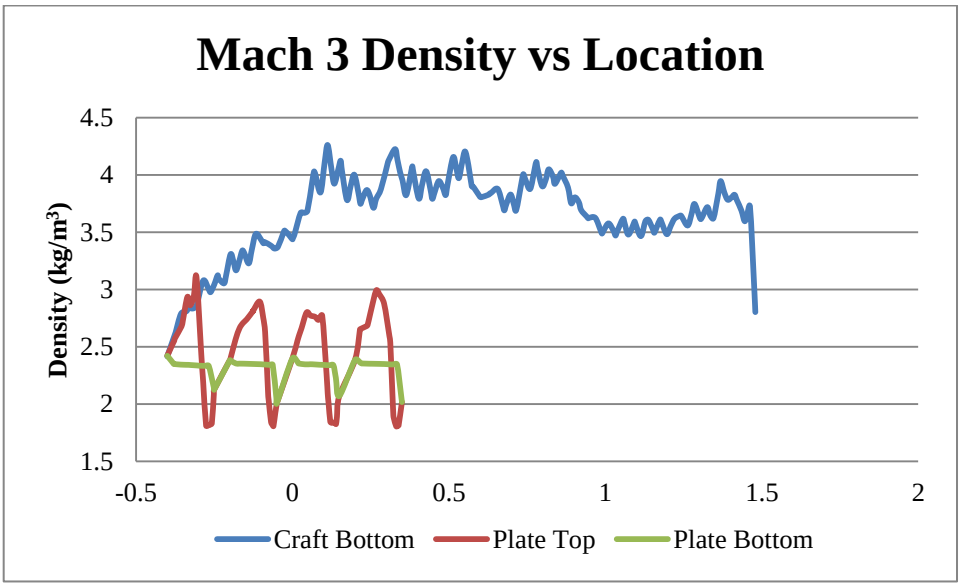

Figure 3.20 Mach 3 Density vs Location

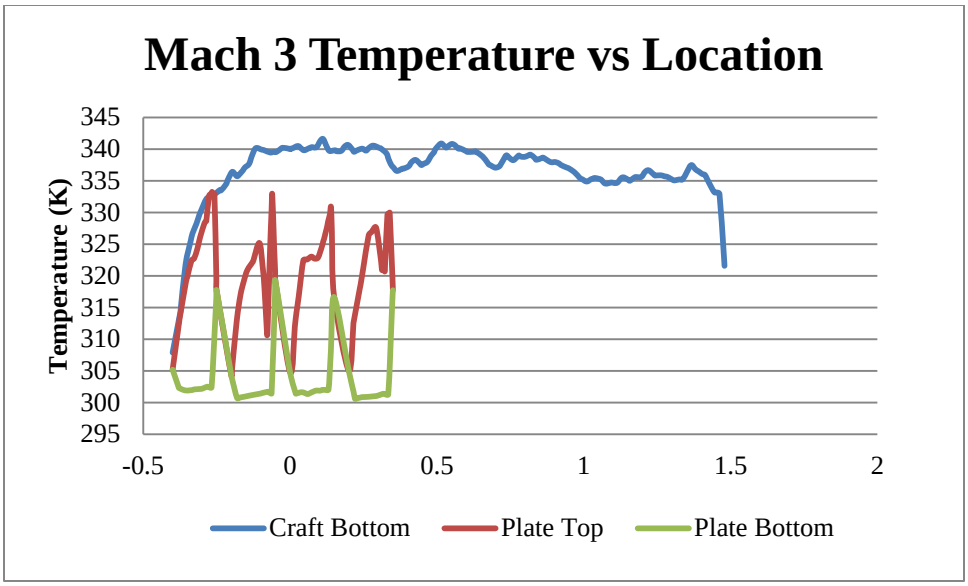

Figure 3.21 Mach 3 Temperature vs Location

The pressure distribution created on the underside of the craft during Mach 3 flow, with hanging plate angle of 20^{o}, peaks at 353 kPa. This compares to the 299 kPa generated by the conventional case. The hanging plate top surface has an average pressure of 124 kPa and an average pressure over the bottom of the plates of 99 kPa. Temperature distribution rises to a maximum of 341 K on the craft body and 336 K for the top and bottom surfaces of the hanging plates. The average temperature on the craft body is 321 K, and along the top and bottom of the plates, 321 K and 303 K, respectively. Areas of compression along the bottom surface of the craft are identified in the density plot. Points of compression along the bottom of the craft reach 4.3 kg/m^3, above an average density of 3.6 kg/m^3. The density increases compared to the freestream density along the top surface of the craft, until the flow turns around the corner and speeds up, decreasing the density. Along the plate tops the maximum density is 3.1 kg/m^3, and along the plate bottoms it is 2.4 kg/m^3. The density at the craft bottom reaches 3.4 kgm^{-3} and maintains an average of 3.13 kgm^{-3}.

Pressure, temperature, and density plots for the Mach 4 case are for tier 5 at a neutral x-position relative to the bow of the main craft with hanging plate shock angles of 20^{o}, and figures are shown in Figures (3.22) to (3.24)

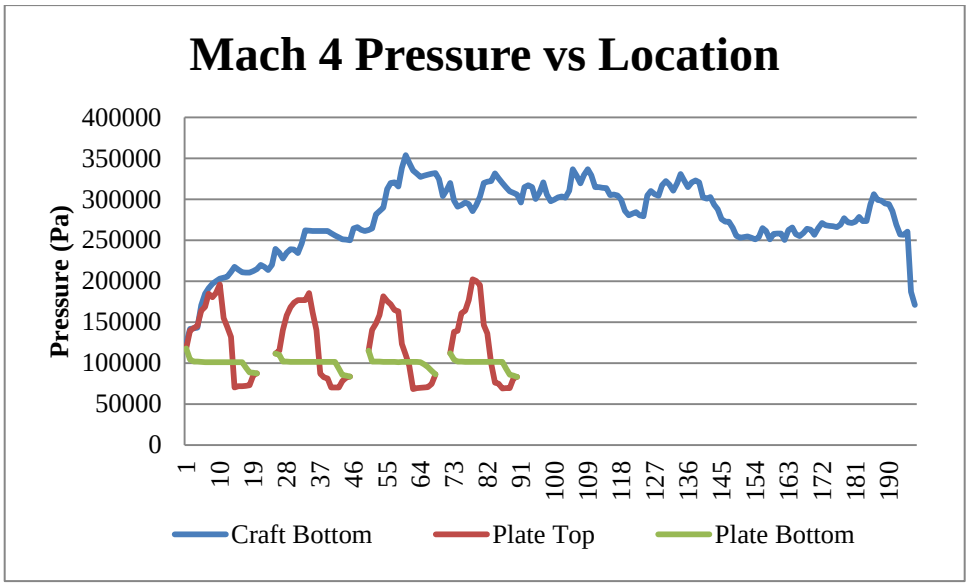

Figure 3.22 Mach 4 Pressure vs Location

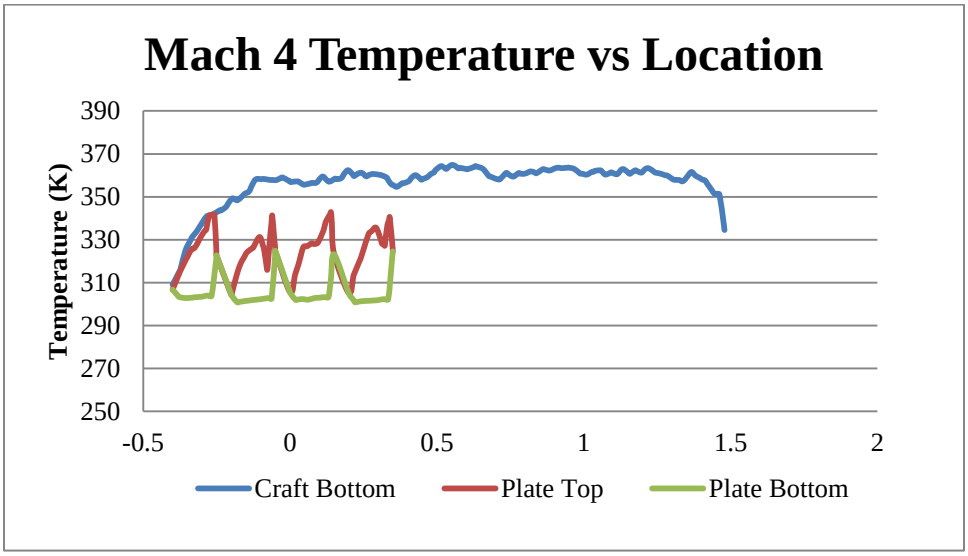

Figure 3.23 Mach 4 Temperature vs Location

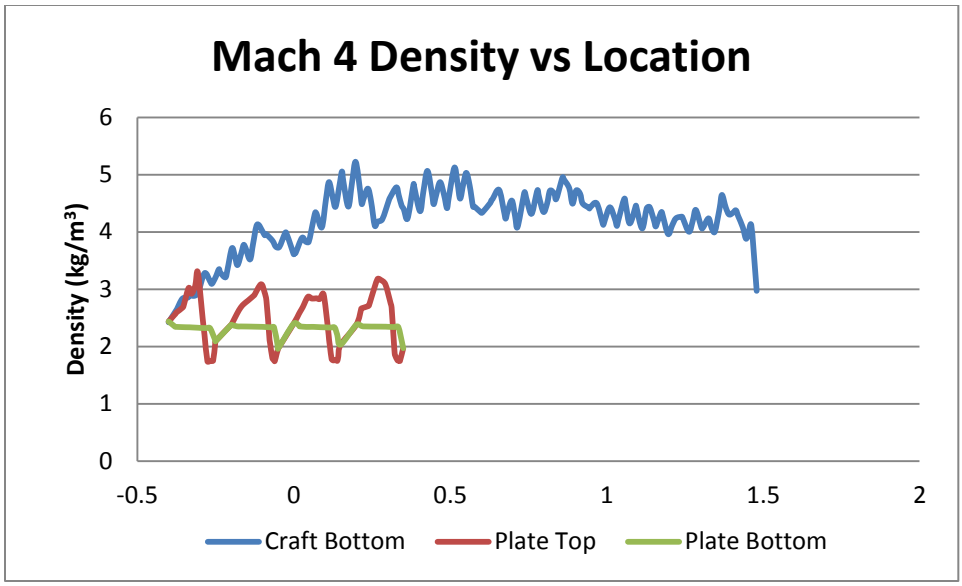

Figure 3.24 Mach 4 Density vs Location

The pressure distribution created on the underside of the craft during Mach 4 flow, with hanging plate angle of 20^{o}, peaks at 531 kPa. This compares to the 480 kPa generated by the conventional case. The hanging plate top surface has an average pressure of 133 kPa and an average pressure over the bottom of the plates of 99 kPa. Temperature distribution rises to a maximum of 364 K on the craft body and 342 K for the top and bottom surfaces of the hanging plates. The average temperature on the craft body is 356 K, and along the top and bottom of the plates, 326 K and 305 K, respectively. Areas of compression along the bottom surface of the craft are identified in the density plot. Points of compression along the bottom of the craft reach 5.2 kg/m^3, above an average density of 4.2 kg/m^3. Along the plate tops the maximum density is 3.2 kg/m^3, and along the plate bottoms it is 2.4 kg/m^3. The complete results for all cases ran can be found in Appendix A and Appendix C.

CHAPTER 4 : FINDINGS AND DISCUSSION

In order to determine the viability of hanging plates under a lifting wing as a lift generation device, comparisons between the net pressure, temperature gradients, and density fluctuations must be examined for failure cases.

The comparison between the Mach 2 conventional case and the hanging plate case shows that using hanging plates to create shock wave interactions in the boundary layer and in the freestream can greatly increase the pressure acting on the bottom surface of the craft. However, it also shows an increase in pressure acting with a net downwards force acting on the hanging plates. To verify if the hanging plate formation is beneficial to the craft, the net forces acting on the surfaces must be examined.

For a conventional lifting wing design traveling at Mach 2, the plot of the pressure is easily translated into net force on the bottom surface of the craft. Assuming the craft fits under the same dimensions used in the model, the net force on the bottom surface of the craft would adhere to

$$F_{net} = A_w * P_{static} \tag{4.1}$$

F_{net} is the net force, A_w is the wetted surface area of the bottom surface of the craft, and P_{static} is the static pressure on the bottom surface. The net lifting force and drag force would be the sin and cosine of the deflection angle,

$$F_{lift} = |F_{net} * \cos(\theta_{deflection})| \tag{4.2}$$

$$F_{drag} = |F_{net} * \sin(\theta_{deflection})| \tag{4.3}$$

Using the mean pressure and wetted area of the bottom surface of the craft in equation (4.1), the mean net force is calculated along the bottom surface of the craft.

In the examination of heat transfer from a supersonic fluid, the top case from each of the previous simulations is used. These cases are displayed in Table (4.1)

Table 4.1 Top Locations with Plate Angle

Horizontal Displacement	Vertical Displacement	Plate Angle
40 cm	20 cm	10^o
40 cm	20 cm	15^o
40 cm	15 cm	20^o
42.5 cm	15 cm	20^o

The heat transfer coefficient for air at the varying supersonic speeds and temperatures needs to be approximated for the purpose of this simulation. For forced convection due to the velocity of the craft in the freestream, the convective heat transfer coefficient is assumed to be 250 W/m^2-C. This value is determined based on the average film temperature, the specific heat of air, assumed thermal conductivity, dynamic viscosity, plate dimensions, plate and ambient temperature, and flow velocity. The film temperature was determined as the average temperature along the wall of the craft and a sink condition imposed as the craft. The thermal conductivity, dynamic viscosity, and flow velocity are all The calculation is based on Nusselt number correlations. Due to limitations in the software, only convective heat transfer from the air is considered. In determining the potential heat flow into the craft, the equation to be used is

$$q = hAx(T_p - T_a)$$

(4.4)

the average heat transfer coefficient is h, the area of the craft is A, T_p is the plate temperature, and T_a is the temperature of the ambient air. The value h is defined by

$$h = Nu * k/L \tag{4.5}$$

where Nu is the Nusselt number, k is the conductivity of the fluid, and L is the length of the craft. The Nusselt number is determined by the Reynold's number, which varies based on the flow being laminar or turbulent. For the laminar flow regions, the Reynold's number is less than 500,000, while in turbulent regions it is greater than 500,000. These values are used to determine Nusselt number in the following equations – laminar then turbulent.

$$Nu = 0.664 * Re^{0.5} Pr^{0.33} \tag{4.6}$$

$$Nu = Pr^{0.33} * (0.037 * Re^{0.8} - 871) \tag{4.7}$$

The Reynold's number and the Prandtl number for the simulation are calculated using the following equations,

$$Re = fluid\ velocity * \frac{Length}{kinematic\ viscosity} \tag{4.8}$$

$$Pr = \frac{kinematic\ viscosity}{thermal\ diffusivity} \tag{4.9}$$

The film property is defined as the average of the working fluid and the wall temperatures. Using these equations and the values determined during the simulations, the approximate value for the convective heat transfer coefficient is used in equation (4.4) to give heating values for the material in the cases.

ANALYSIS OF DATA

The net force, lifting force, and drag force for the Mach 2 conventional lifting wing design is shown in Table (4.2).

Table 4.2 Force Data for Conventional Lifting Wing

Force	**Value (kN)**
Net Force	165
Lifting Force	155
Drag Force	56
Lift/Drag Ratio	2.75

The following graph shows the forces for a slice of the wing, including the net force generated by the pressure along the sample line, the lifting force, and the drag force. The lift/drag ratio is not displayed on the chart because the sample gives a constant Lift/Drag ratio of 2.75.

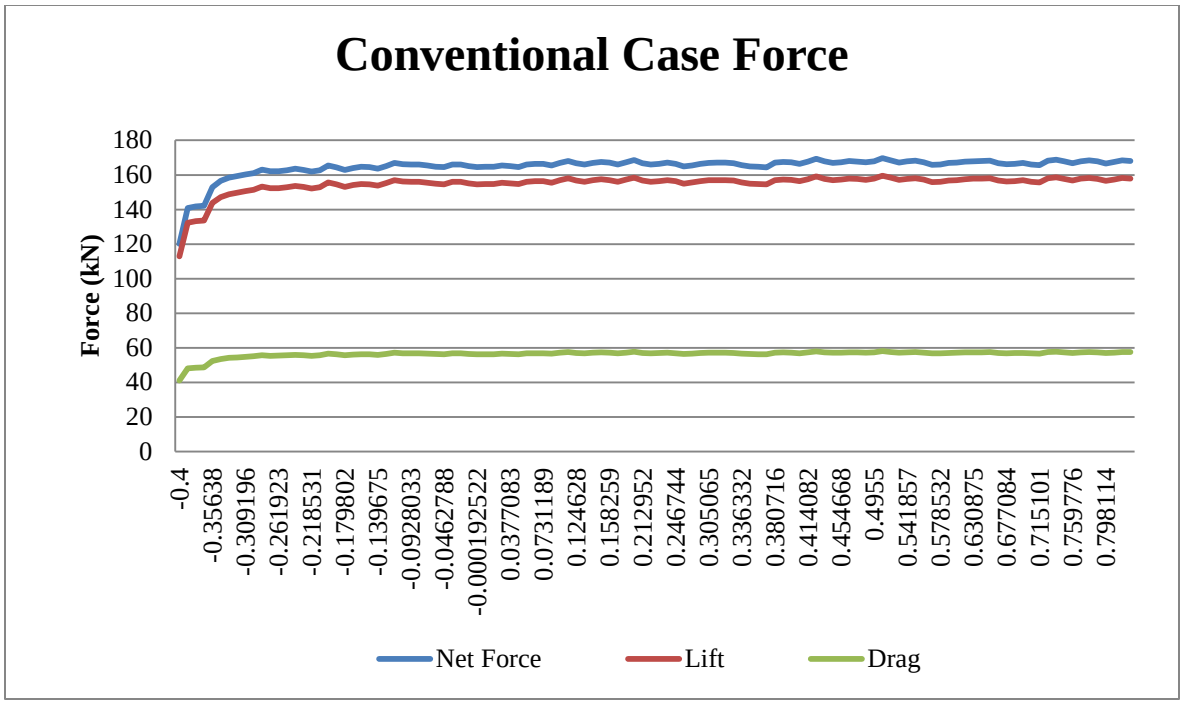

Figure 4.1 Conventional Case Force

From the previous plot, we see that the conventional lifting wing design can generate a consistent value – approximately its average – of 168 kN. For the hanging plate design, equation (4.1) is used again, except now it is used on three separate surfaces – the bottom surface of the main craft, the top surface of the hanging plate, and the bottom surface of the hanging plate. The total lifting force for the assembly is the lifting force on the plate top subtracted from the lifting force on the bottom surface of the main craft and the plate bottom. The total drag will be the drag generated from the craft bottom and the hanging plate. The ratio from these values gives the lift-to-drag ratio. For the 5^{o} case, the tables displaying the lift-to-drag ratio, the total lift, and the total drag are shown in Figures (4.2), (4.3) and (4.4), and are displayed next to the associated values for the control case.

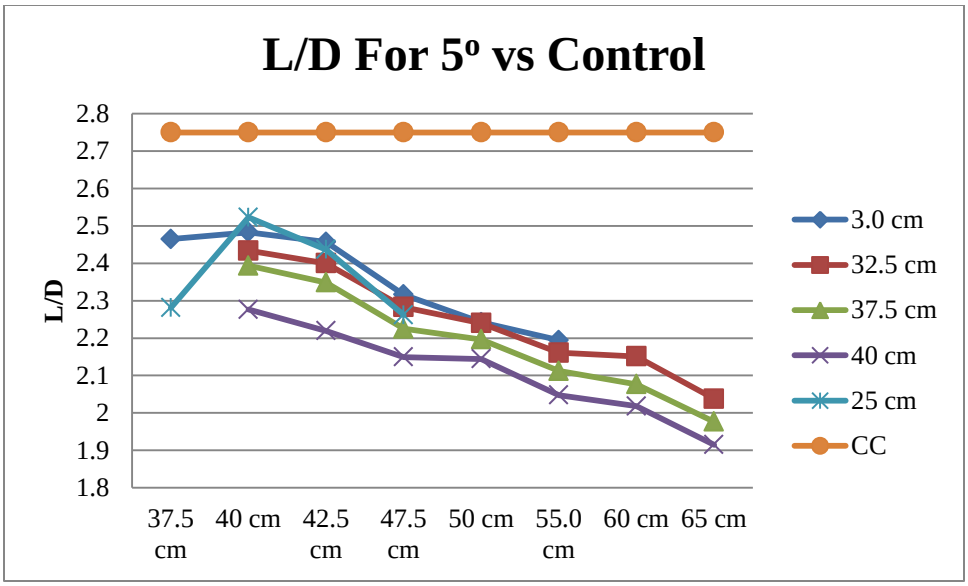

Figure 4.2 L/D For 5º vs Control

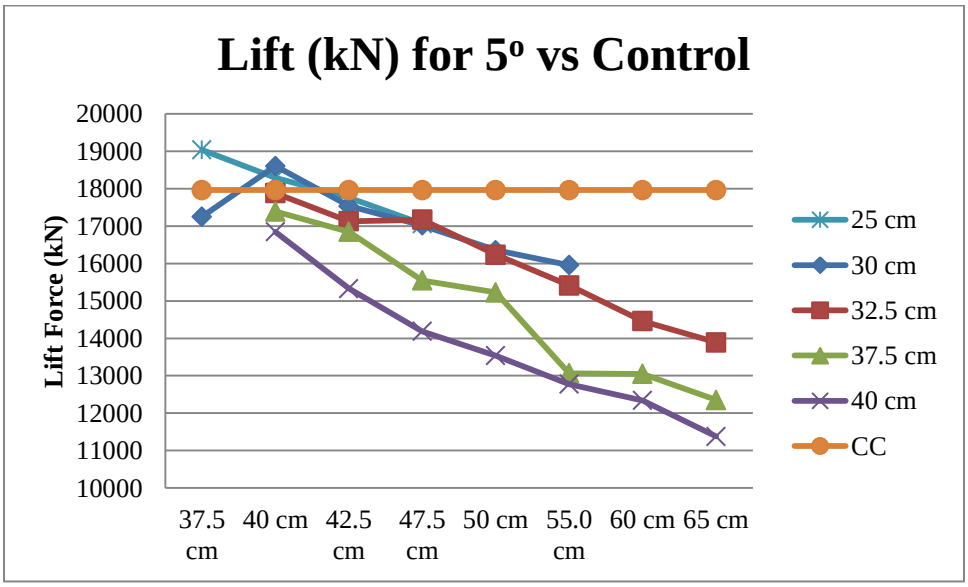

Figure 4.3 Lift (kN) for 5º vs Control

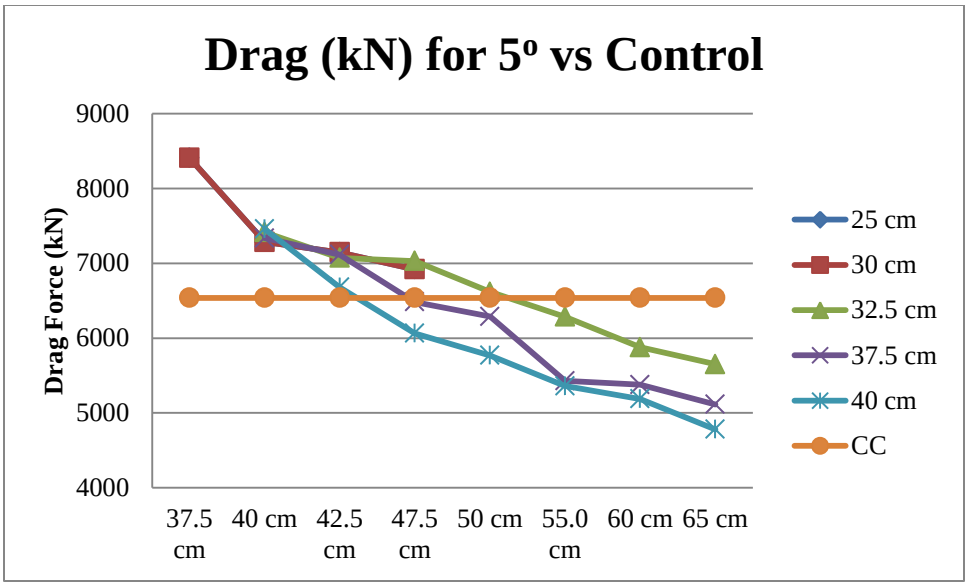

Figure 4.4 Drag (kN) for 5^{o} vs Control

The L/D solutions for the 5^{o} case does not reach the optimum value found from the control case simulation, however it does approach a workable value. From the Lift plot there are two potential arrangements which generate more total lift than the control case. These are the vertical offset cases of 25 cm and the 30 cm, but only for the horizontal locations of 37.5 cm and 40 cm. When examining the proportional difference between the lift and drag of the control case and the hanging plate case, we see the results shown in the Table (4.2)

Table 4.3 Horizonatal and Vertical Offset Peak Cases

Horizontal Offset	Vertical Offset	Ratio	Value
37.5	25	L/D	0.85
		Lift	1.10
		Drag	1.15
37.5	30	L/D	0.89
		Lift	0.96
		Drag	1.08
40	25	L/D	0.92
		Lift	1.02
		Drag	1.15

40	30	L/D	0.90
		Lift	1.04
		Drag	1.15

From Table (4.2) we see that despite having similar lift-to-drag ratios, the total lift generated by the hanging plates in this simulation does not generate substantial lift to be a viable candidate, and generates too much drag relative to the control case. The 25 cm vertical offset case at 37.5 cm only generates 10% more lift at the expense of 15% more drag while the same vertical offset at a 40 cm displacement manages only a 2% increase lift to a 15% increase in drag. The other two cases generate worse results.

The next hanging plate case is for a ramp angle of 10^{o}. The notable force values are taken from the simulations measured at a range of horizontal displacements from 37.5 cm to 45 cm, and vertical displacements from 25 cm to 40 cm. The plots for the 10^{o} hanging plate case are shown below.

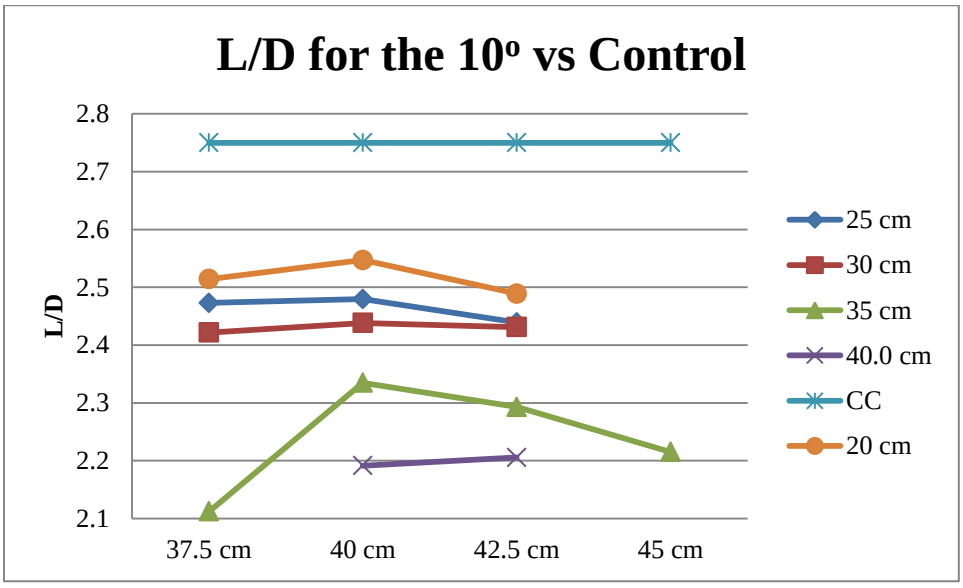

Figure 4.5 L/D for 10^{o} vs Control

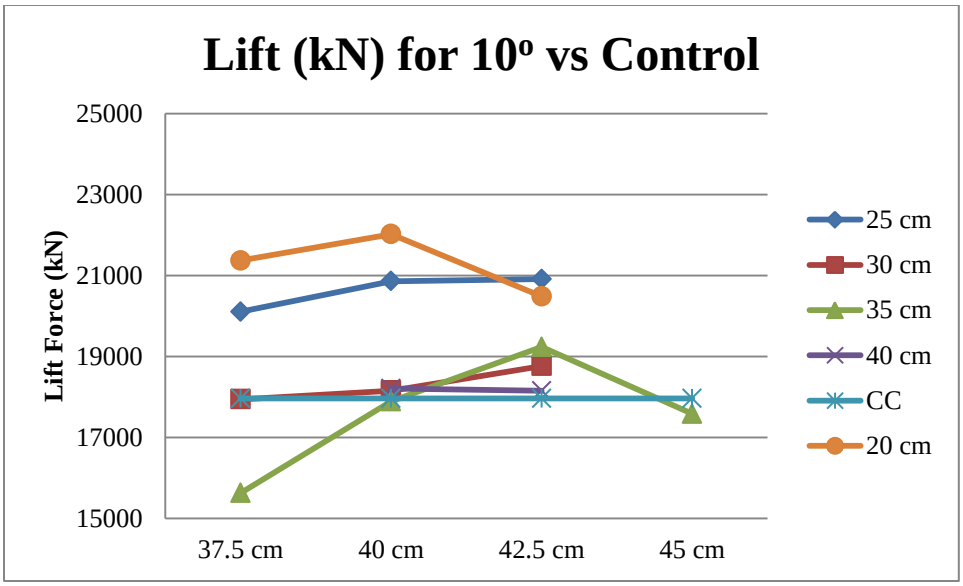

Figure 4.6 Lift (kN) for 10^{o} vs Control

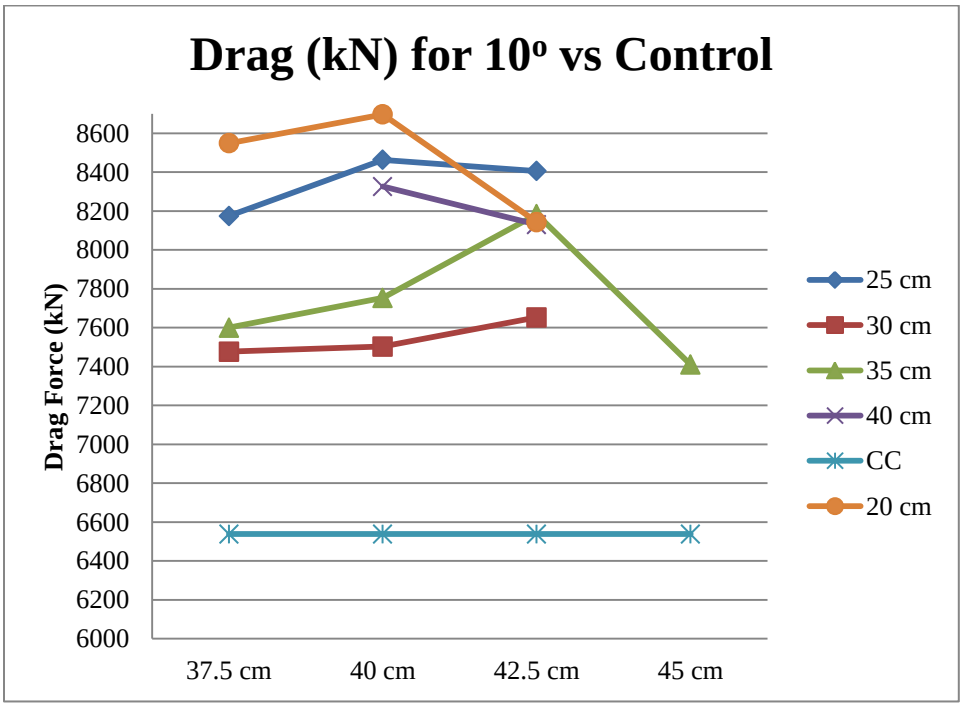

Figure 4.7 Drag (kN) for 10^{o} vs Control

The 10^{o} case has multiple points of interest when examining the lift. However, the lift-to-drag ratio and the drag force for the craft are still detrimental factors. Closer examination

of these points is found from the ratio of the usable points to the control case, shown in Table (4.3)

Table 4.4 Ratio for 10^o Hanging Plate Cases Compared to Control Case

	L/D Ratio			
Tier	X Location	37.5 cm	40 cm	42.5 cm
Y Location				
20 cm		0.914182	0.926182	0.905091
25 cm		0.899276	0.901644	0.886905
30 cm		0.880604	0.886648	0.884077
35 cm		0.768162	0.849071	0.833867
40.0 cm		0	0.796931	0.802001
CC		1	1	1
	Lift Ratio			
20 cm		1.189647	1.225772	1.140384
25 cm		1.119046	1.161227	1.164024
30 cm		0.998864	1.010724	1.044619
35 cm		0.869805	0.995896	1.070701
40 cm		0	1.013495	1.010546
CC		1	1	1
	Drag Ratio			
20 cm		1.307586	1.330223	1.245488
25 cm		1.25035	1.294514	1.285754
30 cm		1.143594	1.147536	1.17045
35 cm		1.162499	1.185798	1.251728
40 cm		0	1.273455	1.243506
CC		1	1	1

From the above table, the ideal locations for the 10^o hanging plate case are at a vertical displacement of 20 cm and a horizontal displacement of 40 cm. While the drag shows an

increase of 33% from the control case drag, the lift-to-drag ratio is within 8% of the control case and there is a 22.5% increase in total lift for the craft.

The next case to be examined is the 15^{o} hanging plates. From the previous evaluations of the 5^{o} case and the 10^{o} case, the points of interest can be narrowed down to the vertical displacements below 30 cm, and the horizontal displacements of 37.5 cm, 40 cm, 42.5 cm. Under this assumption the plots for the next case are shown in Figure (4.8) through (4.10) in comparison to the control case.

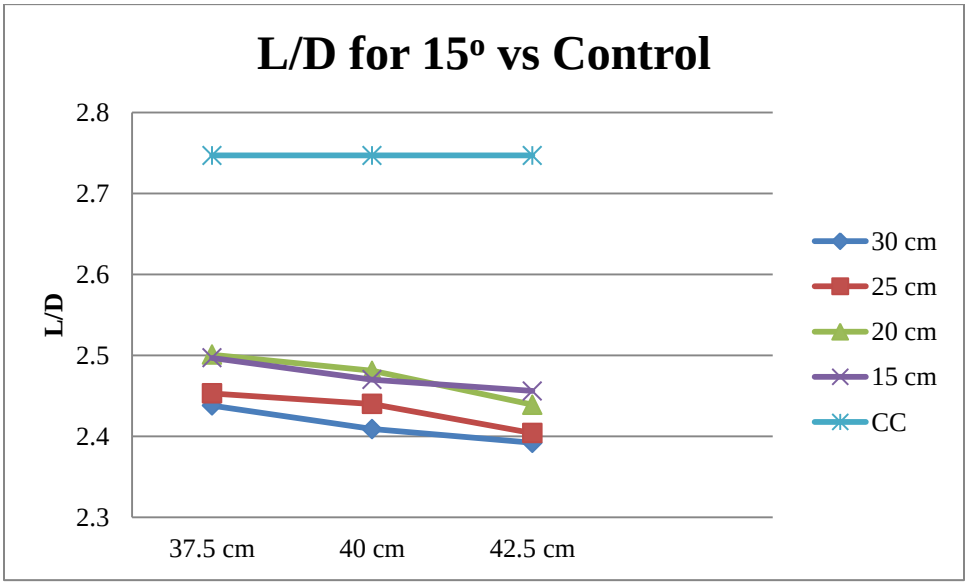

Figure 4.8 L/D for 15^{o} vs Control

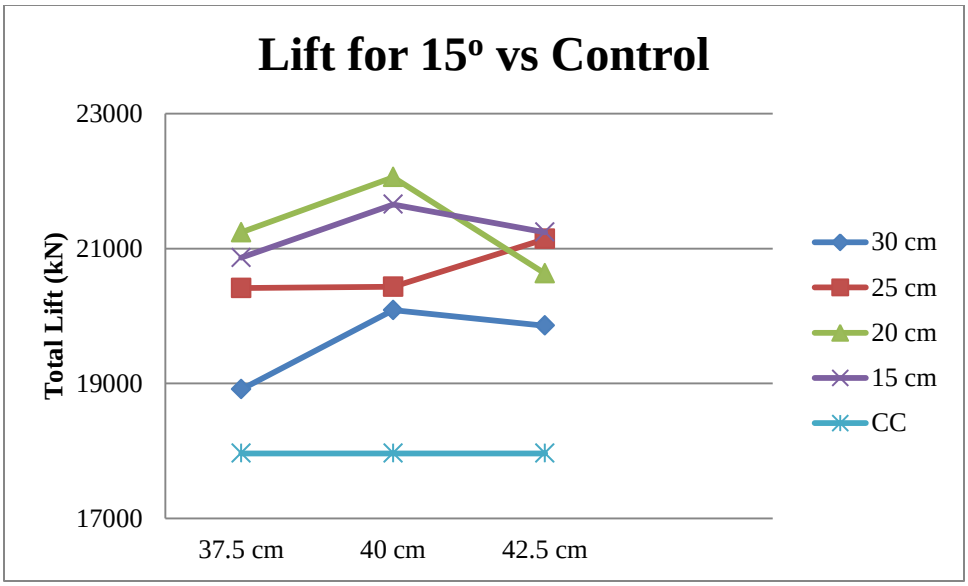

Figure 4.9 Lift For 15º vs Control

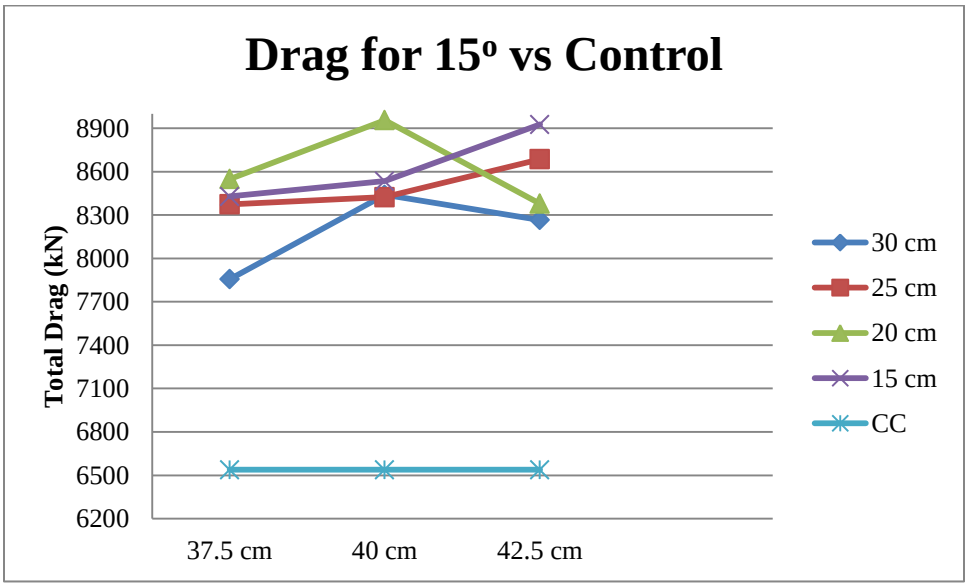

Figure 4.10 Drag for 15º vs Control

In order to verify trends for accuracy, a fourth level was placed on this simulation to check a decreasing overall value when the vertical displacement moved below 20 cm. The 15 cm case shows a drop in lift-to-drag ratio, total lift, and total drag. The ideal location for the

hanging plate continues its trend of being at the 40 cm horizontal displacement, which is in line with the nose of the craft, and as shown in Table (4.4), it also generates a higher percentage increase for total lift from the control case.

Table 4.5 Ratio for 15^{o} Hanging Plate Cases Compared to Control Case

	L/D Average			
Y Location	X Location	37.5 cm	40.0 cm	42.5 cm
30 cm		0.887514	0.876957	0.870768
25 cm		0.892974	0.888242	0.875137
20 cm		0.910448	0.903167	0.887878
15 cm		0.908992	0.899163	0.894066
CC		1	1	1
	Total Lift			
30 cm		1.052714	1.118063	1.105316
25 cm		1.136376	1.137434	1.1769
20 cm		1.182243	1.227888	1.1484
15 cm		1.161481	1.205344	1.182355
CC		1	1	1
	Total Drag			
30 cm		1.201744	1.290915	1.264301
25 cm		1.28082	1.288467	1.328694
20 cm		1.307586	1.369991	1.281585
15 cm		1.289232	1.305445	1.365402
CC		1	1	1

As the table shows, there is an increase of 20.5% for the 15 cm location, while the 20 cm displacement has an increase of 22.7% greater lift than the control case, while still being within 10% of the control lift-to-drag ratio. Another notable point to consider is the 37.5 cm displacement for the 20 cm hanging plate case. For the current simulation, the displacement has been within approximately 10% of the control lift-to-drag ratio, generated

18.2% more lift while only generating 30.7% less drag. In order to generate more lift, the final case of the 20^{o} hanging plate will be examined next. Throughout the simulations, it must be noted that the ideal case will be a combination of beneficial lift and drag ratios when compared to the control case. The plots for the 20^{o} simulation are shown in Figure (4.11) through (4.13)

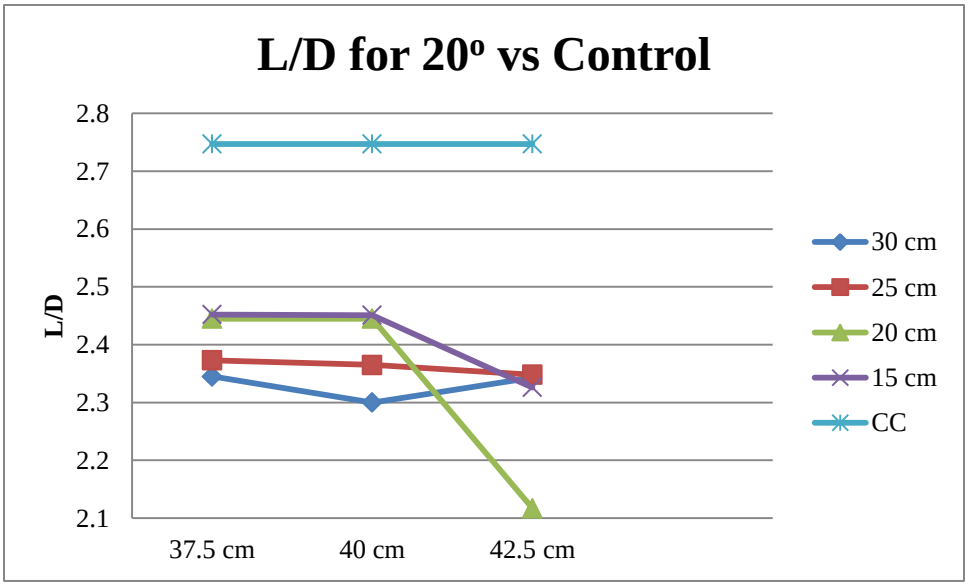

Figure 4.11 L/D for 20^{o} vs Control

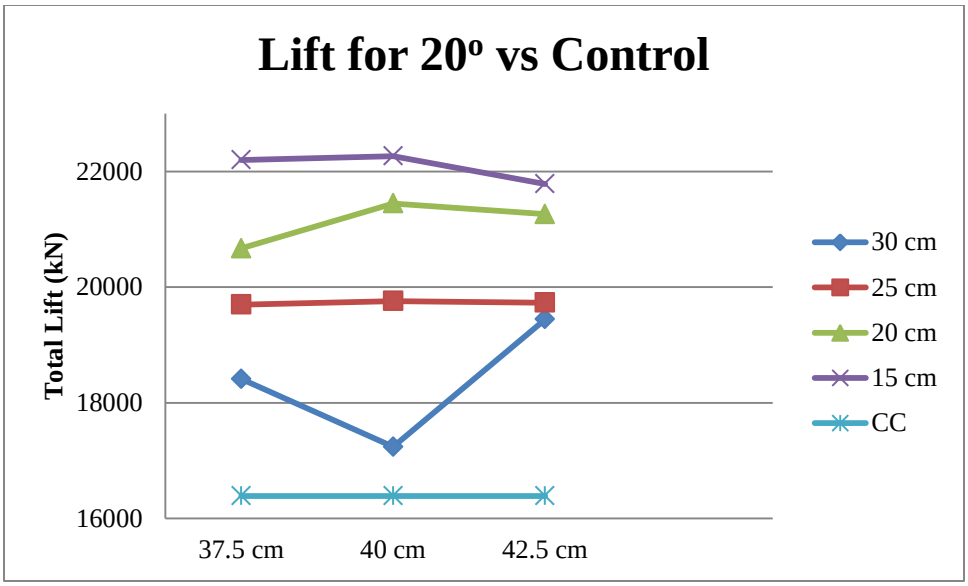

Figure 4.12 Lift for 20^{o} vs Control

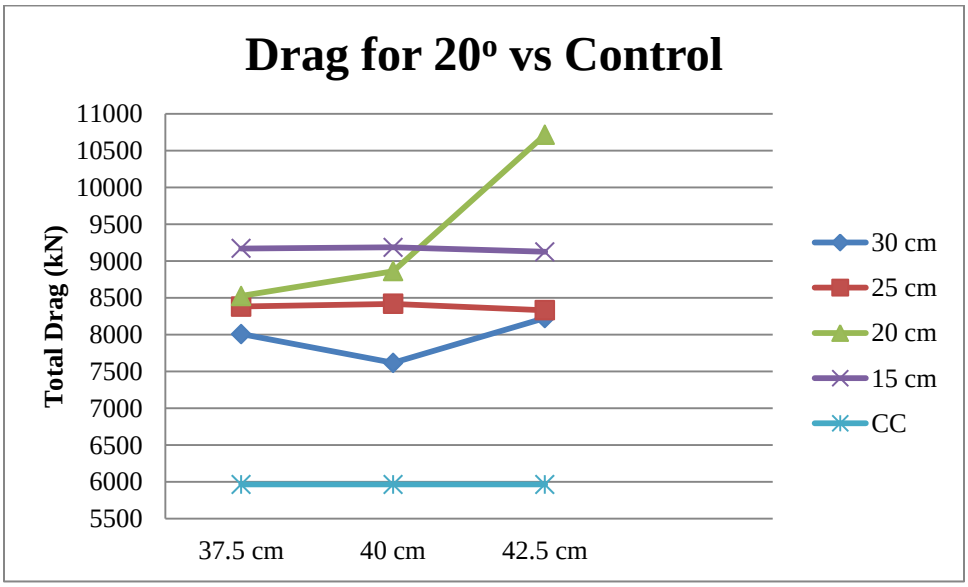

Figure 4.13 Drag for 20^{o} vs Control

Unlike during previous simulations, the shockwave created by the 20^{o} hanging plate is strong enough to still have a greater lift generation than its counterparts. Table (4.5) summarizes the ratios for the arrangements examined in the 20^{o} case.

Table 4.6 Ratio for 20° Hanging Plate Cases Compared to Control Case

	L/D Average			
Y Location				
30 cm		0.853659	0.837277	0.85293
25 cm		0.863851	0.860939	0.854751
20 cm		0.890062	0.890062	0.770659
15 cm		0.89261	0.892246	0.846742
CC		1	1	1
	Total Lift			
30 cm		1.123444	1.051867	1.186417
25 cm		1.202038	1.20576	1.204113
20 cm		1.26135	1.308701	1.297474
15 cm		1.354589	1.358677	1.329326
CC		1	1	1
	Total Drag			
30 cm		1.342891	1.276995	1.379108
25 cm		1.405433	1.411636	1.397217
20 cm		1.42941	1.485915	1.796781
15 cm		1.537726	1.540241	1.530013
CC		1	1	1

The 15 cm location is able to generate 30% more lift than the conventional craft, a decrease in 11% to the lift-to-drag ratio, and a increase of 54% in drag. The previous calculations were done over a distance based on the area of effect from the shock-shock interactions along the bottom surface of the craft. When comparing the four plates and their effect over the entire length of the craft (including areas which are not directly affected by the plates), the inclusion of shockwave interactions increase the total lift by 12%. The plates only affect 40% of the craft bottom, instead of a continual chain of lifting devices. The data points used are sampled from a midline along both the main craft and the hanging plates so

as to negate end effects, and only take into account drag generated as a component of the net pressure along the body. As seen, one configuration of plates can generate above 1/3 more lift than the conventional craft alone. The next effect of shockwave interaction is Heat Transfer from the working fluid to the craft.

The Mach 3 and Mach 4 trials were performed at tier 5 (a 15 cm offset from the X-axis) and at tier 6 (a 10 cm offset from the X-axis), horizontal displacement of 25 cm forward from the bow of the main craft, even with the bow of the main craft, and 25 cm aft from the bow of the main craft. The control case for the Mach 3 trials is shown in Figure (4.14),

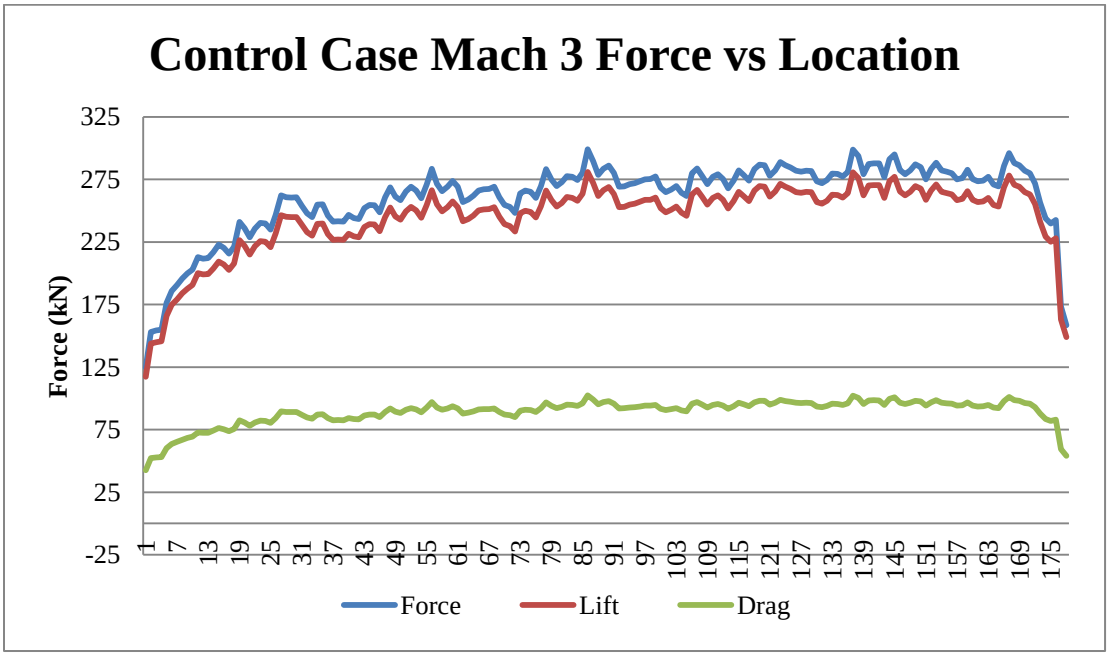

Figure 4.14 Control Case Mach 3 Force vs Location

For the Mach 3 control case, the craft generates an average force of 260 kN, an average lift of 243 kN, and an average drag of 89 kN. Over the span of the craft bottom, the

conventional case generates 35288 kN of lift and 12843 kN of drag. The Lift-Drag ratio is constant at 2.75. The Mach 4 case is shown in Figure (4.15)

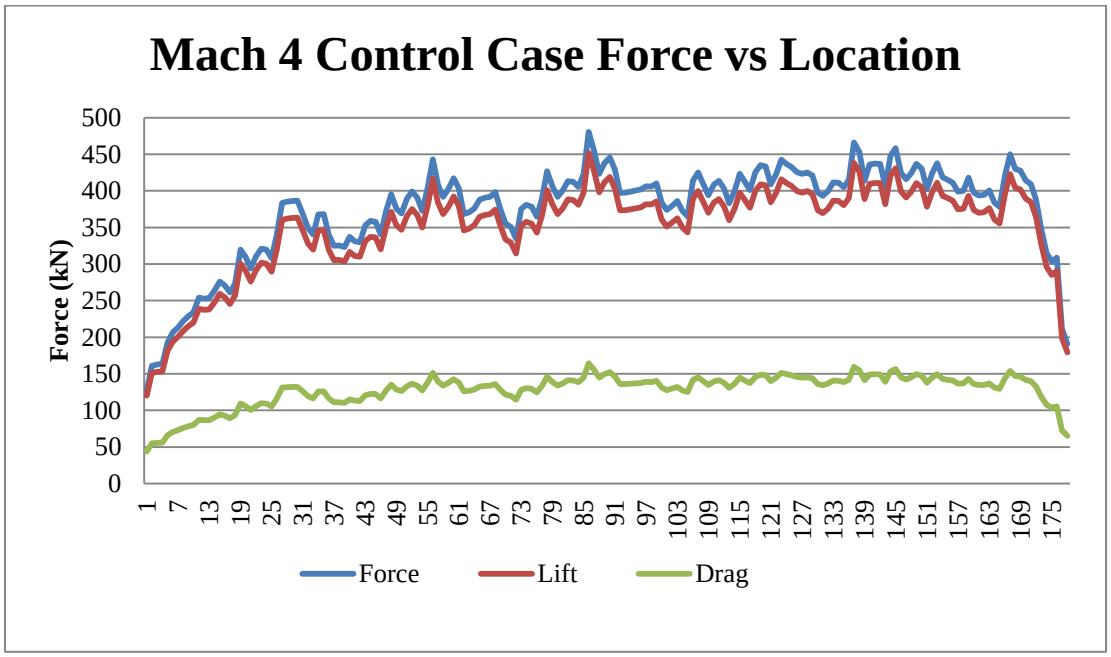

Figure 4.15 Mach 4 Control Case Force vs Location

For the Mach 4 control case, the craft generates an average force of 370 kN, an average lift of 348 kN, and an average drag of 126 kN. Over the span of the craft bottom, the conventional case generates 50514 kN of lift and 18385 kN of drag. The Lift-Drag ratio is constant at 2.75. The Control Cases are similar in trend while variable in magnitude. The notable values are displayed in Table (4.6)

Table 4.7 Control Case Notable Variables

	Total Lift	Total Drag	Average Force	Average Lift	Average Drag
Mach 2	26944	9806	164.81	154.87	56.37
Mach 3	35288	12843	259	243	86
Mach 4	50515	18385	371	348	127

From Mach 2 to Mach 3, the conventional lifting wing craft increases in total lift and total drag by 30%, and increases in average force over the span of the craft by 57%. The craft increases in total lift and total drag, between the Mach 3 and Mach 4 cases, by 43%, and average force over the span of the craft by 43%. The Mach 3 Hanging Plate Lift-Drag ratio, Lift and Drag plots are shown in Figures (4.16) through (4.18)

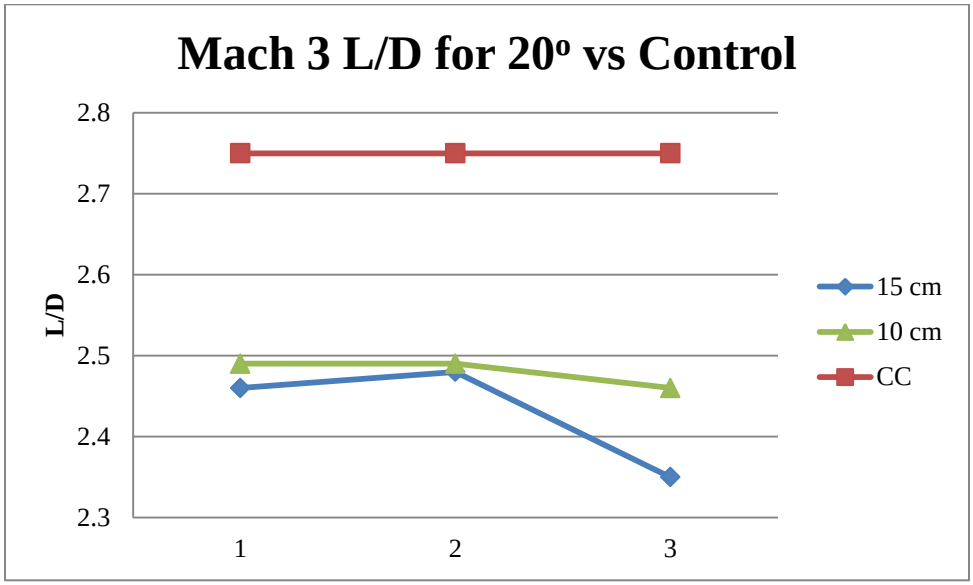

Figure 4.16 Mach 3 L/D for 20^{o} vs Control

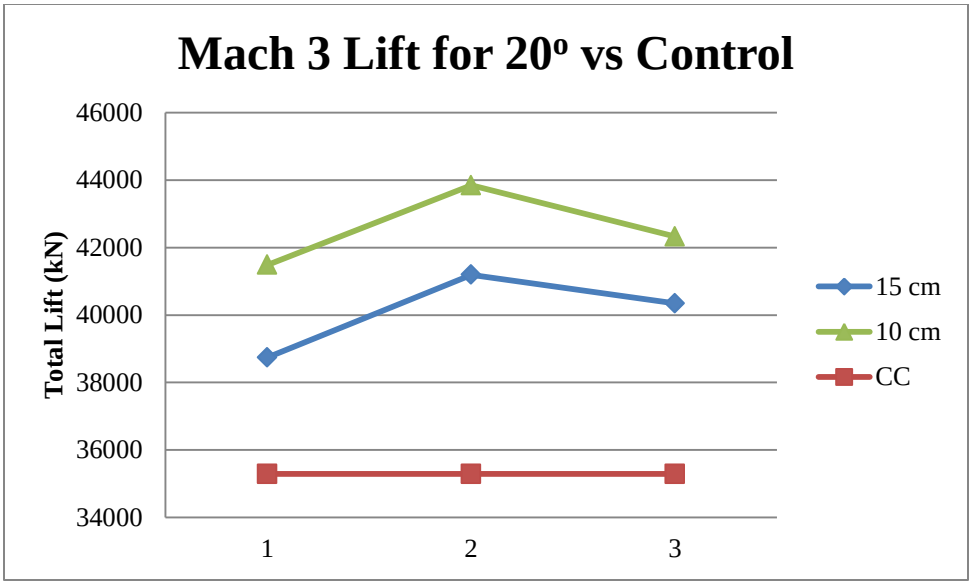

Figure 4.17 Mach 3 Lift for 20^{o} vs Control

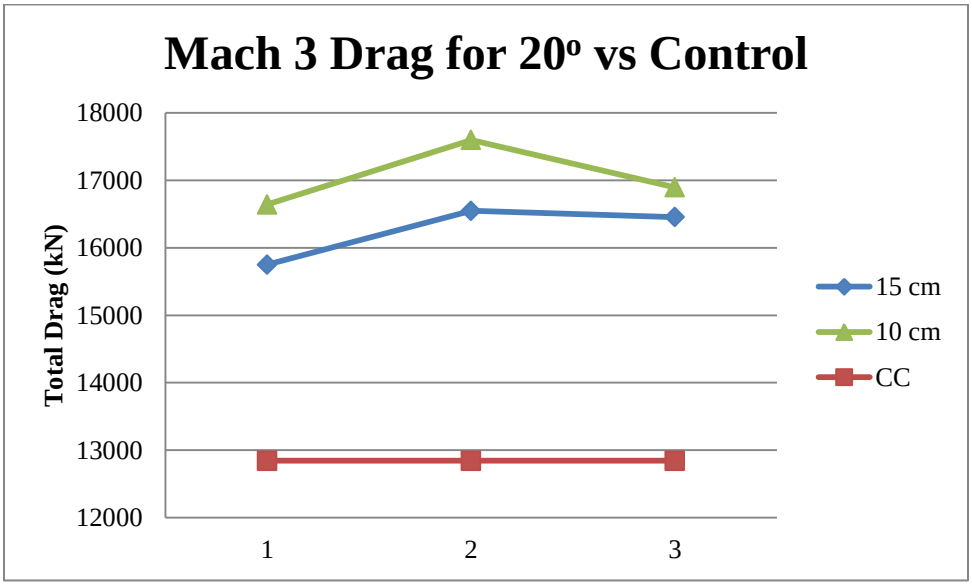

Figure 4.18 Mach 3 Drag for 20^{o} vs Control

Upon visual inspection, among the Mach 3 Hanging Plate cases, the optimum location for the hanging plates was found at the neutral location (0.0 cm offset from main craft), at a

vertical offset of 15 cm from the X-axis. The comparisons between the hanging plate case and control case are shown in Table (4.7)

Table 4.8 Mach 3 Hanging Plate Values vs Control

L/D Average				
Y Location	X Location	37.5 cm	40 cm	42.5 cm
15 cm		0.894545	0.901818	0.854545
10 cm		0.905455	0.905455	0.894545
CC		1	1	1
Total Lift				
15 cm		1.097824	1.167366	1.143278
10 cm		1.175669	1.242575	1.199558
CC		1	1	1
Total Drag				
15 cm		1.226505	1.288406	1.281243
10 cm		1.295959	1.370318	1.31558
CC		1	1	1

The hanging plate case at the neutral location at a 10 cm offset from the X-axis shows a decreased Lift-Drag ratio of 9.5%, an increase in lift of 24.3%, and an increase in drag of 37%. Moving the tier to a 5 cm offset from the x-axis decreases the lift, drag, and Lift-Drag ratio. The Mach 4 hanging plate case force plots are shown in Figures (4.19) through (4.21),

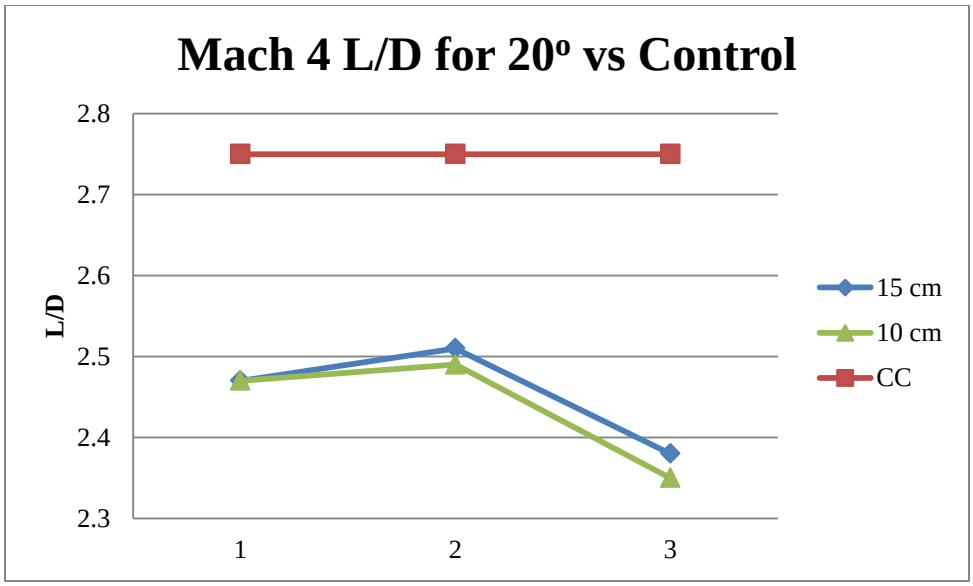

Figure 4.19 Mach 4 L/D for 20^{o} vs Control

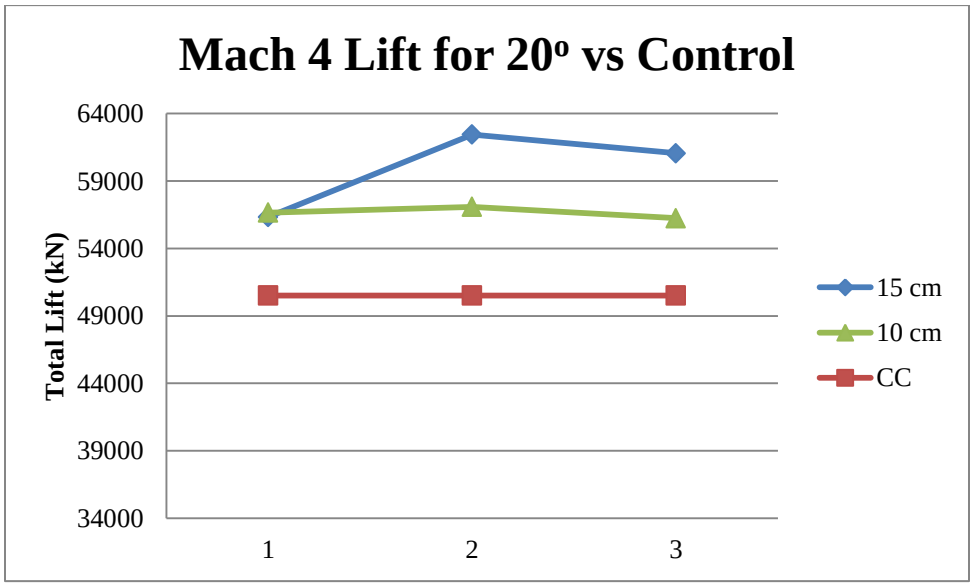

Figure 4.20 Mach 4 Lift for 20^{o} vs Control

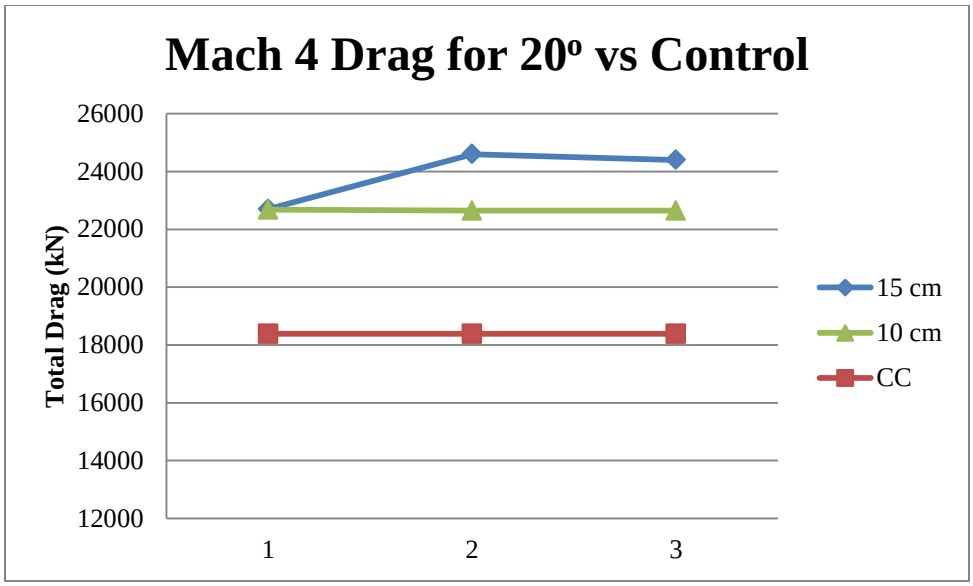

Figure 4.21 Mach 4 Drag for 20^{o} vs Control

From Figure (4.19) through (4.21), tier 5 in the neutral position is the optimal position for the hanging plates in Mach 4 flow. The Lift-Drag ratio for the conventional case is higher than the hanging plate cases by approximately 10%, however the 15 cm line in Figure (4.20) shows an increase in lift of almost 24%. The 10 cm case shows an increase in lift as well, however it only generates 13% more lift, and 23% more drag. The ratios relating the Lift-Drag ratio, the lift, and the drag of the hanging plate case to the conventional case are shown in Table (4.9).

Table 4.9 Mach 4 Hanging Plate cases vs Control

L/D Average				
Y Location	X Location	37.5 cm	40 cm	42.5 cm
15 cm		0.898182	0.912727	0.865455
10 cm		0.898182	0.905455	0.854545
CC		1	1	1
Total Lift				
15 cm		1.115213	1.236068	1.208611
10 cm		1.121508	1.130001	1.113352

CC		1	1	1
Total Drag				
15 cm		1.234581	1.337866	1.326934
10 cm		1.233493	1.231752	1.231644
CC		1	1	1

The heat transfer from the air moving past the craft in both conventional form and in the four most optimal cases for hanging plate configuration at Mach 2 is shown in Figure (4.22).

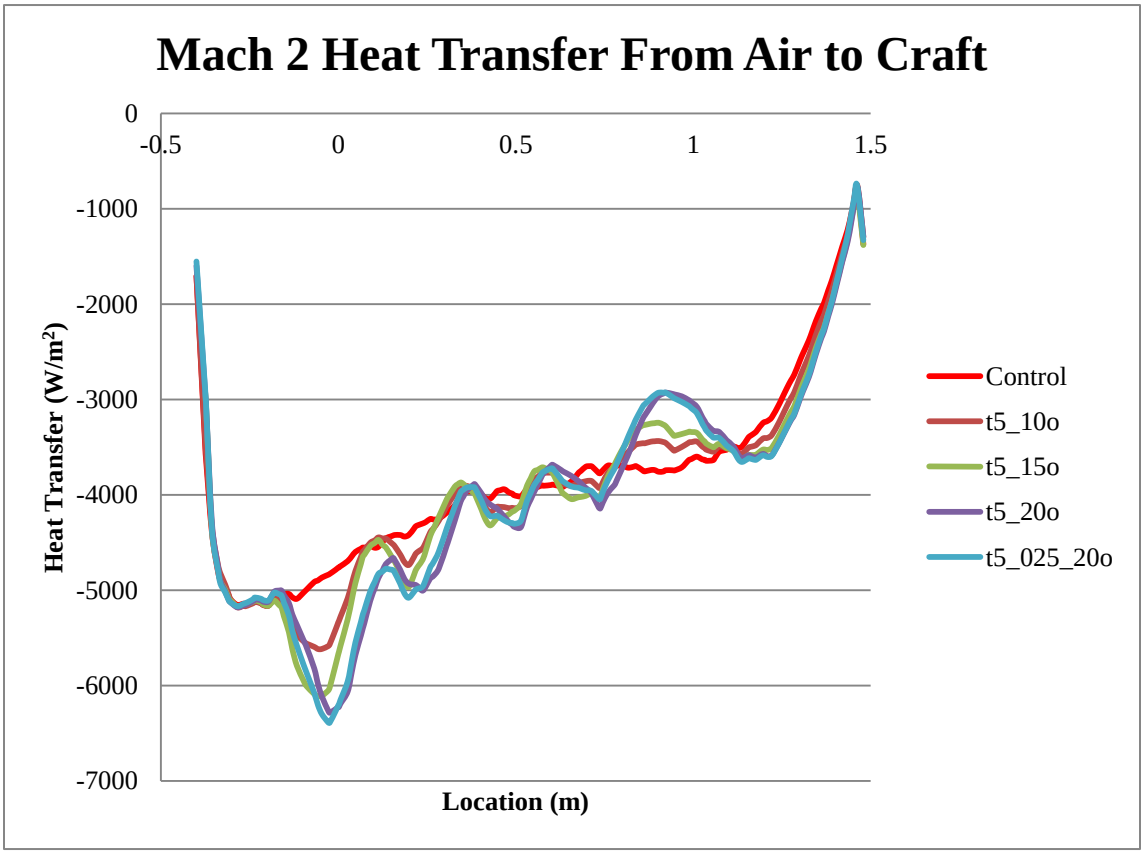

Figure 4.22 Mach 2 Heat Transfer from Air to Craft

The heat transfer into the main body during the control simulation achieves steady state 0.1 m after the bow shock. The control system passes approximately 5100 W/m^2 of energy

into the craft at any point along the surface, whereas the intersecting shockwave charts transfer almost 6400 W/m^2 at their peak points. Taking into account the continual disruption of the thermal boundary layer, where real world effects are considered (generally not considered by the program), the turbulent boundary layer along the craft bottom will tend towards a higher heat transfer rate. This would necessitate a craft with capable heat sinks in order to disperse heat, however the increase flow of thermal energy onto the outside plate could also be tapped as an energy source. For the shockwave interaction cases, the potential heat transfer to the plates is shown in Figures (4.23) and (4.24).

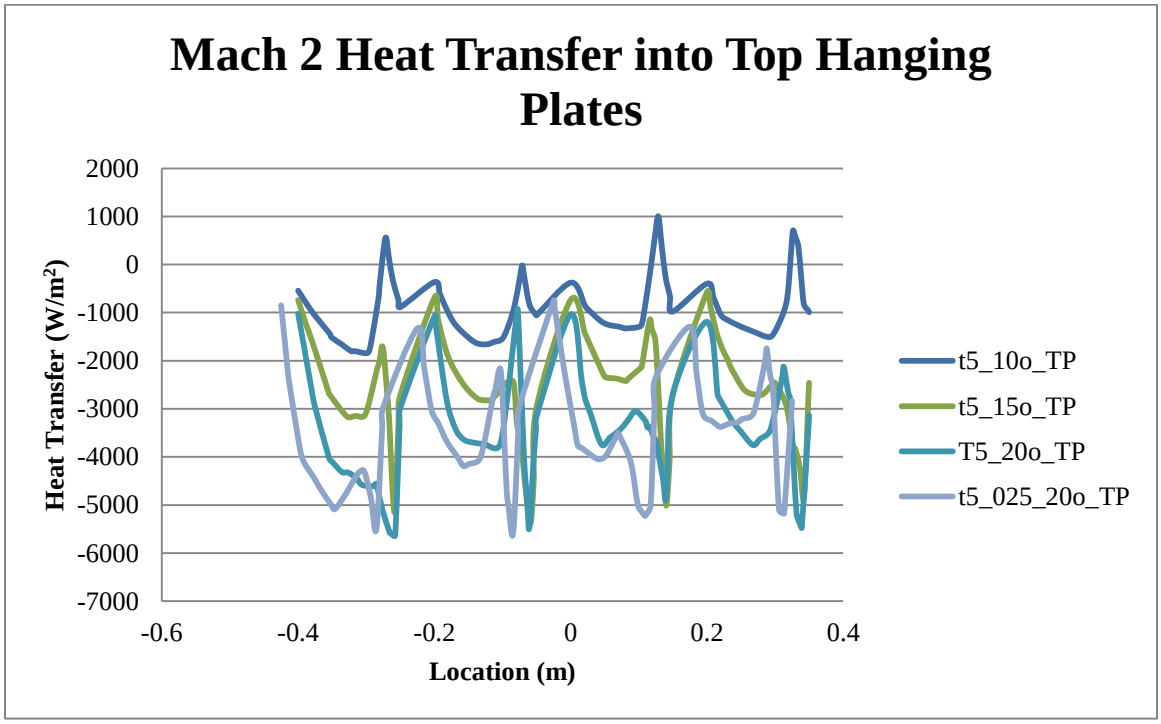

Figure 4.23 Mach 2 Heat Transfer into Top Hanging Plates

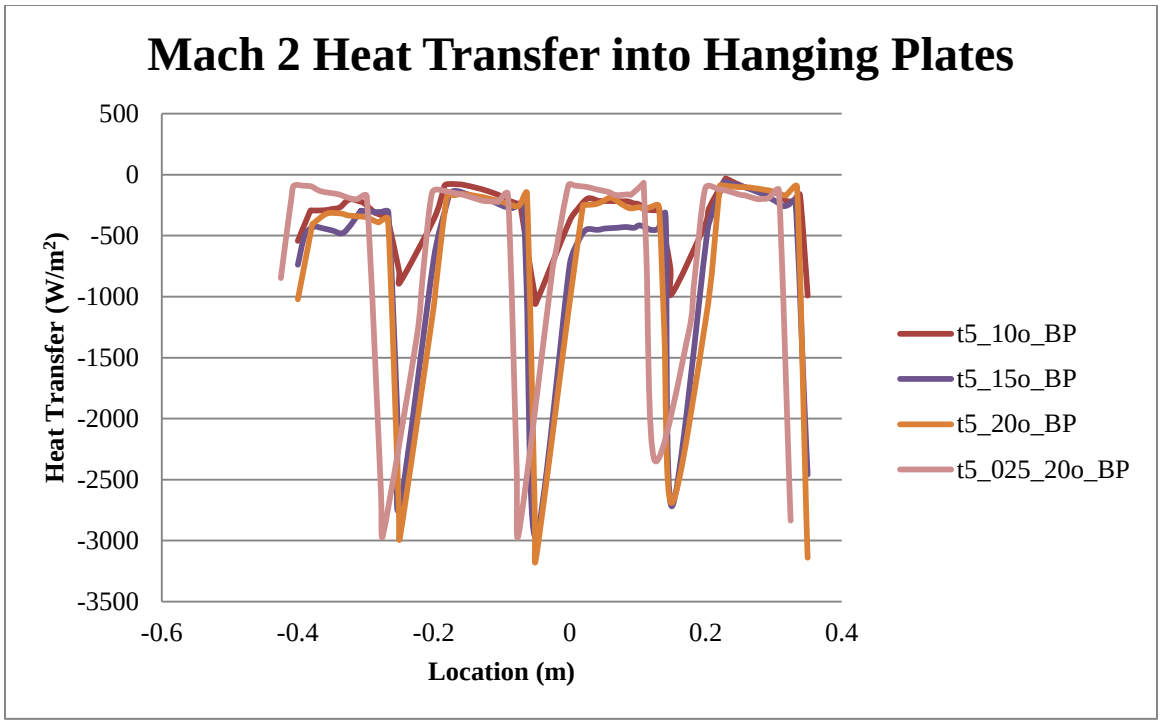

Figure 4.24 Mach 2 Heat Transfer into Hanging Plates

Similar to the heat transfer plots for the primary craft body, the hanging plates can potentially generate almost 6000 W/m^2 into the top surface of the hanging plate, and approximately 3000 W/m^2 into the bottom surface of the hanging plate which must be dissipated or transferred as a usable energy source. The heat generation examined is limited to convective heat transfer from the air and does not include frictional heating.

Heat transfer from the air to the craft and plates for the Mach 3 hanging plate cases was measured at two tiers, 5 and 6, at the optimal lift locations – the front of the hanging plate is even with the front of the main craft. Heat transfer from the air to the craft is shown in Figure (4.25).

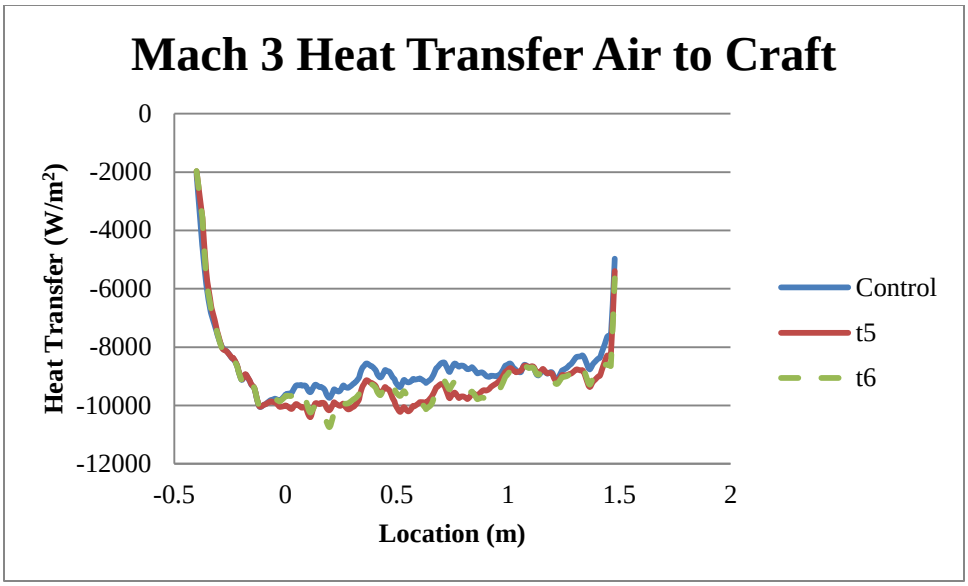

Figure 4.25 Mach 3 Heat Transfer Air to Craft

At Mach 3, heat transfer from the air to the craft peaks at approximately 10 kW/m^2 , for both a 15 cm displacement from the x-axis and a 10 cm displacement from the x-axis. A transitional boundary layer exists for both hanging plate cases and the conventional case for the first 40 cm of the craft. The conventional case has an established boundary layer after 40 cm, reducing the heat transfer into the craft from the air. Heat transfer during the hanging plate simulations is elevated above the conventional case due to the continued turbulence generated by the shock waves existing in the medium. It is seen in Figure (4.25) where the hanging plates cease to have an effect on the craft, as that is where the heat transfer values converge for all three cases – located at approximately 1 m back from the bow of the main craft.

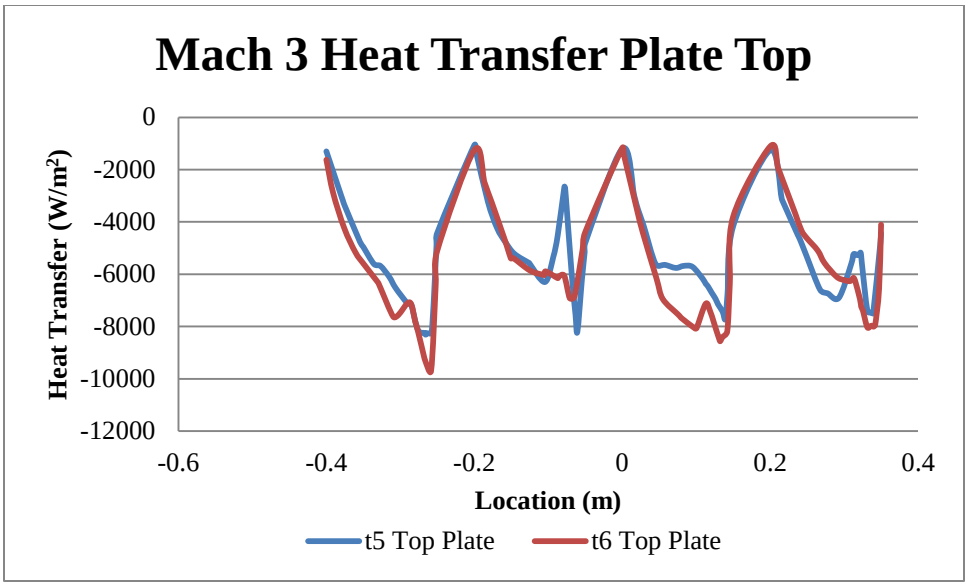

Figure 4.26 Mach 3 Heat Transfer Plate Tops

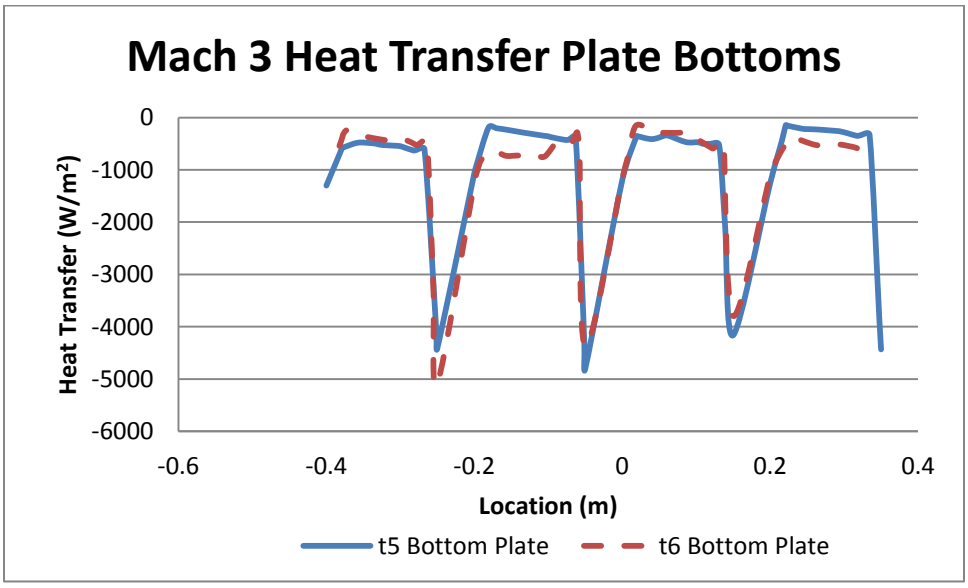

Figure 4.27 Mach 3 Heat Transfer Plate Bottoms

Between the two hanging plate cases examined, heat transfer between the air and plats is virtually the same. On the top surface of the plate, 8 kW/m^2 to 10 kW/m^2 transfers from

the air at most, and along the bottom surface of the plate, 4.4 kW/m^2 to 5 kW/m^2 transfers from the air.

The heat transfer from the air to the craft during the Mach 4 simulation is shown in Figures (4.28) through (4.30).

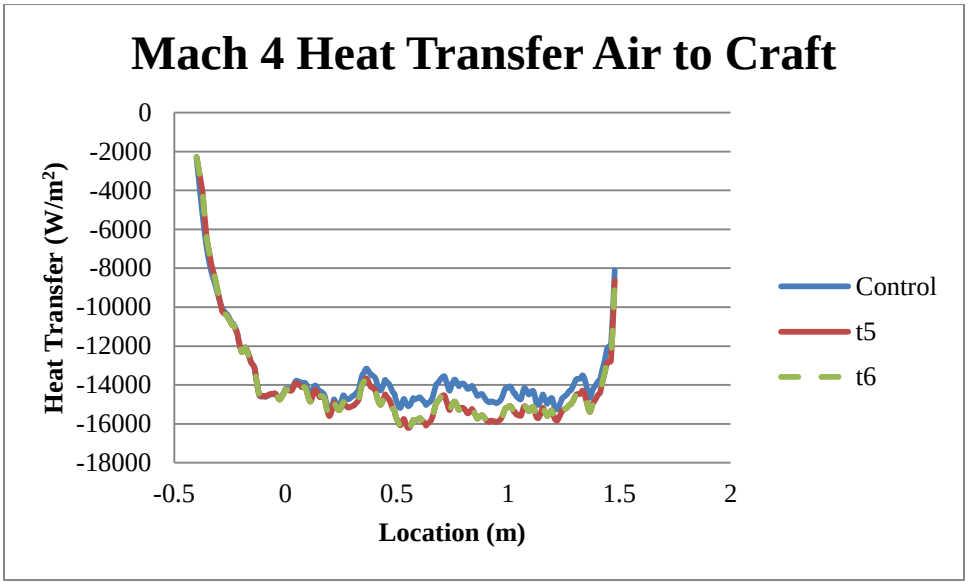

Figure 4.28 Mach 4 Heat Transfer Air to Craft

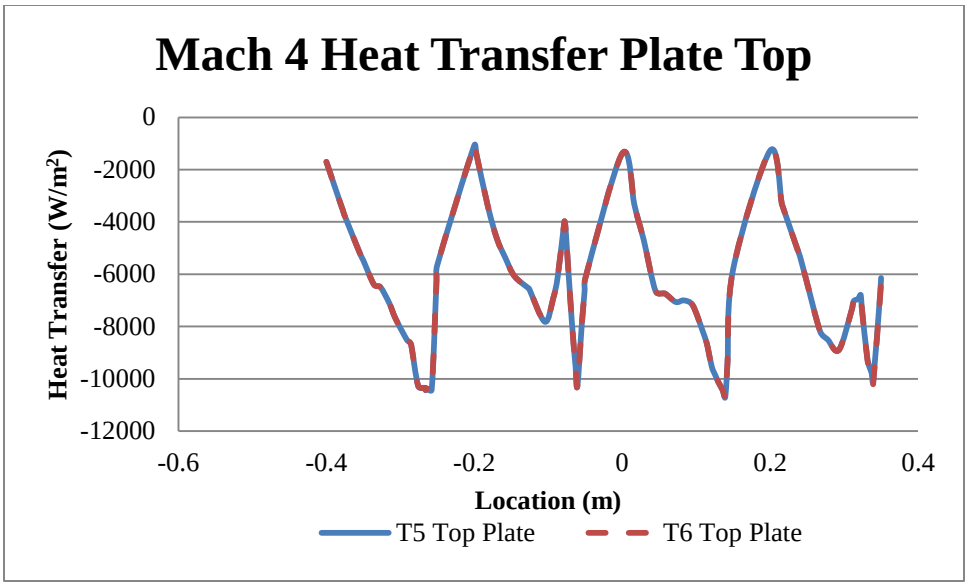

Figure 4.29 Mach 4 Heat Transfer Plate Top

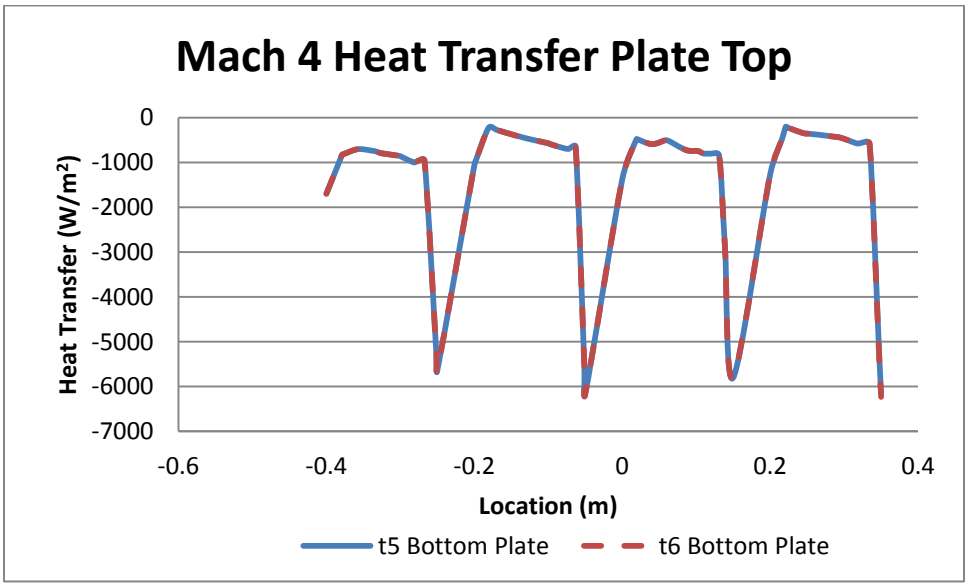

Figure 4.30 Mach 4 Heat Transfer Plate Bottom

For Mach 4 flow, transferred heat into the main craft reaches above 16 kW/m^2. The conventional case is also maximized at 16 kW/m^2, however has reduced values for the remainder of the locations sampled along the craft. Similar to the Mach 3 case, the area of

effect the hanging plates have on the main is located based on where the heat transfer values of the conventional case reconnect with those of the hanging plate case around 1.25 m from the bow. Heat transfer during the Mach 4 case has very few differences between the two locations of the hanging plates. The top plate cases generate a maximum of 10.2 kW/m^2, while the bottom plates generate a maximum of slightly above 6 kW/m^2. Both locations for the hanging plates reach the same maximum and minimum, and values differ by less than 100 W/m^2 at any given point.

SUMMARY

In the Mach 2 hanging plate simulation, the optimal arrangement for hanging plates is at a neutral location relative to the bow of the main craft, a 15 cm offset from the y-axis, and use an angle of 20^o to generate the oblique shock waves from the plates. This case generates 35.8% more lift than the conventional case and keeps 90% of the Lift-Drag ratio. As the craft moves through variable velocities, the Mach 3 flow has an optimal location of similar X location and shock angle, but a y-axis offset of only 10 cm. This case generates 24.3% more lift when compared to the conventional case, and is still able to maintain 90% of the Lift-Drag ratio. At Mach 4, the optimal location is at a vertical offset of 15 cm, and creates 23.6% more lift than the conventional case. The Lift-Drag ratio is 91% of the conventional cases L/D ratio.

Heat transfer from the air to the craft peaked at 6400 W/m^2, 10.2 kW/m^2, and 16 kW/m^2 for the Mach 2, 3, and 4 cases, respectively. When compared to conventional

cases, heat transfer into the craft does not generate substantial increases, and is used to determine the area of effect of the four hanging plates on the body of the main craft.

CHAPTER 5 : SUMMARY, CONCLUSIONS, AND RECOMMENDATIONS

DISCUSSION OF RESULTS

When shock waves interact with each other they need a specific configuration to create a useful lifting or dragging force, and these forces result in pressure and heating gradients. We have shown that after supersonic speed is achieved, the aerodynamic properties of the rarefied gas can be manipulated to generate enough lift to keep the craft aloft, and in other applications generate the escape velocity necessary to reach orbit with the minimum expense of fuel. Our examination of the aerodynamic properties contributing to the pressure gradients has also resulted in an increased understanding of shock wave interactions and their usefulness in air travel. The examination of the heating gradients has given insight into turning waste and potentially damaging – heating issues into useable energy sources for extended flights.

Creating a cost effective reusable launch vehicle unlocks an entirely new section of space. If the craft can trade fuel and structural mass for payload mass, more opportunities for moving into space become available. One opportunity currently being explored is space tourism. Space tourism not only provides a monetary income for multiple new space companies, it also reignites interest in space travel in the general population. However, the cost of one time launch vehicles is prohibitive to the majority of the population, as well as for companies with long term interest. In response to this, multiple forms of "Waverider" lifting wing hypersonic planes have been created to slowly reach the desired Mach 25

escape velocity. The RAM/SCRAM jet engine uses high stagnation pressure to compress the air through the inlet, and then expels it to generate a momentum transfer which translates to lift. While the planes are able to breach hypersonic speeds, they experience failure due to the complex flow fields of viscous interactions. The viscous interactions produce boundary layer separation, regions of high pressure, and heat transfer, which can result in flow degradation or separation in an inlet. The shock wave interaction removes the combustion instability through the inlet and engine, and instead relies on creating areas of high pressure to create a lifting force between the top and bottom surface of the craft. In essence it is a RAM/SCRAM jet engine without the engine, and instead of relying on the momentum transfer to generate lift, it is generated directly by manipulating the forces above and below the craft.

CONCLUSION AND RECOMMENDATION FOR FURTHER STUDY

The use of shockwave reflection in order to create compressive effects and generate increased lift has notable benefits, but also has limitations that could not be overcome in this research. While the most useful cases gave an increase of more than 35% over conventional cases, the increase in drag by 50% means that more optimization needs to take place in order to find a workable solution with minimal negative effects. The potential heat transfer from the working fluid to the surface of the craft is not detrimental, as in many ramp induced shock-shock interaction simulation, however there are many potential positives for having a steady energy source without the use of fuel. Also, shockwave

reflection with a non-detrimental outcome is also a method to eliminate adverse sonic phenomena during supersonic travel. Mitigating the air effects as the craft passes through while still maintaining a similar lift to drag ratio could reopen the door for supersonic commercial flights.

APPENDIX A: FIGURES

CONTROL CASE FIGURES

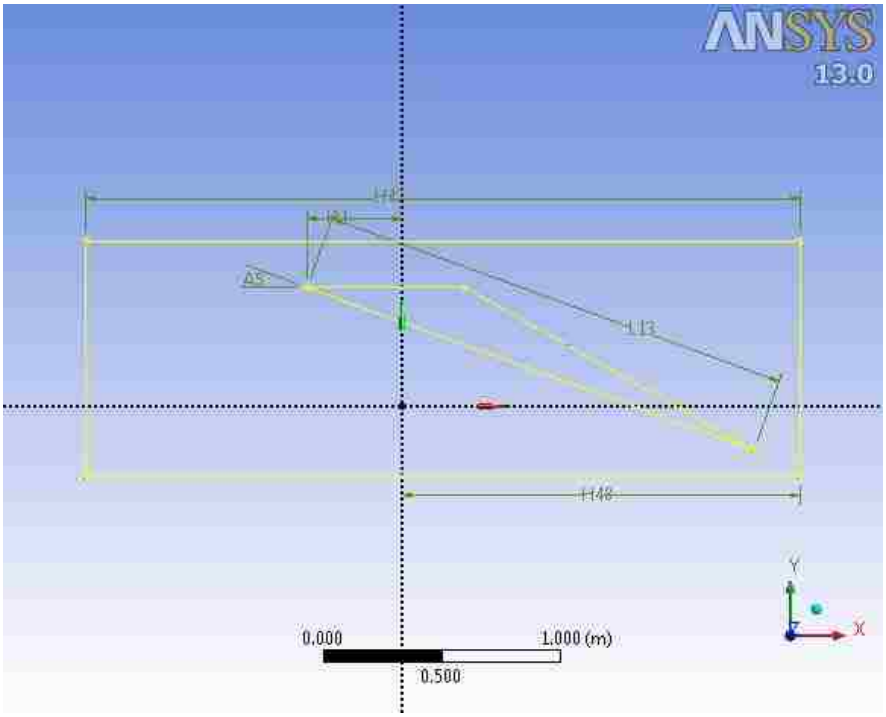

Figure 0.1

Figure 0.2

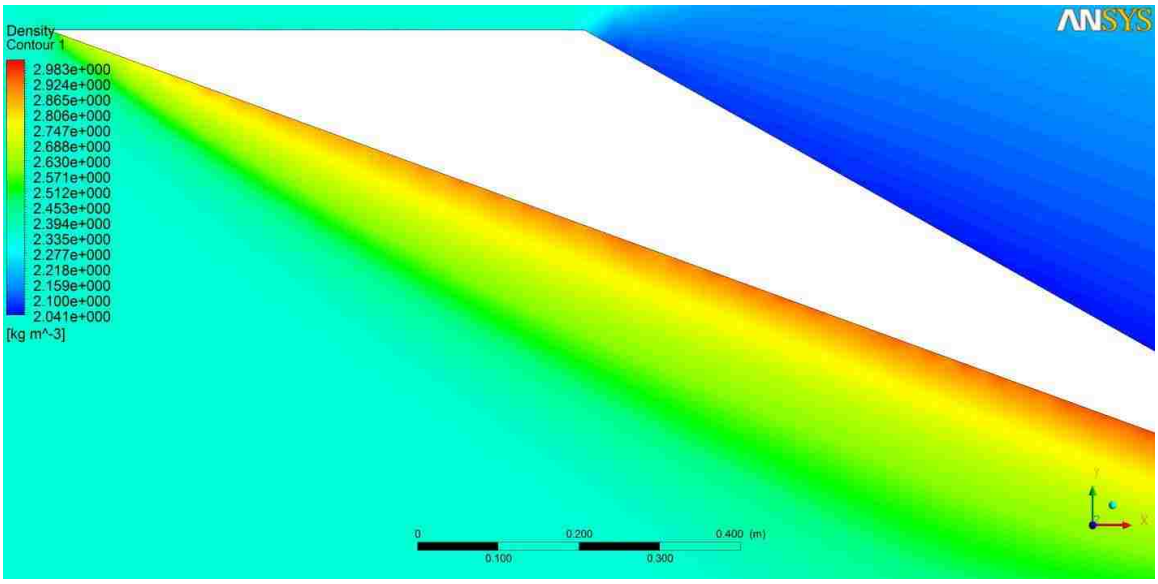

Figure 0.3

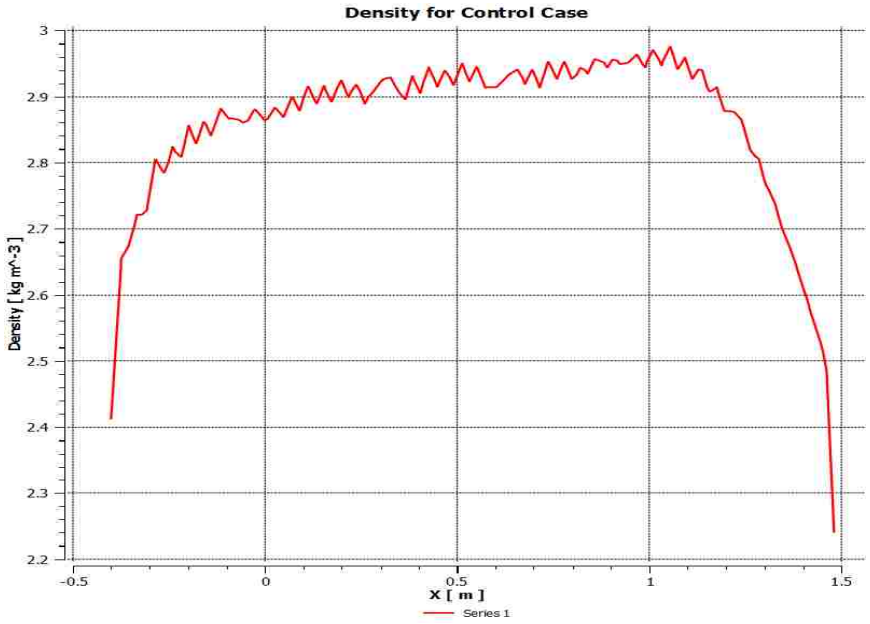

Figure 0.4

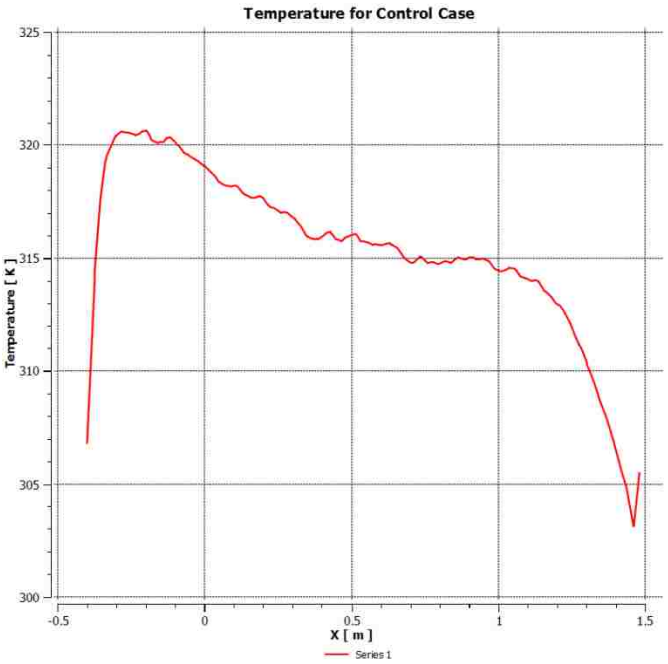

Figure 0.5

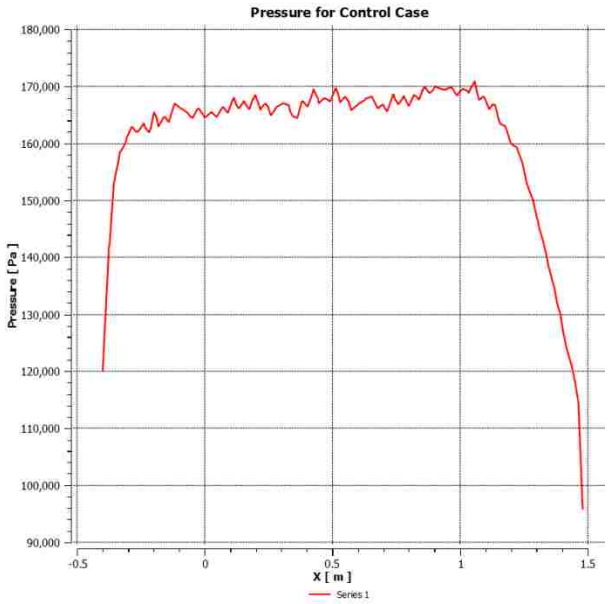

Figure 0.6

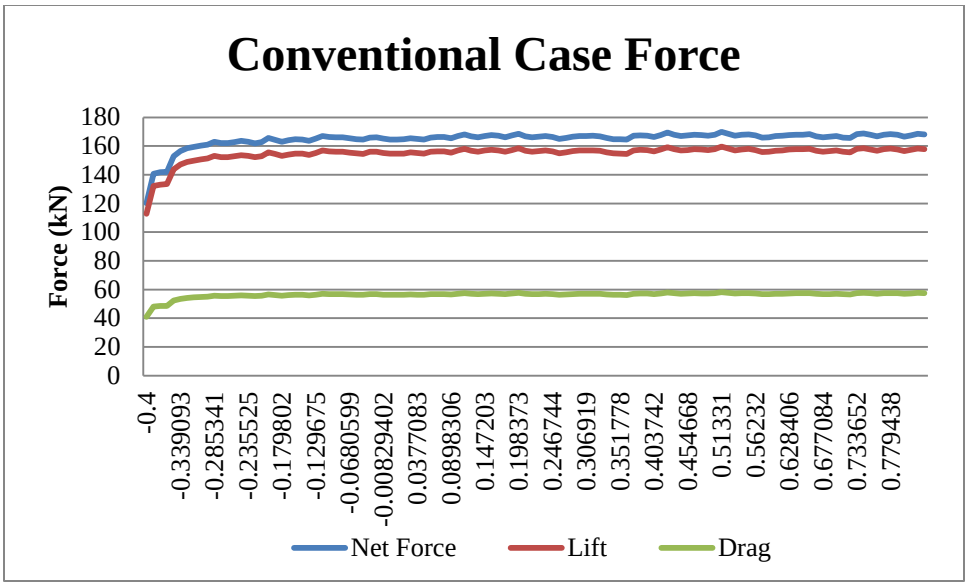

Figure 0.7

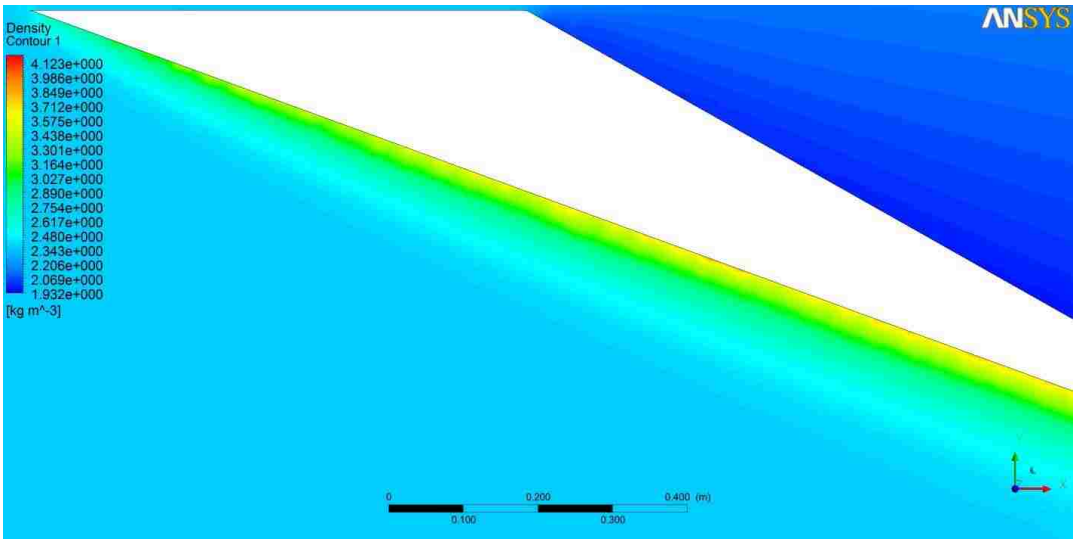

Figure 0.8

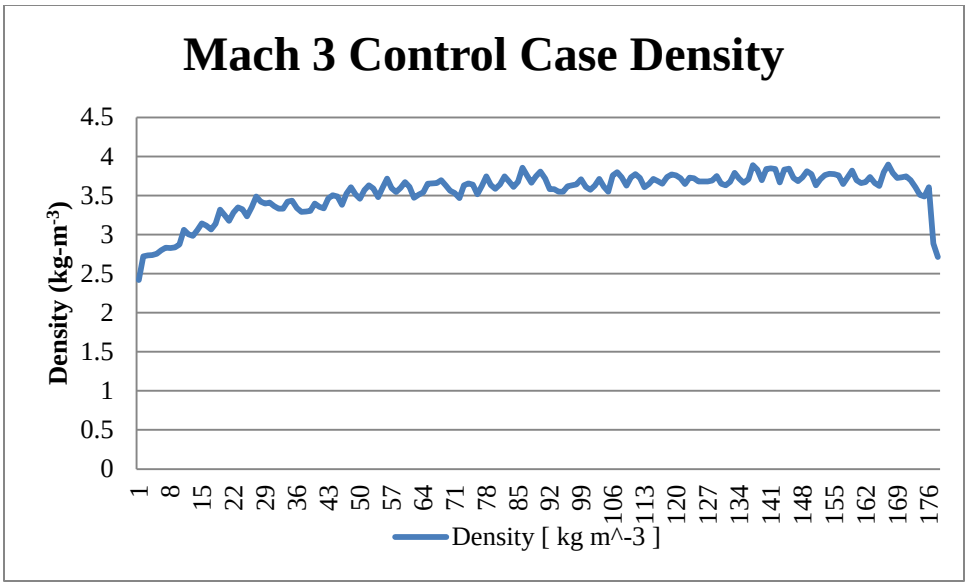

Figure 0.9

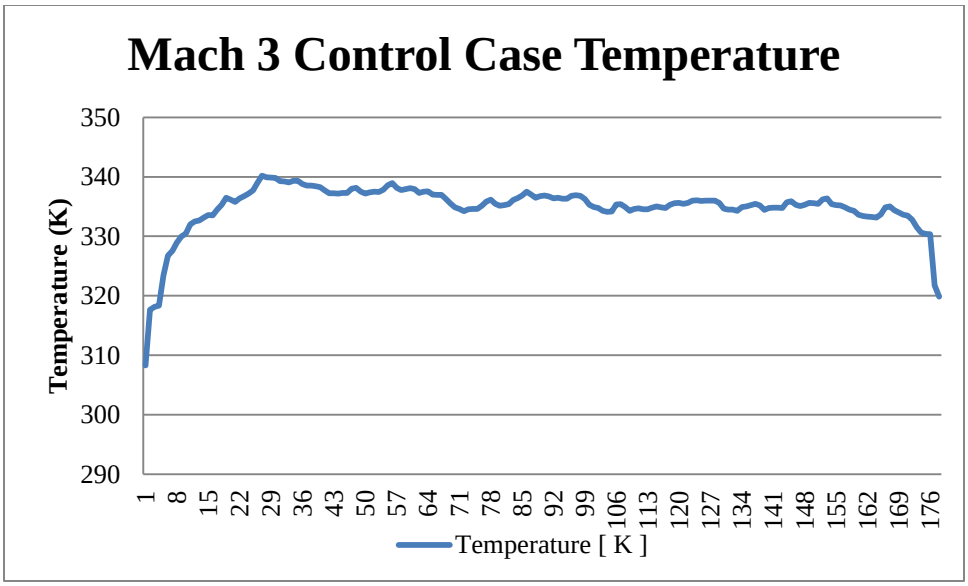

Figure 0.10

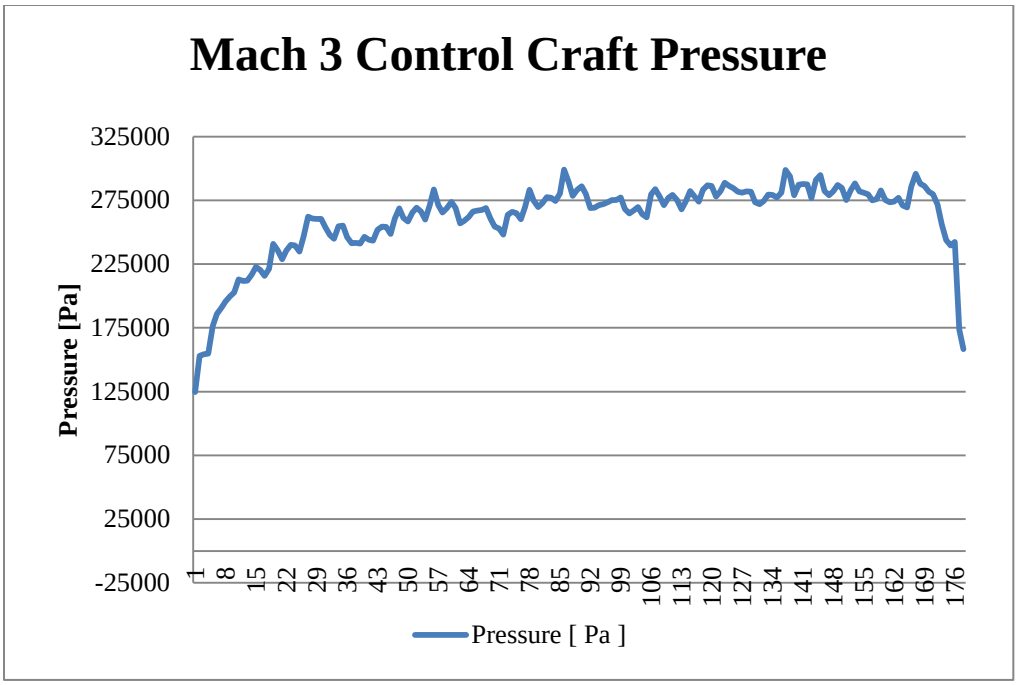

Figure 0.11

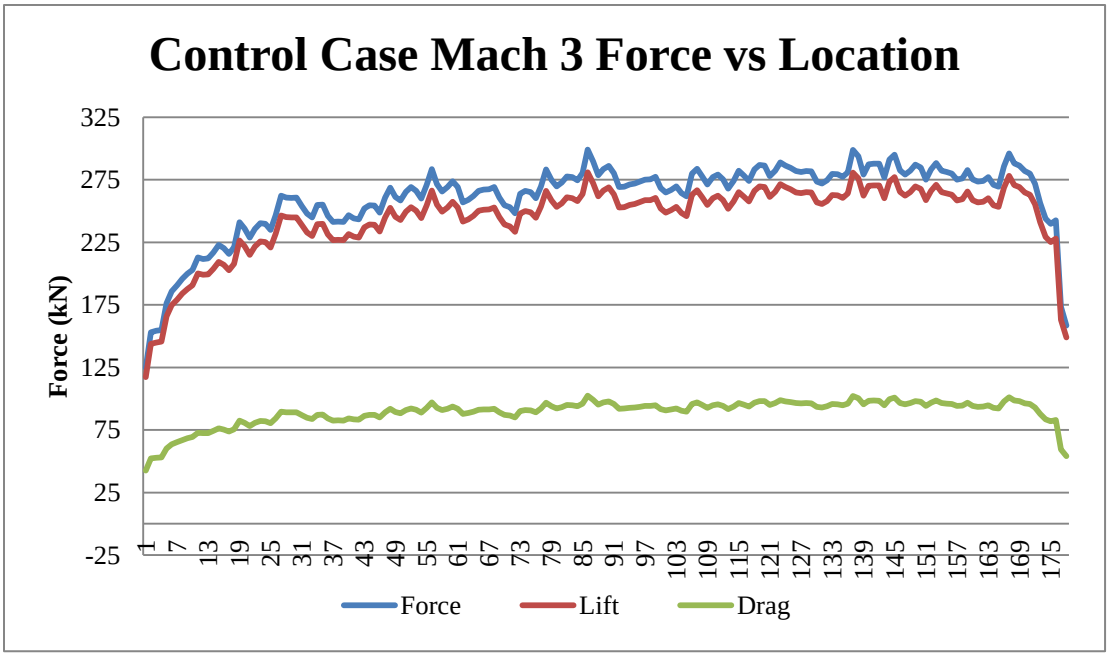

Figure 0.12

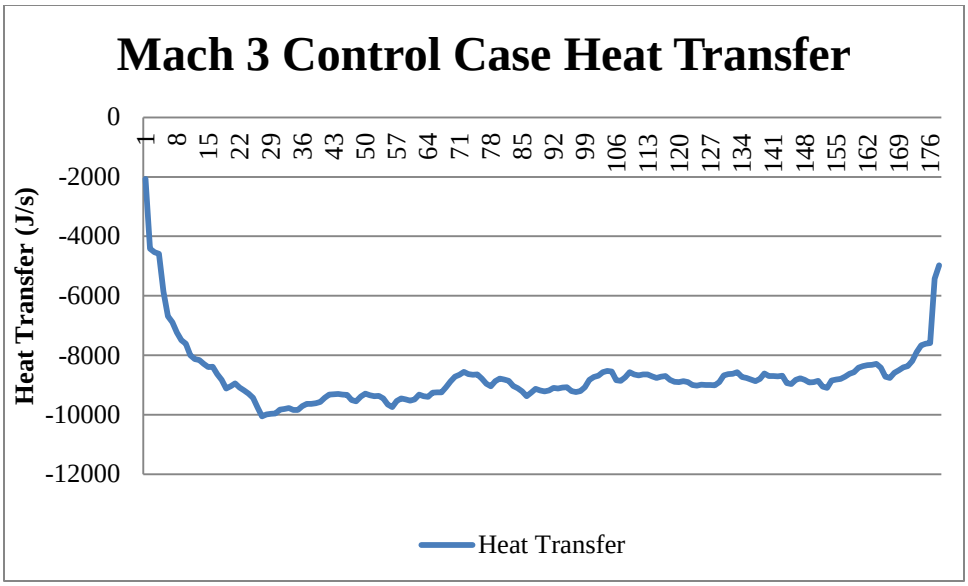

Figure 0.13

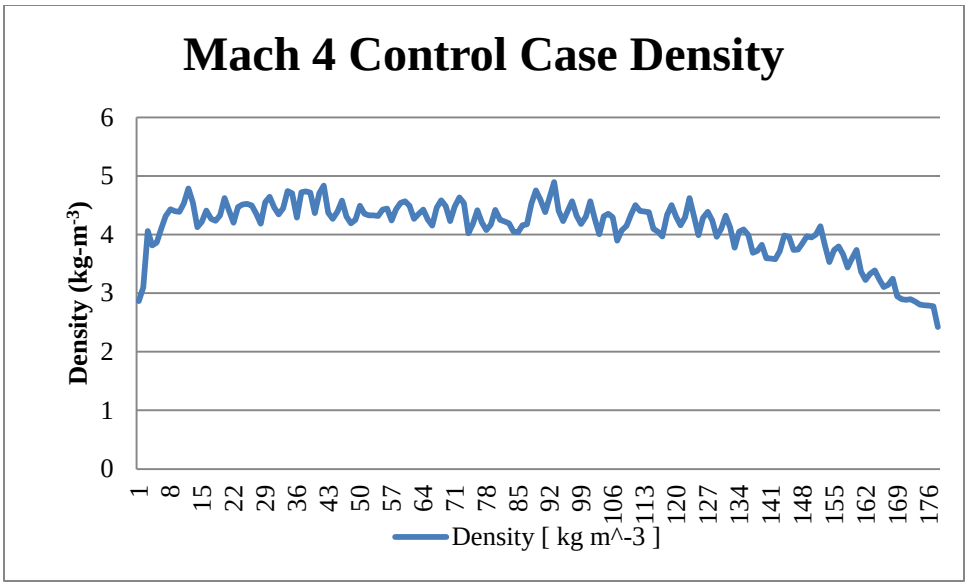

Figure 0.14

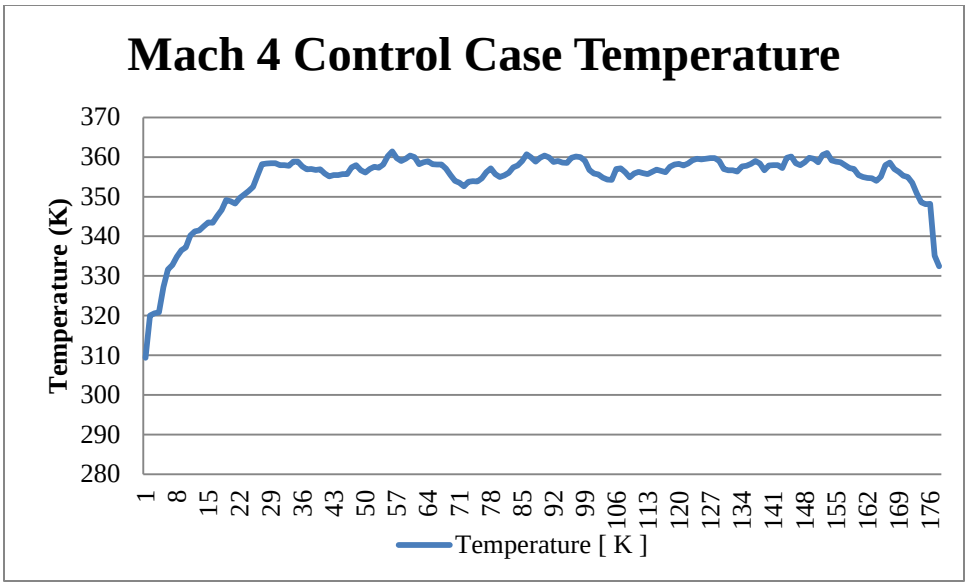

Figure 0.15

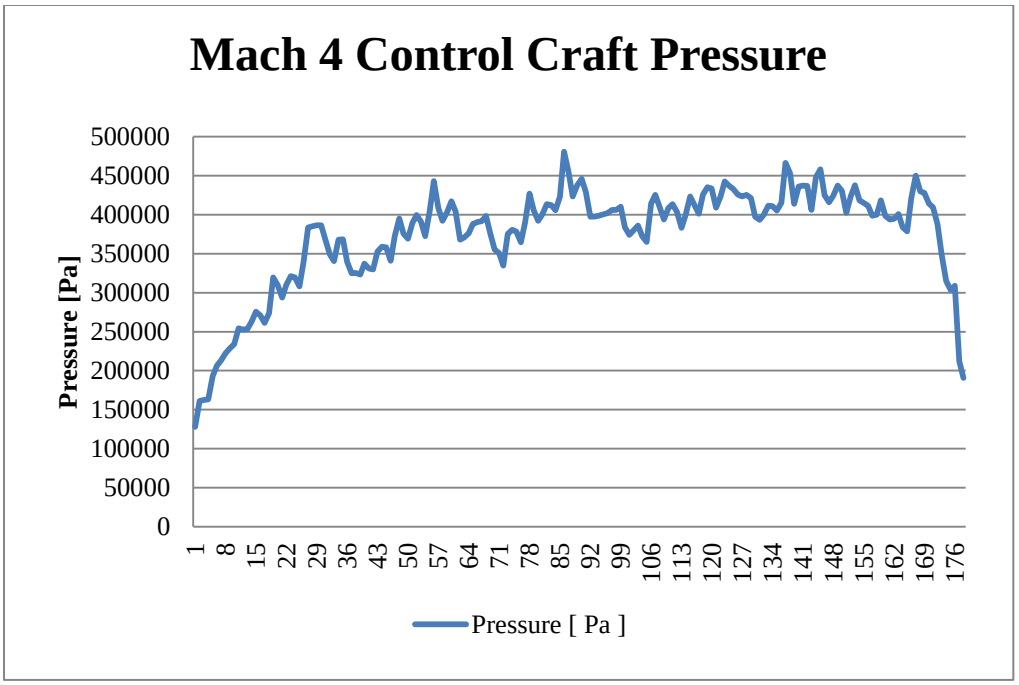

Figure 0.16

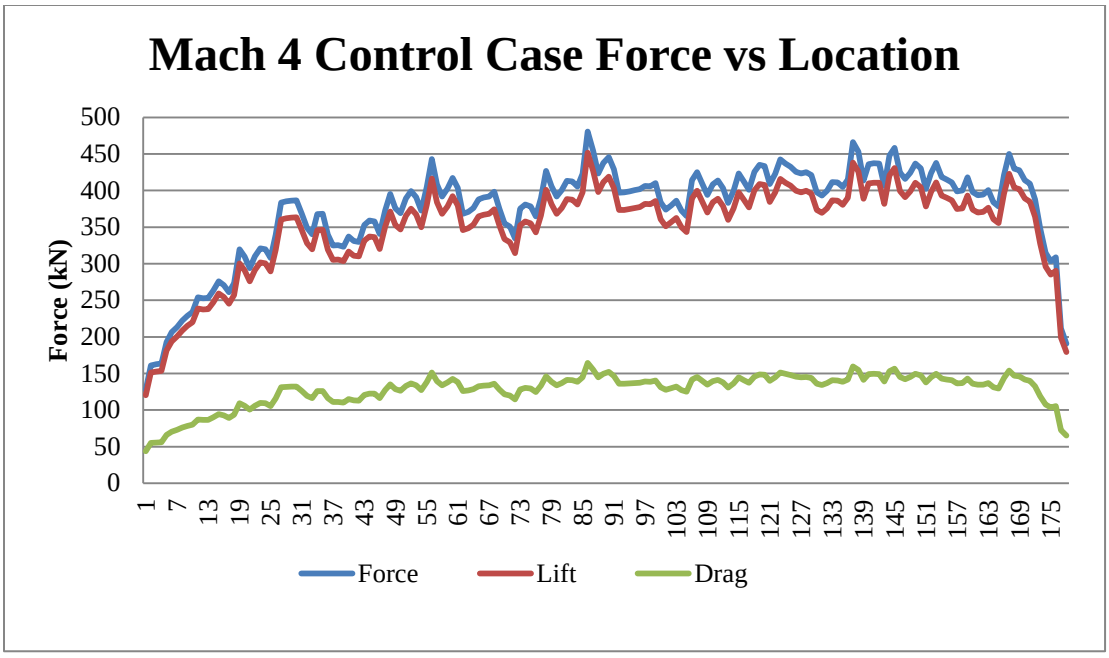

Figure 0.17

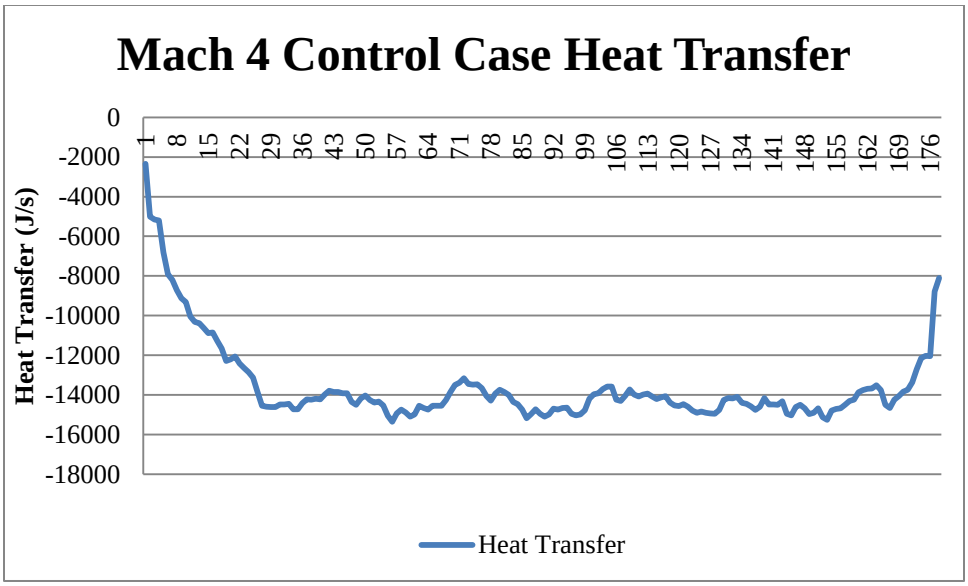

Figure 0.18

MACH 2 5^{O} TIER 1 DENSITY CONTOUR FIGURES

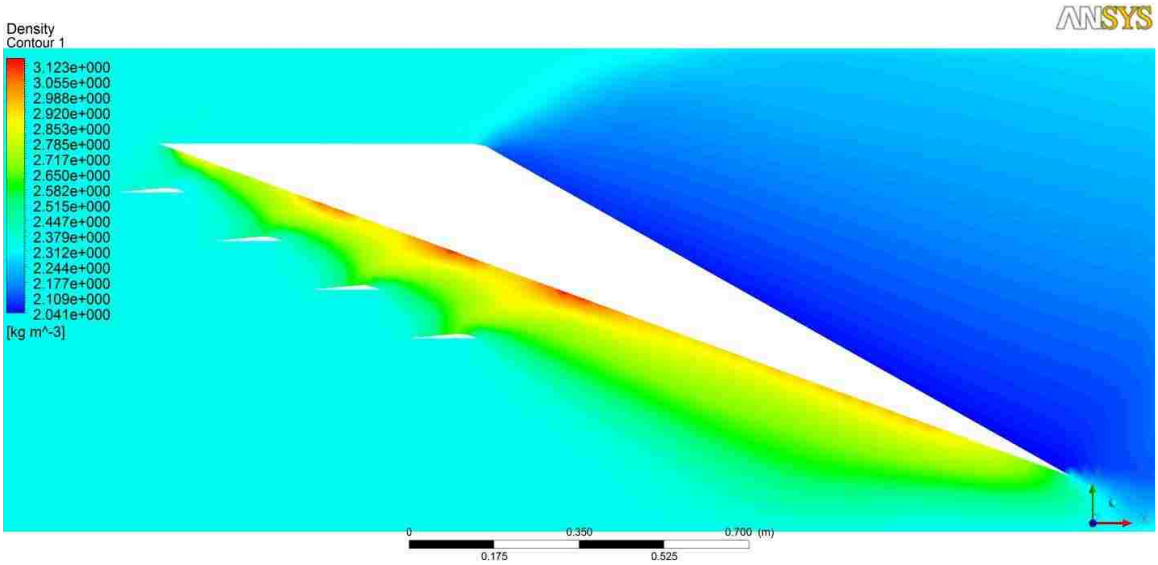

Figure 0.19

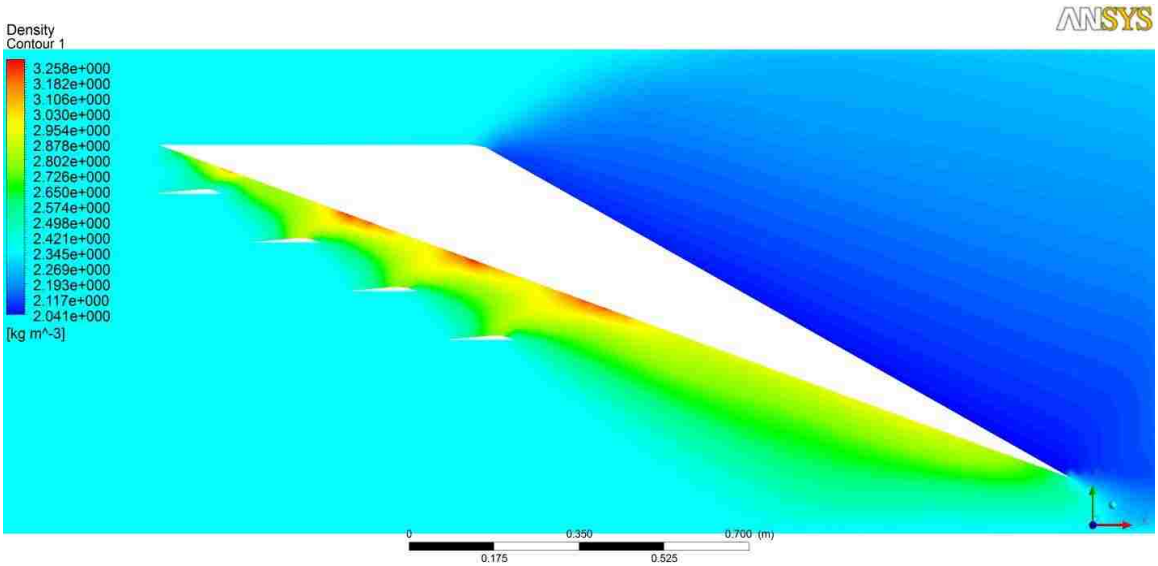

Figure 0.20

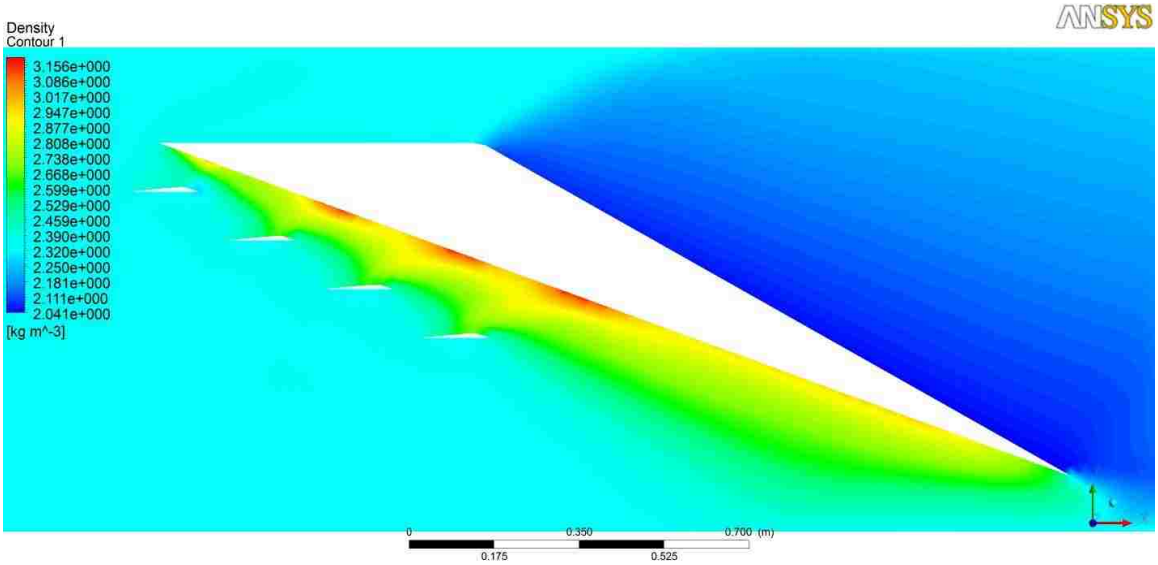

Figure 0.21

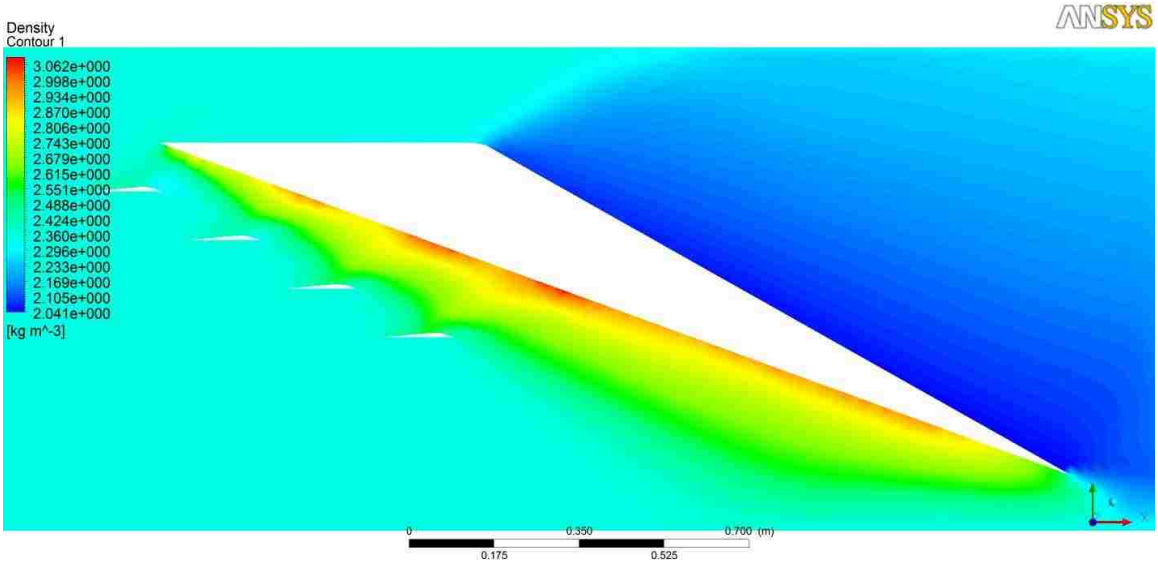

Figure 0.22

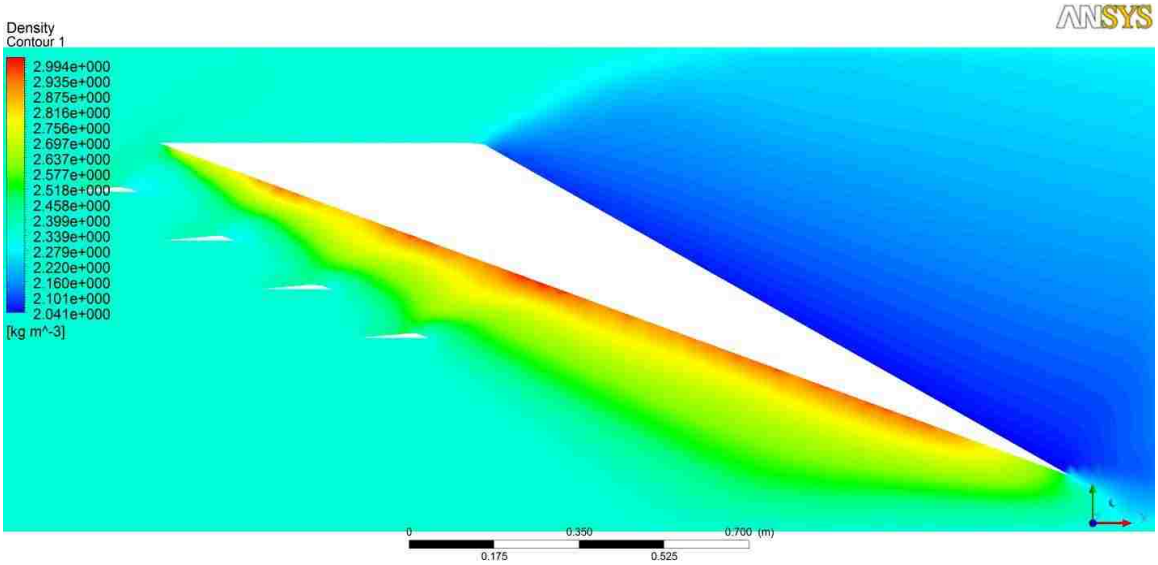

Figure 0.23

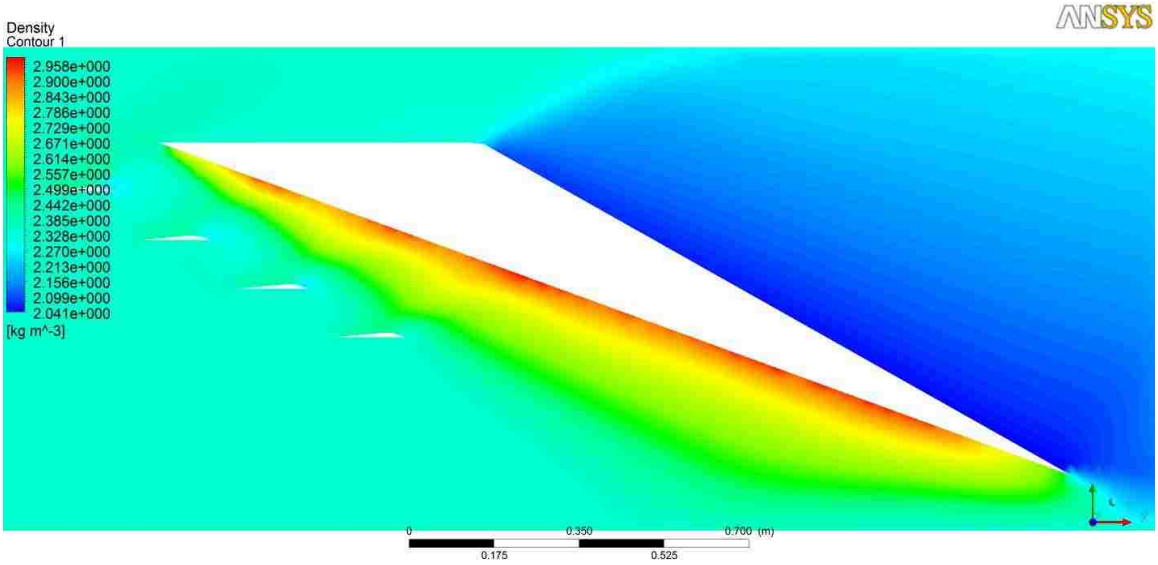

Figure 0.24

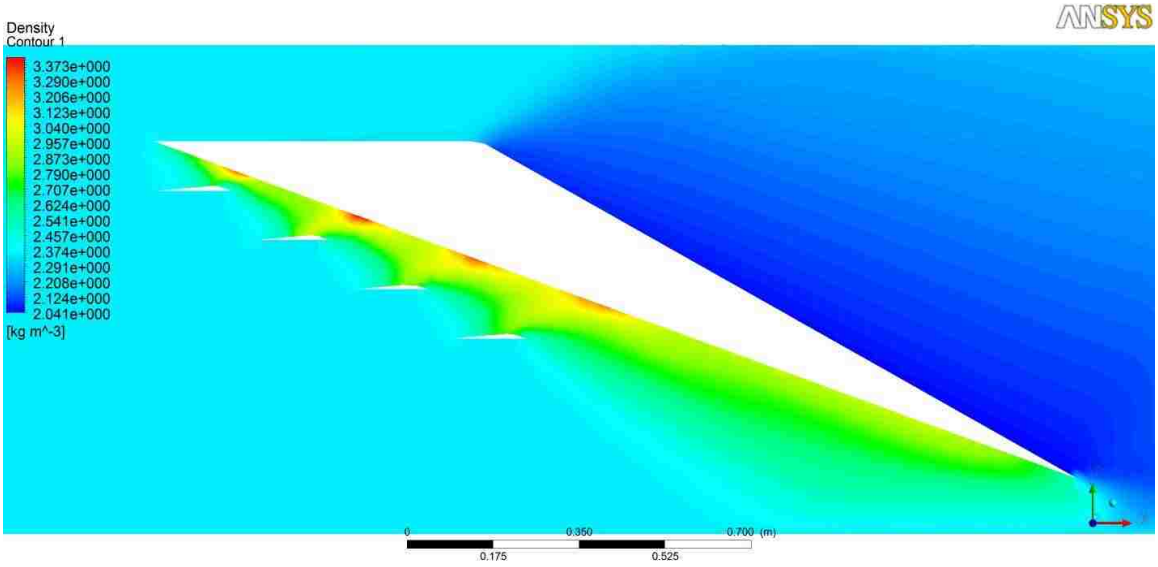
ANSYS
Density
Contour 1
3.373e+000
3.290e+000
3.206e+000
3.123e+000
3.040e+000
2.957e+000
2.873e+000
2.790e+000
2.707e+000
2.624e+000
2.541e+000
2.457e+000
2.374e+000
2.291e+000
2.208e+000
2.124e+000
2.041e+000
[kg m^-3]
0
0.350
0.700 (m)
0.175
0.525

Figure 0.25

MACH 2 5^{O} TIER 2 DENSITY CONTOUR FIGURES

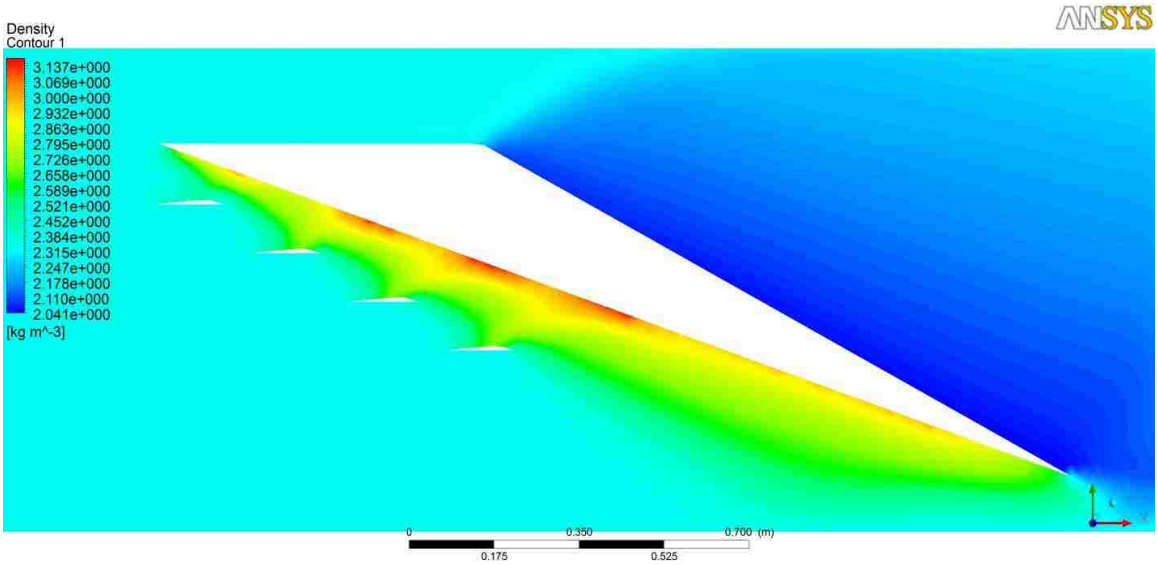

Figure 0.26

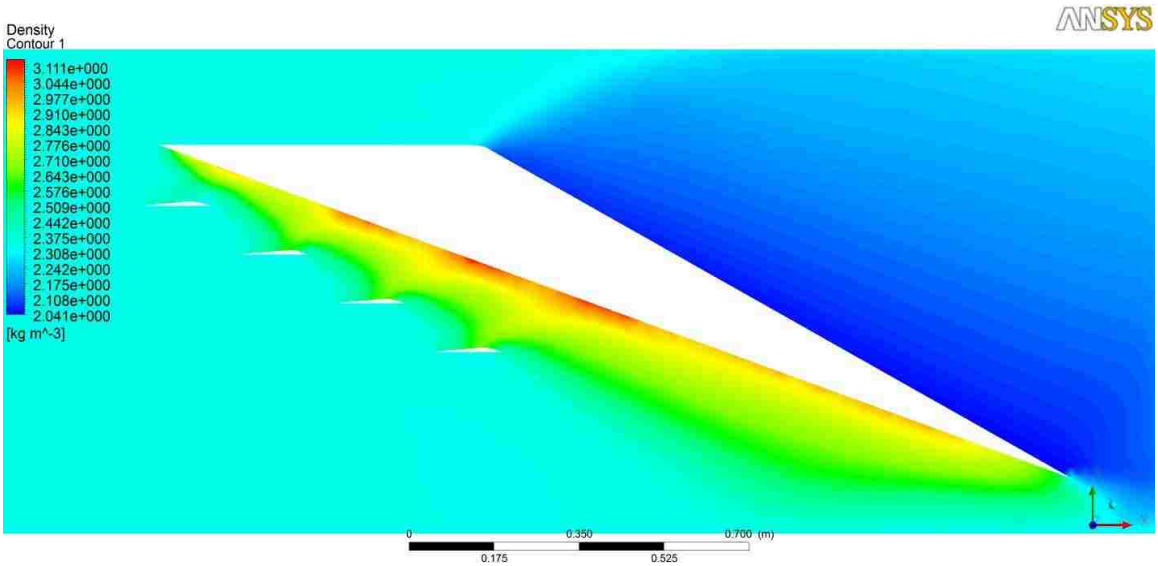

Figure 0.27

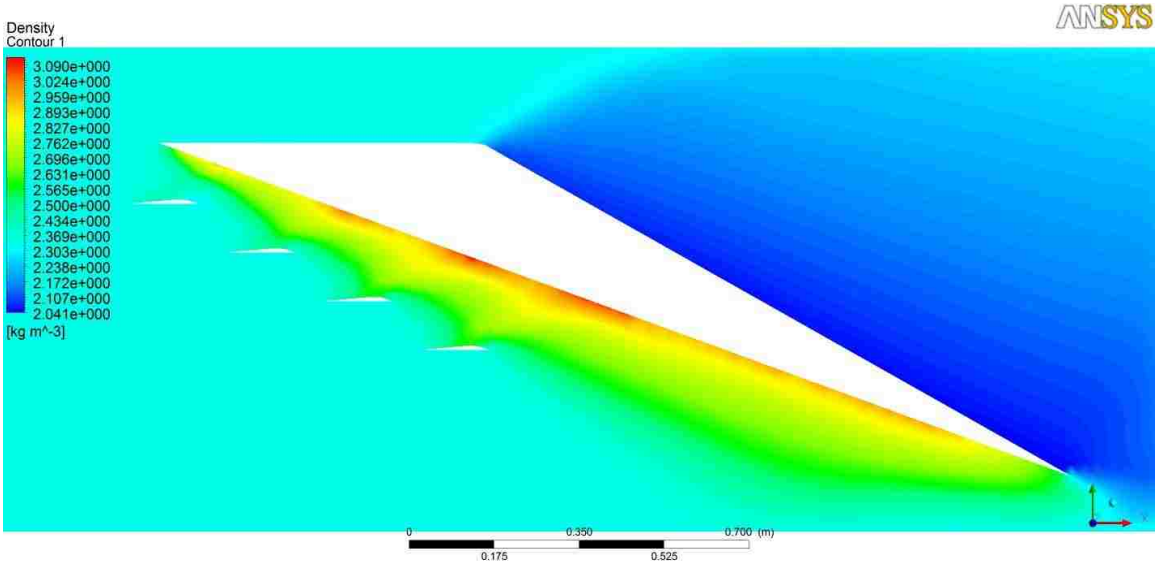

Figure 0.28

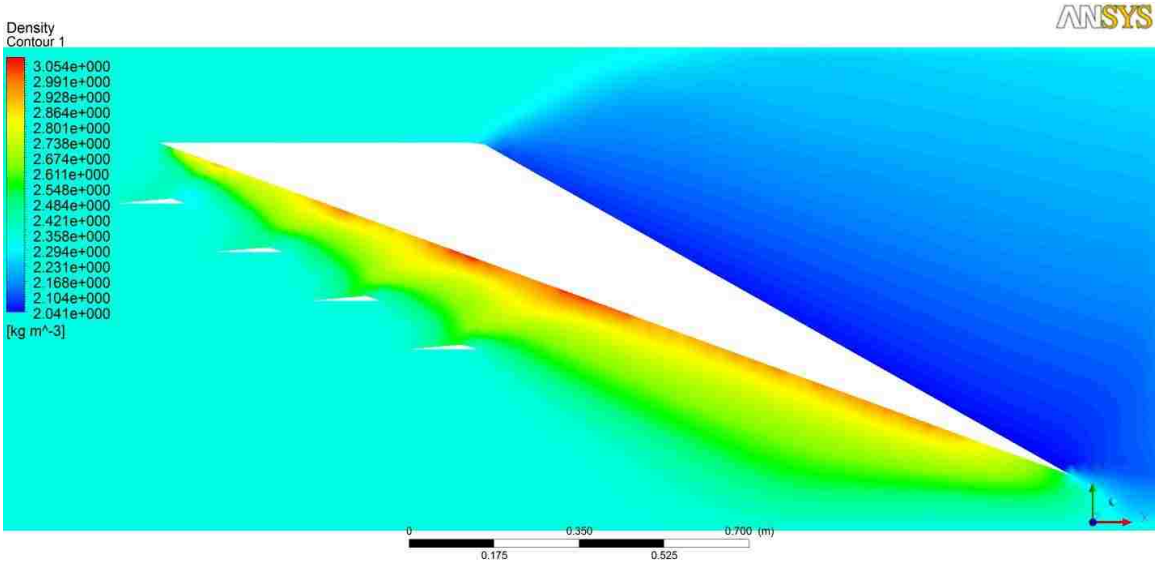

Figure 0.29

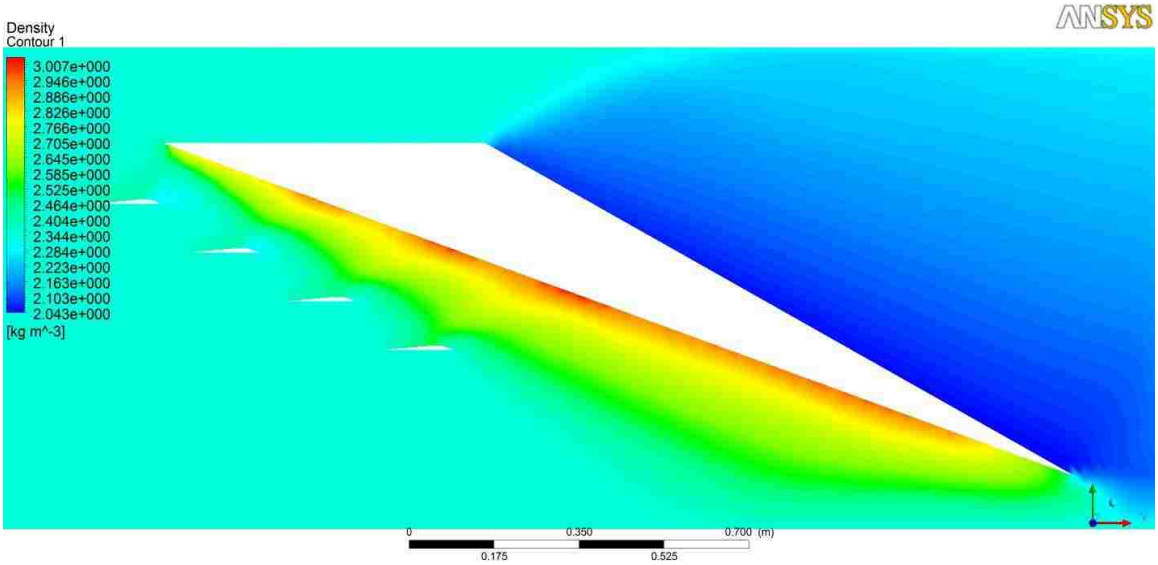

Figure 0.30

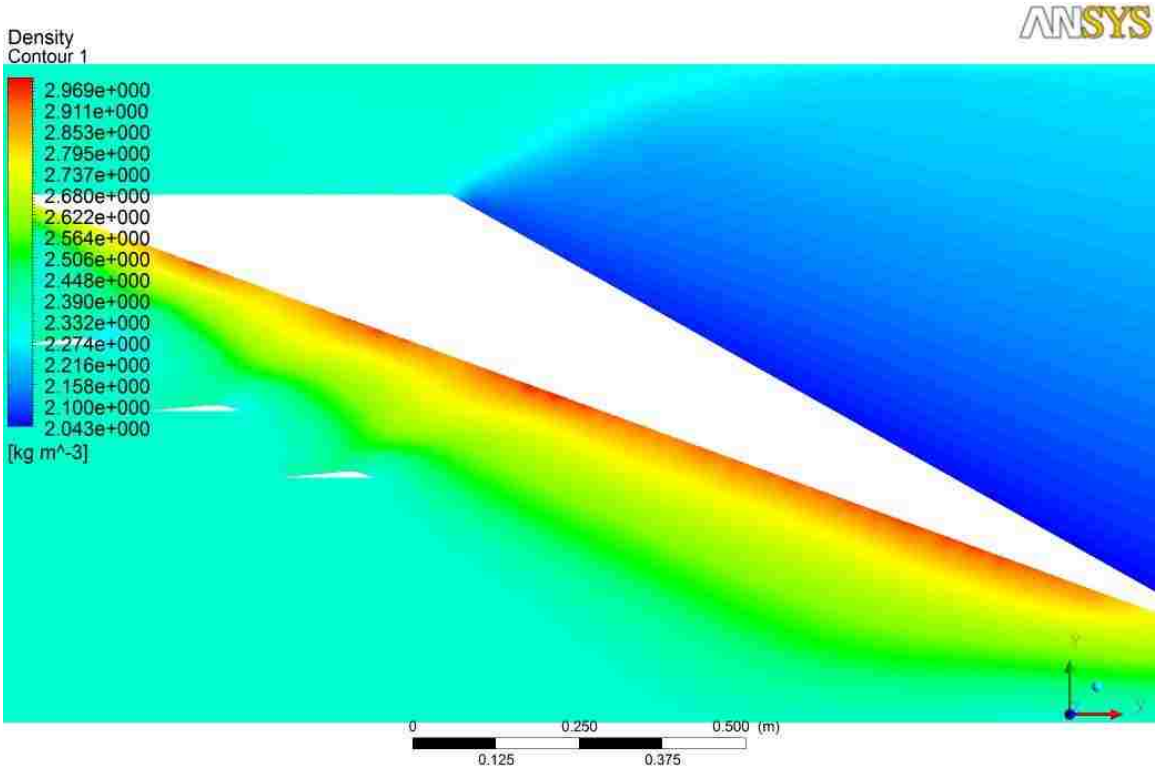

Figure 0.31

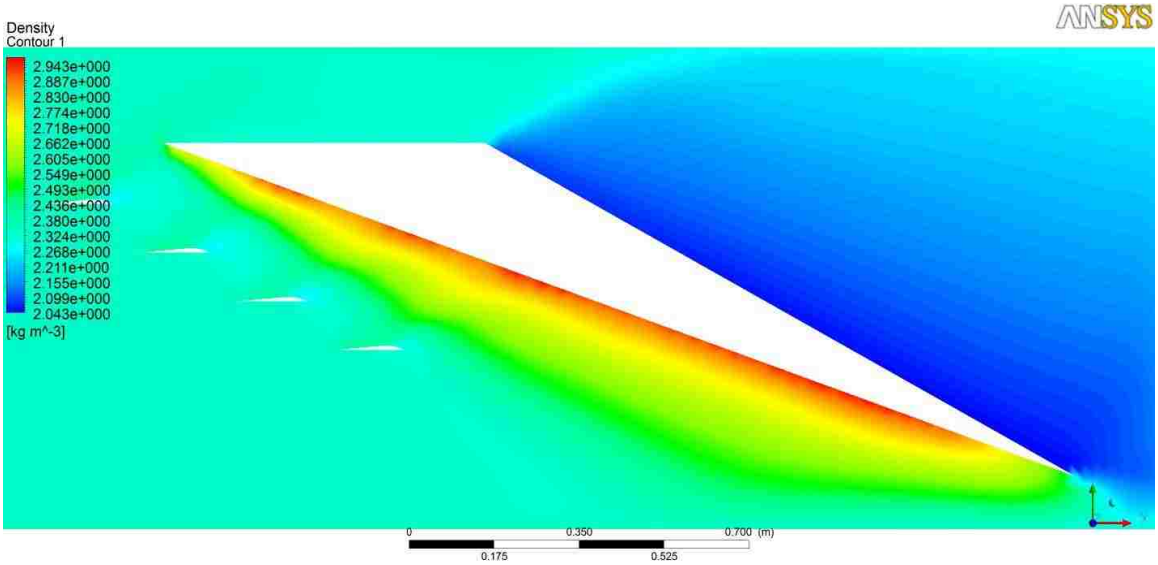

Figure 0.32

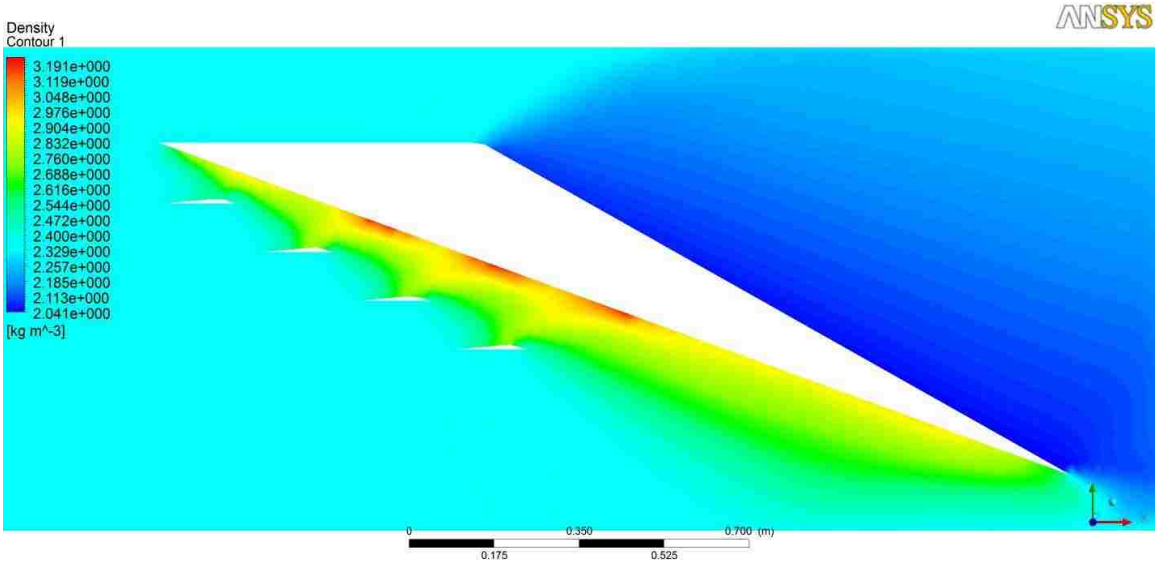

Figure 0.33

MACH 2 5^{O} TIER 3 DENSITY CONTOUR FIGURES

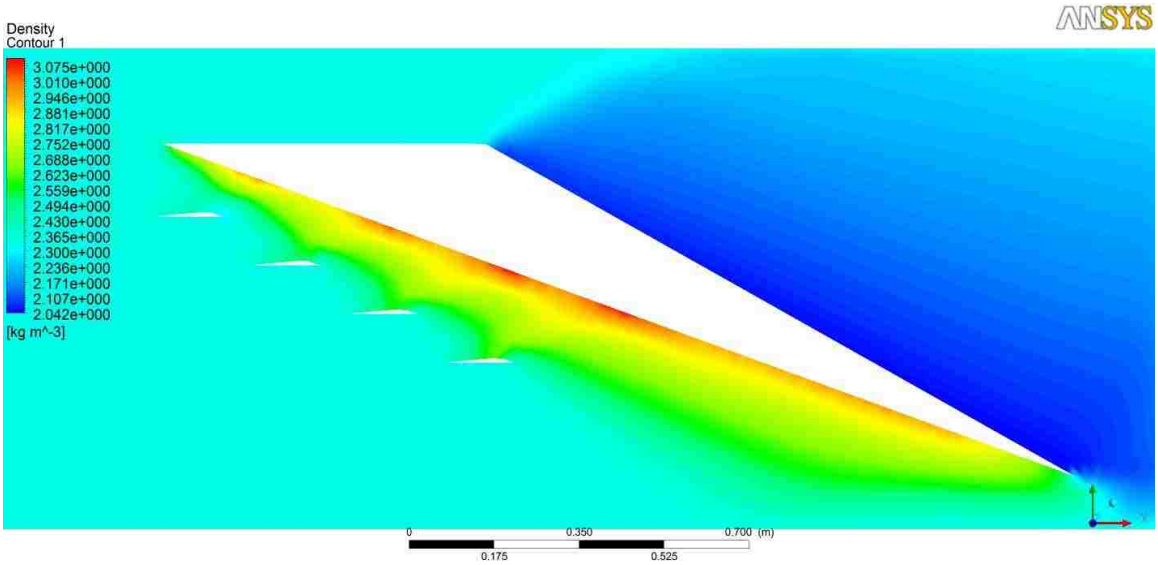

Figure 0.34

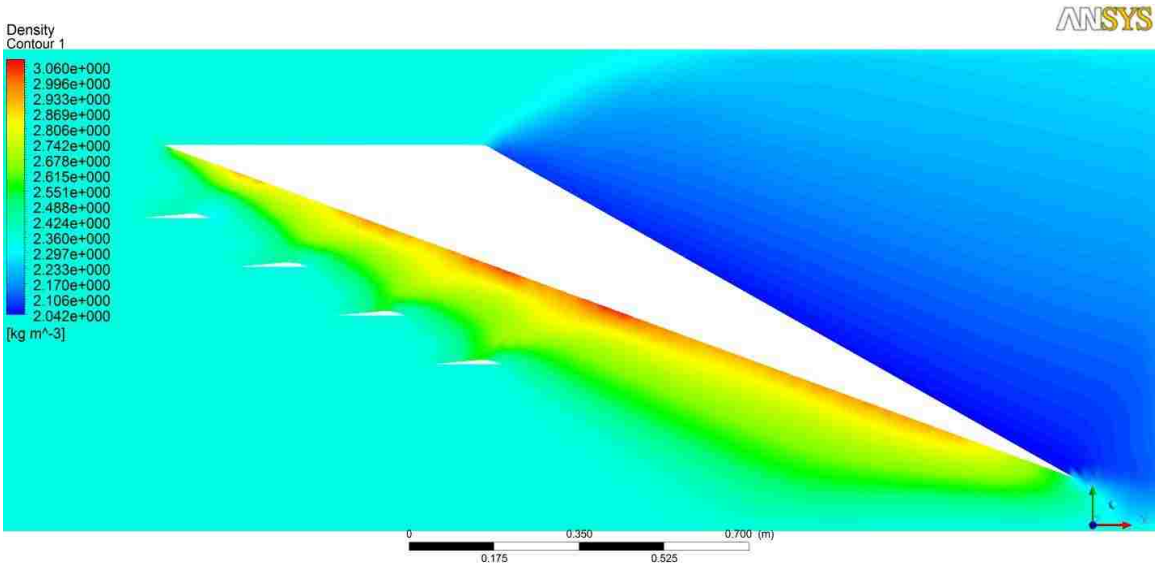

Figure 0.35

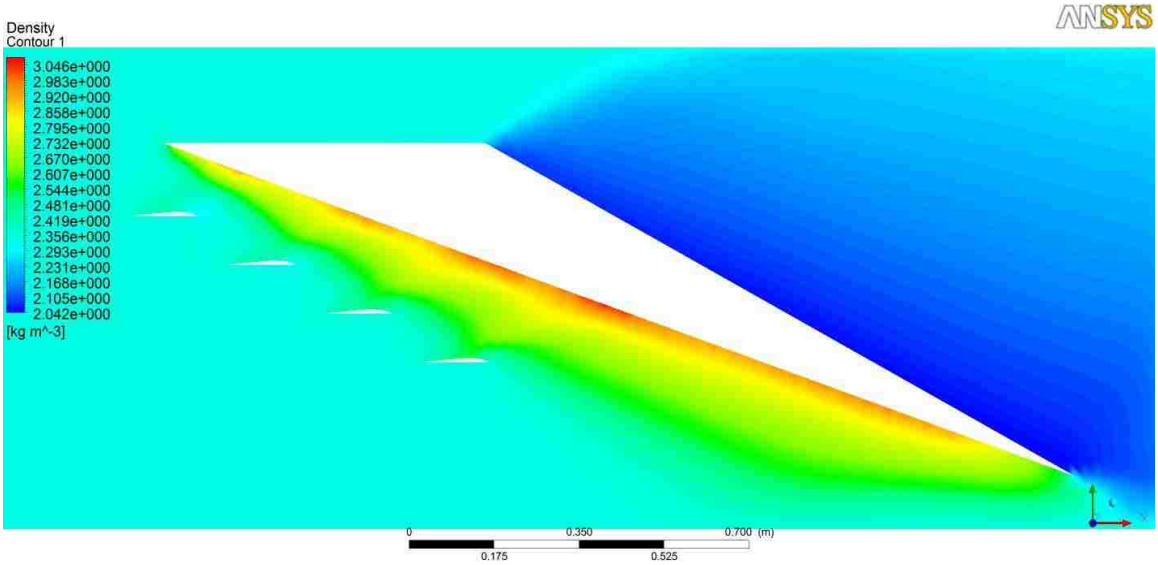

Figure 0.36

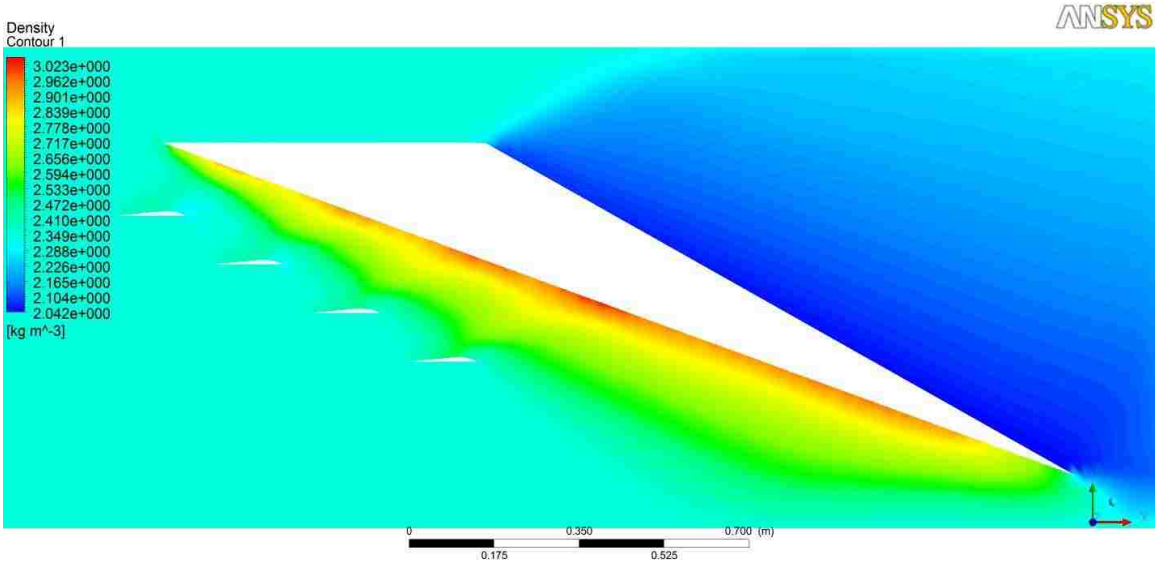

Figure 0.37

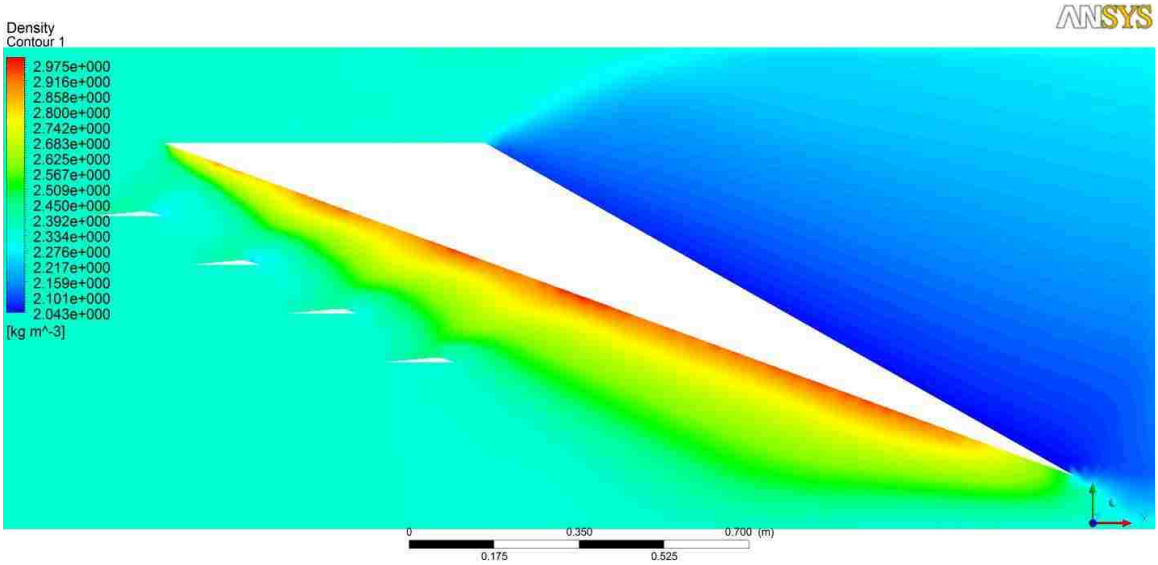

Figure 0.38

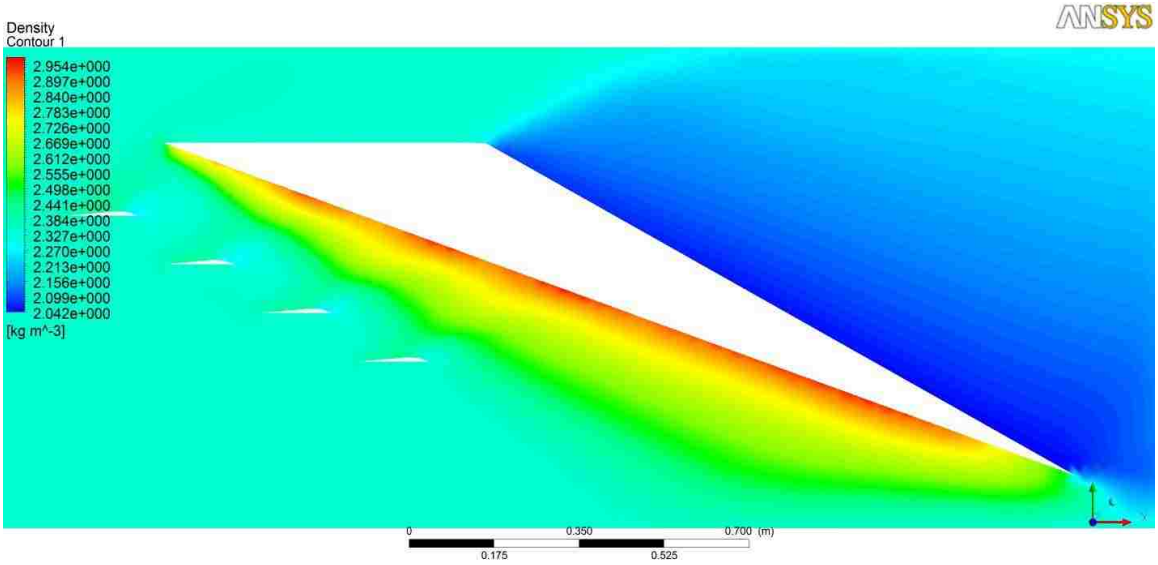

Figure 0.39

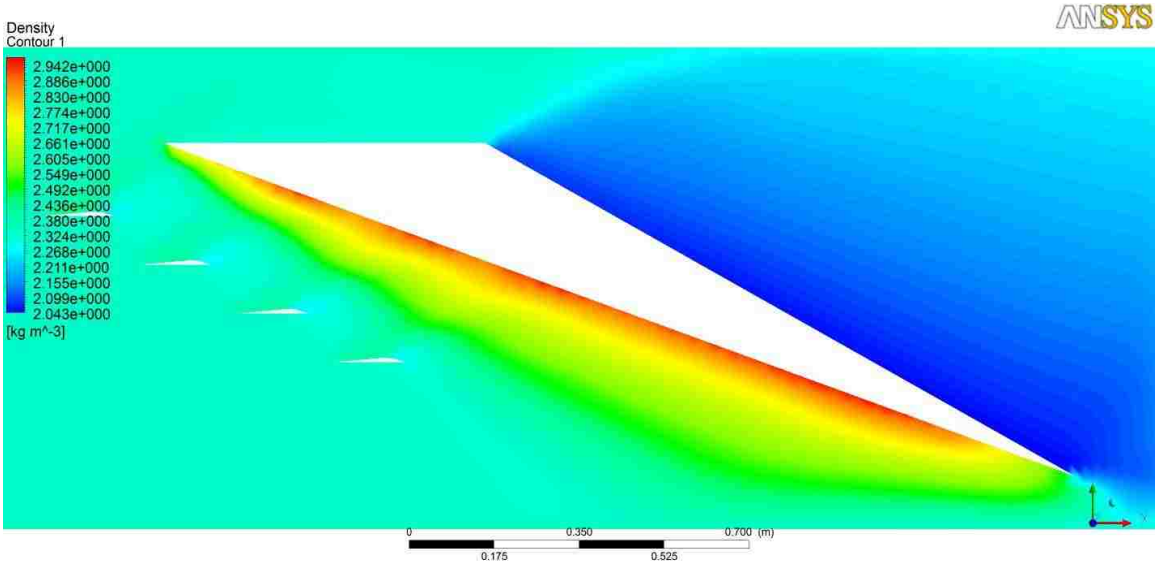

Figure 0.40

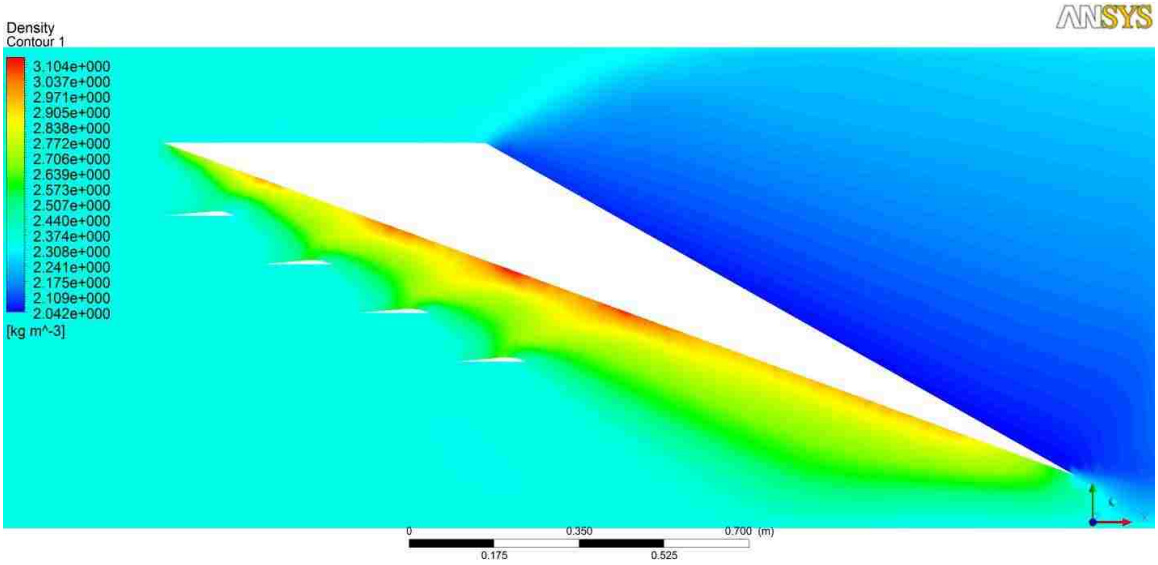

Figure 0.41

MACH 2 5^{O} TIER 4 DENSITY CONTOUR FIGURES

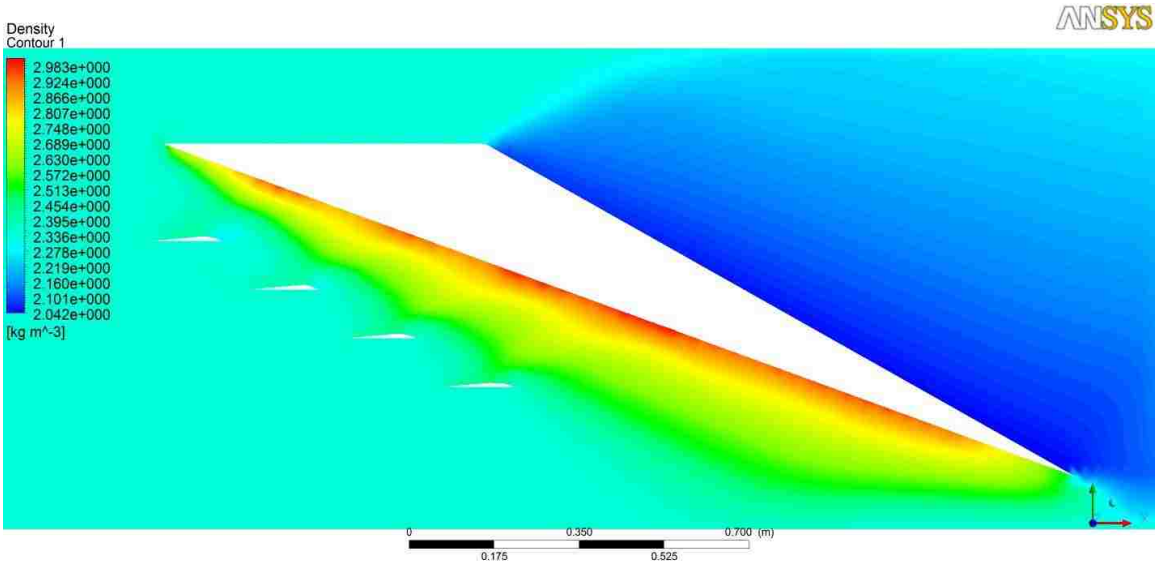

Figure 0.42

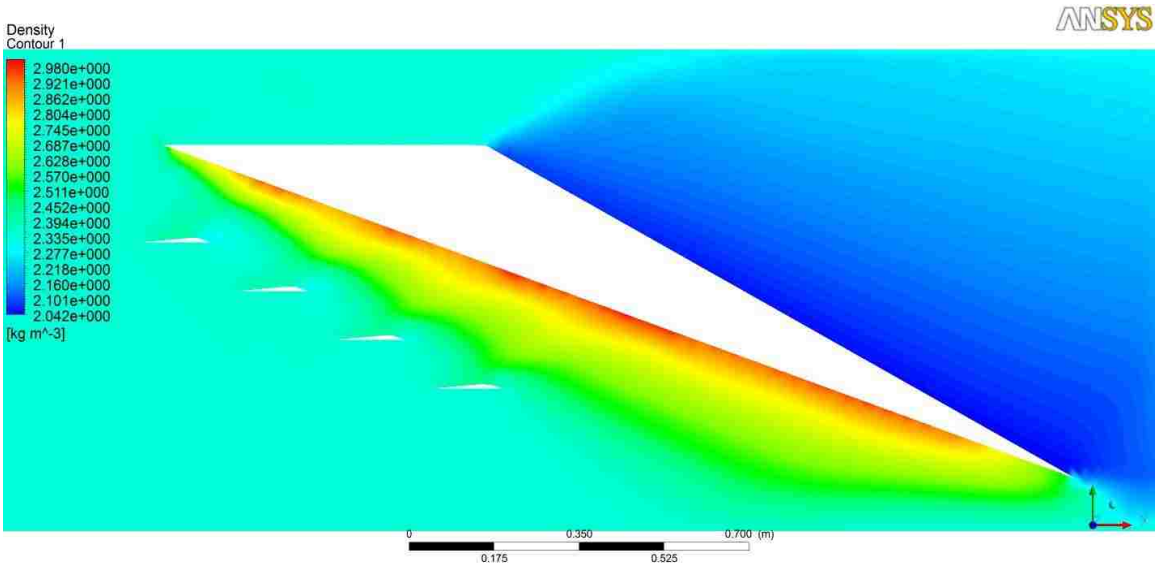

Figure 0.43

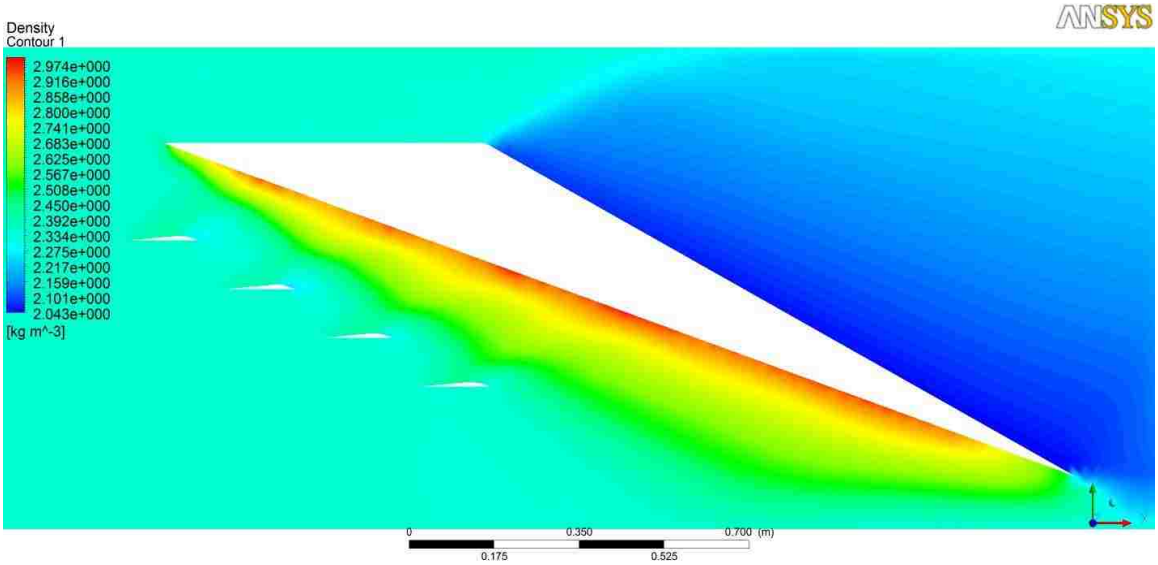

Figure 0.44

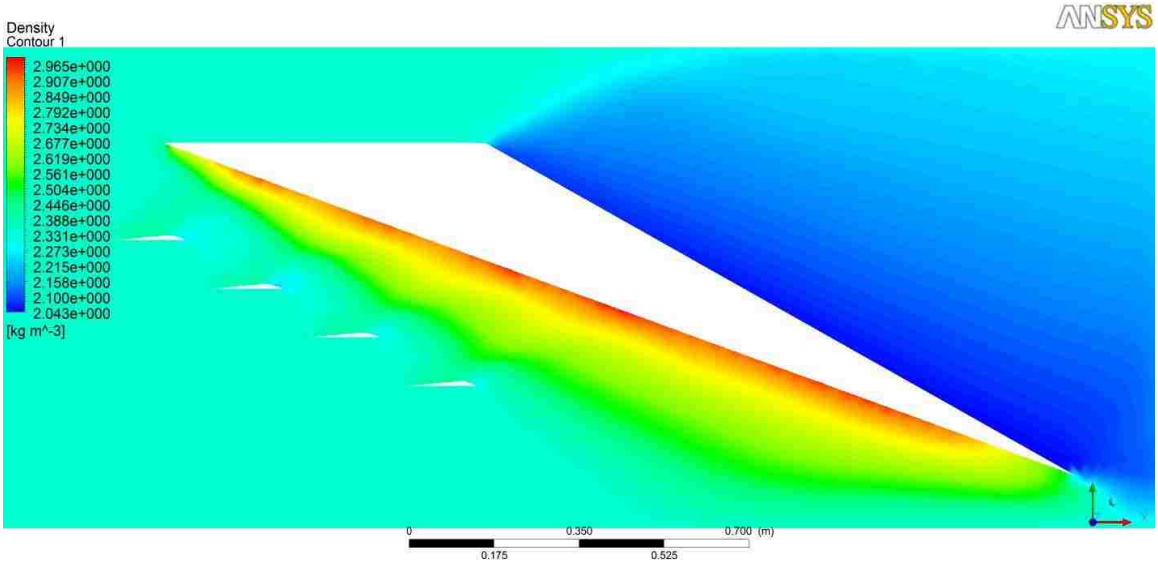

Figure 0.45

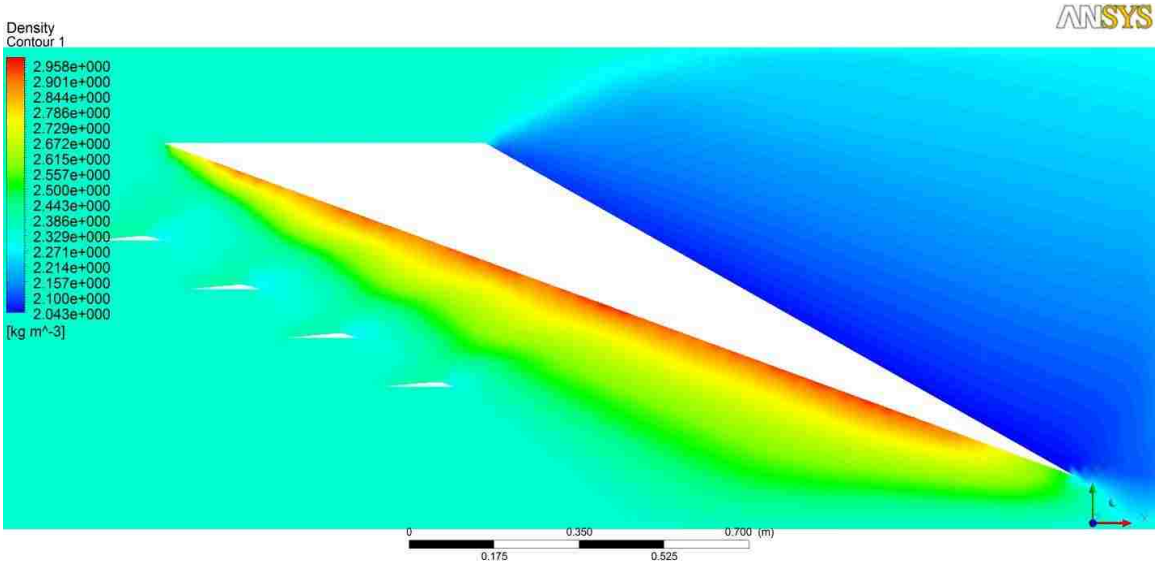

Figure 0.46

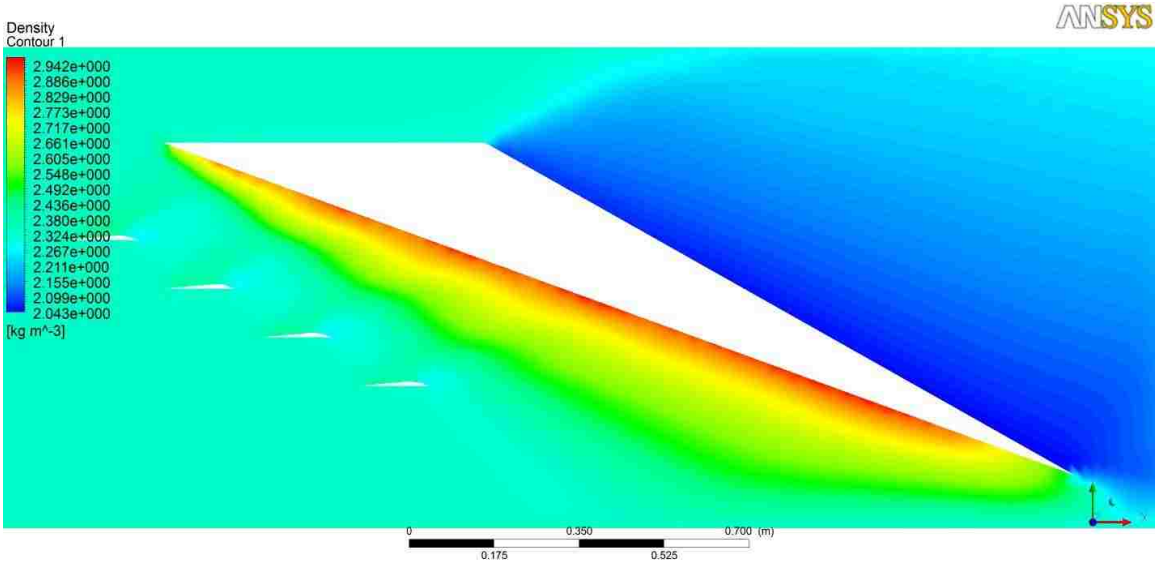

Figure 0.47

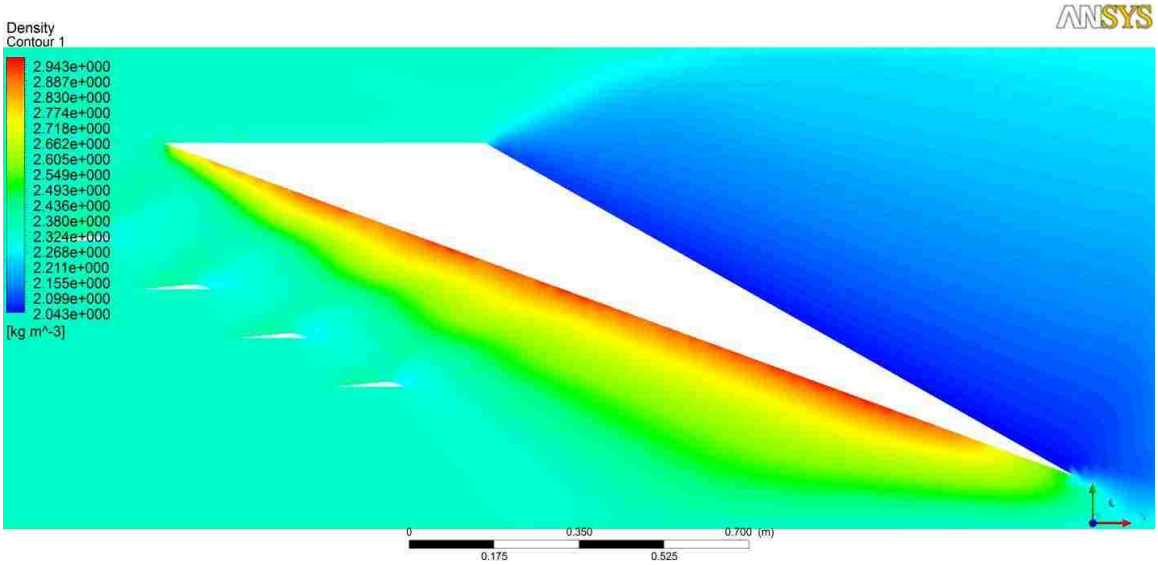

Figure 0.48

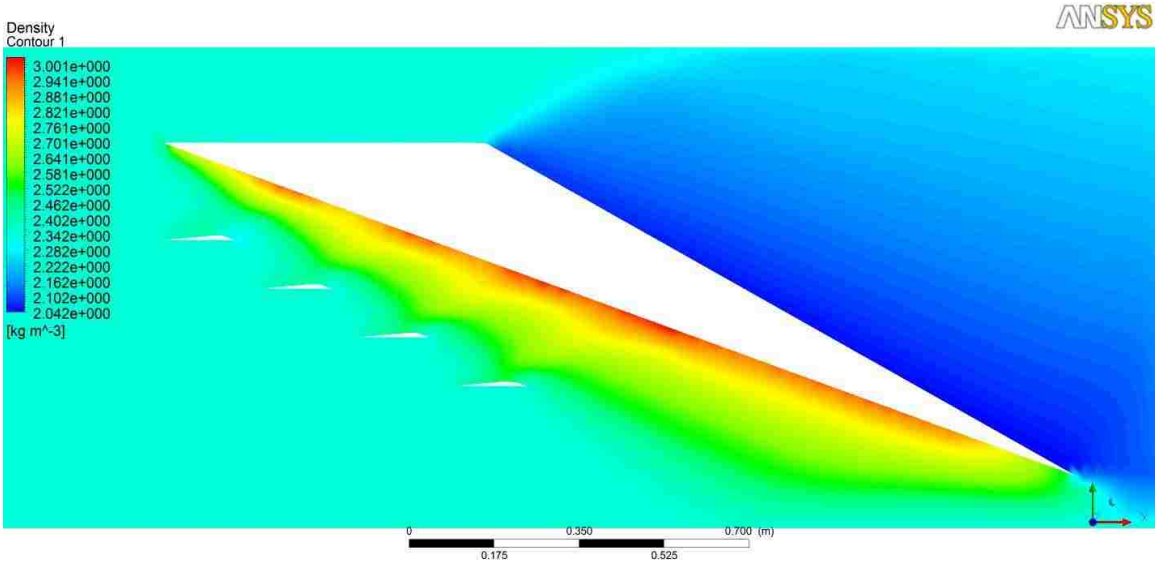

Figure 0.49

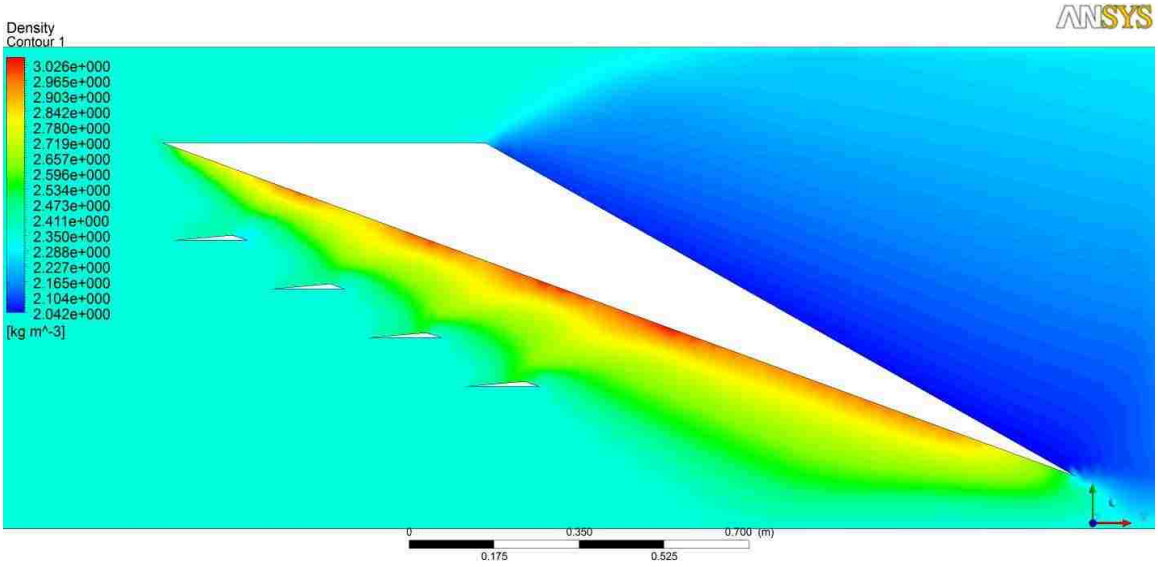
ANSYS
Density
Contour 1
3.026e+000
2.965e+000
2.903e+000
2.842e+000
2.780e+000
2.719e+000
2.657e+000
2.596e+000
2.534e+000
2.473e+000
2.411e+000
2.350e+000
2.288e+000
2.227e+000
2.165e+000
2.104e+000
2.042e+000
[kg m^-3]
0
0.350
0.700 (m)
0.175
0.525

Figure 0.50

MACH 2 5^{O} TIER 5 DENSITY CONTOUR FIGURES

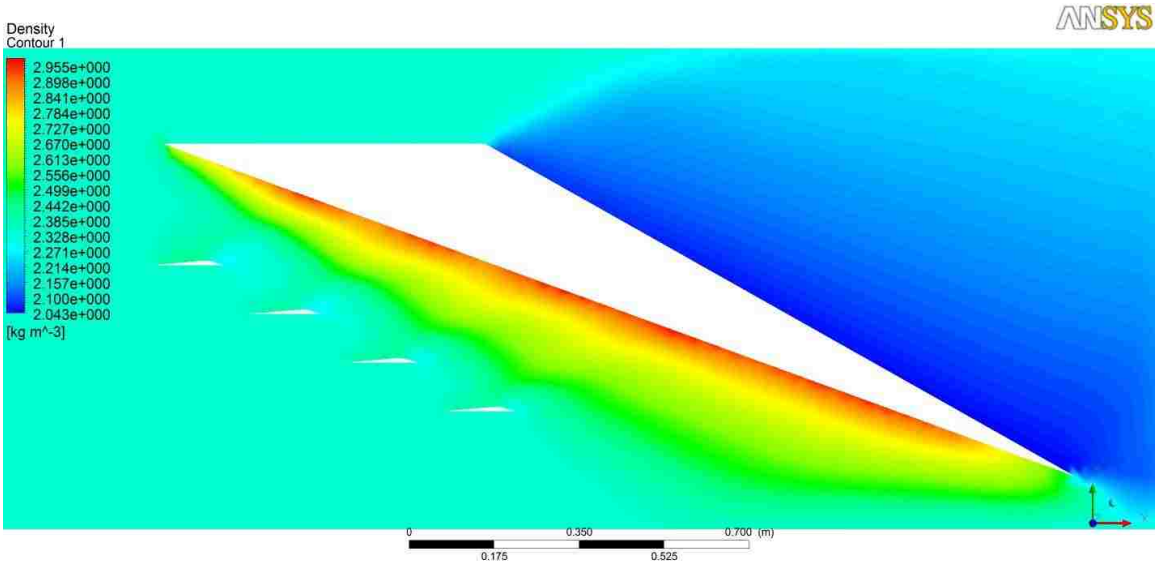

Figure 0.51

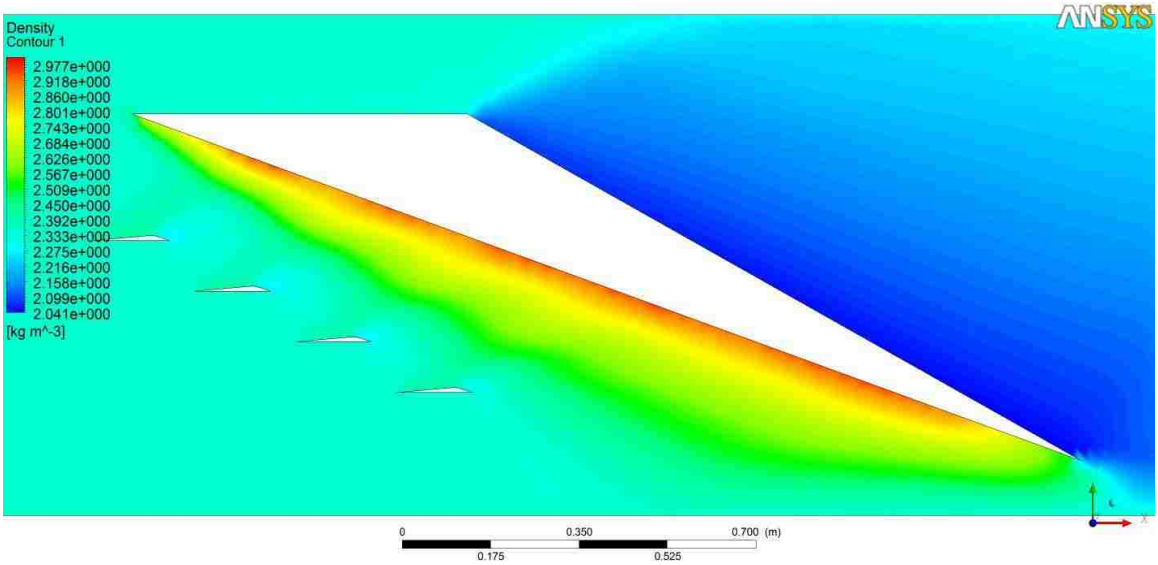

Figure 0.52

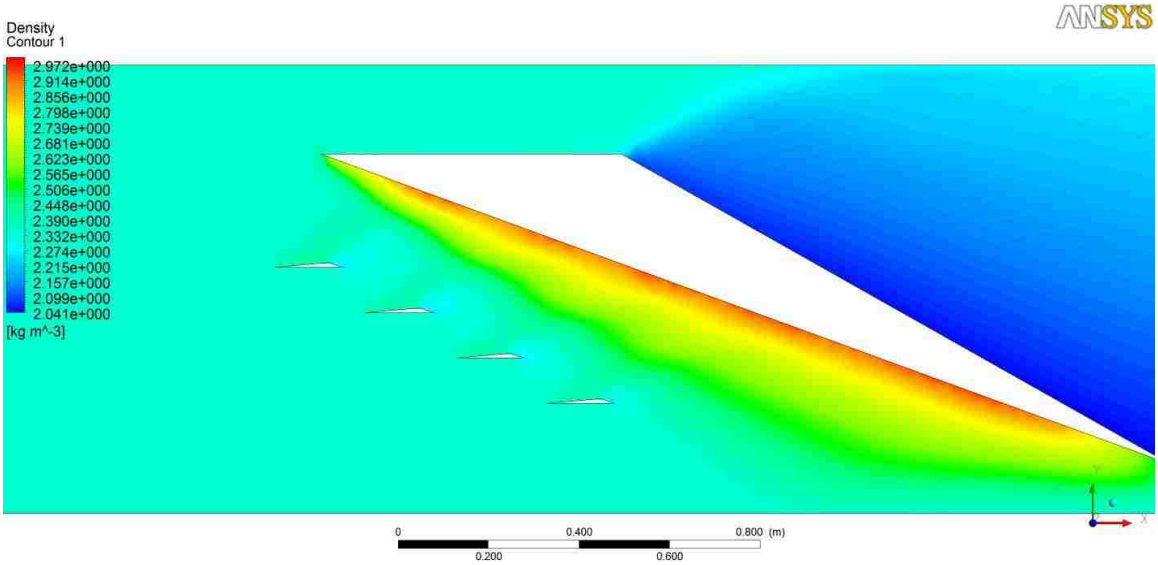

Figure 0.53

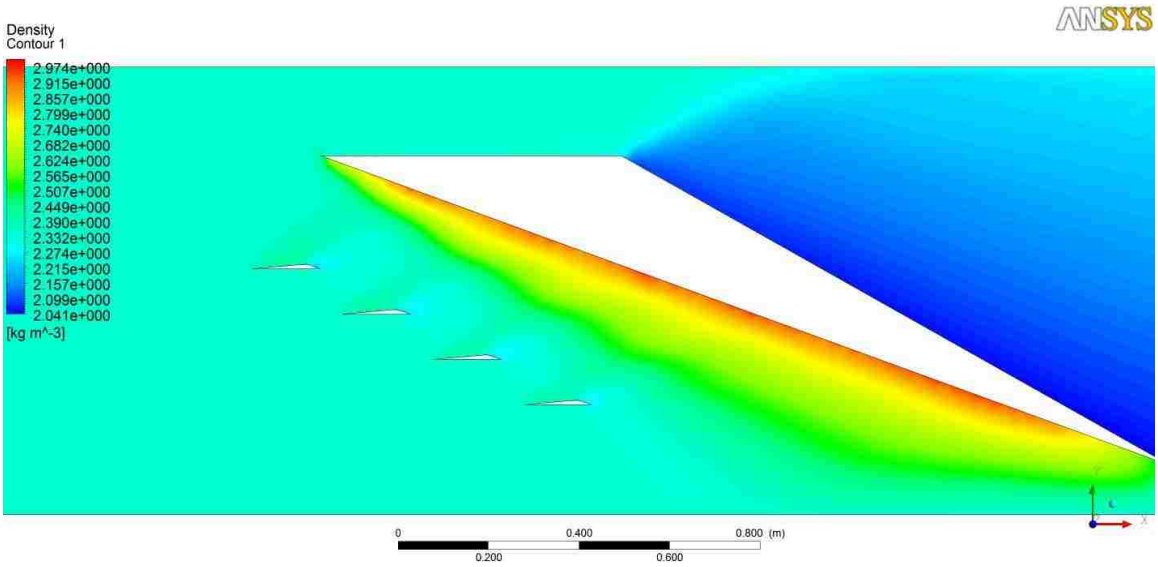

Figure 0.54

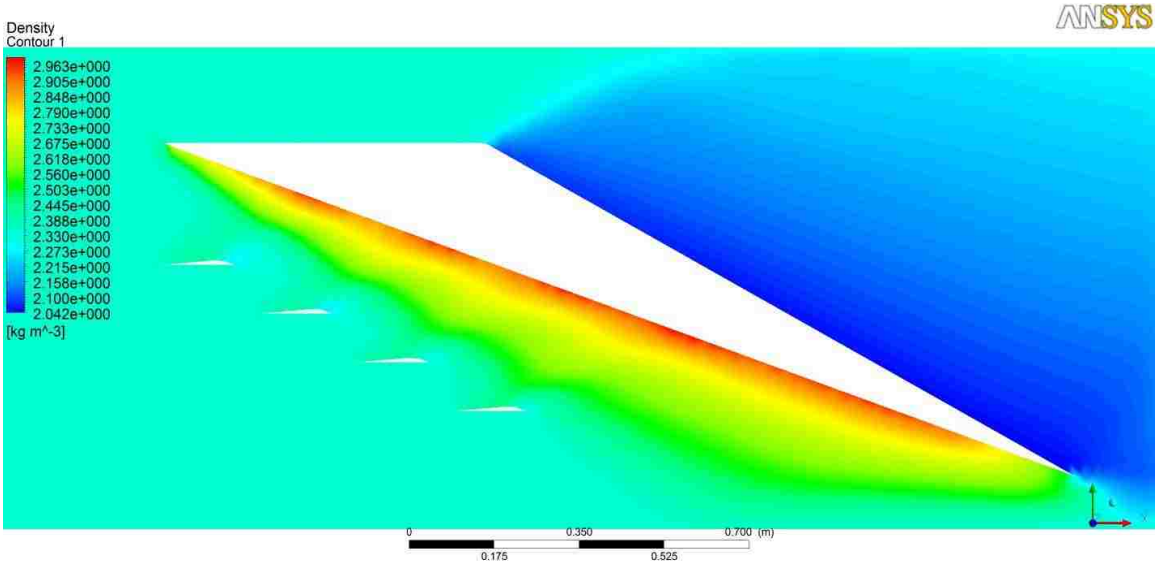
ANSYS
Density
Contour 1
2.963e+000
2.905e+000
2.848e+000
2.790e+000
2.733e+000
2.675e+000
2.618e+000
2.560e+000
2.503e+000
2.445e+000
2.388e+000
2.330e+000
2.273e+000
2.215e+000
2.158e+000
2.100e+000
2.042e+000
[kg m^-3]
0
0.350
0.700 (m)
0.175
0.525

Figure 0.55

MACH 2 10^{O} TIER 1 DENSITY CONTOUR FIGURES

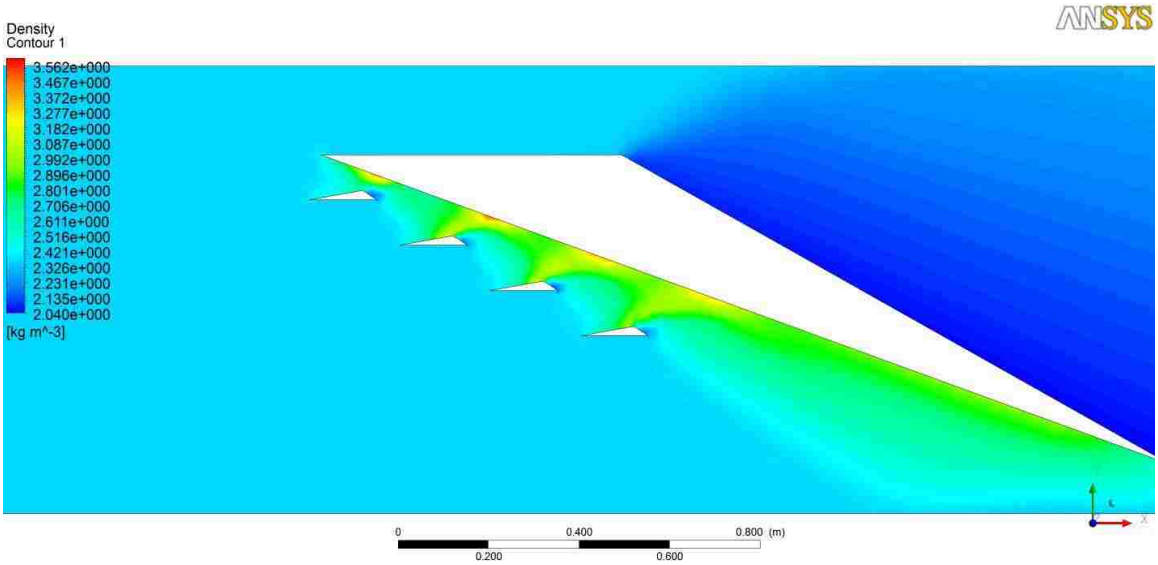

Figure 0.56

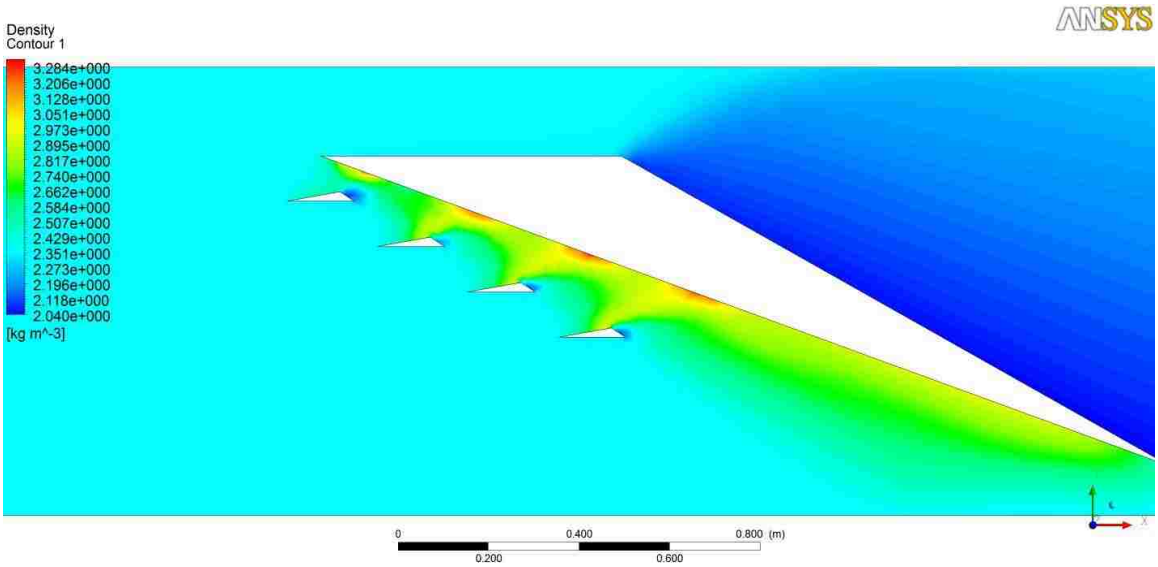

Figure 0.57

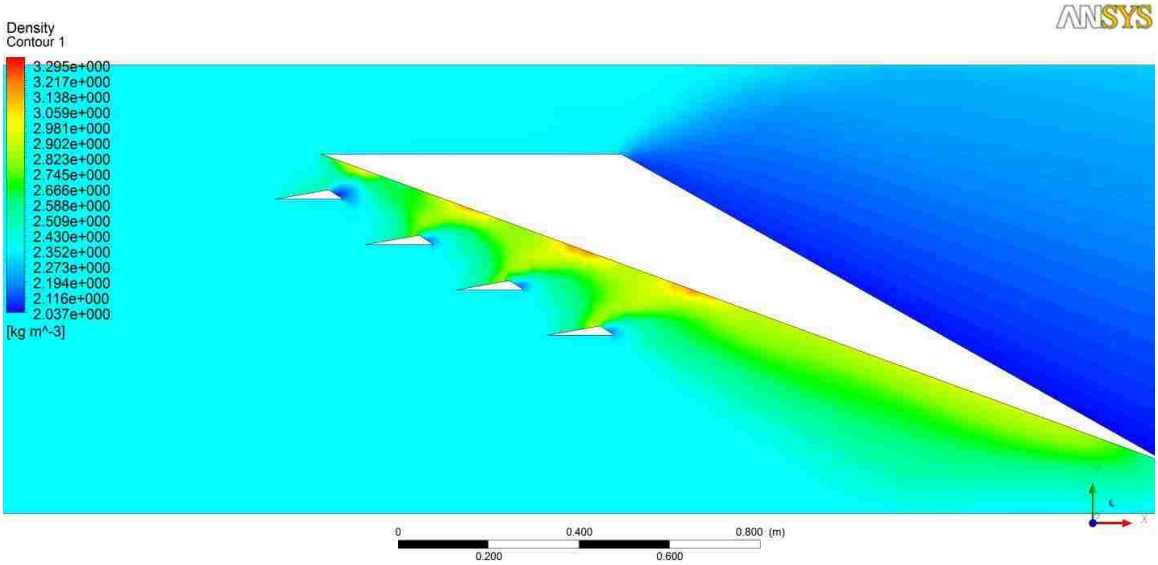

Figure 0.58

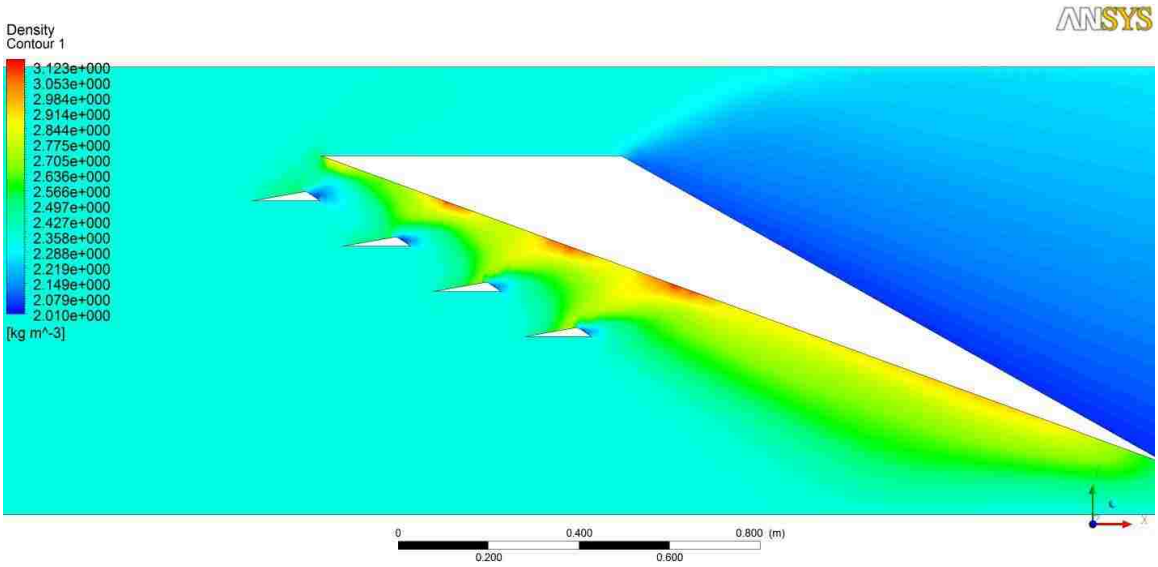

Figure 0.59

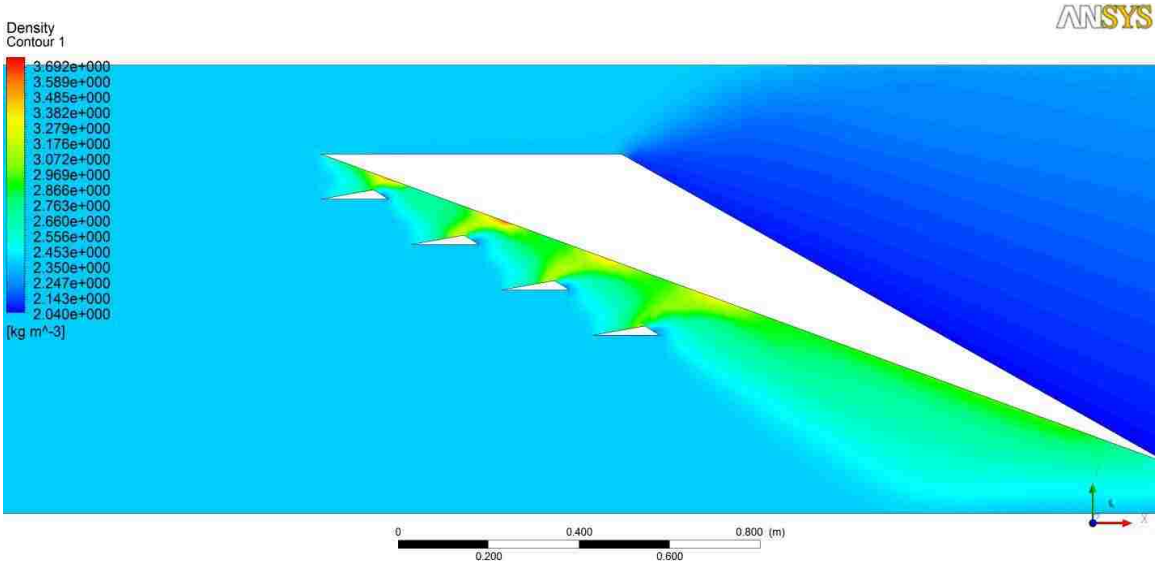

Figure 0.60

MACH 2 10^{O} TIER 2 DENSITY CONTOUR FIGURES

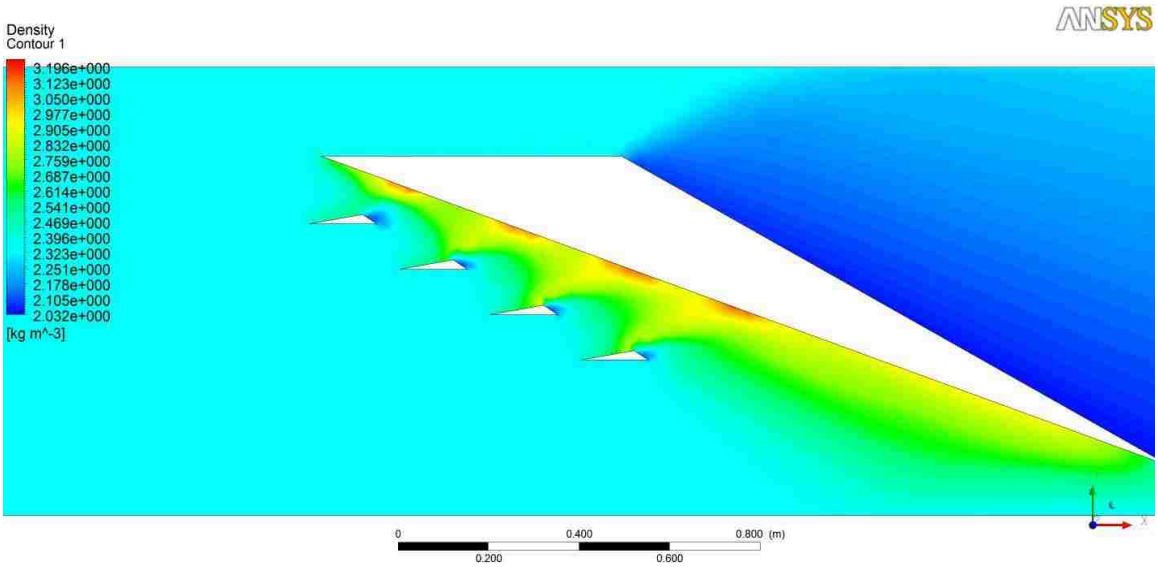

Figure 0.61

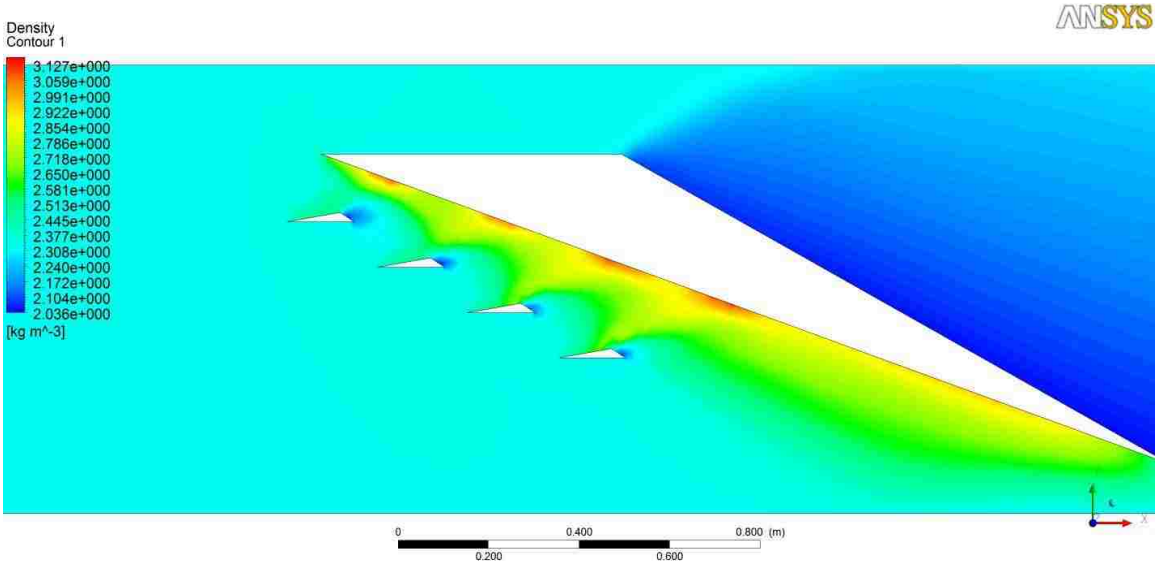

Figure 0.62

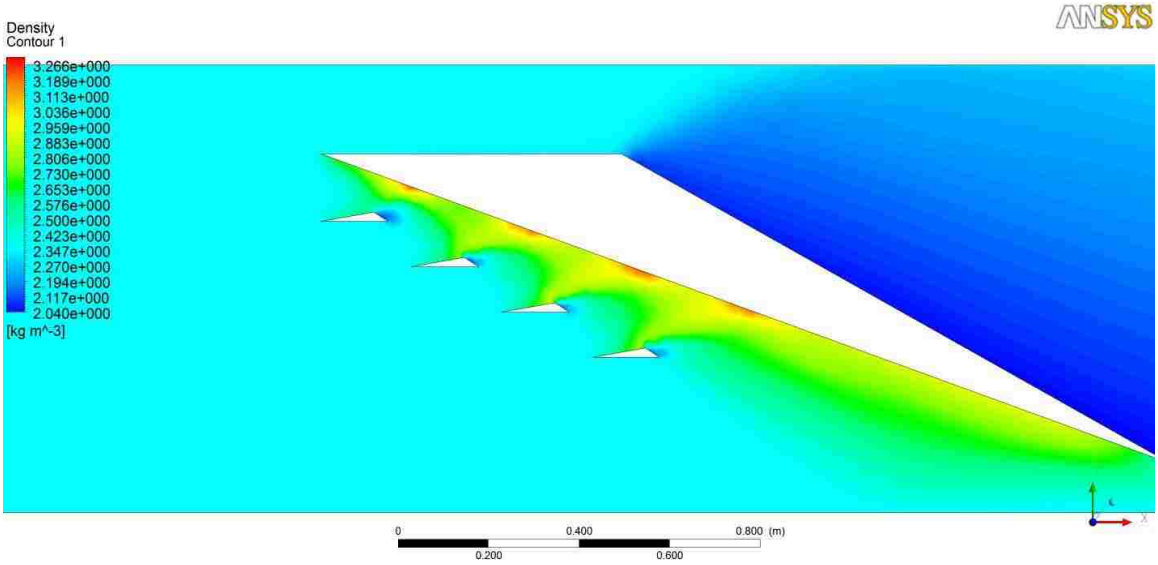

Figure 0.63

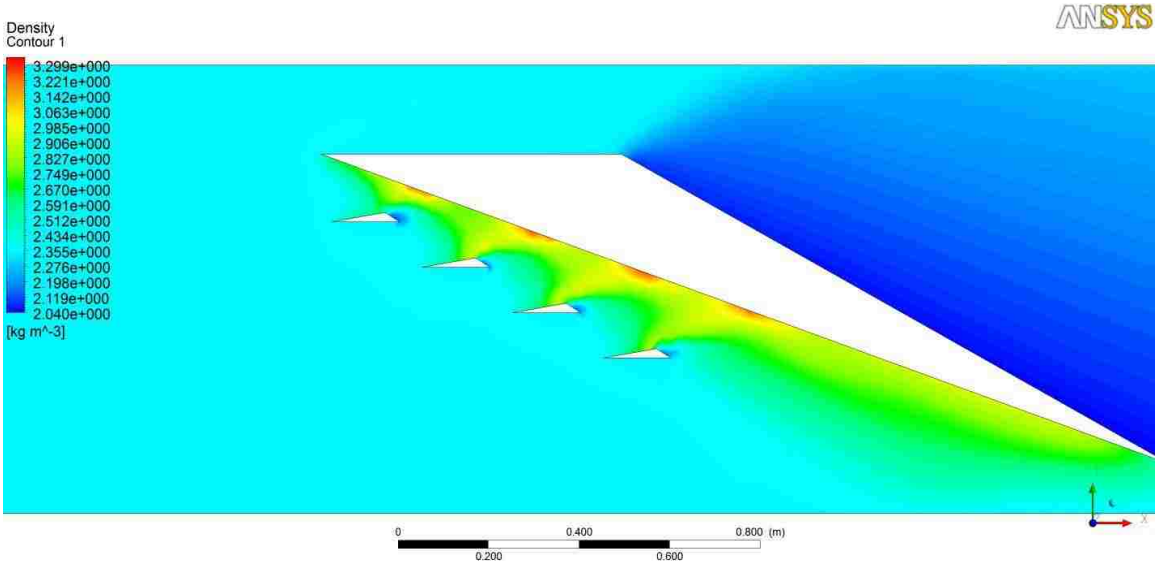

Figure 0.64

MACH 2 10^{O} TIER 3 DENSITY CONTOUR FIGURES

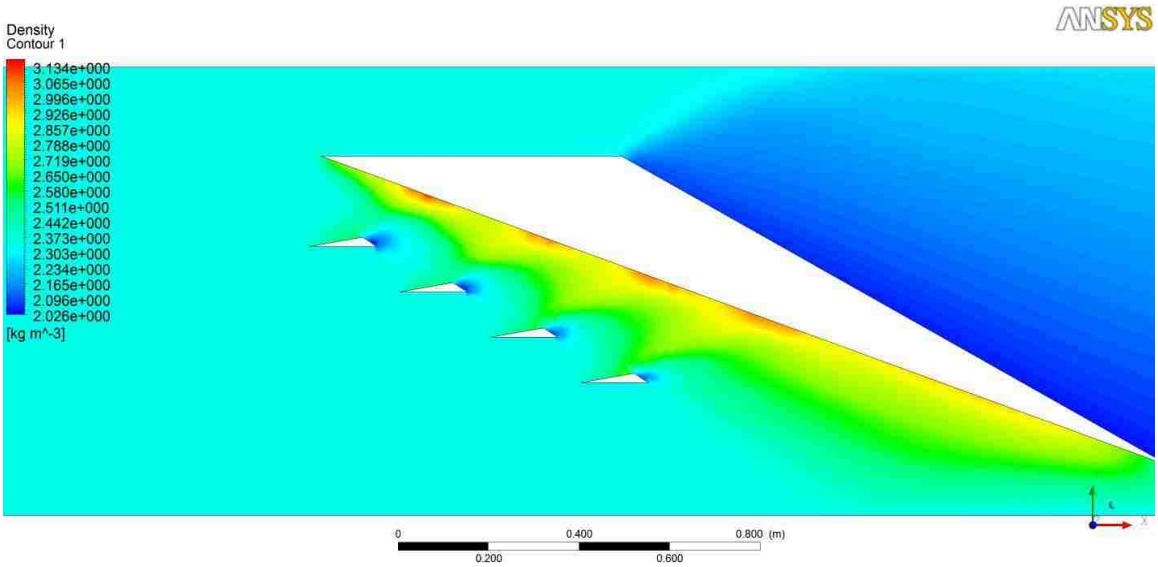

Figure 0.65

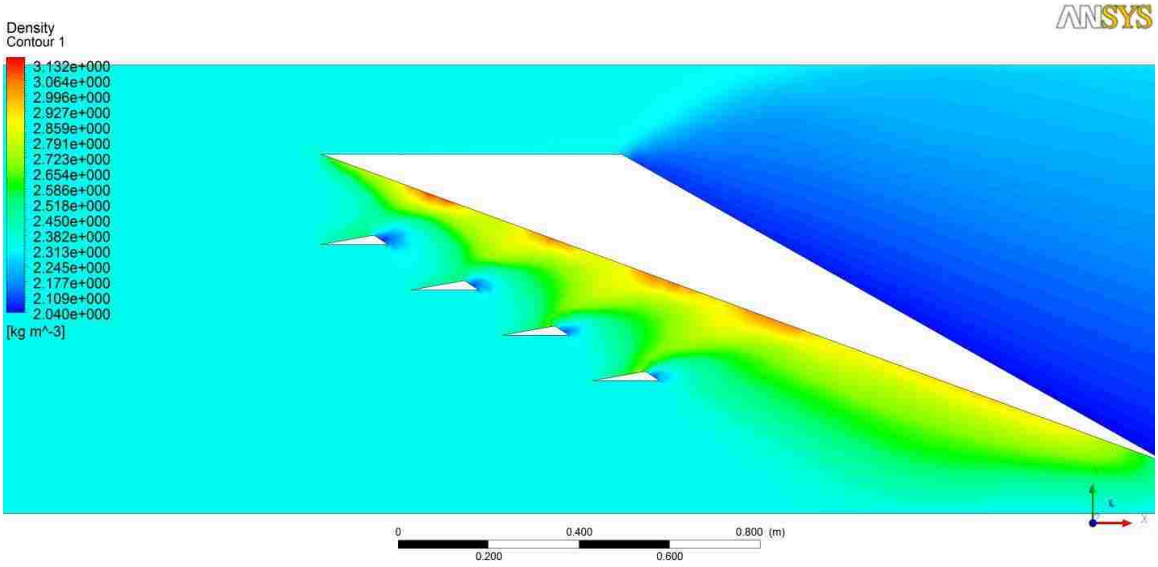

Figure 0.66

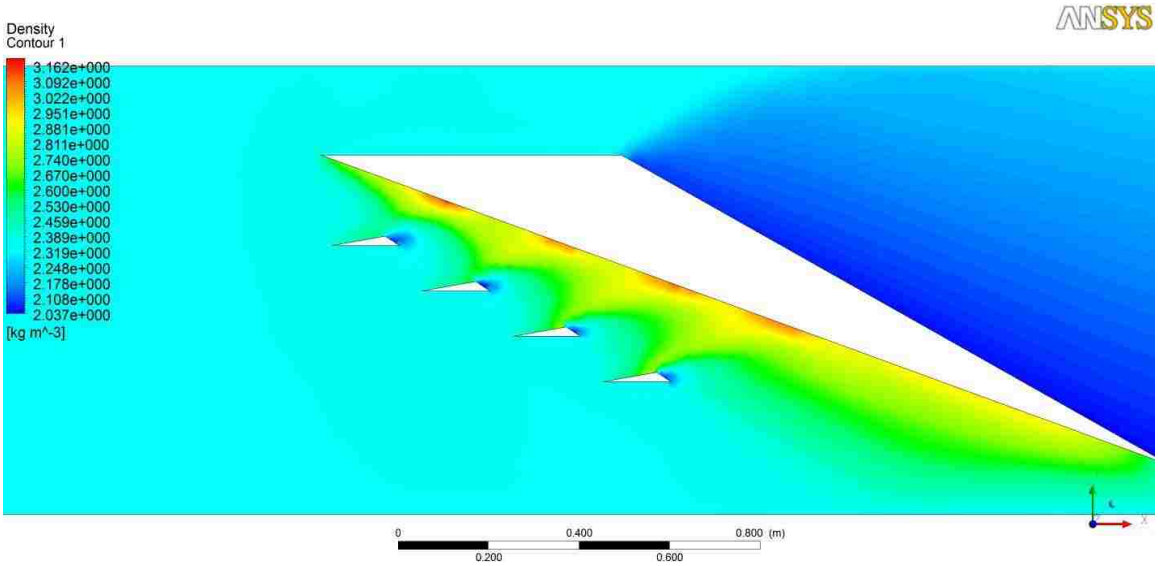

Figure 0.67

MACH 2 10^{O} TIER 4 DENSITY CONTOUR FIGURES

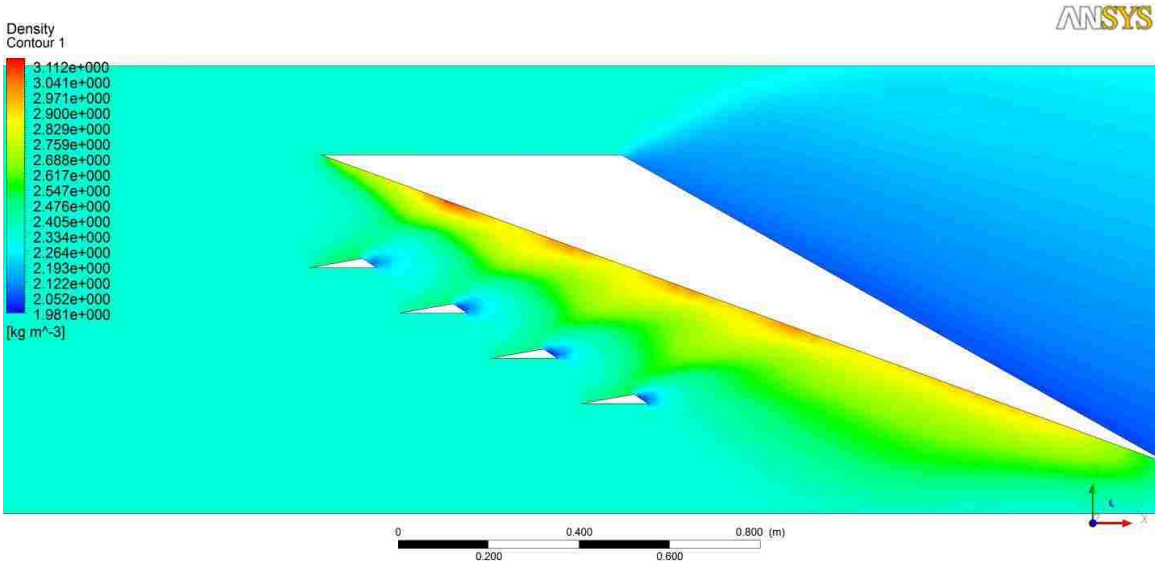

Figure 0.68

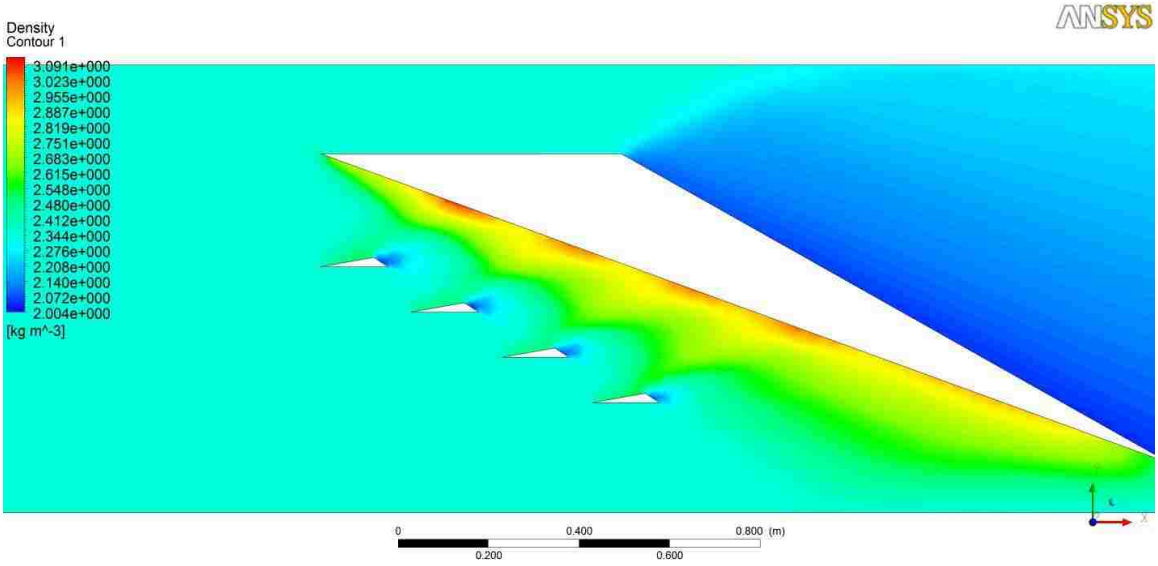

Figure 0.69

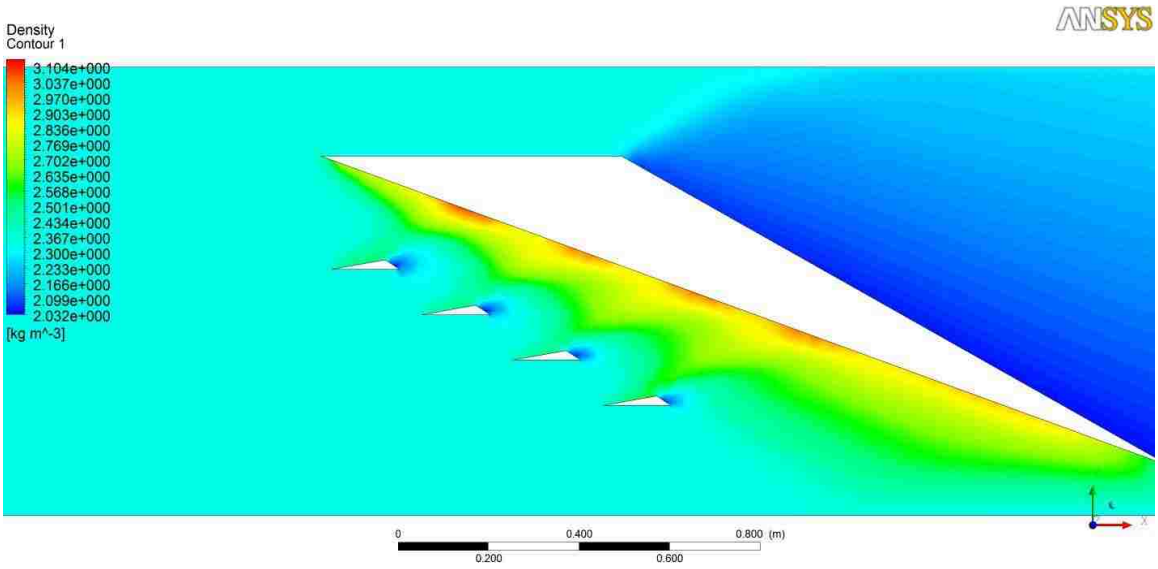

Figure 0.70

MACH 2 10^{O} TIER 5 DENSITY CONTOUR FIGURES

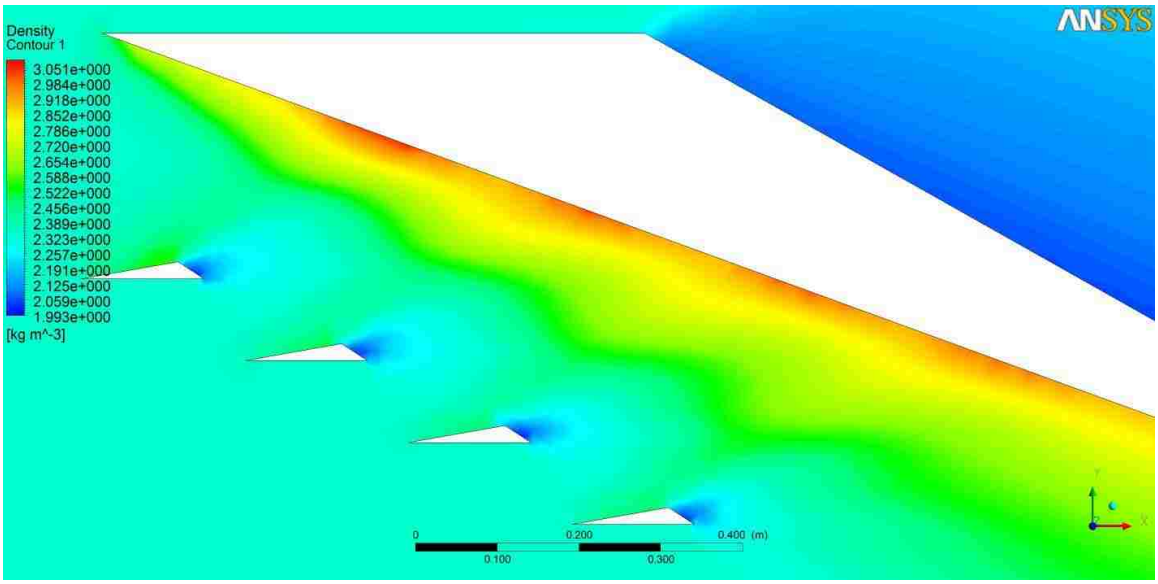

Figure 0.71

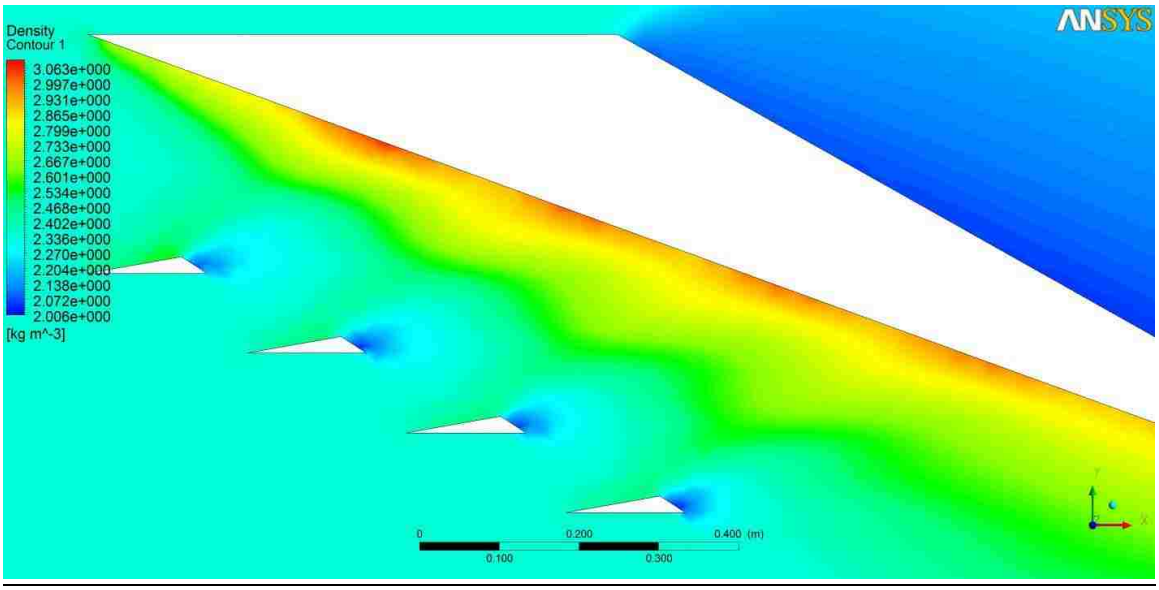

Figure 0.72

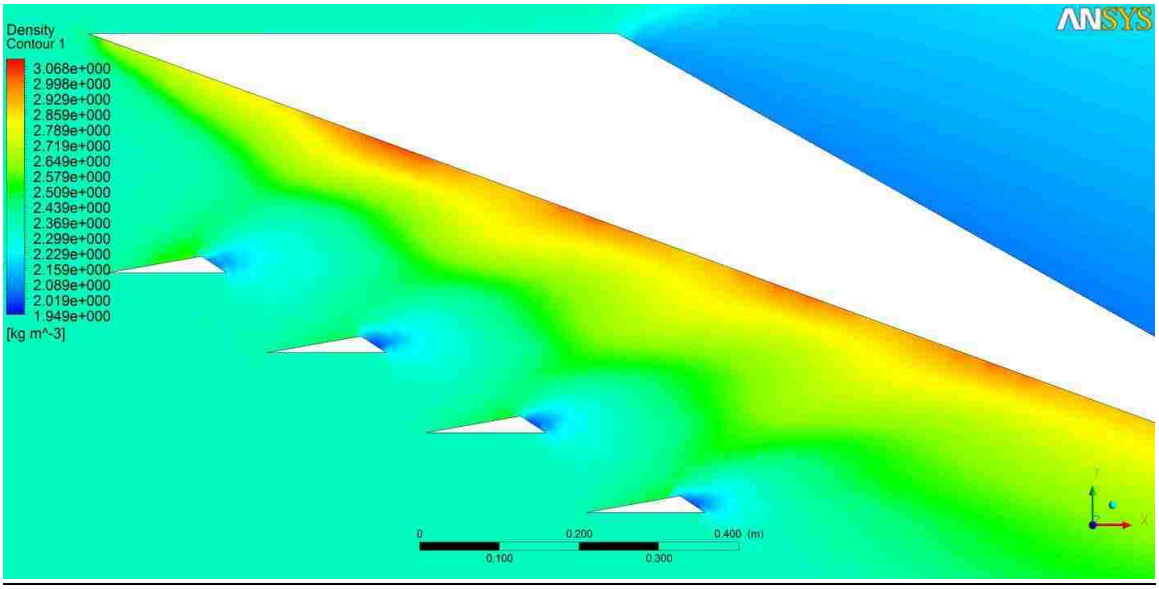

Figure 0.73

MACH 2 10^{O} TIER 6 DENSITY CONTOUR FIGURES

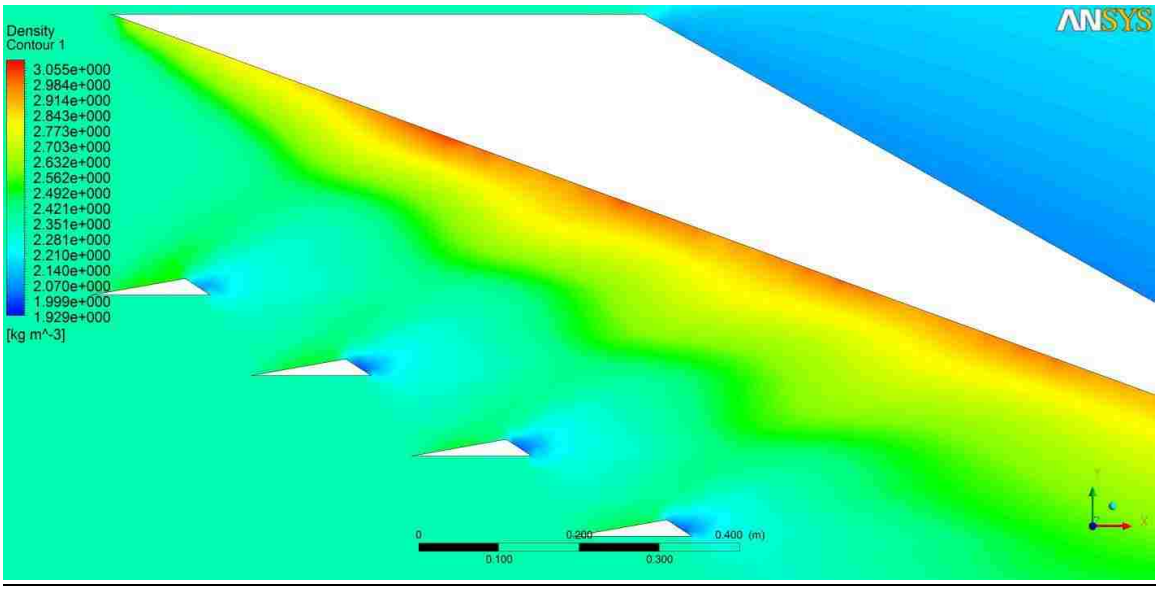

Figure 0.74

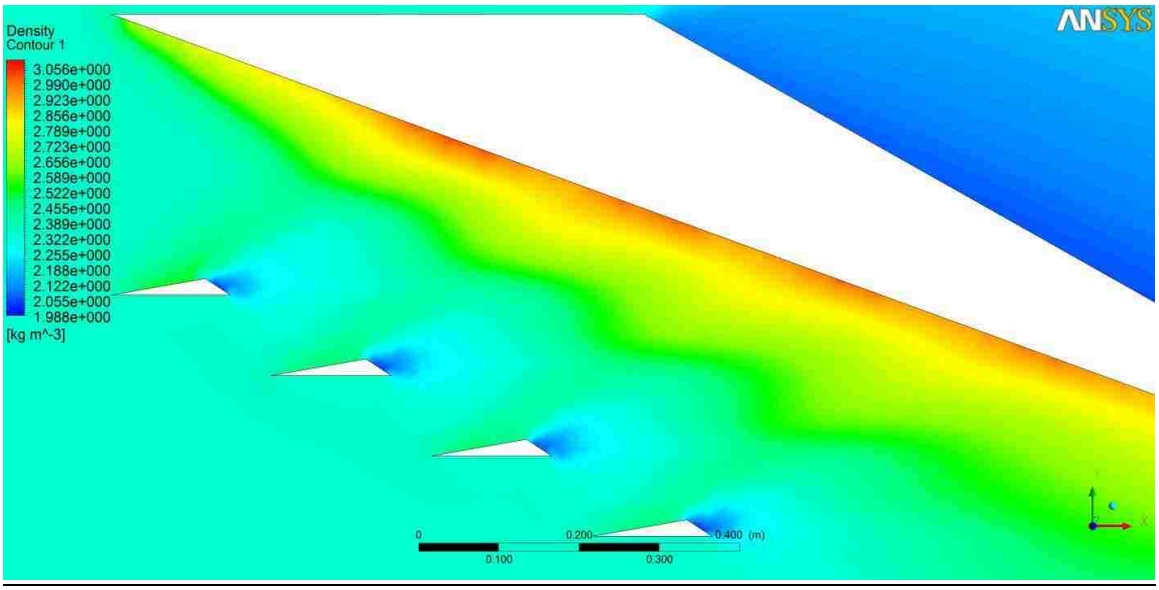

Figure 0.75

MACH 2 15^{O} TIER 1 DENSITY CONTOUR FIGURES

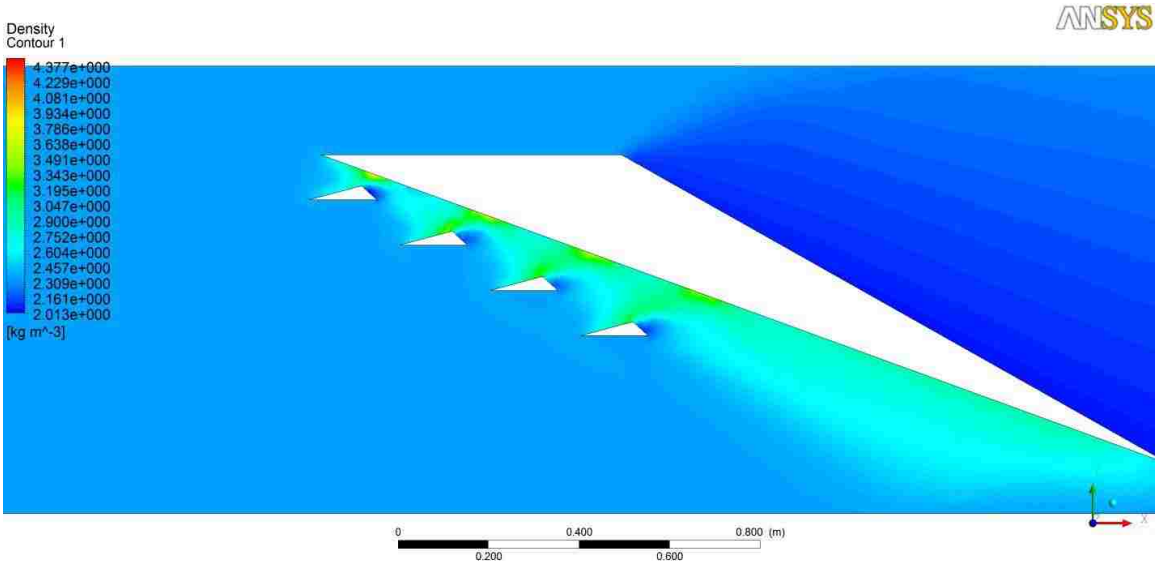

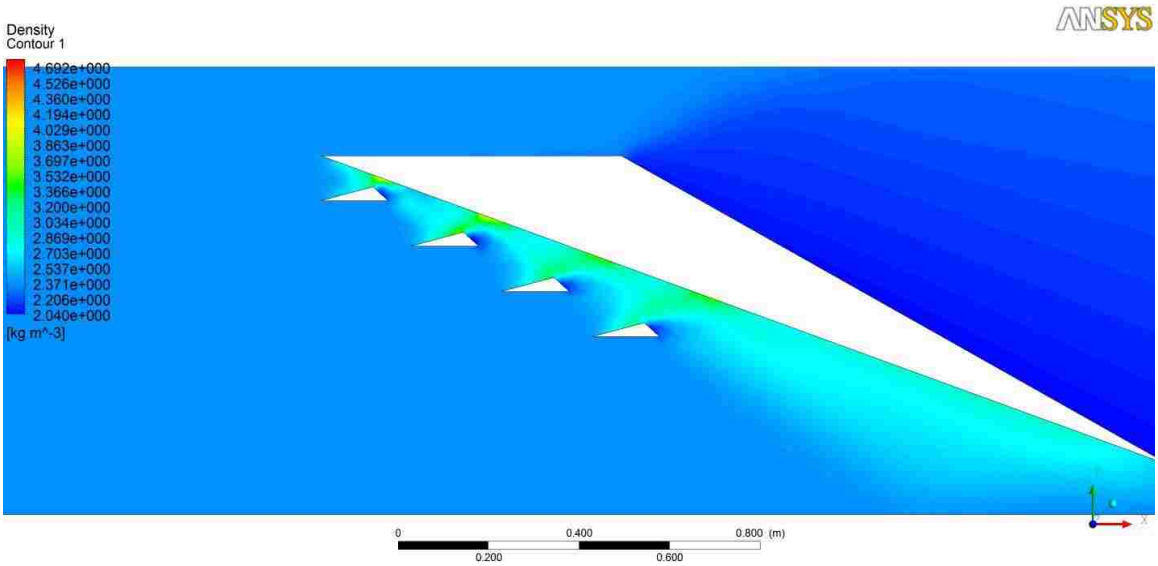

Figure 0.76

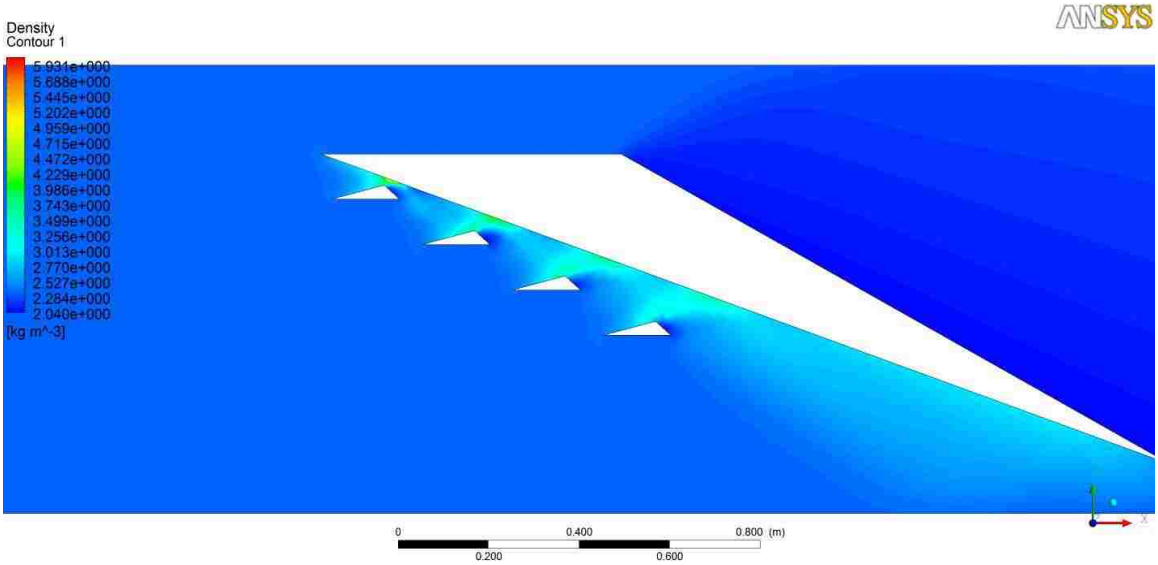

Figure 0.77

MACH 2 15^{O} TIER 2 DENSITY CONTOUR FIGURES

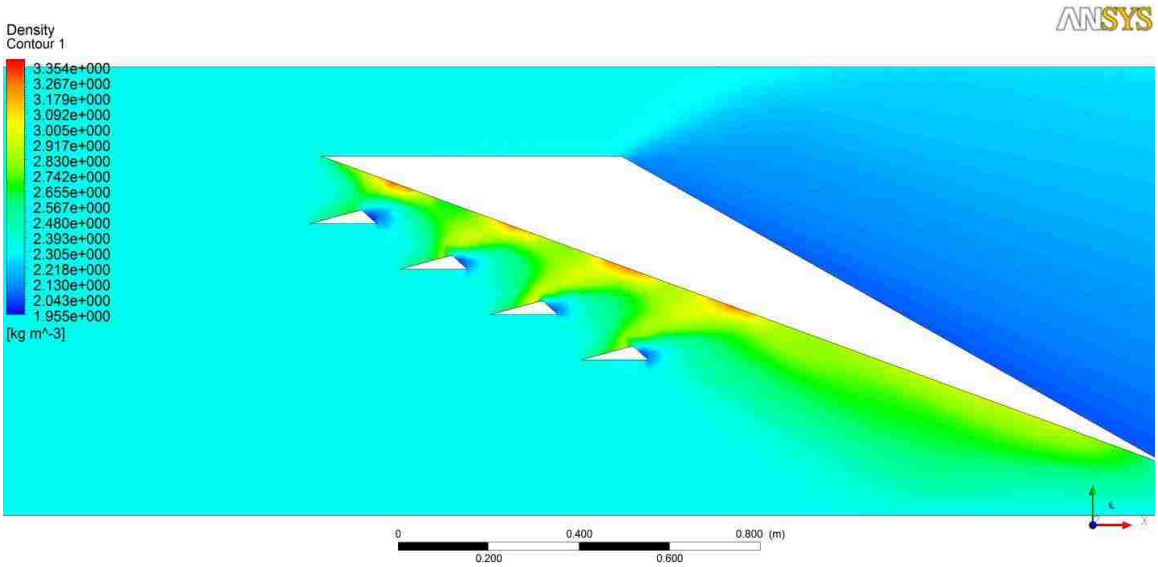

Figure 0.78

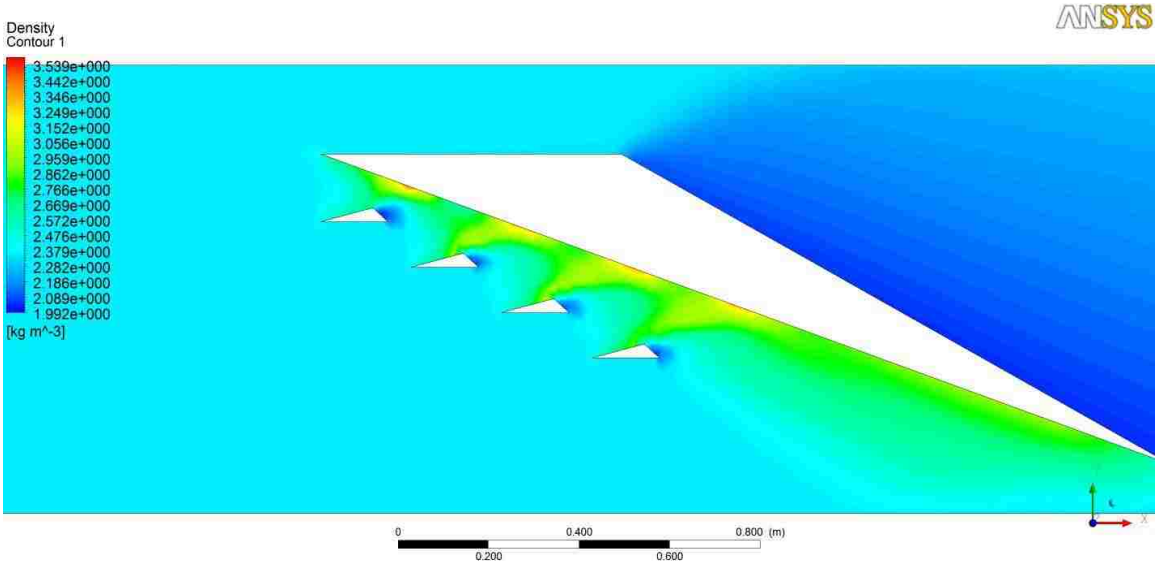

Figure 0.79

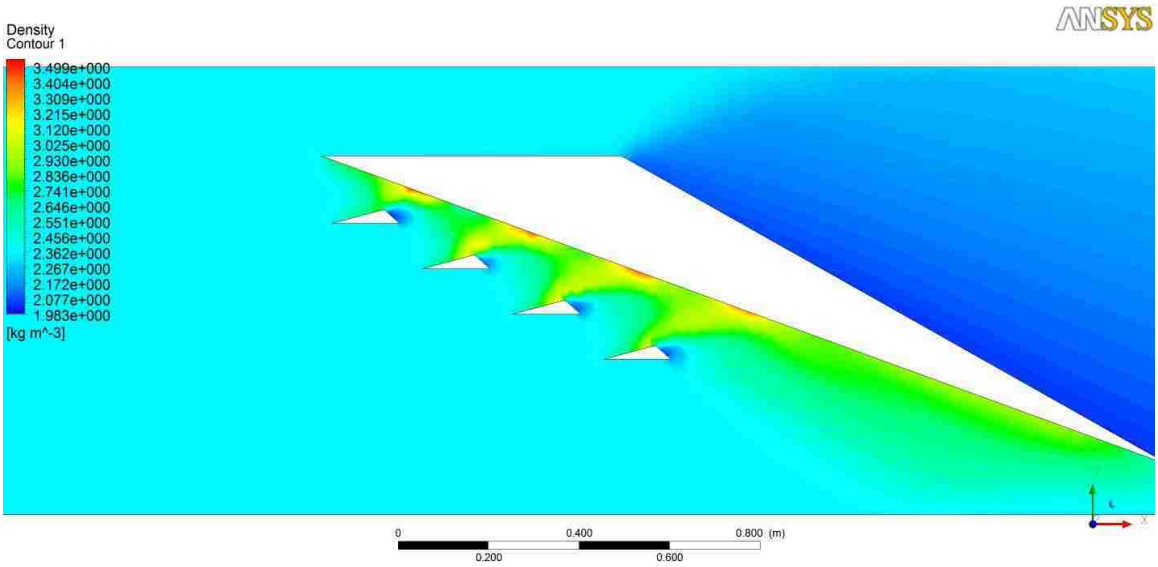

Figure 0.80

MACH 2 15^{O} TIER 3 DENSITY CONTOUR FIGURES

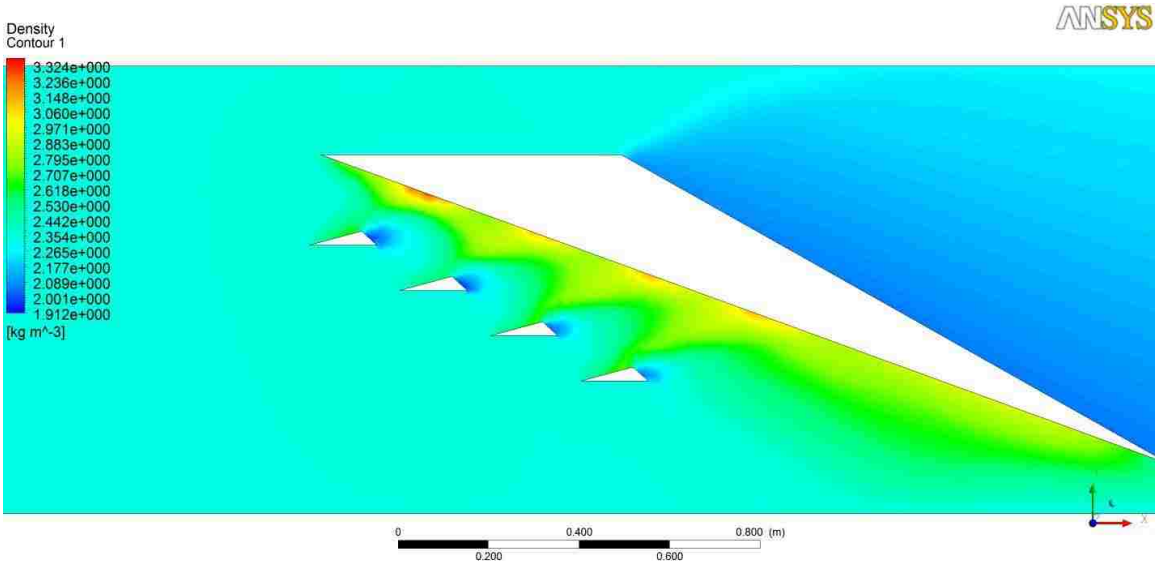

Figure 0.81

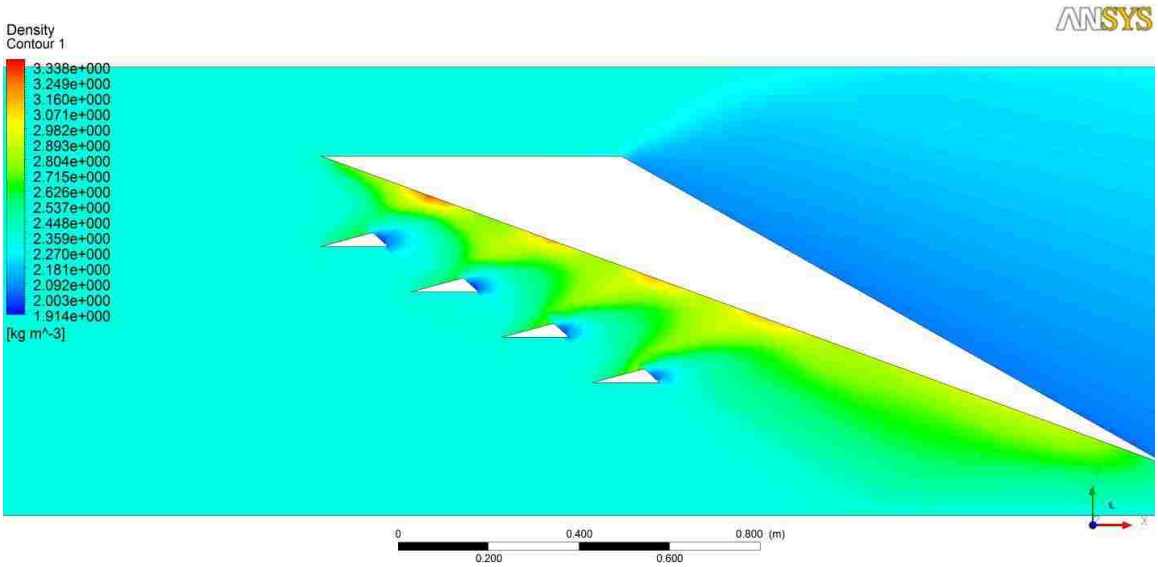

Figure 0.82

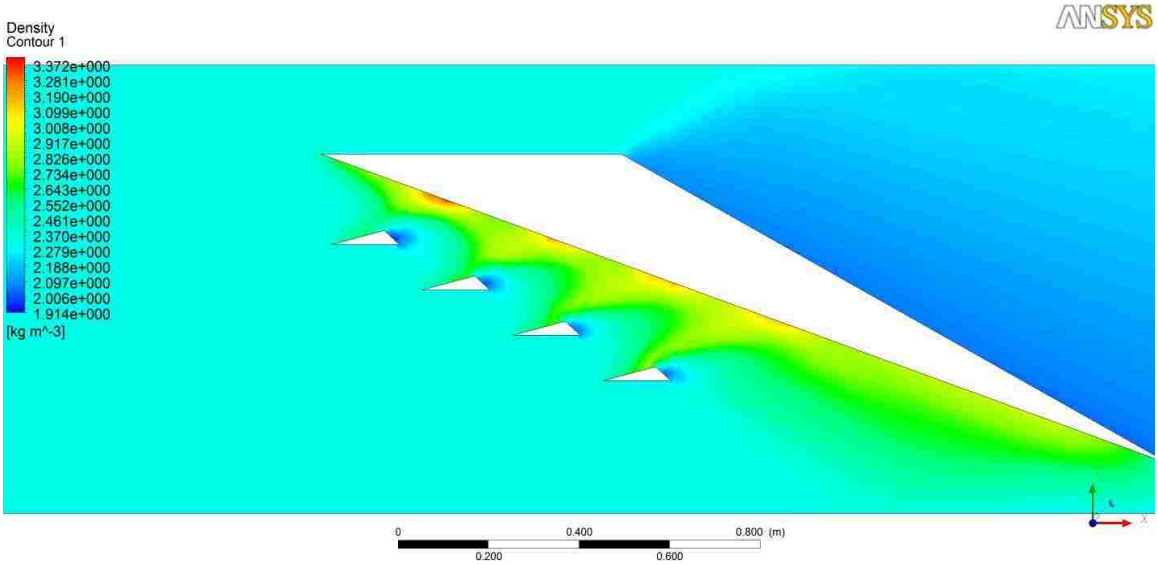

Figure 0.83

MACH 2 15^{O} TIER 4 DENSITY CONTOUR FIGURES

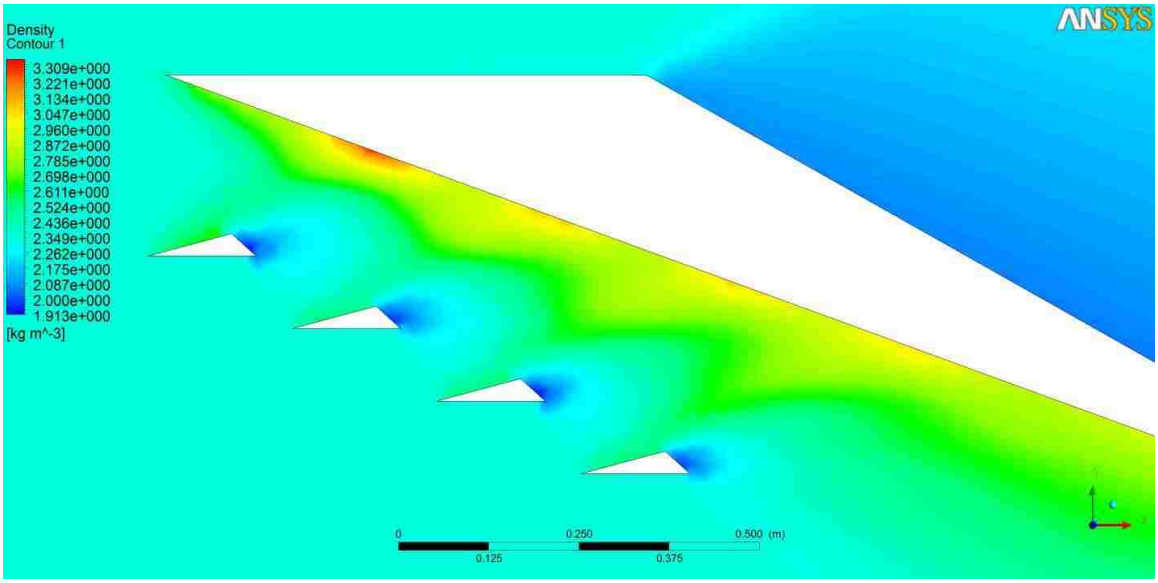

Figure 0.84

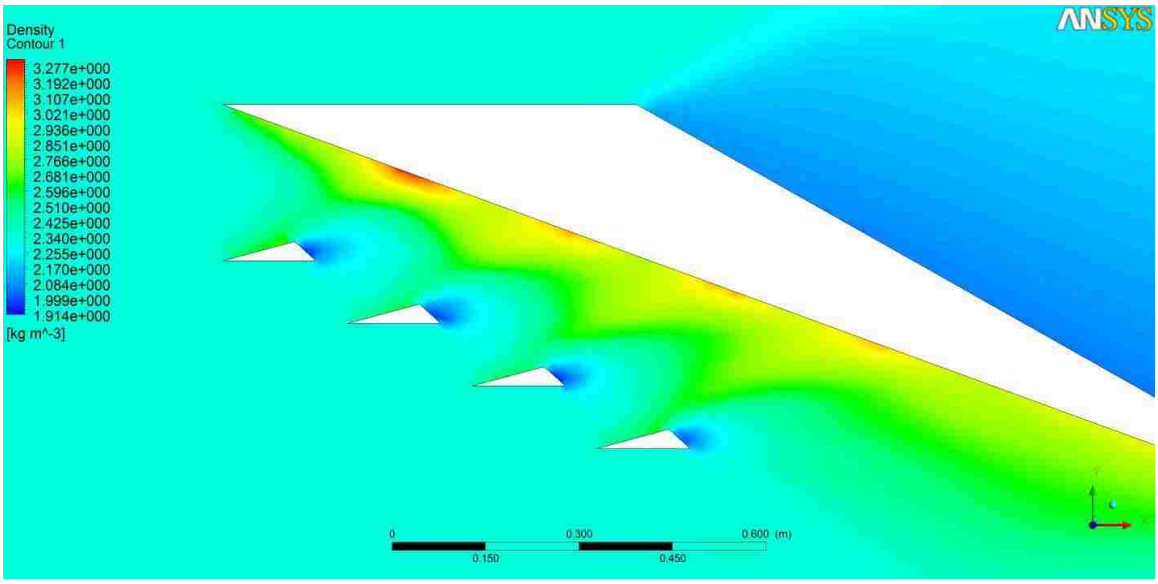

Figure 0.85

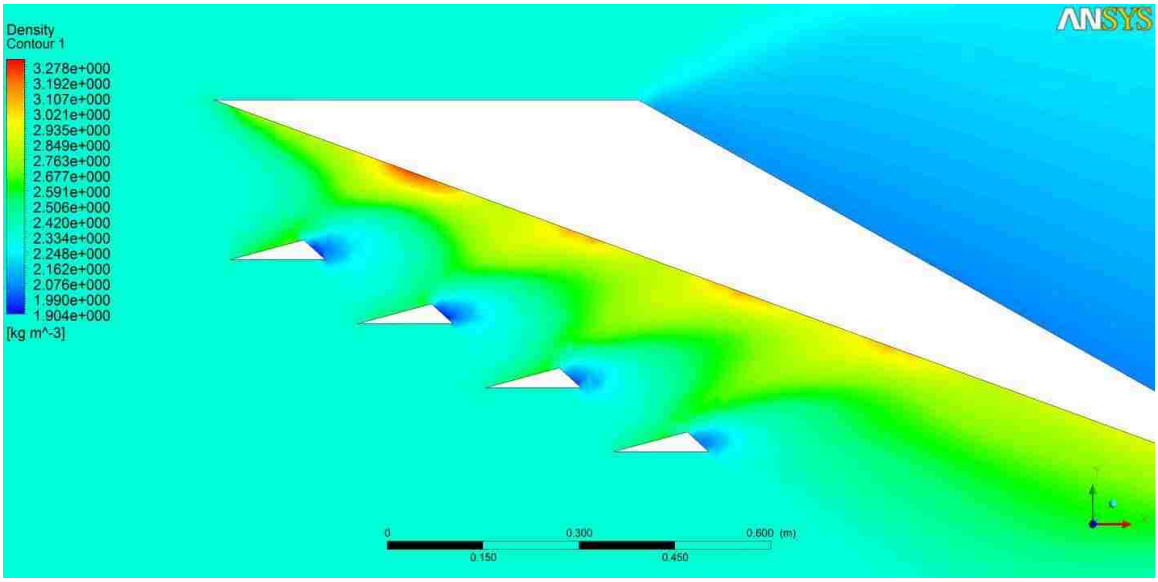

Figure 0.86

MACH 2 15^{O} TIER 5 DENSITY CONTOUR FIGURES

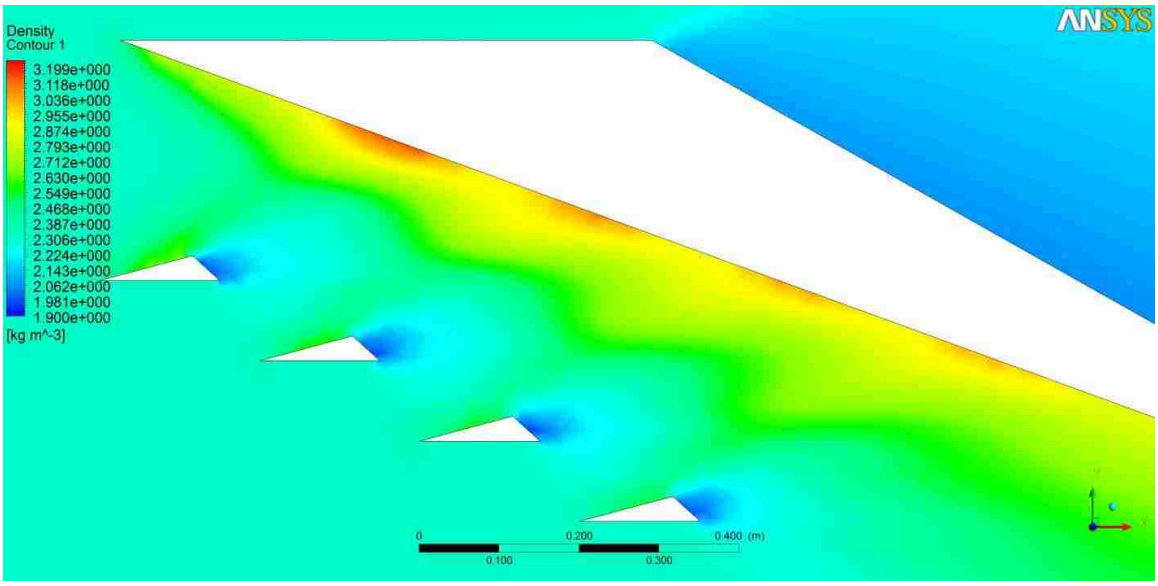

Figure 0.87

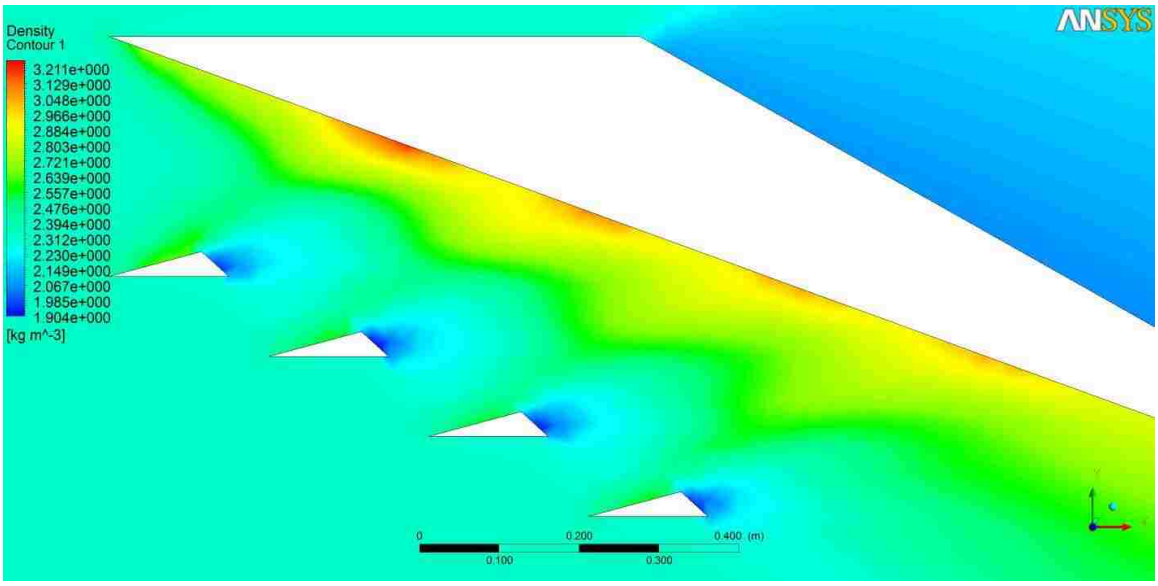

Figure 0.88

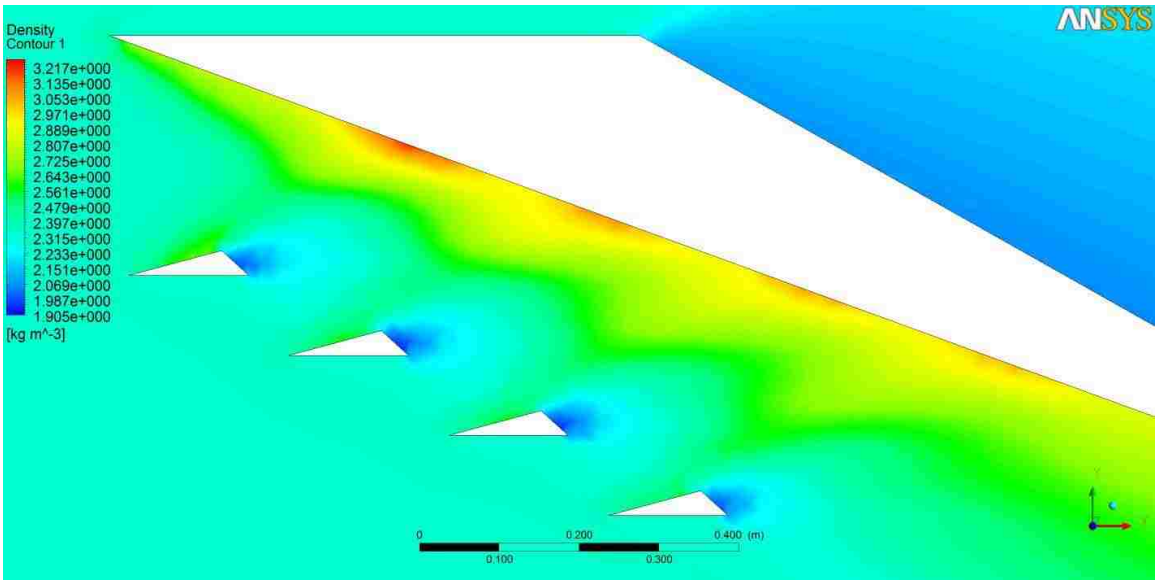

Figure 0.89

MACH 2 15^{O} TIER 6 DENSITY CONTOUR FIGURES

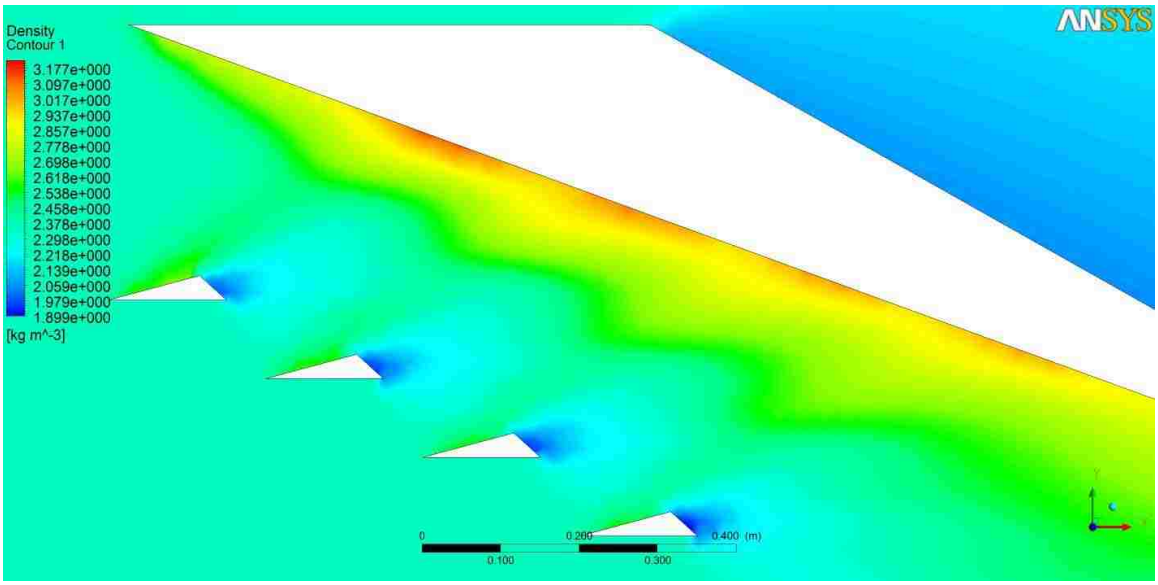

Figure 0.90

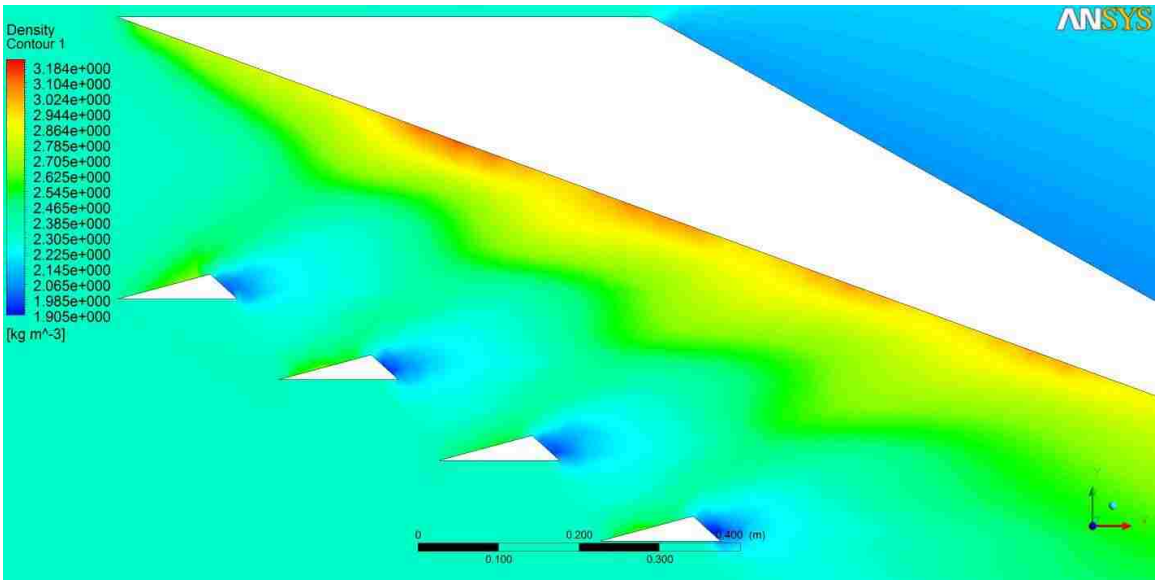

Figure 0.91

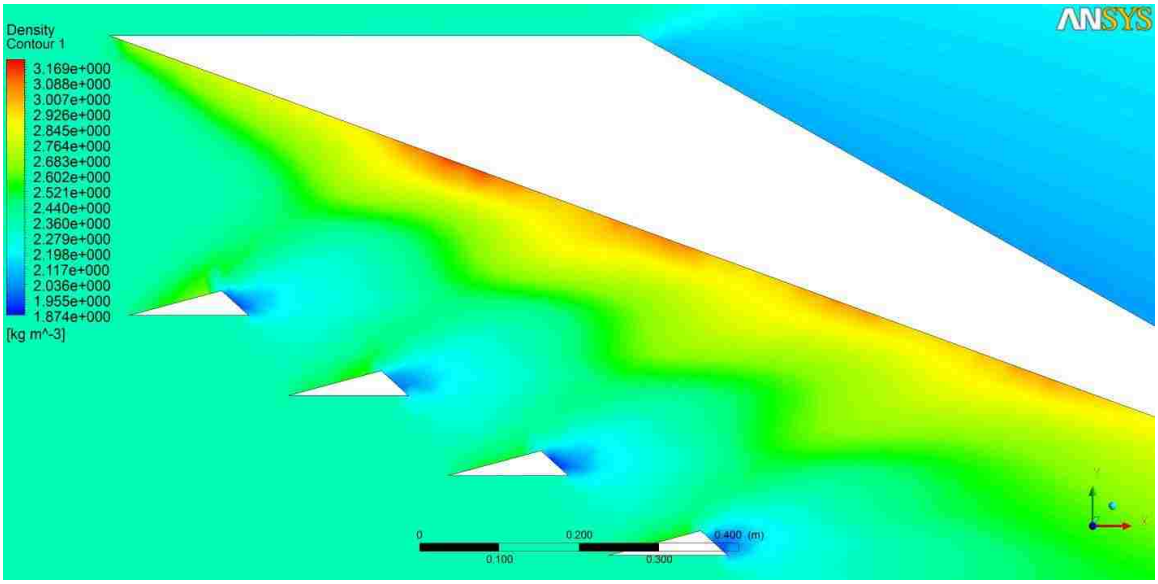

Figure 0.92

MACH 2 20^{O} TIER 1 DENSITY CONTOUR FIGURES

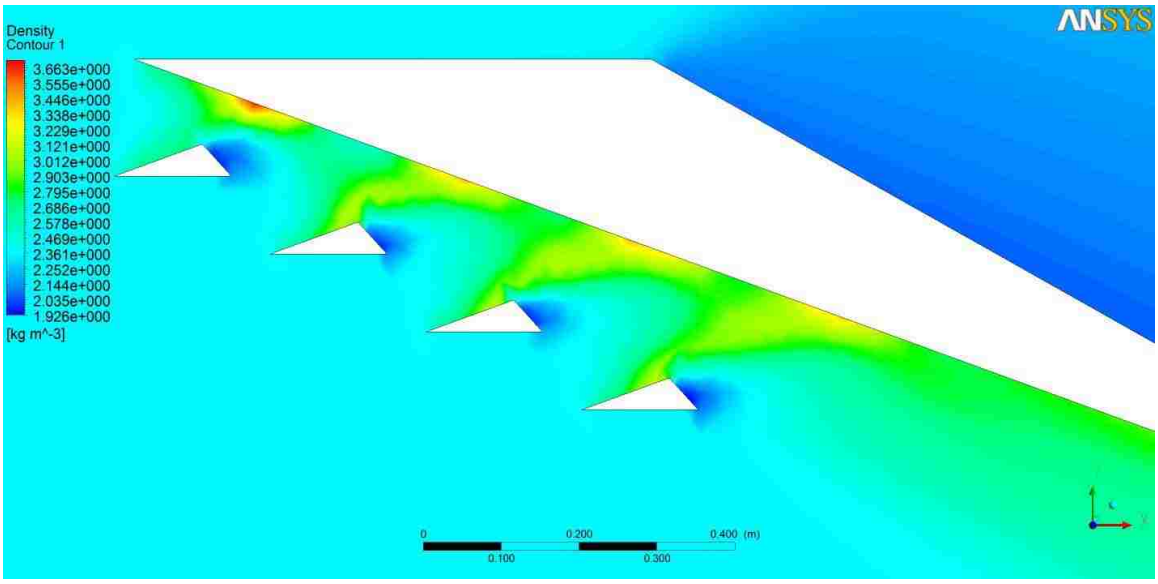

Figure 0.93

MACH 2 20^{O} TIER 2 DENSITY CONTOUR FIGURES

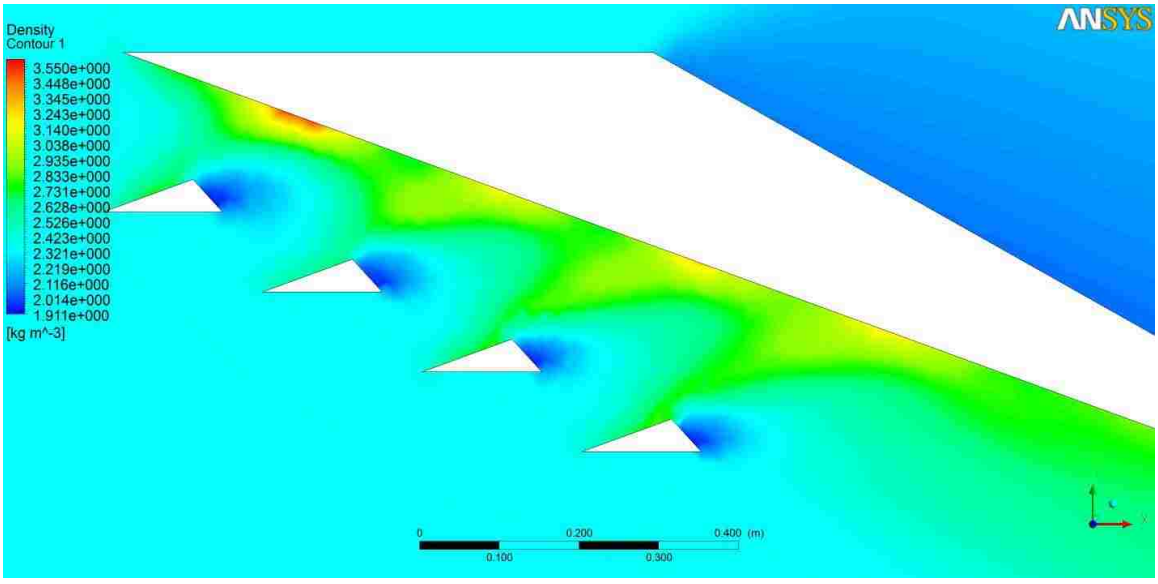

Figure 0.94

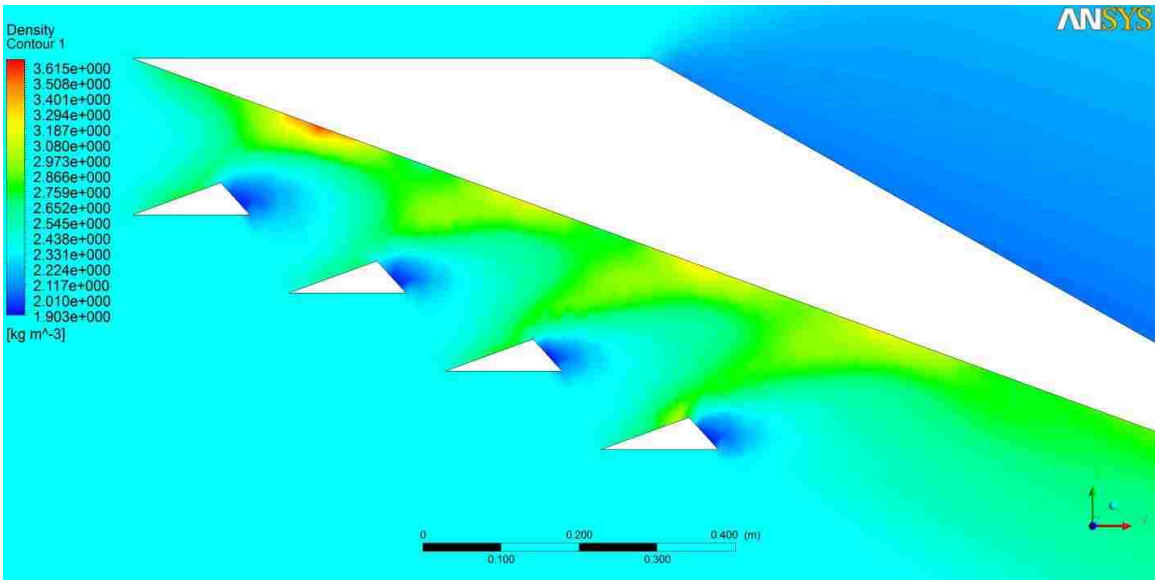

Figure 0.95

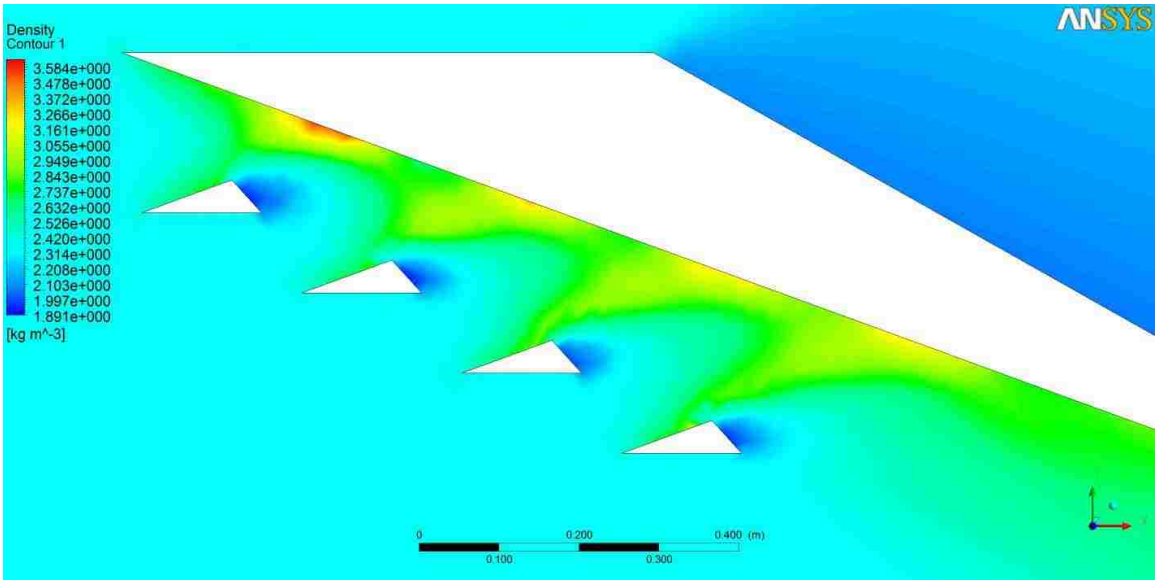

Figure 0.96

MACH 2 20^{O} TIER 3 DENSITY CONTOUR FIGURES

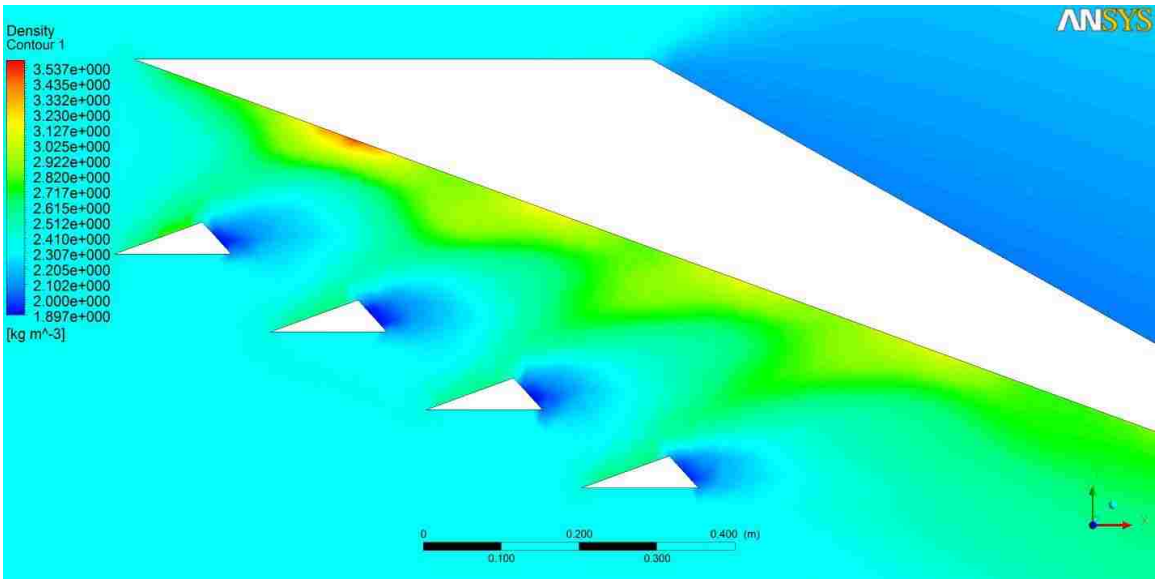

Figure 0.97

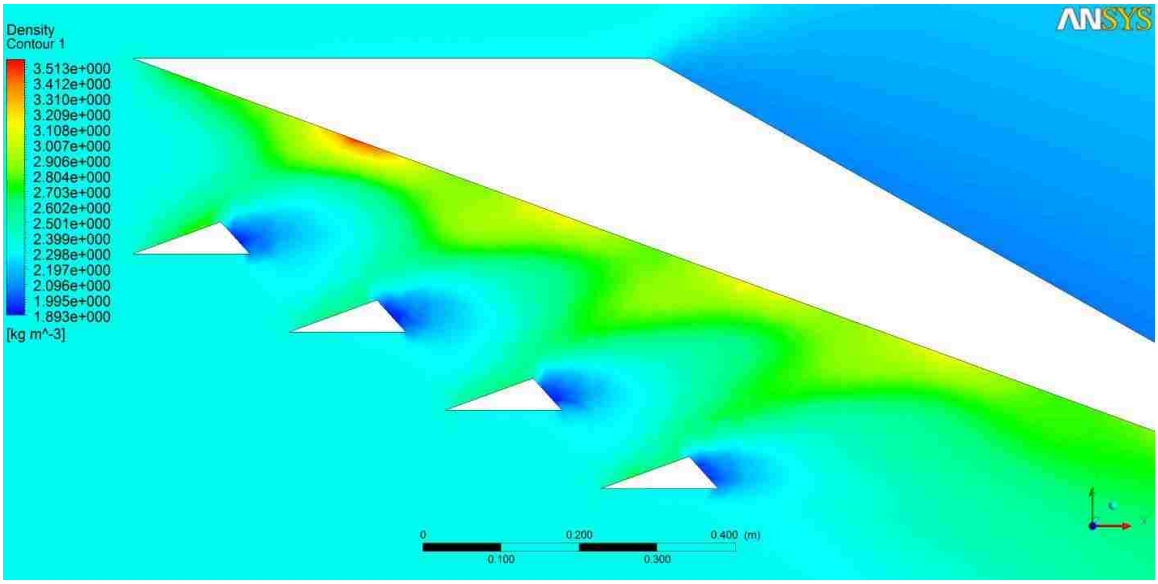

Figure 0.98

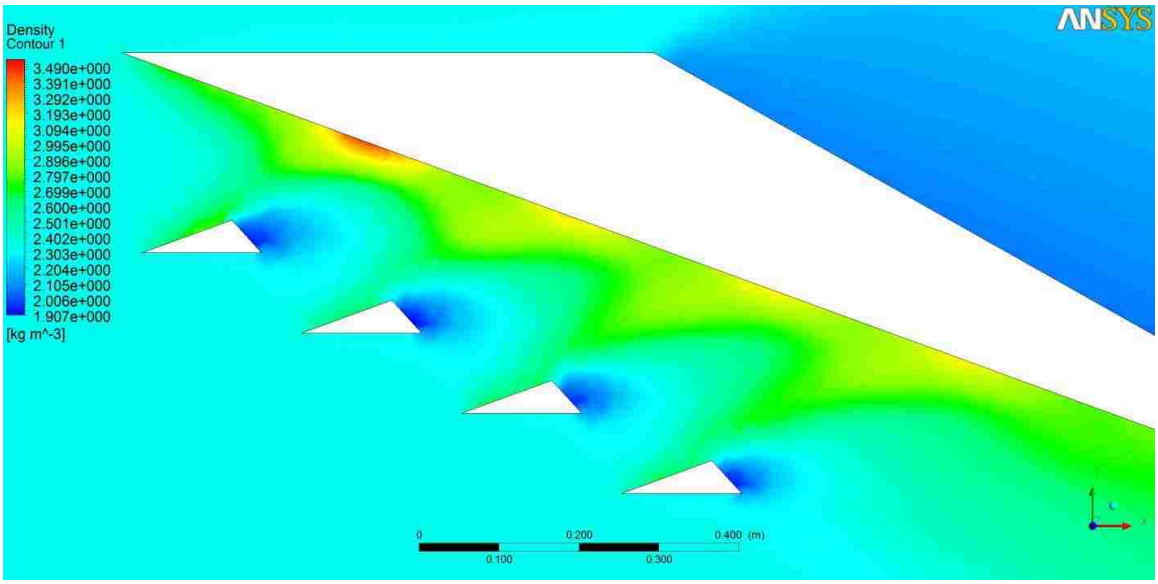

Figure 0.99

MACH 2 20^{O} TIER 4 DENSITY CONTOUR FIGURES

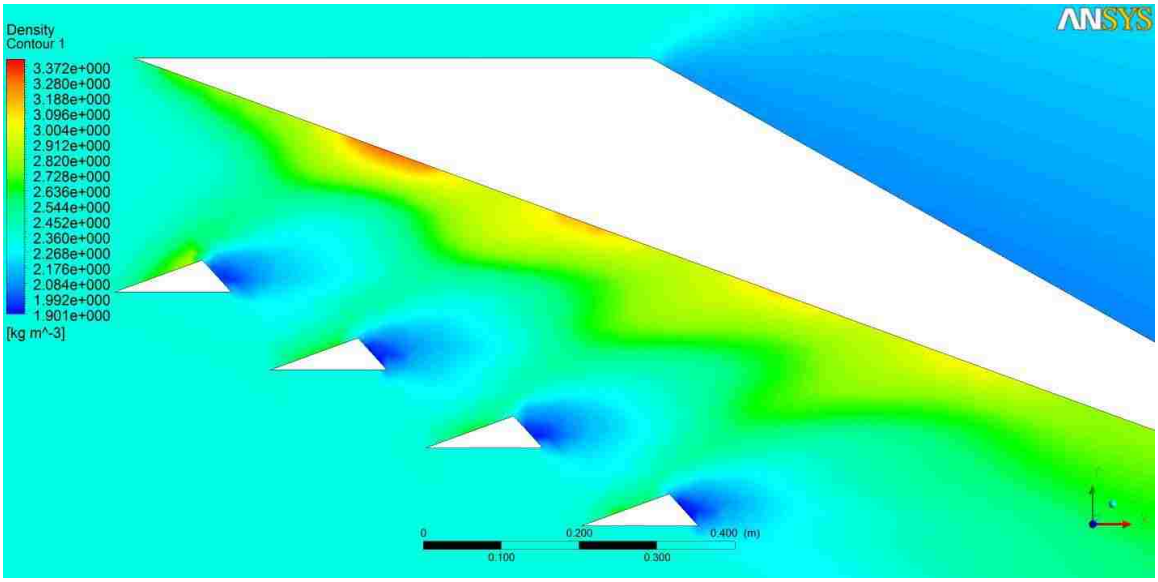

Figure 0.100

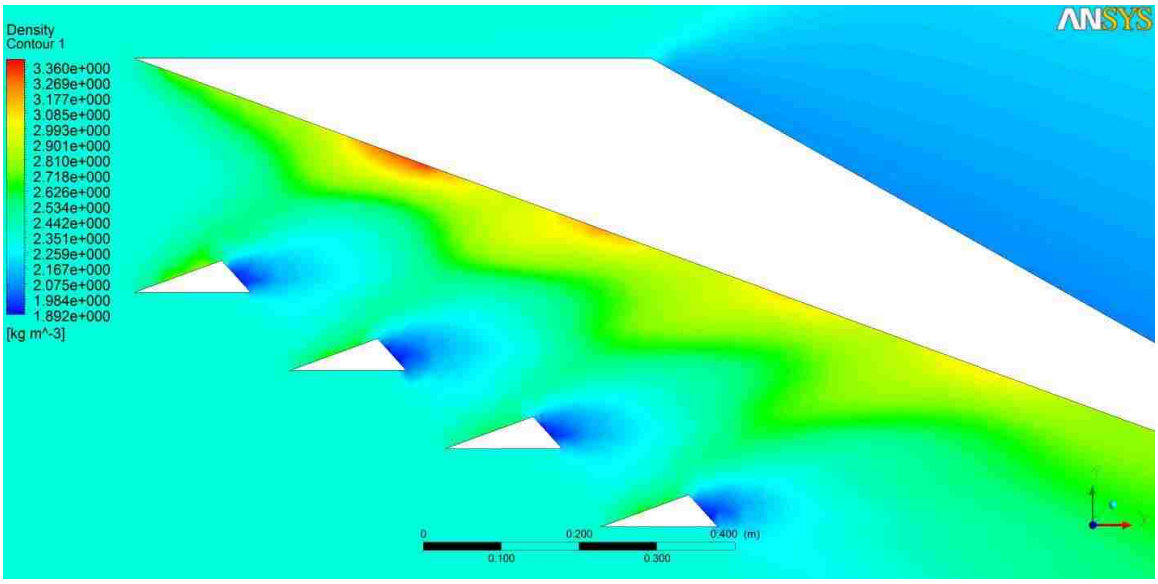

Figure 0.101

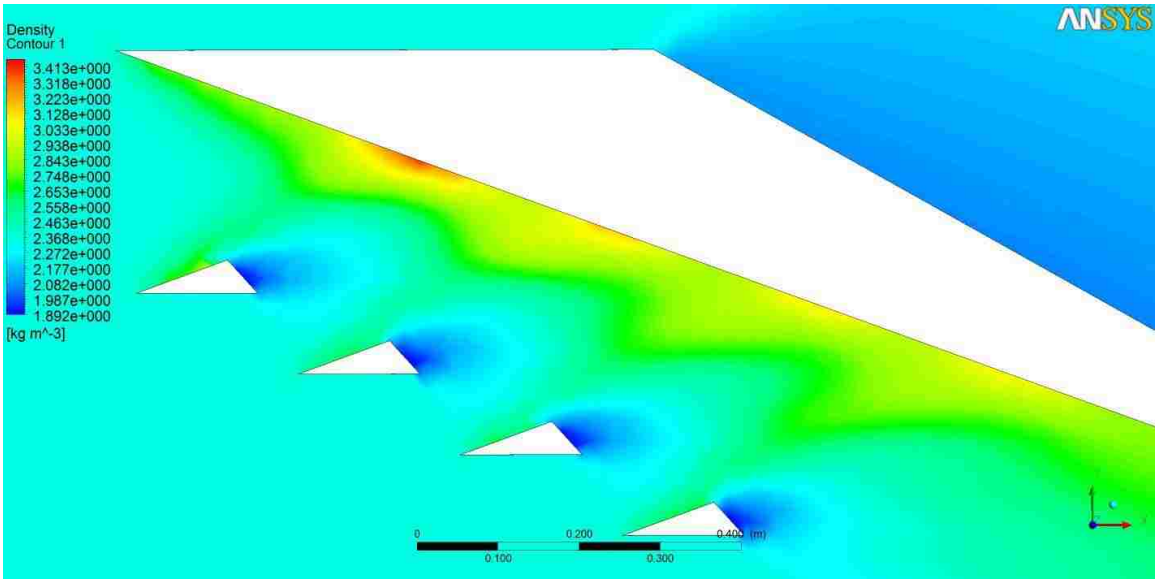

Figure 0.102

MACH 2 20^{O} TIER 5 DENSITY CONTOUR FIGURES

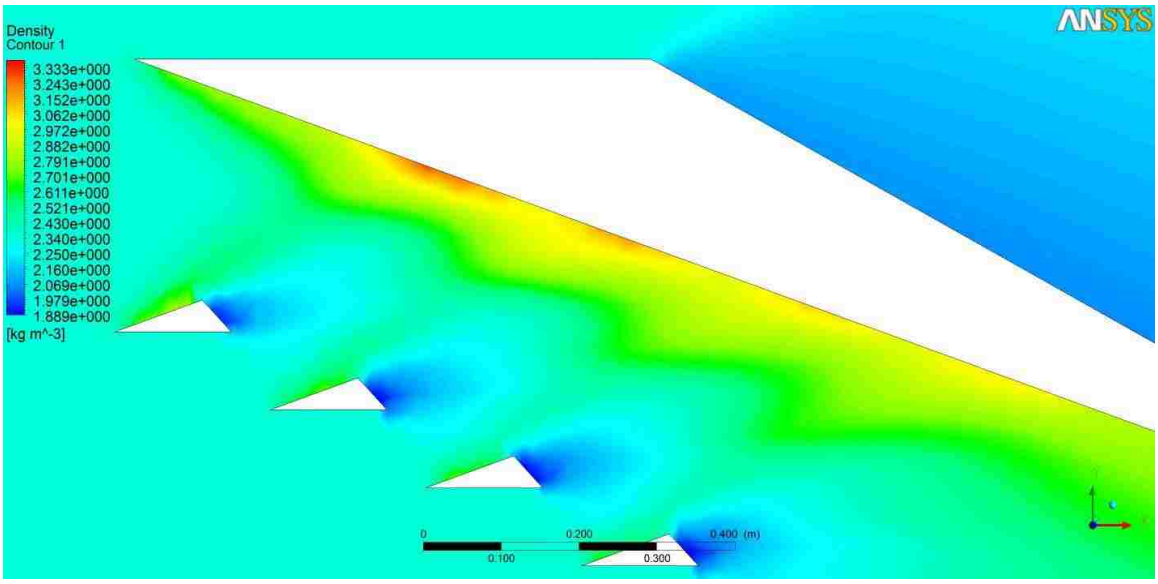

Figure 0.103

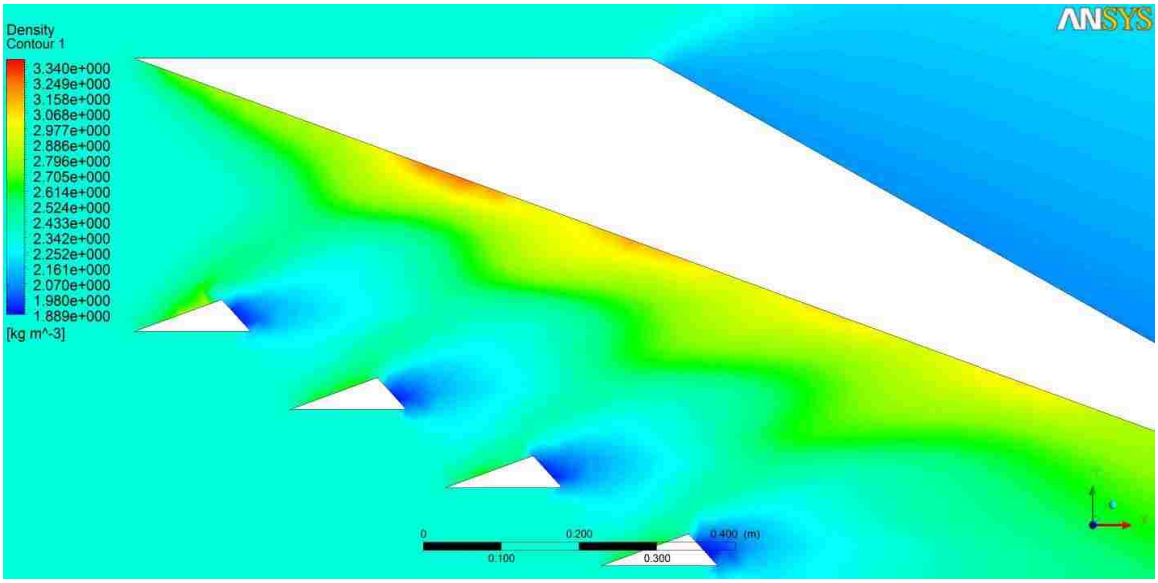

Figure 0.104

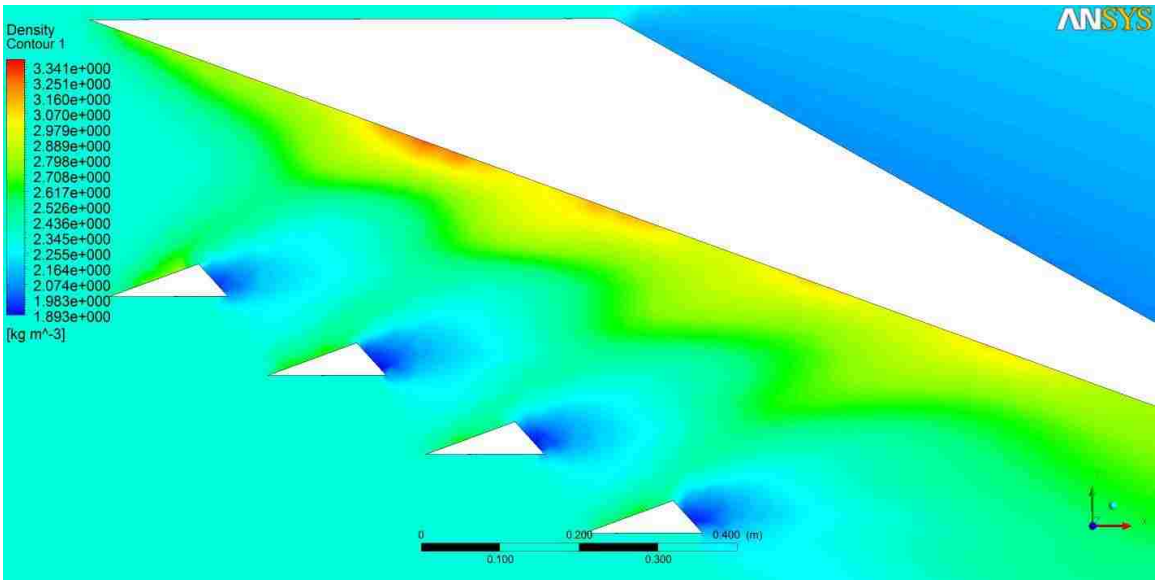

Figure 0.105

MACH 2 RESULTS FIGURES

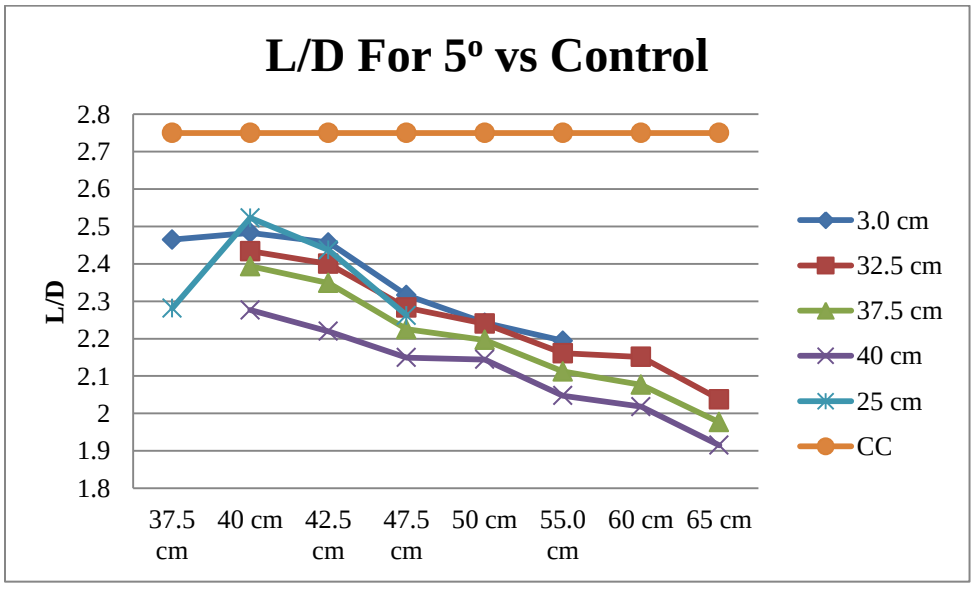

Figure 0.106

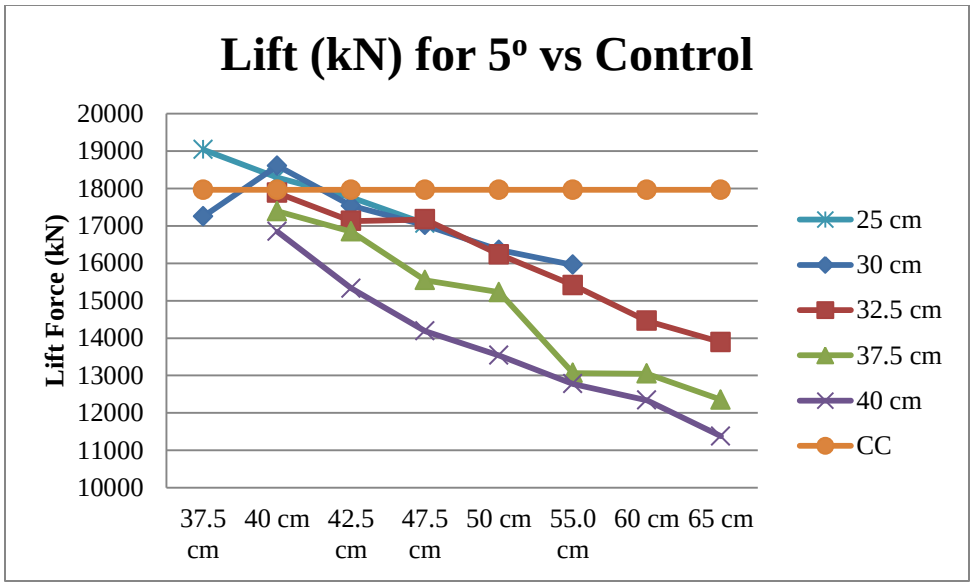

Figure 0.107

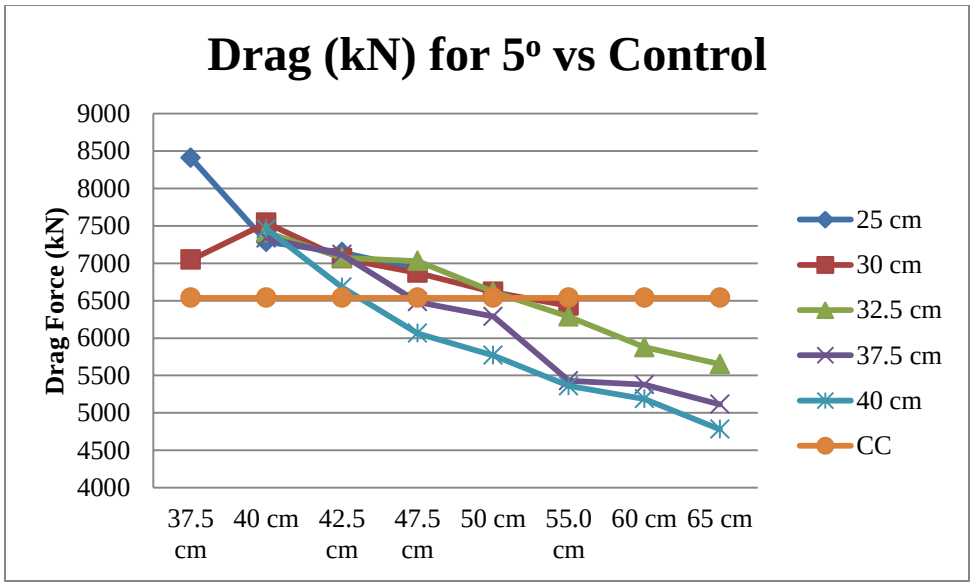

Figure 0.108

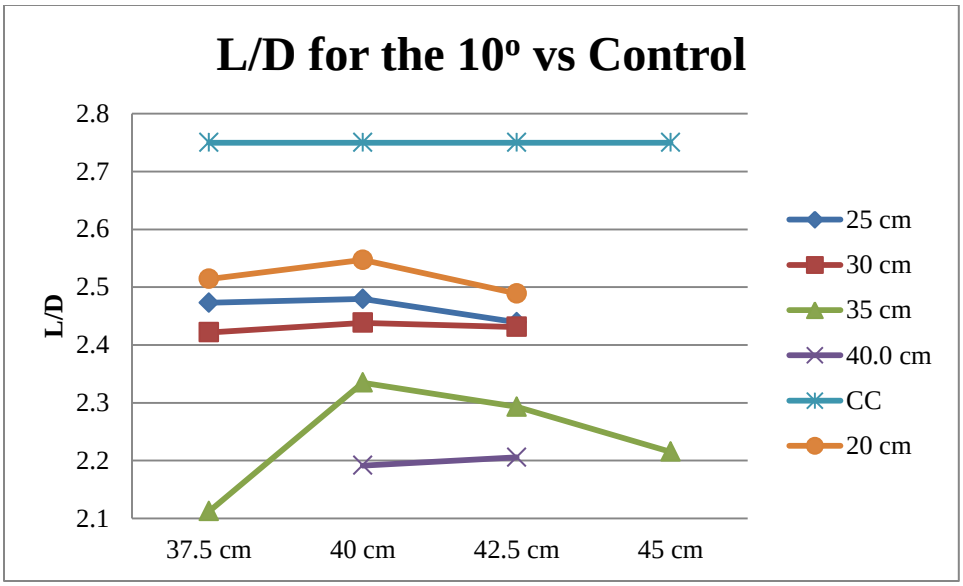

Figure 0.109

Figure 0.110 L/D for 10^{o} vs Control

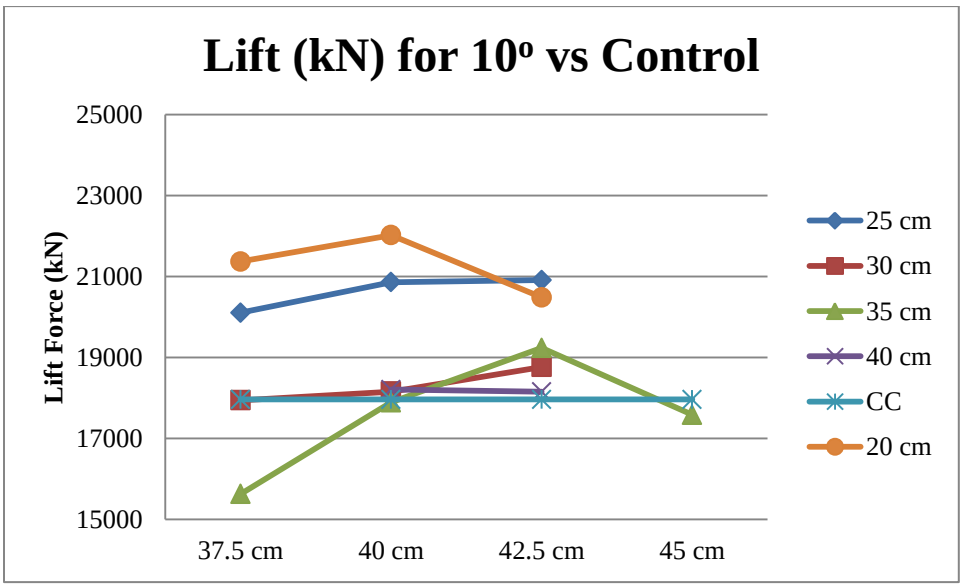

Figure 0.111 Lift (kN) for 10^{o} vs Control

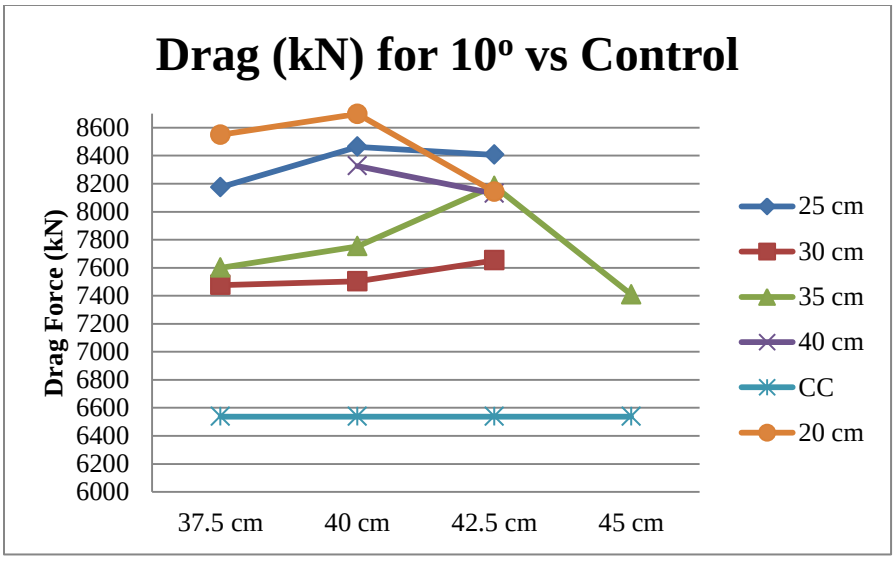

Figure 0.112

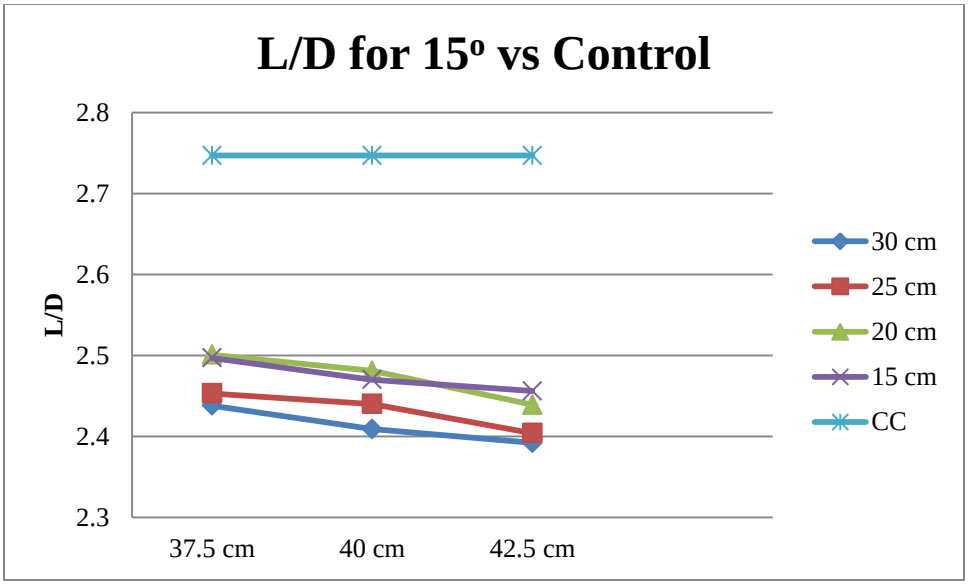

Figure 0.113 L/D for 15º vs Control

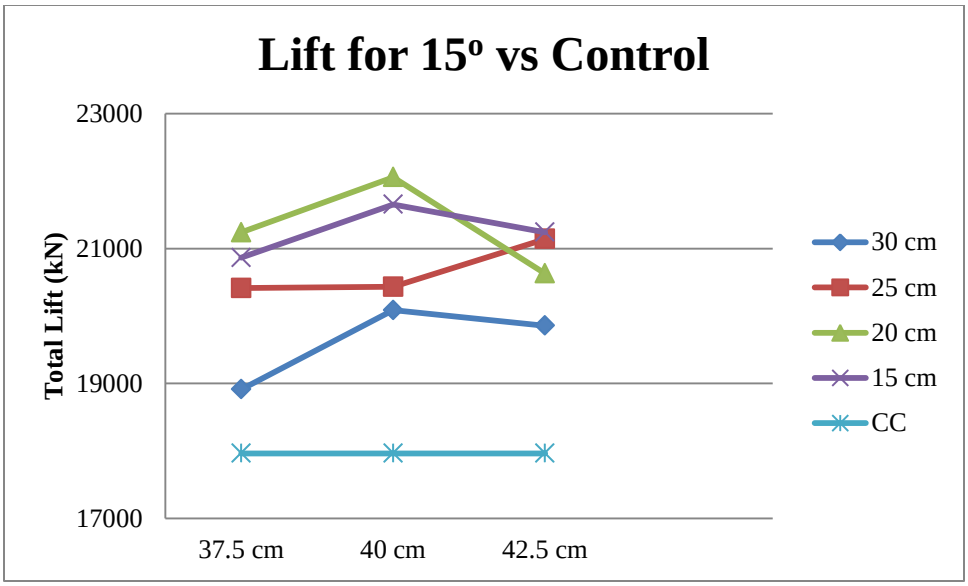

Figure 0.114 Lift For 15° vs Control

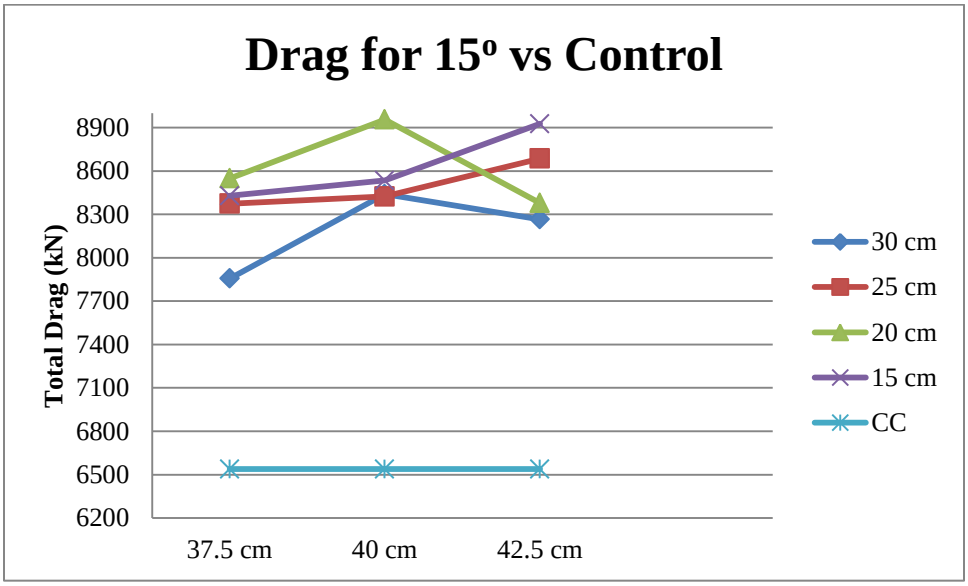

Figure 0.115

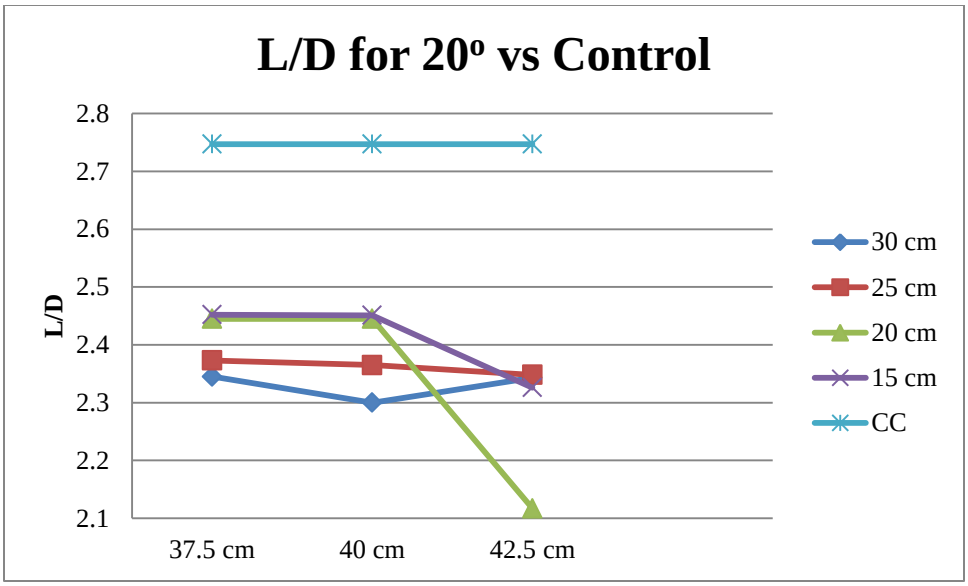

Figure 0.116 L/D for 20º vs Control

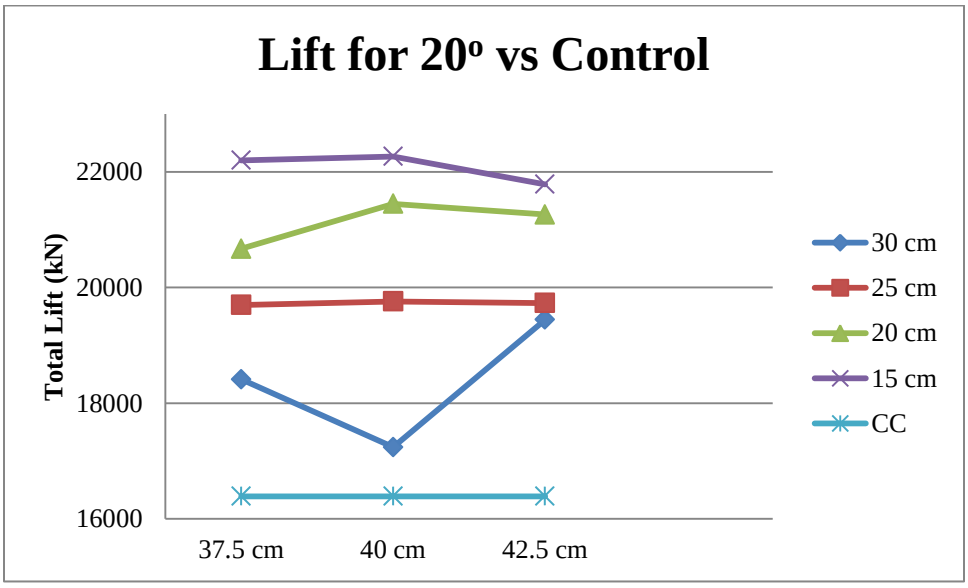

Figure 0.117 Lift for 20º vs Control

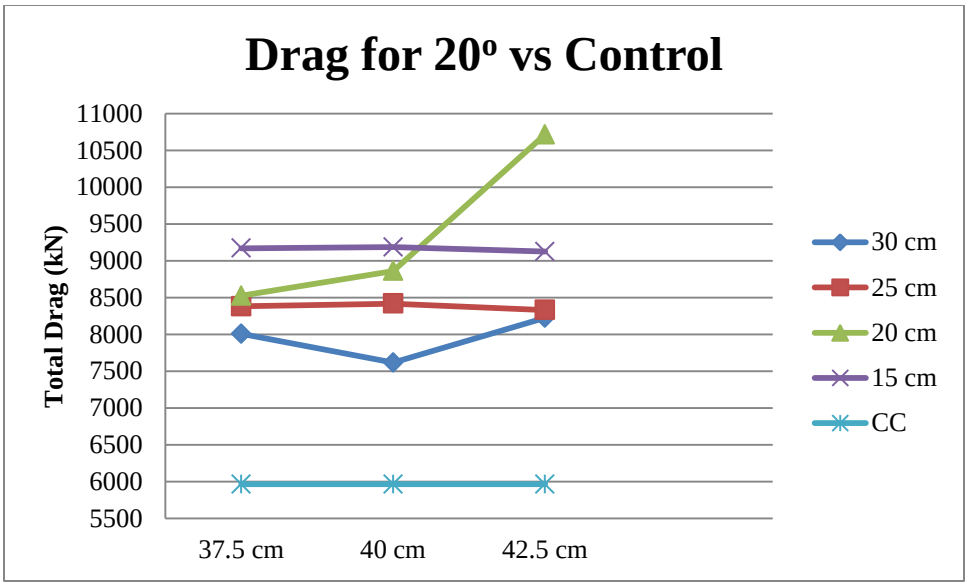

Figure 0.118 Drag for 20º vs Control

MACH 3 RESULTS FIGURES

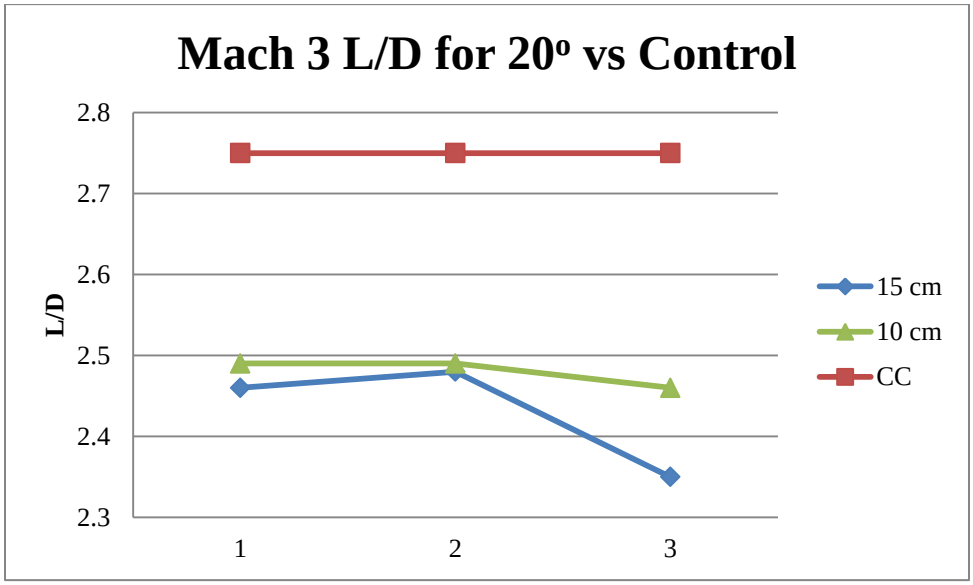

Figure 0.119 Mach 3 L/D for 20º vs Control

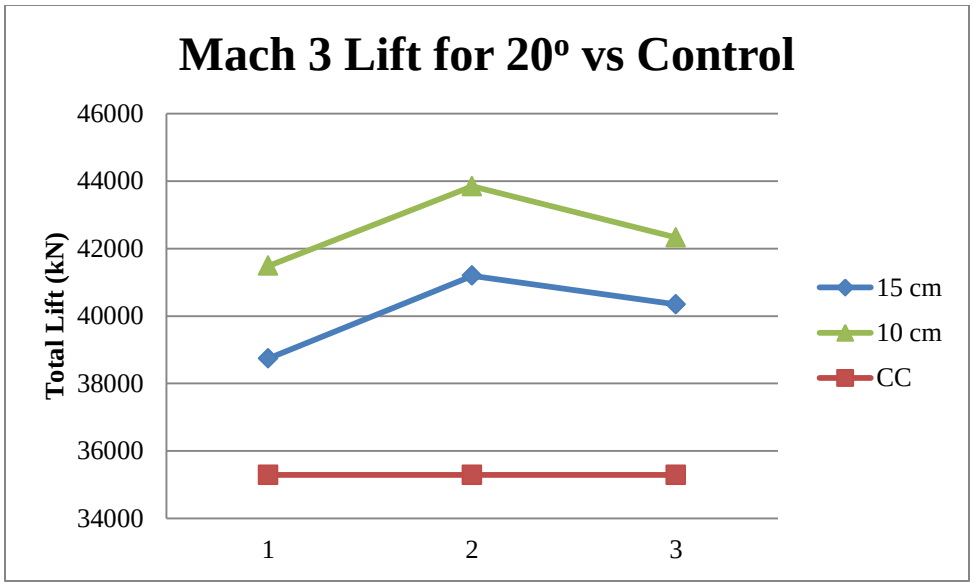

Figure 0.120 Mach 3 Lift for 20^{o} vs Control

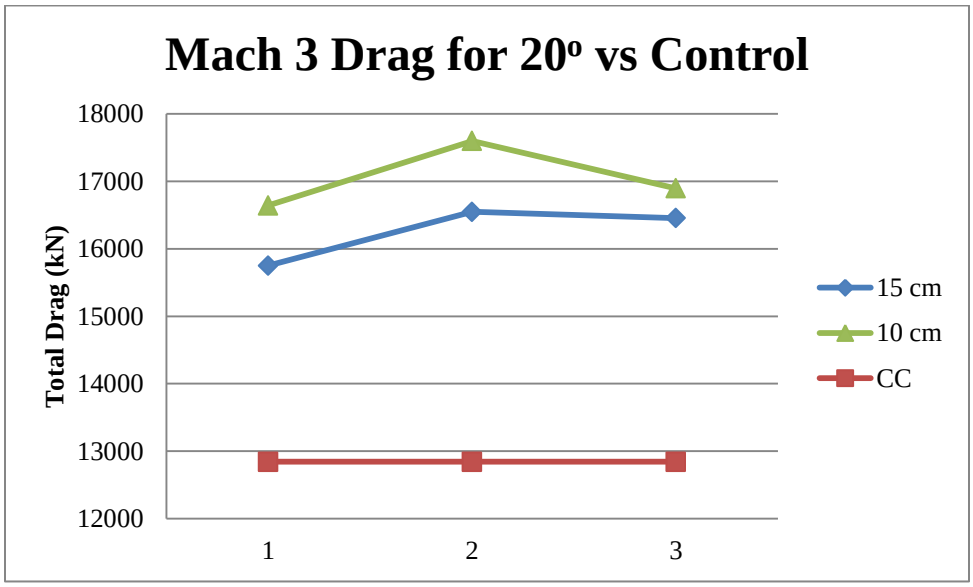

Figure 0.121 Mach 3 Drag for 20^{o} vs Control

MACH 4 RESUTS FIGURES

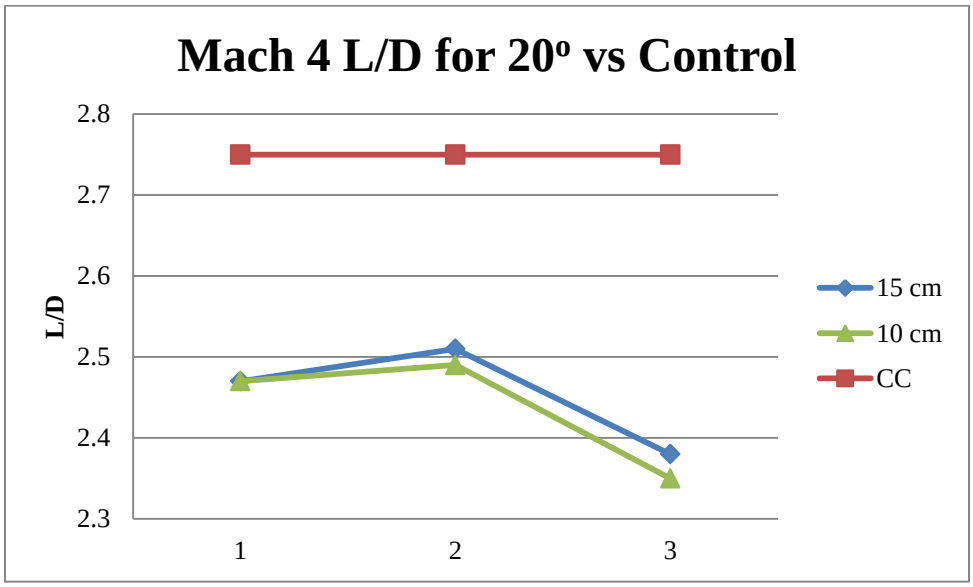

Figure 0.122 Mach 4 L/D for 20^{o} vs Control

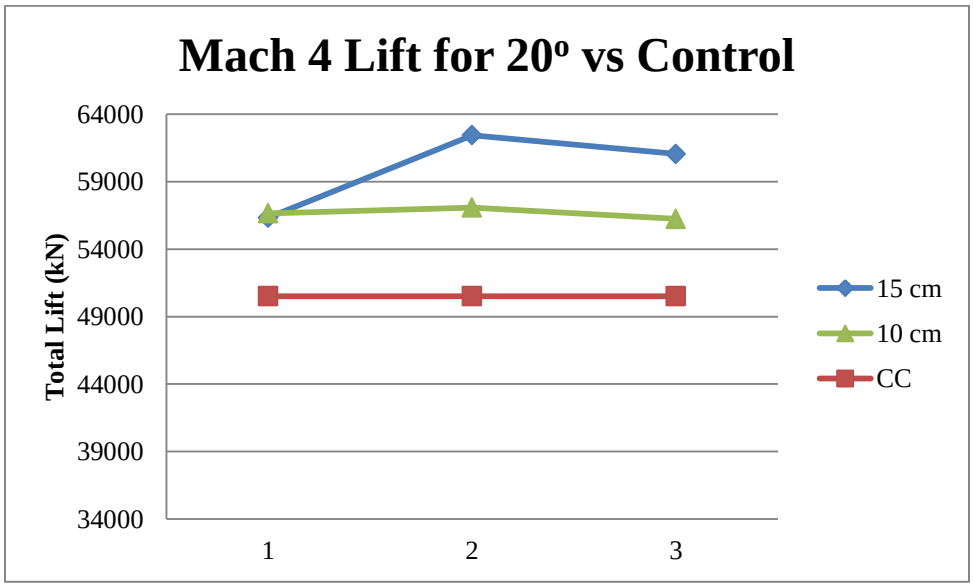

Figure 0.123 Mach 4 Lift for 20^{o} vs Control

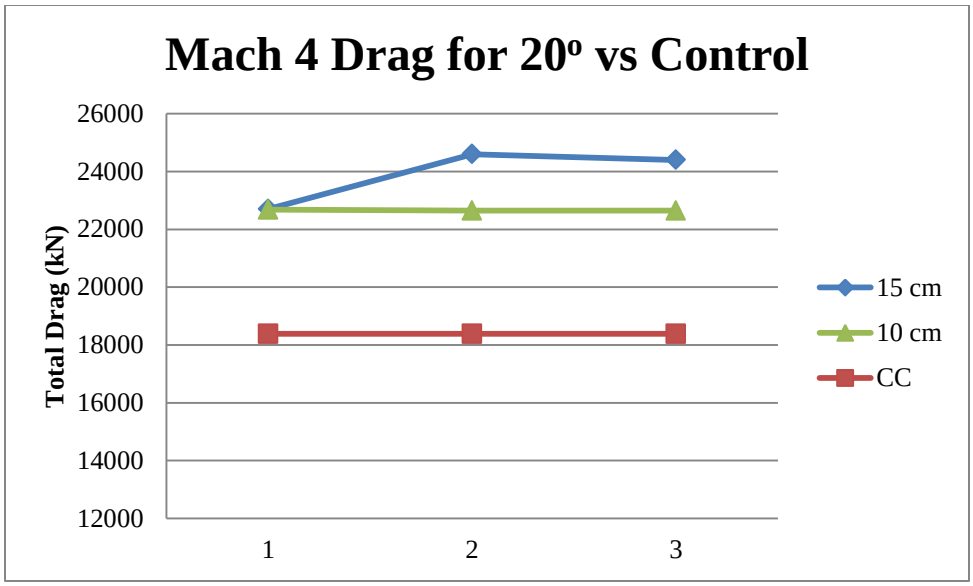

Figure 0.124 Mach 4 Drag for 20^{o} vs Control

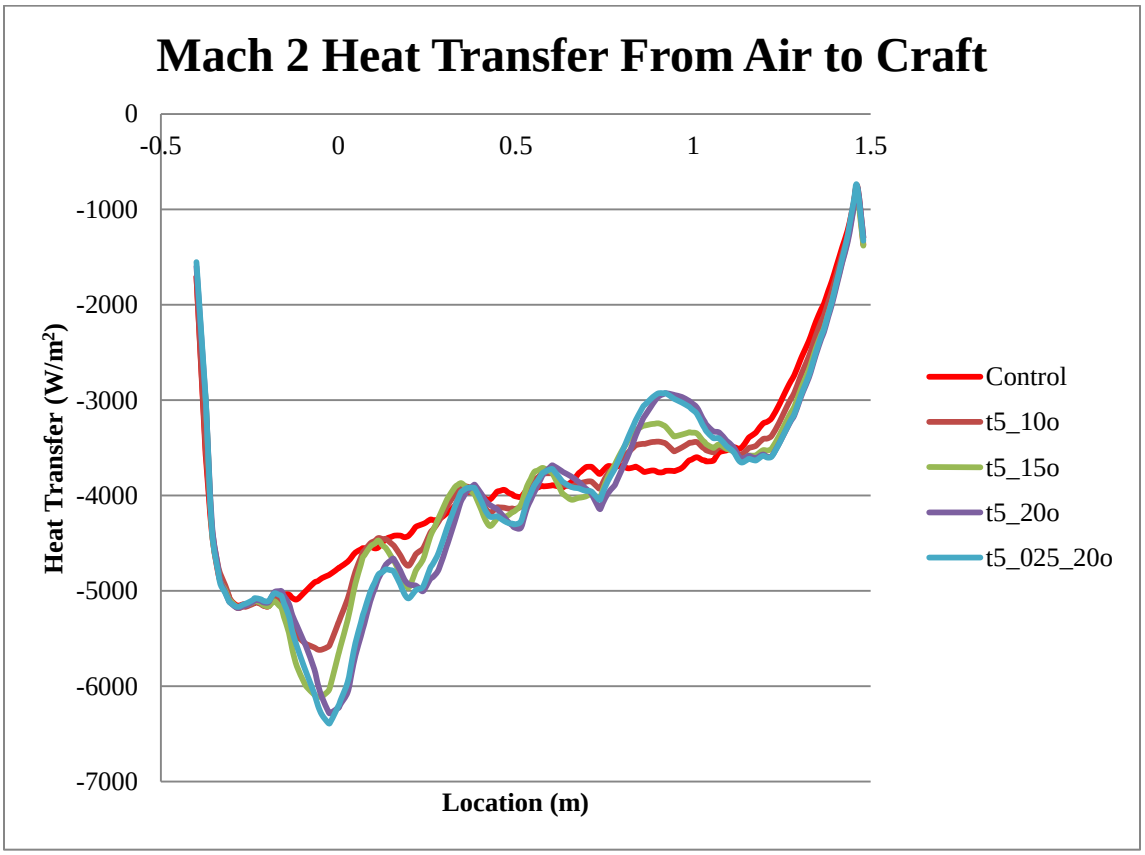

Figure 0.125 Mach 2 Heat Transfer from Air to Craft

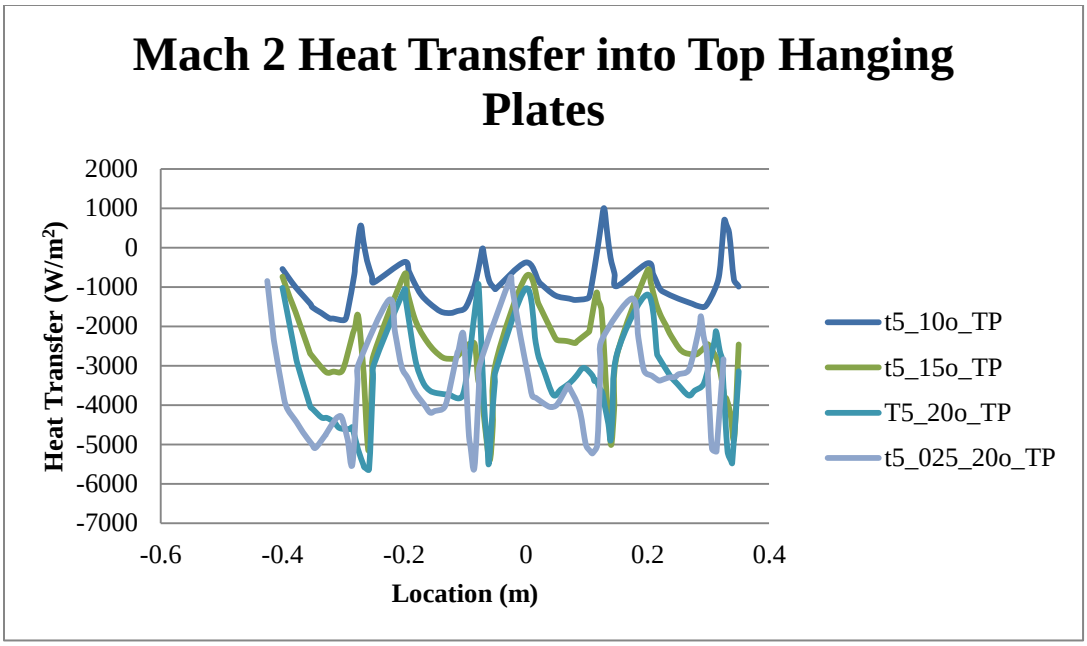

Figure 0.126 Mach 2 Heat Transfer into Top Hanging Plates

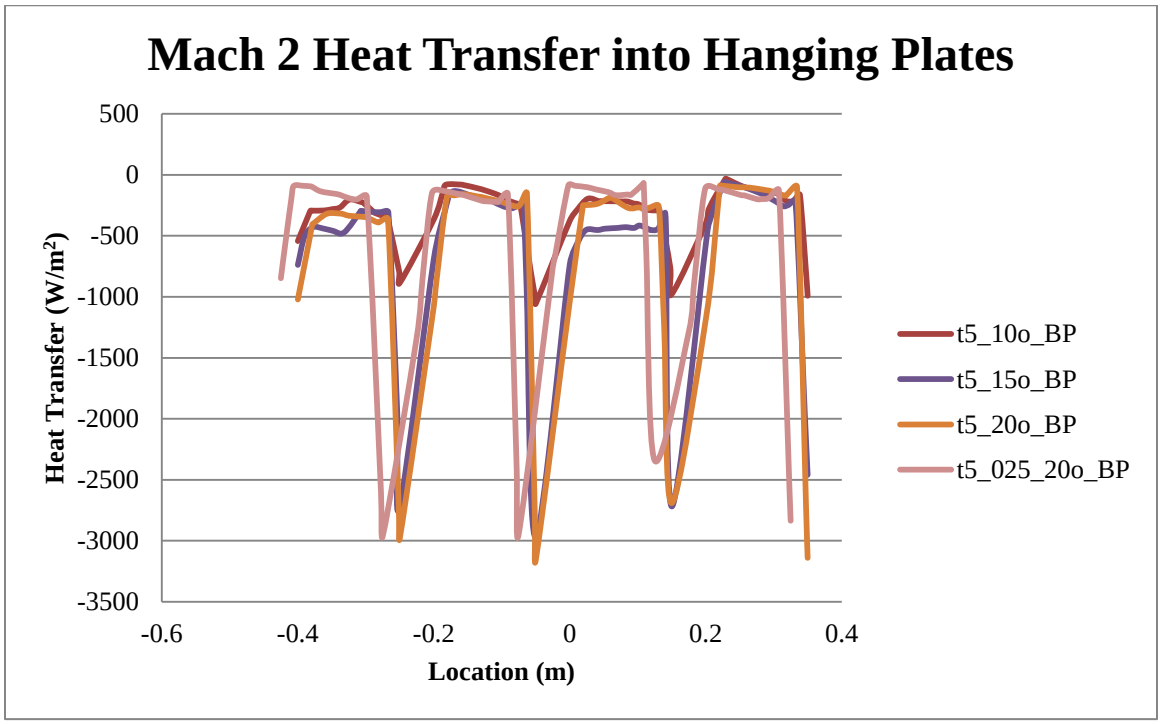

Figure 0.127 Mach 2 Heat Transfer into Hanging Plates

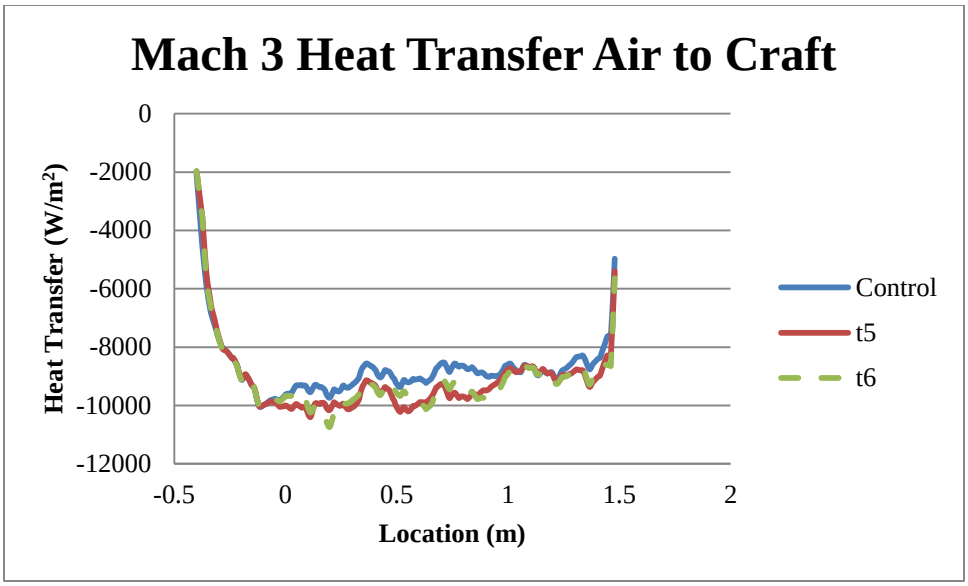

Figure 0.128 Mach 3 Heat Transfer Air to Craft

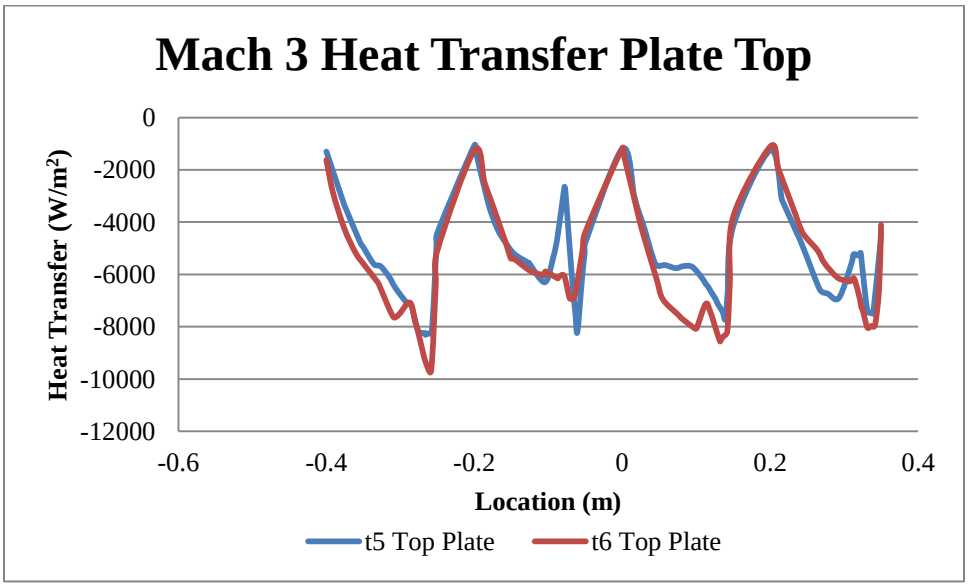

Figure 0.129 Mach 3 Heat Transfer Plate Tops

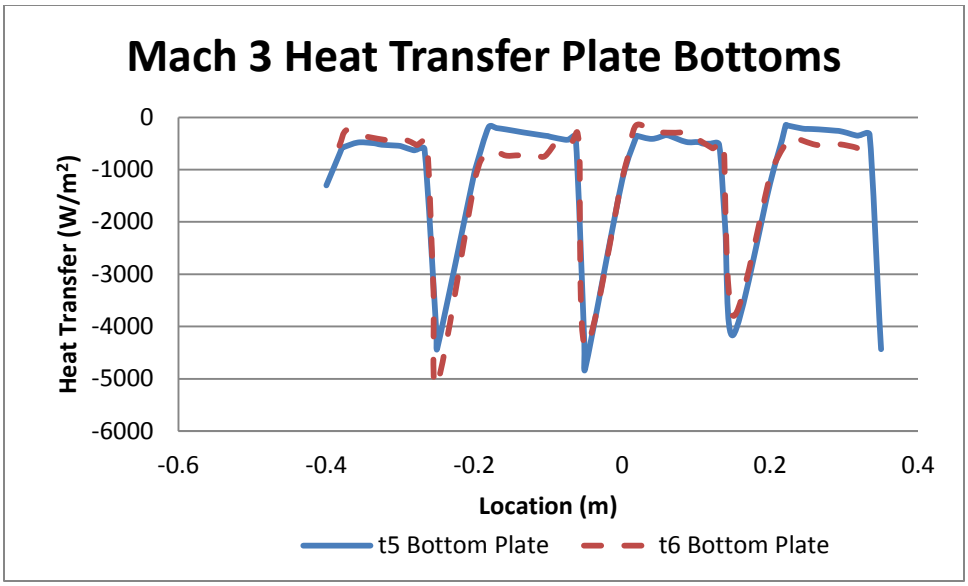

Figure 0.130 Mach 3 Heat Transfer Plate Bottoms

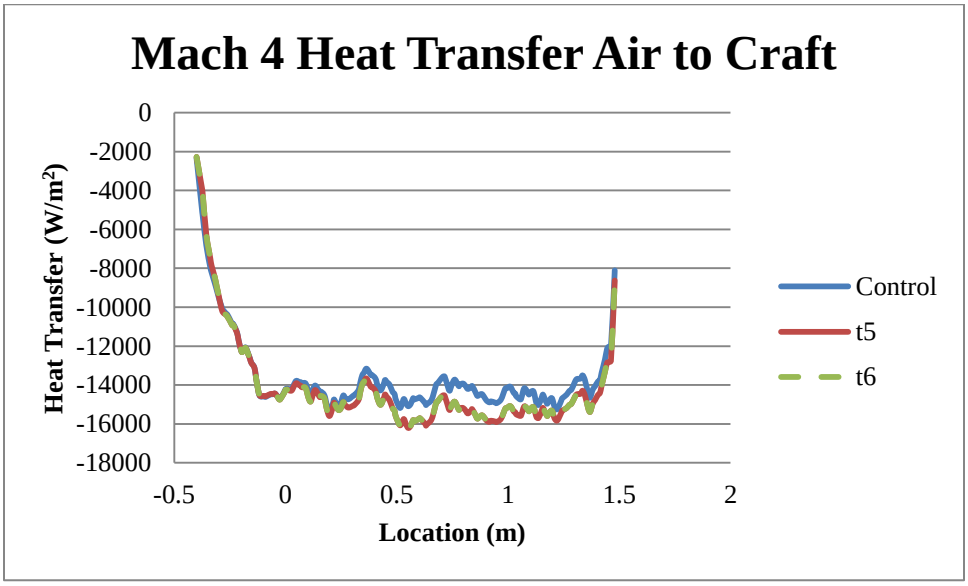

Figure 0.131 Mach 4 Heat Transfer Air to Craft

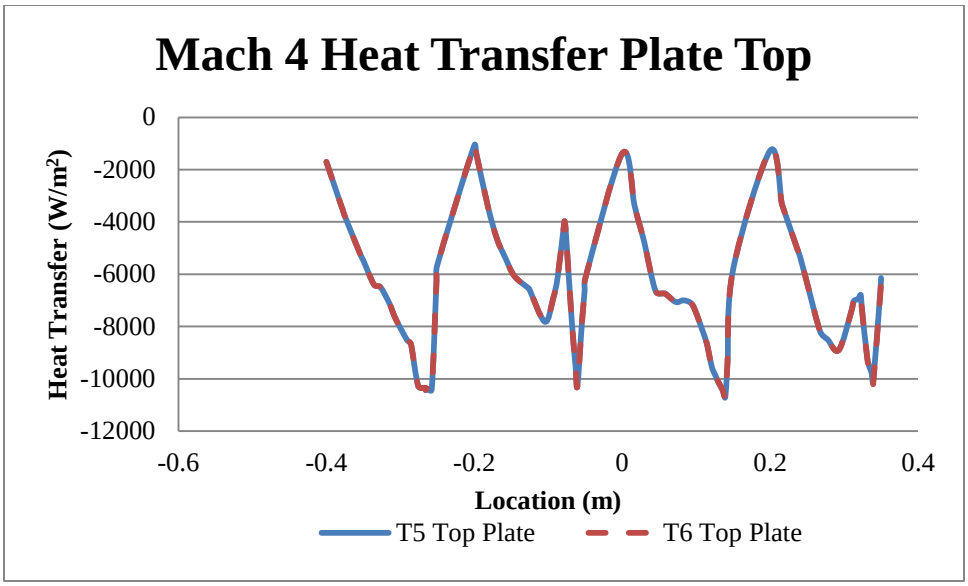

Figure 0.132 Mach 4 Heat Transfer Plate Top

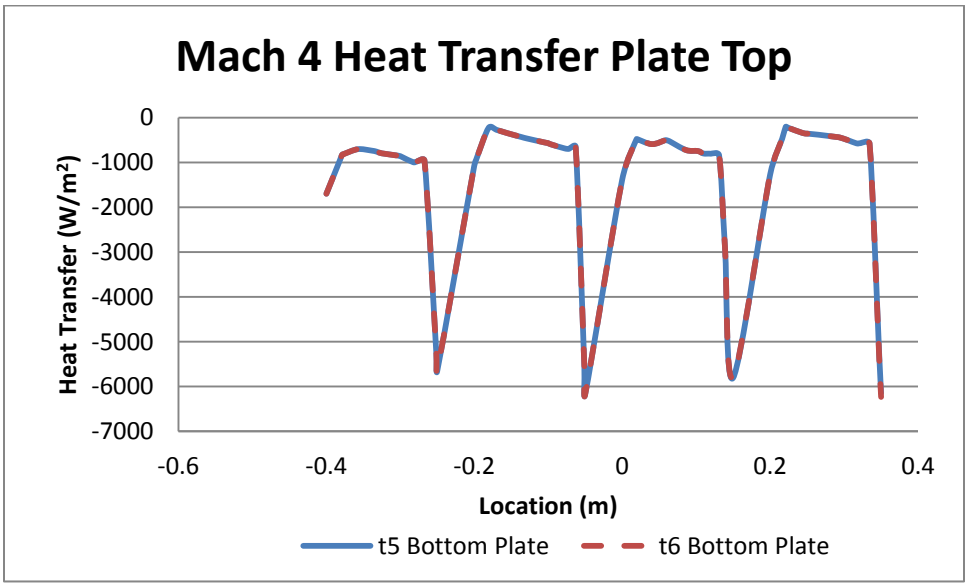

Figure 0.133 Mach 4 Heat Transfer Plate Bottom

APPENDIX B: TABLE

Table 0.1 Control Vehicle Dimensions

Dimension	Value
H1	0.4 m
L13	1.6718 m
A5	20°

Table 0.2 Mach 2 Hanging Place Location

Dimension	Value
A4	5deg
A44	5deg
A45	5deg
A46	5deg
H2	0.375m
H32	0.2m
H33	0.2m
H34	0.2m
H42	0.15m
H7	0.15m
L38	0.15m
L39	0.12m
L40	0.15m
L41	0.12m
L43	0.12m
L6	0.12m
V3	0.4m
V35	0.1m
V36	0.2m
V37	0.3m

Table 0.3 Wave Angles for Experimental Mach Speeds

Mach Speed	Wave Angle (at θ = 20°)

2	53^o
3	38^o
4	33^o
5	30^o

Table 0.4 Control Case and Mach 2 Hanging Plate Case Values

	Value	Unit
Pressure, Mean, CC	161	kPA
Temperature, Mean, CC	315	K
Density, Mean, CC	2.81	$Kg\text{-}m^{-3}$
Pressure, Max, CC	170	kPA
Temperature, Max, CC	321	K
Density, Max, CC	2.98	$Kg\text{-}m^{-3}$
Pressure, Mean, HP, BB	175	kPA
Density, Mean, HP, BB	3.1	$Kg\text{-}m^{-3}$
Temperature, Mean, HP, BB	320	K
Pressure, Max, HP, BB	235	kPA
Density, Max, HP, BB	3.4	$Kg\text{-}m^{-3}$
Temperature, Max, HP, BB	326	K
Pressure, Mean, HP, PT	126	kPA
Density, Mean, HP, PT	2.55	$Kg\text{-}m^{-3}$
Temperature, Mean, HP, PT	308	K
Pressure, Max, HP, PT	165	kPA
Density, Max, HP, PT	2.98	$Kg\text{-}m^{-3}$
Temperature, Max, HP, PT	316	K
Pressure, Mean, HP, PB	104	kPA
Density, Mean, HP, PB	2.42	$Kg\text{-}m^{-3}$
Temperature, Mean, HP, PB	304	K
Pressure, Max, HP, PB	118	kPA
Density, Max, HP, PB	2.54	$Kg\text{-}m^{-3}$
Temperature, Max, HP, PB	309	K
CC=Control Case HP=Hanging Plate Case BB=Bottom Body PT=Plate Top PB=Plate Bottom		

Table 0.5 Top Locations with Plate Angle

Horizontal Displacement	Vertical Displacement	Plate Angle
40 cm	20 cm	10^o

40 cm	20 cm	15^o
40 cm	15 cm	20^o
42.5 cm	15 cm	20^o

Table 0.6 Force Data for Conventional Lifting Wing

Force	**Value (kN)**
Net Force	165
Lifting Force	155
Drag Force	56
Lift/Drag Ratio	2.75

Table 0.7 Horizonatal and Vertical Offset Peak Cases

Horizontal Offset	Vertical Offset	Ratio	Value
37.5	25	L/D	0.85
		Lift	1.10
		Drag	1.15
37.5	30	L/D	0.89
		Lift	0.96
		Drag	1.08
40	25	L/D	0.92
		Lift	1.02
		Drag	1.15
40	30	L/D	0.90
		Lift	1.04
		Drag	1.15

Table 0.8 Ratio for 10^o Hanging Plate Cases Compared to Control Case

	L/D Ratio			
Tier	X Location	37.5 cm	40 cm	42.5 cm
Y Location				
20 cm		0.914182	0.926182	0.905091
25 cm		0.899276	0.901644	0.886905
30 cm		0.880604	0.886648	0.884077

35 cm		0.768162	0.849071	0.833867
40.0 cm		0	0.796931	0.802001
CC		1	1	1
	Lift Ratio			
20 cm		1.189647	1.225772	1.140384
25 cm		1.119046	1.161227	1.164024
30 cm		0.998864	1.010724	1.044619
35 cm		0.869805	0.995896	1.070701
40 cm		0	1.013495	1.010546
CC		1	1	1
	Drag Ratio			
20 cm		1.307586	1.330223	1.245488
25 cm		1.25035	1.294514	1.285754
30 cm		1.143594	1.147536	1.17045
35 cm		1.162499	1.185798	1.251728
40 cm		0	1.273455	1.243506
CC		1	1	1

Table 0.9 Ratio for 15^{o} Hanging Plate Cases
Compared to Control Case

	L/D Average			
Y Location	X Location	37.5 cm	40.0 cm	42.5 cm
30 cm		0.887514	0.876957	0.870768
25 cm		0.892974	0.888242	0.875137
20 cm		0.910448	0.903167	0.887878
15 cm		0.908992	0.899163	0.894066
CC		1	1	1
	Total Lift			
30 cm		1.052714	1.118063	1.105316
25 cm		1.136376	1.137434	1.1769
20 cm		1.182243	1.227888	1.1484
15 cm		1.161481	1.205344	1.182355
CC		1	1	1
	Total Drag			
30 cm		1.201744	1.290915	1.264301

25 cm		1.28082	1.288467	1.328694
20 cm		1.307586	1.369991	1.281585
15 cm		1.289232	1.305445	1.365402
CC		1	1	1

Table 0.10 Ratio for 20^{o} Hanging Plate Cases Compared to Control Case

	L/D Average			
Y Location				
30 cm		0.853659	0.837277	0.85293
25 cm		0.863851	0.860939	0.854751
20 cm		0.890062	0.890062	0.770659
15 cm		0.89261	0.892246	0.846742
CC		1	1	1
	Total Lift			
30 cm		1.123444	1.051867	1.186417
25 cm		1.202038	1.20576	1.204113
20 cm		1.26135	1.308701	1.297474
15 cm		1.354589	1.358677	1.329326
CC		1	1	1
	Total Drag			
30 cm		1.342891	1.276995	1.379108
25 cm		1.405433	1.411636	1.397217
20 cm		1.42941	1.485915	1.796781
15 cm		1.537726	1.540241	1.530013
CC		1	1	1

Table 0.11 Control Case Notable Variables

	Total Lift	Total Drag	Average Force	Average Lift	Average Drag
Mach 2	26944	9806	164.81	154.87	56.37
Mach 3	35288	12843	259	243	86
Mach 4	50515	18385	371	348	127

Table 0.12 Mach 3 Hanging Plate Values vs Control

L/D Average				
Y Location	X Location	37.5 cm	40 cm	42.5 cm
15 cm		0.894545	0.901818	0.854545
10 cm		0.905455	0.905455	0.894545
CC		1	1	1
Total Lift				
15 cm		1.097824	1.167366	1.143278
10 cm		1.175669	1.242575	1.199558
CC		1	1	1
Total Drag				
15 cm		1.226505	1.288406	1.281243
10 cm		1.295959	1.370318	1.31558
CC		1	1	1

Table 0.13 Mach 4 Hanging Plate cases vs Control

L/D Average				
Y Location	X Location	37.5 cm	40 cm	42.5 cm
15 cm		0.898182	0.912727	0.865455
10 cm		0.898182	0.905455	0.854545
CC		1	1	1
Total Lift				
15 cm		1.115213	1.236068	1.208611
10 cm		1.121508	1.130001	1.113352
CC		1	1	1
Total Drag				
15 cm		1.234581	1.337866	1.326934
10 cm		1.233493	1.231752	1.231644
CC		1	1	1

BIBLIOGRAPHY

Amaha, A. H., Singh, A., & Martis, R. R. (2011, March). *Shock Wave Turbulent Boundary Layer Interaction in a 2-D Compression Corner*. Retrieved August 13, 2011, from International Journal of Engineering Science and Technology: http://www.ijest.info/docs/IJEST11-03-03-214.pdf

Arnal, D., & Delery, J. (2004, May 14). *Shock Wave/Boundary Layer Interaction*. Retrieved August 13, 2011, from Laminar-Turbulent Transition and Shock Wave/Boundary Layer Interaction: http://ftp.rta.nato.int/public//PubFullText/RTO/EN/RTO-EN-AVT-116///EN-AVT-116-04.pdf

Berry, C., & Vas, I. (1972). *An Experimental Investigation of Laminar Heat Transfer to Cones at Hypersonic Speeds*. Air Force System Commands.

Bruno, C. (1986). Real Gas Effects. In J. Bertin, R. Glowinski, & J. Periaux, *Hypersonics, Volume 1* (pp. 303-310). Cambridge: Birkhauser Boston.

Chernyi, G. (1961). *Introduction to Hypersonic Flow*. New York: Academic Press.

Courant, R., & Friedrichs, K. O. (1948). *Supersonic Flow and Shock Waves*. New York: Interscience Publishers Inc.

Freytag, D. B. (2010, November 5). *Rankine–Hugoniot conditions*. Retrieved August 12, 2011, from Department of Astronomy of Space Physics, Uppsala University: http://www.astro.uu.se/~bf/course/numhd_course/4_2_2Rankine_Hugoniot_condi.html

Hayes, W. D., & Probstein, R. F. (1966). *Hypersonic Flow Theory*. New York: Academic Press.

Hunt, J. L. (1989). Hypersonic Airbreathing Vehicle Design (Focus on Aero-Space Place). In J. Bertin, R. Glowinski, & J. Periaux, *Hypersonics, Volume 1* (pp. 205-262). Cambridge: Birkhauser Boston.

Kienappel, K., Koppenwallner, G., & Legge, H. (1974). Force and Heat Transfer Measurements on Inclined Cones in the Hypersonic Range from Continuum to Free Molecular Flow. *Rarefied Gas Dynamics* (pp. 317-325). New York: Academic Press.

Koppenwallner, G. (1987). Low Reynolds Number Influence on Aerodynamic Performance of Hypersonic Vehicles. *AGARD Conference on Aerodynamic of Hypersonic Lifting Vehicles*, (pp. 11-1 - 11-14). Bristol.

Mikhailov, G. K., & Parton, V. Z. (1993). Supersonic Flows at Low to Moderate Reynolds Number. In E. A. Gershbin, S. V. Peigin, & G. A. Tirskii, *Super- and Hypersonic Aerodynamics and Heat Transfer* (pp. 3 - 69). Boca Raton: CRC Press.

NASA. (2010, November 11). *Euler equations (fluid dynamics)*. Retrieved August 12, 2011, from NASA: http://www.grc.nasa.gov/WWW/k-12/airplane/eulereqs.html

NASA. (2010, September 10). *Oblique shock*. Retrieved August 12, 2011, from NASA: http://www.grc.nasa.gov/WWW/k-12/airplane/oblique.html

NASA. (2010, September 8). *Prandtl-Meyer Angle*. Retrieved August 12, 2011, from NASA: http://www.grc.nasa.gov/WWW/k-12/airplane/pranmyer.html

National Aeronautics and Space Administration. (2008, July 29). *Crossed Shock Waves*. Retrieved August 12, 2011, from NASA - Glenn Research Center: http://www.grc.nasa.gov/WWW/k-12/airplane/crosshock.html

Pepper, D. W., & Heinrich, J. C. (2006). *The Finite Element Method* (Second ed.). Boca Raton: Taylor & Francis Group.

Zienkiewicz, O. C., Taylor, R. L., & Nithiarasu, P. (2005). *The Finite Element Method for Fluid Dynamics* (Sixth ed.). Jordan Hill: Butterworth-Heinemann.

VITA

Graduate College
University of Nevada, Las Vegas

John Michael Dixon

Degrees:
Bachelor of Science, Aerospace and Aeronautical Engineering, 2009
Purdue University

Thesis Title: Heat, Mass and Force Flows in Supersonic Shockwave Interaction

Thesis Examination Committee:
Chairperson, Darrell Pepper, Ph. D.
Committee Member, William Culbreth, Ph. D.
Committee Member, Hui Zhao, Ph. D.
Graduate Faculty Representative, Evangelos Yfantis, Ph. D.